

UNIVERSITY OF SÃO PAULO
SCHOOL OF ENGINEERING OF SÃO CARLOS

BRUNA CALLEGARI

**Understanding the impact of microstructure on the response of titanium alloys to aging
treatments**

São Carlos

2020

BRUNA CALLEGARI

**Compreendendo o impacto microestrutural na resposta de ligas de titânio a tratamentos
de envelhecimento**

Versão Corrigida

Tese apresentada ao Programa de Pós-Graduação em Engenharia Mecânica da Escola de Engenharia de São Carlos, Universidade de São Paulo, como parte dos requisitos para obtenção do título de Doutora em Ciências.

Área de concentração: Materiais

Orientador: Prof. Dr. Haroldo Cavalcanti Pinto

São Carlos

2020

I AUTHORIZE THE TOTAL OR PARTIAL REPRODUCTION OF THIS WORK,
THROUGH ANY CONVENTIONAL OR ELECTRONIC MEANS, FOR STUDY AND
RESEARCH PURPOSES, SINCE THE SOURCE IS CITED.

Catalog card prepared by Patron Service at "Prof. Dr. Sergio
Rodrigues Fontes" Library at EESC/USP

C157u Callegari, Bruna
Understanding the impact of microstructure on the
response of titanium alloys to aging treatments / Bruna
Callegari; promoters Haroldo Cavalcanti Pinto. -- São
Carlos, 2010.
Doctorate (Thesis) - Graduate Program in Mechanical
Engineering and Research Area in Materials of the School of
Engineering of São Carlos at University of São Paulo, 2020.
1. Titanium alloys. 2. Phase transformations.
3. Hardening. 4. Thermomechanical processing. 5. Aging.
6. Electron backscatter diffraction. 7. X-ray diffraction.
8. Synchrotron radiation. I. Title.

Elena Luzia Palloni Gonçalves - CRB 8/4464

FOLHA DE JULGAMENTO

Candidata: Engenheira **BRUNA CALLEGARI**.

Título da tese: "Compreendendo o impacto microestrutural na resposta de ligas de titânio a tratamentos de envelhecimento".

Data da defesa: 29/07/2020

Comissão Julgadora	Resultado
Prof. Associado Haroldo Cavalcanti Pinto (Orientador) (Escola de Engenharia de São Carlos – EESC/USP)	APROVADO
Prof. Dr. Conrado Ramos Moreira Afonso (Universidade Federal de São Carlos/UFSCar)	APROVADO
Prof. Dr. Frank Thomas Mücklich (Universität des Saarlandes)	APROVADO
Prof. Dr. Piter Gargarella (Universidade Federal de São Carlos/UFSCar)	APROVADO
Prof. Dr. Rodrigo Santiago Coelho (Faculdade de Tecnologia SENAI)	APROVADO

Coordenador do Programa de Pós-Graduação em Engenharia Mecânica:
Prof. Associado **Carlos de Marqui Junior**

Presidente da Comissão de Pós-Graduação:
Prof. Titular **Murilo Araujo Romero**

DEDICATION

To my beloved parents, who have supported me lovingly and unconditionally in each and every way throughout this true academic quest, giving me strength to accomplish my goals.

ACKNOWLEDGEMENTS

To my supervisor, Prof. Dr. Haroldo C. Pinto, for continuously pushing me to overcome my limits and allowing me to prove myself capable of evolving independently.

To Prof. Dr. Hugo Ricardo Z. Sandim (DEMAR-EEL-USP) and to Priv.-Doz. Dr. José García and Dr. M. Ibrahim Sadik (Sandvik Machining Solutions, Stockholm, Sweden) for kindly providing the alloys used in this work.

To my friends and colleagues from the Physical Metallurgy Laboratory, Bruno C. N. M. de Castilho, Leandro Henrique M. Guimarães, Maiara Fernanda Moreno, Pedro Renato T. Avila, Rafael P. M. Guimarães, Raira C. Apolinário, for the companion and support during the development of this work.

To Dr. Javier A. M. Chaves and Dr. Paulo W. B. Marques, from UFSCar, whose help was also essential in many ways, but especially for the execution of the in situ experiments at the LNLS.

To Prof. Dr. João Pedro Oliveira (Universidade Nova de Lisboa) for the help during the execution of HEXRD experiments at DESY and during the writing of resulting papers.

To Prof. Dr. Rodrigo S. Coelho for discussions vital to the improvement of XRD texture measurements.

To scientific initiation students João Vitor Marçola and Mariane B. de Castro and pre-scientific initiation student Karina M. Prediger for carrying out part of the practical work presented in this thesis.

To technicians Dr. Alberto C. Nassour, Denilson Kleber Vila, Pedro Luiz Di Lorenzo, MSc. Wagner Rafael Correr (SMM-EESC-USP), Edson Roberto D'Almeida, Rover Belo (DEMa-UFSCar) and Vitor A. S. Mendes (LCE-UFSCar) also for helping with practical activities and analyses.

To Prof. Dr. Marcelo F. de Oliveira and his students Felipe Santa Maria and Nelson D. de C. Neto (SMM-EESC-USP), to Prof. Dr. Conrado R. M. Afonso and Prof. Dr. Piter Gargarella (DEMa-UFSCar) and to Prof. Dr. Carlos Angelo Nunes and his student Paula Letícia C. de T. Cury (DEMAR-EEL-USP) for kindly allowing the use of their laboratories and equipment, carrying out analyses on my behalf and/or providing consumables.

To Cinthia Cristina C. Kleiner, Joel de S. Alencar, Thais Alonso (CPM-LNNano-CNPEM), Fabiano Emmanuel Montoro, João Marcos da Silva (LME-LNNano-CNPEM) and Leonardo Wu (LNLS-CNPEM) for the support and guidance during the development of activities at CNPEM.

To the Department of Materials Engineering and Department of Mechanical Engineering (EESC-USP), Department of Materials Engineering (UFSCar), Brazilian Nanotechnology Laboratory and Brazilian Synchrotron Light Laboratory (CNPEM) for the access to their facilities to develop the majority of experiments and analyses presented in this work.

To Ms. Ana Paula Bueno (*in memoriam*) and Ms. Iara Alice Oliveira, secretary members of the Graduate Program in Mechanical Engineering (EESC-USP), for the attention and support throughout the course of my doctorate.

To the National Council for Scientific and Technological Development (process number 161959/2015-6) and to the Coordination for the Improvement of Higher Education Personnel (process number 88887.302880/2018-00) for the funding of the project.

To Dr.-Ing. Jenifer Barrirero, Dr.-Ing. Maria Agustina Guitar, Dr.-Ing. Sebastián Suárez, Dr.-Ing. Flavio Andres Soldera, Prof. Dr.-Ing. Frank Mücklich, Nadine Kreutz, Nadja Schorr and Susanne Kern-Schumacher, from the Chair of Functional Materials at the Saarland University (Saarbrücken, Germany), for warmly receiving me and for all the support provided before, during and even after my stay at FuWe. Dr.-Ing. Christoph Pauly, Sebastian Slawik, Sven Ebner and Wolfgang Ott are also not to be forgotten for providing assistance during practical activities in the laboratories.

To my friends from Saarbrücken for making my stay in Germany so fun and pleasant, but productive at the same time.

To my friends in Brazil for the emotional support, either from near or far, which was vital to get through hard times, which certainly existed, and to get the most out of good times.

To my pups (why not?), whose tiny noses, fluffy paws, floppy bellies and wagging tails are my best therapy.

To my parents, sister and grandmother, also for the unconditional and vital support and continuous motivation.

*“Du hast gelernt was Freiheit heisst und das
vergiss nicht mehr.“ (Unknown authorship)*

RESUMO

CALLEGARI, B. **Compreendendo o impacto microestrutural na resposta de ligas de titânio a tratamentos de envelhecimento.** 2020. 198 p. Tese (Doutorado em Engenharia Mecânica) – Escola de Engenharia de São Carlos, Universidade de São Paulo, São Carlos, 2020.

O impacto da microestrutura inicial no comportamento da liga β metaestável Ti-5Al-5Mo-5V-3Cr (Ti-5553, composição em peso) e da liga $\alpha+\beta$ Ti-6Al-4V (Ti-64, composição em peso) durante tratamentos de envelhecimento foi avaliado neste trabalho. Tratamentos térmicos e termomecânicos foram impostos para alcançar tal variabilidade microestrutural. Com relação à liga Ti-5553, concluiu-se que a fase β sofre recuperação dinâmica acima e abaixo da β -*transus*, sendo mais dominante em taxas de deformação mais baixas. Enquanto isso, a fase α sofre não apenas quebra e globularização, mas também decomposição, o que contribui para o amolecimento. O aumento na taxa de deformação causou recuperação não uniforme no campo β e um refinamento mais intenso da fase α no campo $\alpha+\beta$. A avaliação de macrotextura após a deformação indica que a textura da fase β é muito mais forte que a da fase α , com seu componente (200) sendo o mais intenso. Microestruturas relevantes foram subsequentemente selecionadas para tratamentos de envelhecimento. Os resultados mostram que a presença de defeitos induzidos por deformação acelera a precipitação da fase durante o envelhecimento e que a composição da matriz β , afetada pela quantidade de fase α primária presente, desempenha um papel importante. A fase α'' tende a se formar a partir da matriz β em grandes quantidades sem a presença da fase α primária ou com uma fração baixa dessa fase, e a conversão de α'' em α é lenta, sendo mais rápida após tratamento térmico no campo β , enquanto uma transformação $\beta \rightarrow \alpha$ contínua, com pouca ou nenhuma precipitação de α'' , ocorre após tratamento térmico no campo $\alpha+\beta$. Com relação à Ti-64, taxas de deformação mais baixas no campo β parecem diminuir a razão de aspecto e a razão c/a das ripas martensíticas, e aumentar a quantidade de fase β retida. Taxas mais baixas durante a deformação no campo $\alpha+\beta$ também aumentam a fração da fase β . Porém, uma quantidade excessiva de fase β causa sua instabilidade durante a têmpera, com consequente transformação na fase α secundária. Em temperaturas mais baixas no campo $\alpha+\beta$, a tendência de globularização da liga é significativamente aumentada, especialmente durante deformação

lenta. Textura significativa do tipo fibra da fase α/α' foi observada somente após deformação no campo β . Análises de dispersão da orientação dos grãos mostraram um alto grau de desorientação interna nas lamelas deformadas de α e a tendência de globularização das lamelas pela evolução dos contornos internos de baixo ângulo para contornos de alto ângulo. Condições de interesse foram escolhidas para tratamentos de envelhecimento posteriores. Os resultados mostram que a decomposição de β em uma refinada fase α secundária, a transformação da martensita metaestável na fase α de equilíbrio e a precipitação do intermetálico Ti_3Al podem ocorrer durante o envelhecimento. Foi demonstrado que a composição e distribuição da fase β afetam a precipitação de α secundária, enquanto a composição da fase α desempenha um papel fundamental na formação de Ti_3Al . Os estudos de difração de raios-X in situ indicam a contribuição para o endurecimento pelo aumento da razão c/a durante a conversão $\alpha' \rightarrow \alpha$ e a homogeneização química da fase β .

Palavras-chave: Ligas de titânio. Transformações de fase. Endurecimento. Processamento termomecânico. Envelhecimento. Difração de elétrons retroespalhados. Difração de raios-X. Radiação sincrotron.

ABSTRACT

CALLEGARI, B. **Understanding the impact of microstructure on the response of titanium alloys to aging treatments.** 2020. 198 p. Thesis (Doctorate in Mechanical Engineering) – School of Engineering of São Carlos, University of São Paulo, São Carlos, 2020.

The impact of the initial microstructure on the behavior of the β -metastable alloy Ti-5Al-5Mo-5V-3Cr (Ti-5553, composition in wt%) and the $\alpha+\beta$ alloy Ti-6Al-4V (Ti-64, composition in wt%) during subsequent isothermal treatments has been evaluated in this work. Thermal and thermomechanical treatments were imposed to the alloys to achieve such microstructural variability. Regarding Ti-5553, it was concluded that the β phase undergoes dynamic recovery above and below its β -*transus* temperature, and recovery is more dominant at lower strain rates. Meanwhile, α phase undergoes not only a process of breakage and globularization, but also decomposition, which contributes to flow softening. The increase in strain rate caused non-uniform recovery in the β field and a more intense refinement of α precipitates in the $\alpha+\beta$ field. Macrotecture evaluation after deformation indicates that β 's texture is much stronger than that of α , with its (200) component being the strongest one. Relevant microstructures were then selected to undergo aging treatments. Results show that the presence of deformation-induced defects accelerates phase precipitation during aging, and that the composition of the β matrix, which is affected by the amount of primary α , plays a major role. The α'' phase tends to form from the β matrix in high quantities without the presence of primary α phase or with a low fraction of this phase, and the conversion of α'' into α is sluggish, being faster in the β -heat-treated condition, whereas a continuous $\beta \rightarrow \alpha$ transformation occurs, with little or no precipitation of α'' in the $\alpha+\beta$ -heat-treated condition. With respect to Ti-64, during deformation in the β field, lower strain rates appear to cause a decrease in the aspect ratio and in the c/a ratio of final martensitic laths and an increase in the final amount of retained β phase. Lower strain rates during deformation in the $\alpha+\beta$ field also increase the β phase fraction. However, an excessive amount of β causes its instability during quenching, with consequent transformation into secondary α . At a lower temperature in the $\alpha+\beta$ field, the globularization tendency of the alloy is significantly enhanced, especially during slow deformation. Significant fiber texture of the α/α' phase was observed only after

deformation in the β field. Grain orientation spread analyses have shown a high degree of internal misorientation in deformed α lamellae and the tendency of globularization of lamellae by the evolution of internal low angle boundaries to high angle boundaries. Conditions of interest were chosen for aging treatments. Results show that β decomposition into fine secondary α laths, transformation of the metastable martensitic α' into the equilibrium α phase and precipitation of the intermetallic Ti_3Al can take place during aging. The composition and distribution of the β phase was shown to affect the precipitation of secondary α during aging, while the composition of the α phase plays a key role on the formation of Ti_3Al . In situ X-ray diffraction studies indicate the contribution to hardening by the increase of the c/a ratio during the $\alpha' \rightarrow \alpha$ conversion and the chemical homogenization of the β phase.

Keywords: Titanium alloys. Phase transformations. Hardening. Thermomechanical processing. Aging. Electron backscatter diffraction. X-ray diffraction. Synchrotron radiation.

LIST OF FIGURES

Figure 1 – Unit cells of a) α and b) β phases of pure titanium.	41
Figure 2 – The distorted HCP cell derived from the parent BCC cell.	44
Figure 3 – Distortion of the $(110)\beta$ plane to form the $(0001)\alpha$ plane during the $\beta \rightarrow \alpha$ transformation according to the Burgers orientation relationship.	45
Figure 4 – Schematic representation of the crystallographic relationship between α and β phases within α colonies.	46
Figure 5 – Lamellar microstructure of Ti-6Al-4V alloy.	46
Figure 6 – Possible reactions from the β phase in titanium alloys upon quenching.	48
Figure 7 – TEM images showing the structure of titanium alloy martensites: a) HCP α' laths in Ti-1.8Cu quenched from 900°C, b) HCP lenticular α' containing twins in Ti-12V quenched from 900°C and c) orthorhombic α'' in Ti-8.5Mo-0.5Si quenched from 950°C.	50
Figure 8 – a) The HCP lattice of the α' martensite., where the (0002) plane is shaded in pink and dashed lines delineate the edges of an equivalent C-centered orthorhombic unit cell, b) the unit cell of the C-centered orthorhombic α'' martensite where the $(002)\alpha''$ plane is shaded in pink and c) two unit cells of the BCC β phase where one $\{110\}\beta$ plane is shaded in pink and dashed lines delineate the edges of an equivalent C-centered orthorhombic unit cell. The magnitude of y determines the position of atoms on the $(002)\alpha''$ plane along the $[010]\alpha''$ direction.	52
Figure 9 – Representation of the $\beta \rightarrow \omega$ transformation showing the (222) planes of the BCC lattice.	55
Figure 10 – a) BCC lattice of β , b) hexagonal lattice of ω , c) relationship between β and ω prior to shuffle along $[111]$ direction and d) unit cell of ω after shuffle (represents a third of the hexagonal lattice of ω shown in a).	56
Figure 11 – Schematic representation of formation of the ω lattice from the β lattice	56
Figure 12 – a) TEM dark field micrograph of ellipsoidal ω precipitates in Ti-16Mo aged 48h at 450°C and b) TEM dark field micrograph of cuboidal ω precipitates in Ti-8Fe aged 4h at 400°C.	57
Figure 13 – Basis for the classification of commercial Ti and alloys into α alloys, $\alpha+\beta$ alloys and β alloys.	59
Figure 14 – TEM image of coherent β' particles in Ti-15Zr-20V aged 6 h at 450°C.	60
Figure 15 – Crystal structure of the Ti_3Al phase.	61
Figure 16 – TEM dark field micrograph of α_2 particles in IMI 834 alloy aged 24h at 700°C.	62

Figure 17 – a) Configuration of α -Ti lattice and Al atoms before annealing. b) During annealing, Al atoms solubilize in Ti and a Ti-Al substitutional solid solution is formed. c) During cooling, the formation of stacking faults on $\{1100\}_\alpha$ planes is observed. d) Precipitation of α_2 -Ti ₃ Al near stacking faults and relative positions of α -Ti and α_2 -Ti ₃ Al.	63
Figure 18 – Schematic influence of alloying elements on phase diagrams of Ti alloys.	65
Figure 19 – The [Al] _{eq} and [Mo] _{eq} values for some Ti alloys showing the different alloy classes based on Lütjering and Williams’ classification (solid black lines) and Donachie’s classification (dashed red lines).	68
Figure 20 – Division of commercial titanium alloys into α , $\alpha+\beta$ and β groups on the Bo \times Md diagram.	70
Figure 21 – Lamellar microstructures of Ti-6242 alloy cooled from β field at a) 1°C/min and b) 8000°C/min, c) Ti-6242 alloy in the β -processed condition cooled at approximately 100°C/min, bi-modal microstructure of IMI 834 alloy cooled from β field at d) slow cooling rate and e) fast cooling rate, f) fully equiaxed microstructure of Ti-6242 alloy slowly cooled from the recrystallization annealing temperature, and g) mill-annealed microstructure of a Ti-6Al-4V alloy plate.	73
Figure 22 – Pseudo-binary β -isomorphous phase diagram showing locations of metastable and stable β titanium alloys. β_c refers to the critical minimum addition of a β -stabilizer to retain 100% β on water quenching. β_s denotes the β - <i>transus</i>	75
Figure 23 – a) β 21S alloy annealed and aged for 8 h at 500°C + 24 h at 725°C, b) β annealed microstructure of β -CEZ, c) β processed microstructure of Ti-6246, d) through- <i>transus</i> processed microstructure of Ti-6246 and e) bi-modal microstructure of β -CEZ alloy.	78
Figure 24 – Slip planes and slip directions in the hexagonal α phase.	81
Figure 25 – Influence of deformation temperature and mode on texture of Ti-6Al-4V (schematic (0002) pole figures).	85
Figure 26 – Schematic representation of the processing routes applied to Ti-5553 and Ti-64 alloys.	87
Figure 27 – a) Overview and b) internal chamber view of the Gleeble® 3800 located at the Metals Characterization and Processing Laboratory at CNPEM; c) overview and d) internal chamber view of the Gleeble® 3S50 located at the XTMS beamline of the Brazilian Synchrotron Light Laboratory.	89
Figure 28 – Schematic representations of the most important components of a modern synchrotron radiation source.	91

Figure 29 – Schematic experimental setups for synchrotron x-ray diffraction experiments at a) ID15B beamline of the European Synchrotron Radiation Facility (energy: 90 keV) and b) XTMS experimental station of the Brazilian Synchrotron Light Laboratory (energy: 12 keV).	92
Figure 30 – Examples of difference curve behavior for a) a good fit between experimental (dots) and calculated (lines) profiles, b) too high (left) and too low (right) calculated intensities, c) too large (left) and too small (right) calculated FWHM, d) too large (left) and too small (right) 2θ and e) too small FWHM combined with too small peak asymmetry (left) and too small FWHM combined with too low intensity (right).	96
Figure 31 – Overview of EBSD indexing procedure showing pattern capture through to determination of crystal orientation.	99
Figure 32 – a) Origin of backscattered Kikuchi lines from the EBSD (i.e., tilted specimen) perspective, and b) EBSD pattern from copper (accelerating voltage: 15 kV).	100
Figure 33 – SE-SEM image of the as-received mill-annealed microstructure of Ti-64 alloy.	106
Figure 34 – Schematic representation of thermomechanical and heat treatments imposed to Ti-64 alloy.	107
Figure 35 – a) Flow curves of Ti-64 alloy deformed at 1050°C, 900°C and 700°C with strain rates of 0.1, 0.01 and 0.001 s ⁻¹ ; b) temperature reading with insets showing the adiabatic heating during deformation at 700°C and 900°C.	109
Figure 36 – a) LOM image of Ti64_1050C_HT condition, and SE-SEM images of the microstructures of b) Ti64_1050C_HT, c) Ti64_900C_HT and d) Ti64_700C_HT conditions.	111
Figure 37 – LOM images of a) Ti64_1050C_D1, b) Ti64_1050C_D01 and c) Ti64_1050C_D001, and d) their respective calculated ODFs at $\varphi_2 = 0^\circ$ and $\varphi_2 = 30^\circ$. The compression axis is parallel to the height of images.	113
Figure 38 – BSE-SEM images of a) Ti64_900C_D1, b) Ti64_900C_D01 and c) Ti64_900C_D001, and d) an SE-SEM image of Ti64_900C_D001 showing in detail the presence of primary α grains and secondary α laths. The compression axis is parallel to the height of images. In BSE images, the darker phase is α and the brighter phase is β	114
Figure 39 – BSE-SEM images of a) Ti64_700C_D1, b) Ti64_700C_D01 and c) Ti64_700C_D001. The compression axis is parallel to the height of images. The darker phase is α and the brighter phase is β	115

Figure 40 – Calculated ODFs of Ti-64 deformed at 900°C and 700°C at $\varphi_2 = 0^\circ$ and $\varphi_2 = 30^\circ$	116
Figure 41 – Misorientation angle distributions of the α phase in a) Ti64_700C_HT, b) Ti64_700C_D1, c) Ti64_700C_D01 and d) Ti64_700C_D001. The continuous curves correspond to the Mackenzie (random) distributions.	117
Figure 42 – Misorientation axis distributions of the α phase in a) Ti64_700C_D1, b) Ti64_700C_D01 and c) Ti64_700C_D001, and d) an ideal random axis distribution. The scale bar in (g) applies to all plots.....	118
Figure 43 – GOS maps, internal misorientation maps and c-axis tilt maps with respect to the y-direction (compression axis), respectively, of a-c) Ti64_700C_D1 and d-f) Ti64_900C_D01 conditions. Hexagonal lattices are shown in in c-axis tilt maps to aid visualization of the α phase orientation.	119
Figure 44 – Grain size distribution in a) Ti64_700C_D1, b) Ti64_700C_D01 and c) Ti64_700C_D001 conditions, and d) the corresponding relationship between strain rate ($\dot{\epsilon}$) and grain size (GS).	121
Figure 45 – Resulting diffractograms of conditions produced during deformation at a) 1050°C, b) 900°C and c) 700°C, with details showing the behavior of (110) β reflection between (0002) α and (1011) α	122
Figure 46 – Comparison among β phase fractions in the final microstructure of all heat-treated and deformed conditions of Ti-64 alloy.	123
Figure 47 – Lattice parameters of the α phase after heat treatment and deformation at a) 1050°C, b) 900°C and c) 700°C; d) lattice parameters of the β phase in all conditions of Ti-64 alloy.	124

LIST OF TABLES

Table 1 – Physical and mechanical properties of high-purity polycrystalline α titanium (>99.9%) at 25°C.....	40
Table 2 – Some important characteristics of titanium and titanium based alloys as compared to other structural metallic materials based on Fe, Ni and Al.	41
Table 3 – All twelve possible variants of the $\beta \rightarrow \alpha$ transformation according to the BOR....	44
Table 4 – Composition of the α'/α'' martensite boundary in some binary titanium alloy systems with transition metals.....	52
Table 5 – Crystallographic properties of the Ti_3Al phase.	61
Table 6 – Effect of alloying elements on phase stabilization of titanium.	65
Table 7 – List of Bo and Md for alloying elements in titanium.	69
Table 8 – Correlation between some microstructural features and mechanical properties of $\alpha+\beta$ alloys.	74
Table 9 – Ti-6Al-4V composition, in wt%, in Grade 5 and Grade 23 (ELI).	74
Table 10 – Potency of β -stabilizers in titanium.....	76
Table 11 – Correlation between some microstructural features and mechanical properties of β alloys.....	79
Table 12 – Slip systems in the hexagonal α phase.	82
Table 13 – Twinning elements in α titanium.....	83
Table 14 – Composition of the Ti-64 alloy used in this work.....	106
Table 15 – Average aspect ratio values obtained for Ti-64 alloy deformed at 1050°C.	125

LIST OF ABBREVIATIONS

BCC	body-centered cubic
BF	bright field
BOR	Burgers orientation relationship
CAPES	Coordination for the Improvement of Higher Education Personnel
CCD	charge-coupled device
CCDM	Center for Characterization and Development of Materials (Materials Engineering Department, Federal University of São Carlos)
CNPEM	Brazilian Center for Research in Energy and Materials
CNPq	National Council for Scientific and Technological Development
CP	commercially pure
CPM	Metals Characterization and Processing Laboratory (Brazilian Nanotechnology Laboratory, Brazilian Center for Research in Energy and Materials)
DEMa	Materials Engineering Department (Federal University of São Carlos)
DEMAR	Materials Engineering Department (Lorena School of Engineering, University of São Paulo)
DESY	<i>Deutsches Elektronen Synchrotron</i> (Hamburg, Germany)
DF	dark field
DOI	digital object identifier
DRV	dynamic recovery
DRX	dynamic recrystallization
DSC	differential scanning calorimetry
EBSD	electron backscatter diffraction
EDXRD	energy-dispersive X-ray diffraction
EDS	energy-dispersive spectroscopy
EEL	School of Engineering of Lorena (University of São Paulo)
EESC	School of Engineering of São Carlos (University of São Paulo)
ELI	extra-low interstitials
FCC	face-centered cubic
FEG	field emission gun
FIB	focused ion beam
FuWe	Chair of Functional Materials (Saarland University)
FWHM	full width at half maximum

GB	grain boundary
GOS	grain orientation spread
HEXRD	high energy X-ray diffraction
HCP	hexagonal close-packed
HV	Vickers hardness
ICSD	Inorganic Crystal Structure Database
IPF	inverse pole figure
JCR	Journal Citation Reports
KAM	Kernel average misorientation
LCB	low cost beta
LCE	Structural Characterization Laboratory (Materials Engineering Department, Federal University of São Carlos)
LME	Electron Microscopy Laboratory (Brazilian Nanotechnology Laboratory, Brazilian Center for Research in Energy and Materials)
LNLS	Brazilian Synchrotron Light Laboratory (Brazilian Center for Research in Energy and Materials)
LNNano	Brazilian Nanotechnology Laboratory (Brazilian Center for Research in Energy and Materials)
LOM	light optical microscopy
MAUD	Materials Analysis Using Diffraction
ODF	orientation distribution function
PJA	published journal article
PF	pole figure
SAED	selected area diffraction pattern
SEM	scanning electron microscopy
SMM	Department of Materials Engineering (School of Engineering of São Carlos, University of São Paulo)
STA	solution-treated and aged
STEM	scanning-transmission electron microscopy
TEM	transmission electron microscopy
UFSCar	Federal University of São Carlos
USP	University of São Paulo
XRD	X-ray diffraction
XTMS	X-ray Scattering and Thermo-Mechanical Simulation

LIST OF SYMBOLS

α	alpha
α'	alpha prime
α''	alpha double prime
α_2	alpha-two
α_{GB}	grain boundary alpha
α_{m}	massive alpha
α_{W}	Widmanstätten alpha
β	beta (also referred to as β_{rich} in the context of spinodal decomposition)
β'	beta prime (also referred to as β_{lean} in the context of spinodal decomposition)
β_{c}	critical amount of beta-stabilizer element to retain 100% of beta phase upon quenching
η	azimuthal angle
η_1	twinning shear direction
η_2	direction of intersection of shear plane with K_2
θ	diffraction angle
ρ	density
Σ	mass absorption coefficient
τ_0	attenuation length
φ	rotation angle for XRD texture measurements
χ^2	goodness of fit – ratio between R_{wp} and R_{exp} (see below)
ψ	tilt angle for XRD texture measurements
Ω	ohm
ω	omega
a_{n}	lattice parameter in cubic, hexagonal and orthorhombic unit cells (n: phase indication)
A_1, A_2	pre-exponent terms in diffusion coefficient equations
Al	aluminum
Al_2O_3	alumina
[Al]eq	aluminum equivalent
B	boron
Bo	bond order
b	Burgers vector

b_n	lattice parameter in orthorhombic unit cell (n: phase indication)
c_n	lattice parameter in hexagonal and orthorhombic unit cells (n: phase indication)
$^{\circ}\text{C}$	degrees Celsius
C	carbon
cm	centimeter
Co	cobalt
Cr	chromium
Cu	copper
D	diffusion coefficient
E	elastic modulus
FCC	face-centered cubic
Fe	iron
FEL	free electron laser
FeTiO_3	ilmenite
G	gram
GPa	gigapascal
H	hydrogen
J	joule
K	Kelvin
K_1	first undeformed plane
K_2	second undeformed plane
k	wave vector
kg	kilogram
kgf	kilogram-force
kJ	kilojoule
LaB_6	lanthanum hexaboride
m	meter
mbar	millibar
Md	d-orbital energy level
Mn	manganese
Mo	molybdenum
[Mo]eq	molybdenum equivalent
M_F	martensite finish temperature
M_S	martensite start temperature

MPa	megapascal
N	nitrogen
Nb	niobium
Ni	nickel
O	oxygen
Q	activation energy
q	momentum transfer
R	gas constant
R_{exp}	expected residual
R_{wp}	weighted-profile residual
s	second
S	weighted difference between y(obs) and y(calc) (see below)
Si	silicon
Sn	tin
T	temperature
T_{β}	beta- <i>transus</i> temperature
Ta	tantalum
Ti	titanium
TiCl ₄	titanium tetrachloride
TiO ₂	rutile
V	vanadium
V_n	unit cell volume (n: phase indication)
W	tungsten; watt
x	composition
y(calc)	calculated profile
y(obs)	experimental profile
Zr	zirconium

CONTENTS

1 INTRODUCTION	31
<u>1.1 Objectives</u>	34
<u>1.2 Thesis structure</u>	34
2 LITERATURE REVIEW	35
<u>2.1 Historical background and commercial emergence of titanium</u>	35
<u>2.2 Main phases in titanium-based systems</u>	39
2.2.1 <i>Allotropic phases: α and β</i>	39
2.2.2 <i>Martensitic phases: α' and α''</i>	48
2.2.3 <i>Omega (ω) phase</i>	53
2.2.4 <i>Beta phase separation</i>	59
2.2.5 <i>Ordered intermetallic phase: Ti_3Al</i>	60
<u>2.3 Alloying elements of titanium alloys</u>	64
<u>2.4 Classification of titanium alloys</u>	66
2.4.1 <i>Al and Mo equivalents and the $Bo \times Md$ method</i>	67
2.4.2 <i>Alpha+beta alloys</i>	70
2.4.3 <i>Beta alloys</i>	75
<u>2.5 Deformation of titanium alloys</u>	80
2.5.1 <i>Slip modes</i>	80
2.5.2 <i>Deformation twinning</i>	82
2.5.3 <i>Textures</i>	84
3 SUMMARY OF EXPERIMENTAL TECHNIQUES	87
<u>3.1 Differential scanning calorimetry</u>	87
<u>3.2 Chemical analyses</u>	88
<u>3.3 Thermomechanical processing</u>	88
<u>3.4 Metallographic preparation</u>	90

<u>3.5 Synchrotron X-ray diffraction</u>	90
<u>3.6 Rietveld refinement</u>	94
<u>3.7 Microstructural characterization</u>	97
<u>3.8 Macro- and micro-texture analyses</u>	97
<u>3.9 Micro-hardness testing</u>	101
4 THERMOMECHANICAL PROCESSING OF Ti-6Al-4V ALLOY	103
<u>4.1 Introduction</u>	103
<u>4.2 Materials and methods</u>	105
<i>4.2.1 Material</i>	105
<i>4.2.2 Thermomechanical treatments</i>	106
<i>4.2.3 Microstructural characterization</i>	107
<i>4.2.4 Texture analysis</i>	108
<i>4.2.5 Synchrotron high energy X-ray diffraction</i>	108
<u>4.3 Results and discussion</u>	109
<i>4.3.1 Flow curves and adiabatic heating</i>	109
<i>4.3.2 Heat-treated microstructures</i>	110
<i>4.3.3 Deformed microstructures</i>	111
<i>4.3.4 Crystallographic aspects related to α globularization</i>	116
<i>4.3.5 Grain refinement evaluation</i>	120
<i>4.3.6 Dynamic phase evolution</i>	121
<u>4.4 Conclusions</u>	125
5 AGING TREATMENTS OF Ti-6Al-4V ALLOY	127
6 THERMOMECHANICAL PROCESSING OF Ti-5Al-5Mo-5V-3Cr ALLOY	129
7 AGING TREATMENTS OF Ti-5Al-5Mo-5V-3Cr ALLOY	131
8 GENERAL CONCLUSIONS	133
9 SUGGESTIONS FOR FUTURE WORKS	135
REFERENCES	137

APPENDIX A – Example of MTEX macro for the calculation of pole figures	149
APPENDIX B – Example of MTEX macro for EBSD data processing 1	153
APPENDIX C – Example of MTEX macro for EBSD data processing 2	155
ANNEX A – Paper on aging treatments of Ti-6Al-4V alloy	159
ANNEX B – Paper on thermomechanical processing of Ti-5Al-5Mo-5V-3Cr alloy	171
ANNEX C – Paper on aging treatments of Ti-5Al-5Mo-5V-3Cr alloy	185

1 INTRODUCTION

Titanium and its alloys present several benefits which justify their wide application, especially with respect to competing materials, such as steels and iron- or nickel-based superalloys, in terms of advantageous combination of properties such as density, strength, corrosion resistance and processing (DONACHIE JR., 2000). Their most outstanding properties, i.e. high specific strength and excellent corrosion resistance, make titanium alloys extremely attractive, and at times preferable, for applications in aerospace, automotive, biomedical and chemical industries (BOYER, 2010; COTTON *et al.*, 2015; LEYENS; PETERS, 2003; LÜTJERING; WILLIAMS, 2007).

Among the classes of titanium alloys, β (beta)-metastable ones represent the most versatile class, offering the highest strength-to-weight ratios, as well as good combinations of strength, toughness and fatigue resistance in large cross section components (LEYENS; PETERS, 2003). These alloys present high hardenability and, in the β solution-treated condition, good ductility and low flow strength (COTTON *et al.*, 2015; DONACHIE JR., 2000). Their capacity of retaining the soft β phase upon fast cooling provides superior forming characteristics to these alloys, with subsequent strengthening by aging (POLMEAR *et al.*, 2017). In spite of all advantages, beta alloys' usage within titanium market is relatively low and has not expanded significantly along the last decades (COTTON *et al.*, 2015; LÜTJERING; WILLIAMS, 2007). The main reason for their limited utilization is cost (COTTON *et al.*, 2015). However, their attractive general properties, as well as specific properties for singular applications, e.g. low modulus of elasticity for springs, are believed to give rise to beta alloys' utilization (LÜTJERING; WILLIAMS, 2007). To allow such improvement, the definition of appropriate processing windows, by systematically correlating processing, microstructure and properties, is a key factor (LEYENS; PETERS, 2003).

Ti-5553 alloy (Ti-5Al-5Mo-5V-3Cr, composition in wt%) is a β -metastable alloy based on the Russian VT-22 alloy (Ti-5Al-5Mo-5V-1Cr-1Fe) (COTTON *et al.*, 2015). The alloy presents better strength, ductility, and toughness properties than VT22, and is considerably hardenable by solution treatment and aging (FANNING, 2005). In comparison with the famous β alloy Ti-10V-2Fe-3Al (Ti-1023), Ti-5553 can achieve similar or better mechanical properties through easier processing pathways and possesses superior hardenability (FANNING, 2005; JONES *et al.*, 2009a). It is mainly employed in large section forgings in airframes (COTTON *et al.*, 2015).

Structural properties of β alloys are defined by a homogeneous distribution of α precipitates in a β matrix, and the characteristics of the dispersed α phase are strongly dependent on thermal treatments applied to the alloy. Thus, a correct understanding of phase transformation mechanisms is necessary for optimization of such properties (BARRIOBERO-VILA et al., 2015a). Several works exist on the phase precipitation in the Ti-5553 alloy under heat treatments, such as continuous heating (CONTREPOIS; CARTON; LECOMTE-BECKERS, 2011), cooling (JONES et al., 2009b) and aging (MANDA et al., 2016; ZHENG et al., 2016a, 2016b). With respect to the latter, in situ synchrotron X-ray diffraction has shown itself to be a powerful tool for the investigation of phase transformations (AEBY-GAUTIER et al., 2013; COAKLEY et al., 2015). Furthermore, efforts have been done in order to understand elemental partitioning in complex β alloys (CHEN et al., 2016, 2017), including Ti-5553 (LI et al., 2015; NAG et al., 2009; ZHENG; CLARK; FRASER, 2019). Because these alloys consist of several different alloying elements, α precipitation is complicated, since it requires partitioning of these elements between phases, especially slow-diffusing elements such as molybdenum (COAKLEY et al., 2015). However, virtually all studies focus on the aging behavior of the alloy starting from a fully β condition produced by solution treatment in the β field. Thus, the alloy, and β alloys in general, lack studies on the effect of microstructural features such as the presence of primary α (pre-aging) and of defects such as dislocations and low-angle boundaries induced by deformation in subsequent precipitation processes during aging treatments. The only work known to have this focus is the one of Teixeira et al., where the effect of the deformation of the β phase in α precipitation is modelled, but isothermal phase evolution is not tracked (TEIXEIRA et al., 2006).

On the other hand, the $\alpha+\beta$ (alpha+beta) class is the group with the largest number of alloys, which present both α and β phases at room temperature and transform martensitically when rapidly cooled from the β field (FROES, 2015; LÜTJERING; WILLIAMS, 2007). Ti-6Al-4V (composition in weight percent) is the main representative of $\alpha+\beta$ alloys, being responsible for more than 50% of all titanium alloys' applications. Reasons for its wide application involve the equilibrium of properties such as strength, ductility, toughness and fatigue properties. For this reason, it is a widely studied and continuously developed alloy, resulting in advances of great importance for industries interested in its utilization (LEYENS; PETERS, 2003; LÜTJERING; WILLIAMS, 2007).

Properties of $\alpha+\beta$ alloys are consequence of their response to thermal and thermomechanical treatments, in terms of variation of composition, morphology and amounts of present phases (FROES, 2015). Several types of constituents and final microstructures can

be obtained depending on applied treatments routes. Treatment temperature, cooling rate from treatment temperature and the composition of the alloy are the most critical factors, influencing the type and morphology of precipitated α phase, the formation of martensitic phases (α' and/or α'') and the possibility of age hardening (LÜTJERING; WILLIAMS, 2007; PEDERSON, 2002). If submitted to deformation, factors as temperature, degree and mode of deformation can affect final microstructure, phase morphology and the formation of texture (LÜTJERING; WILLIAMS, 2007). In the case of Ti-6Al-4V alloy, aging at temperatures typically between 500°C and 600°C induces the formation of intermetallic phase Ti_3Al (α_2) (BOYER; ELSCH; COLLINS, 1994). Its relevance lies on the fact that the presence of α_2 in the alloy increases its tensile strength and limits its ductility (WU et al., 2013). In addition, as an ordered intermetallic phase, Ti_3Al offers a combination of lightness and high temperature strength, despite its limited room-temperature ductility and toughness, which makes it, again, interesting for the aerospace industry. Since the late 1990's, Ti_3Al -based high temperature alloys have been successfully produced (BANUMATHY; GHOSAL; SINGH, 2005). A study focused on Ti_3Al precipitation in near- α alloys has shown that it occurs preferably at boundaries and dislocations at higher aging temperatures, whereas a more homogeneous precipitation takes place at low temperatures, and aluminum concentration influences precipitation characteristics as well (ZHANG; LI, 2003).

As mentioned above, Ti-6Al-4V is a widely studied alloy due to its commercial relevance. Nonetheless, studies are heavily concentrated on the thermomechanical processing of the alloy. Although phase transformations in titanium alloys have been largely analyzed using in situ techniques such as synchrotron high energy x-ray diffraction, there are very few studies focused on phase evolution kinetics of Ti-6Al-4V during thermal and thermomechanical treatments in general (ELMER et al., 2005; WARCHOMICKA et al., 2019; WARWICK et al., 2013), with no knowledge of studies on the alloy's behavior during isothermal treatments. Instead, focus is usually given to the resulting mechanical properties of the alloy after aging. Furthermore, the alloy lacks a concise study aimed at the understanding of the age hardening potential of different microstructures, such as martensitic, lamellar, bimodal and globular, given that most available works focus on martensite decomposition in the alloy upon aging (GIL MUR; RODRÍGUEZ; PLANELL, 1996; QAZI et al., 2003).

1.1 Objectives

Within this context, this thesis has the following general objectives: systematic correlation of processing and microstructure of titanium alloys; understanding phase precipitation mechanisms, given their influence on the properties of titanium alloys; and exploitation of the age-hardening potential of titanium alloys as function of microstructure.

The specific objective of the thesis is to understand the response of β -metastable and $\alpha+\beta$ titanium alloys, exemplified by Ti-5553 and Ti-64 alloys, respectively, to isothermal aging treatments, based on the variation of their initial microstructure. This variation is given in terms of phase fraction ratio, α phase morphology and presence of deformation-induced defects, such as dislocations and low-angle grain boundaries, achieved by the imposition of different thermal and thermomechanical treatment routes to the alloys.

1.2 Thesis structure

This thesis is divided into six chapters, excluding the present introductory section: **Chapter 2** brings a literature review on titanium alloys and their metallurgy; **Chapter 3** provides a thorough description of the experimental techniques used during the development of this work; **Chapter 4** brings the results on the microstructural tailoring of Ti-64 alloy by thermomechanical processing, which yielded a manuscript to be submitted to “Materials Chemistry and Physics” (JCR 2020 impact factor: 3.408); **Chapter 5** introduces the results on the microstructural evolution of processed Ti-64 alloy during subsequent aging treatments, which yielded a paper published on “Materials Characterization” journal, included in this thesis as **Annex A** (CALLEGARI et al., 2020a); **Chapter 6** introduces the results on the microstructural tailoring of Ti-5553 alloy by thermomechanical processing, which yielded a paper published on “Materials Characterization” journal (JCR 2020 impact factor: 3.562), included in this thesis as **Annex B** (CALLEGARI et al., 2020b); **Chapter 7** introduces the results on the microstructural evolution of processed Ti-5553 alloy during subsequent aging treatments, which yielded a paper published on “Journal of Alloys and Compounds” (JCR impact factor 2020: 4.650), included in this thesis as **Annex C** (CALLEGARI et al., 2020c); **Chapter 8** brings the general conclusion of the work; **Chapter 9** brings suggestions for future works based on the present work. Appendices are also presented to provide complementary information.

2 LITERATURE REVIEW

In this chapter, a literature review is presented, with focus on the most relevant aspects of titanium alloys related to this work: the basics of its phases, alloying and alloy classification, and deformation behavior.

2.1 Historical background and commercial emergence of titanium

Titanium (Ti) is the fourth most abundant structural metal on Earth following aluminum, iron and magnesium. The most important mineral sources of Ti are ilmenite (FeTiO_3) and rutile (TiO_2) (LÜTJERING; WILLIAMS, 2007). The element was discovered by William Gregor in 1790-1791 in England. He analyzed black magnetic sand, today known as ilmenite, found in a local river, then removed the iron with a magnet and treated the sand with hydrochloric acid. As a result, he produced the impure oxide of a new, unknown element (FROES, 2015; LEYENS; PETERS, 2003). Little interest was shown in the discovery until 1795, when the German chemist Martin Heinrich Klaproth independently analyzed a rutile oxide from Hungary and identified an unknown element, the same reported by William Gregor. Klaproth acknowledged priority of the discovery to Gregor, and named the new element titanium after the powerful sons of the earth in Greek mythology (FROES, 2015; LEYENS; PETERS, 2003; LÜTJERING; WILLIAMS, 2007).

Early attempts to obtain pure titanium from its compounds resulted in the formation of Ti nitrides, carbides and carbonitrides, which, because of their metallic appearance, were mistaken for metals (FROES, 2015). The production of high purity titanium was proved to be difficult because of the strong tendency of the metal to react with oxygen and nitrogen (LÜTJERING; WILLIAMS, 2007). In 1887, Lars Frederik Nilson and Otto Peterson obtained a product of 97.4% purity by reducing titanium tetrachloride (TiCl_4) with sodium in an airtight steel cylinder. Henry Moissan also made attempts of producing pure titanium by reducing titanium dioxide with carbon at high temperature with a powerful electric arc. The product contained 5% C, but upon reheating with additional TiO_2 this content was reduced to 2% (FROES, 2015). More than 100 years after Gregor's discovery, Matthew Albert Hunter was the first to prepare pure titanium metal, in the United States, by heating titanium tetrachloride with sodium (LEYENS; PETERS, 2003). Hunter followed the methods of Nilson and Peterson and removed air from the apparatus, obtaining virtually impurity-free metallic titanium. In 1925, A. C. Van Arkel and J. H. deBoer, from Holland, produced pure

titanium by thermal decomposition of titanium tetrachloride. However, the metal made by this procedure was very expensive (FROES, 2015).

It was only later, in the decade of 1930, that Wilhelm Justin Kroll, from Luxembourg, developed an effective and commercially attractive process to produce pure titanium. In 1932, he produced significant amounts of the metal by combining TiCl_4 with calcium. At the beginning of World War II, at the United States Bureau of Mines, he demonstrated that titanium could be extracted commercially by reducing TiCl_4 using magnesium as the reducing agent instead of calcium (LEYENS; PETERS, 2003; LÜTJERING; WILLIAMS, 2007). This process was carried out in an inert argon atmosphere. The resulting product was called “titanium sponge” due to its porous appearance. The development of the Kroll process marked the beginning of the present large-scale titanium industry, and the process remains essentially unchanged, being the main route for titanium production today (LÜTJERING; WILLIAMS, 2007).

Around 1940, the U.S. Bureau of Mines became interested in the characteristics and production of titanium. After reviewing all known processes, the Bureau selected the Kroll process as the one most likely to economically produce ductile titanium, and set up a series of reactors to produce the metal. A Bureau publication in 1946 described a Kroll unit capable of making 7 kg batches of good-quality titanium powder by magnesium reduction, followed by acid leaching to remove the excess Mg and MgCl_2 . In 1949, the Bureau reported the successful operation of a magnesium-reduction unit to produce 40 kg batches of titanium. In 1952, they reported the removal of magnesium and magnesium chloride from titanium sponge by vacuum distillation (FROES, 2015).

Interest in the properties of titanium began to rise after World War II in the late 1940's and early 1950's. In the United States, programs with strong government support led to the installation of large capacity titanium sponge production plants, for example at TIMET (1951) and RMI (1958) (LÜTJERING; WILLIAMS, 2007). A pilot unit created in 1947 at DuPont expanded production to 800 tons of sponge per year by 1952. Production in the early and mid-1950s accelerated rapidly and approached the production levels of aluminum by 1965 (FROES, 2015).

In Europe, large scale production started in 1951 at the Metals Division of Imperial Chemical Industries, in the United Kingdom, which became the main European titanium producer. Its production capacity increased from a few hundred kilograms to 1.5 million kg by 1955. In continental Europe, fabrication started around 1955 at companies in France, Germany, and Sweden. The Soviet Union started sponge production in 1954 and by 1979

became the world's largest producer. Several Japanese industries also became early sponge producers, supplying metal to other countries, including the United States. By 1987, United States' sponge manufacturers had been reduced to three: TIMET, RMI, and Oremet. The Japanese by then had become major sponge producers, with limited capacity in melting and processing (FROES, 2015; LÜTJERING; WILLIAMS, 2007).

During the early 1950s, the advantages of aluminum, manganese, and vanadium additions were established in alloys such as Ti-8Mn, Ti-4Al-4Mn and Ti-6Al-4V, patented by Crucible Steel (FROES, 2015). Combination with Sn additions lead to the development of α (alpha) alloy Ti-5Al-2.5Sn for high temperature applications. The addition of Mo as β (beta) stabilizing element resulted in the $\alpha+\beta$ alloy Ti-7Al-4Mo for high strength applications (LÜTJERING; WILLIAMS, 2007). At the same time that titanium application in airframes and engines increased significantly, its use as corrosion-resistant materials for orthopedic devices was also emerging (FROES, 2015). The appearance of Ti-6Al-4V alloy in the USA in 1954 was a major breakthrough, becoming soon the most important $\alpha+\beta$ alloy, combining excellent properties and good processability. Today, Ti-6Al-4V is still the most widely used alloy. In the United Kingdom, alloy development focused on high temperature applications for aero-engines, leading to the introduction of the alloy Ti-4Al-4Mo-2Sn-0.5Si in 1956. This marked the first time silicon was added as an alloying element to improve creep resistance. In 1955, the first β titanium alloy, B120VCA (Ti-13V-11Cr-3Al), was developed in the USA by Crucible Steel. Starting in the 1960's, this high strength, age-hardenable sheet alloy was used for the skin of surveillance airplane SR-71 (LÜTJERING; WILLIAMS, 2007).

The late-1957 decision by the U.S. military to prioritize missiles over manned aircraft resulted in reduction of titanium production. Space exploration and the launching of new civilian jets during the 1960s resulted in a tripling of mill product shipments in the United States. Non-aerospace use of titanium also increased: desalination plants, power plants, and other fresh- and saltwater applications made use of corrosion-resistant grades. In 1971, with the cancellation of the U.S. SST project, titanium market reached another low, but the production regained momentum in 1974, and by 1978 a new peak of 18.1 million kg was established. There were new alloys available, such as Ti-6Al-6V-2Sn (higher strength than Ti-6Al-4V), Ti-8Al-1Mo-1V (a high-modulus alloy), and Ti-6Al-2Sn-4Zr-2Mo-0.1Si (a high-temperature alloy). In addition to flat product castings, extrusions and tubing were also being fabricated. The service temperature for titanium alloys was increased to 600°C. At the same time, the percentage of titanium in military airframes increased to 20-30% and new cost-effective processing/fabrication techniques were introduced (FROES, 2015).

A rise in titanium shipments occurred in the 1980s in large part due to the U.S. military buildup during President Reagan's term and the increase of aerospace and other non-military uses. In 1989, a new record of U.S. mill shipments of 25 million kg was achieved. With the formation of the Titanium Development Association (renamed The International Titanium Association) and the World Titanium Conferences, held at four-year intervals (initiated in London, 1968), and the development of the ASM International course on titanium and its alloys in the late 1970's, designers became better informed about the characteristics and use of titanium. Alloy processing and fabrication techniques matured with the development of another β alloy (Ti-15V-3Cr-3Al-3Sn) and a forgeable near- β alloy (Ti-10V-2Fe-3Al). Isothermal forging and superplastic forging were now accepted practices. The aerospace industry increased the use of titanium on Boeing and Airbus commercial systems (FROES, 2015).

In the early 1990s, with the end of the Cold War and the collapse of the Soviet Union, defense expenditures declined, and so did the military demand for titanium. The U.S. titanium mill shipments dropped to 15.4 million kg in 1991. On the other side, new alloys, such as β 21S (Ti-15Mo-2.7Zr-3Al-0.2Si) and titanium aluminides (Ti₃Al- and TiAl-based systems) received attention. New demands for sports applications, like lightweight bicycle frames and golf drivers, occurred. Use of titanium by Boeing for commercial aircraft alone increased to an estimated 11 million kg per year by 1996. By the mid-to-late 1990s, a new record of 27 million kg of mill products shipped per year was set in the United States, with 15% of Ti constituting the Boeing 777. This application took place due weight saving needs, volume constraints, operating temperatures, compatibility with polymeric composites, and corrosion resistance. Titanium alloys used included Ti-10V-2Fe-3Al, Ti-15V-3Cr-3Al-3Sn and β 21S. The new record was followed by a downturn after the September 2011 attack, with the U.S. market reaching levels of 13.5 million kg shipments per year. During this period, an interesting new alloy, Ti-4Al-2.5V-1.5Fe (designated alloy 425) was developed by Allegheny Technologies Incorporated. This alloy exhibited many of the characteristics of the Ti-6Al-4V alloy, with the advantage of being cold workable (FROES, 2015).

Between 2003 and 2007, with the advent of the Airbus A380, the Joint Strike Fighter (JSF, F-35), and the Boeing 787, plus military conflicts in Iraq and Afghanistan, U.S. mill products reached a new record of 35.8 million kg per year. This new record was followed by the global recession and banking crisis of 2008-2009, resulting in a drop in U.S. mill products to 24.5 million kg. TIMET also developed two new alloys: a low-cost α + β alloy with iron replacing vanadium (Ti-6Al-2Fe-0.1Si) and a low-cost β alloy (Ti-6.8Mo-4.5Fe-1.5Al).

Demand increased between 2010 and 2014, with large titanium purchases for the A380, JSF, and 787 aircrafts. Titanium use in engines and airframes has been increasing ever since. Major commercial airplane producers Boeing and Airbus use extensive amounts of titanium due to its compatibility with carbon-fiber-reinforced composites. Titanium alloys have been increasingly used to reduce the weight of aircraft structures. TIMET has developed the new $\alpha+\beta$ alloy 54M (Ti-5Al-4V-0.75Mo-0.5Fe), which presents better machinability than Ti-6Al-4V but comparable mechanical properties (FROES, 2015).

A study by Transparency Market Research on titanium alloy market, including forecast, within the period from 2017 to 2025, has shown that the aerospace industry remains as the main application area for Ti alloys for weight reduction and improvement of fuel consumption efficiency without significant loss in mechanical properties. These alloys have been increasingly replacing steels in applications that require high strength due to their lower density. The main drives for the increase of titanium alloy market include the rise in defense and aerospace activities and the higher demand in the automotive industry worldwide. However, the relatively high cost of titanium-based systems remains as the key obstacle for the expansion of titanium alloys market for aerospace industry. Currently, North America and Europe are the lead consumers of titanium alloys for aerospace applications, followed by Asia Pacific, where the steep economic and technological growth is expected to provide great opportunities to the market. Precision Cast Parts Corporation, ThyssenKrupp AG, Allegheny Technologies, Alcoa Howmet Castings, Outokumpu, Nippon Steel, ATI Metals, Aperam, Haynes International Inc. and VSMPO are the major titanium alloys manufacturers around the world (“Titanium Alloys Market - Global Industry Analysis, Size, Share, Growth, Trends and Forecast 2017 - 2025”, 2020).

2.2 Main phases in titanium-based systems

This section brings the theoretical aspects of phases present in titanium-based systems, including allotropic and metastable ones, as well as the correlated phase transformation mechanisms.

2.2.1 Allotropic phases: α and β

Titanium can crystallize in more than one crystal structure. Each variation is only stable within particular temperature ranges. The complete transformation from one crystal

structure into another is called allotropic transformation, and the respective transformation temperature is called the *transus* temperature. Pure titanium and the majority of titanium alloys crystallize at low temperatures in a modified hexagonal close-packed (HCP) structure, called α (alpha) titanium. At high temperatures, the body-centered cubic (BCC) structure is stable and is referred to as β (beta) titanium. The β -*transus* temperature for pure titanium is approximately 882°C (LEYENS; PETERS, 2003). The exact transformation temperature is strongly influenced by interstitial and substitutional elements and therefore depends on the purity of the metal (LÜTJERING; WILLIAMS, 2007). **Table 1** shows physical and mechanical properties of pure α titanium, and **Table 2** presents a comparison of properties among pure titanium (Ti), iron (Fe), nickel (Ni) and aluminum (Al).

Table 1 – Physical and mechanical properties of high-purity polycrystalline α titanium (>99.9%) at 25°C.

Structure prototype	Mg
Pearson symbol	hP2
Space group	P6 ₃ /mmc (194)
β-<i>transus</i> temperature	882°C
Lattice parameters	a = 0.295 nm c = 0.468 nm c/a = 1.587
Thermal expansion coefficient [10⁻⁶ K⁻¹]	8.36
Thermal conductivity [W/m.K]	14.99
Specific heat capacity [J/kg.K]	523
Electrical resistance [10⁻⁹ Ω.m]	564.9
Elastic modulus [GPa]	115
Shear modulus [GPa]	44
Poisson's ratio	0.33

Source: LÜTJERING, WILLIAMS (2007)

The atomic unit cells of the hexagonal close-packed α titanium and the body-centered cubic β titanium are schematically shown in **Figure 1**, with their lattice parameters' values indicated and most densely packed planes and directions highlighted. At room temperature, values of lattice parameters for pure α titanium are $a_\alpha = 0.295$ nm and $c_\alpha = 0.468$ nm. The resulting c/a ratio is 1.587, smaller than the ideal ratio of 1.633 for the HCP crystal structure. Insertion of interstitial atoms in the HCP lattice, e.g. C, N, and O, or the incorporation of substitutional atoms with smaller atomic radii than that of titanium, e.g. Al, slightly increases the c/a ratio. The most densely packed lattice planes are the (0002) plane, also called basal plane, the three $\{10\bar{1}0\}$ planes, also called prismatic planes, and the six $\{10\bar{1}\bar{1}\}$ planes, also called pyramidal planes. The three axes a_1 , a_2 , and a_3 are the $\langle 11\bar{2}0 \rangle$ close-packed directions.

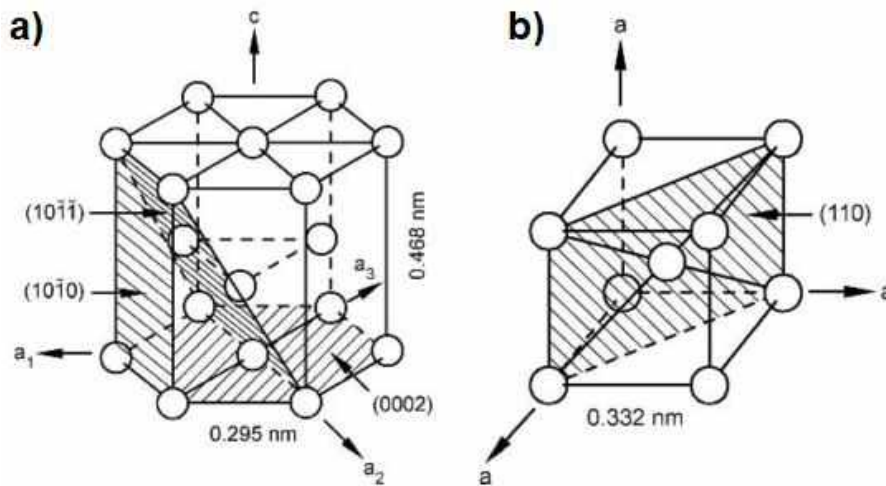
The lattice parameter value of pure β titanium at 900°C is $a_\beta = 0.332$ nm, and its most densely packed systems are the six $\{110\}$ planes and four $\langle 111 \rangle$ directions (LÜTJERING; WILLIAMS, 2007)

Table 2 – Some important characteristics of titanium and titanium based alloys as compared to other structural metallic materials based on Fe, Ni and Al.

Element	Ti	Fe	Ni	Al
Melting temperature (°C)	1670	1538	1455	660
Allotropic transformation (°C)	882 ($\beta \rightarrow \alpha$)	912 ($\gamma \rightarrow \alpha$)	-	-
Crystal structure	BCC \rightarrow HCP	FCC \rightarrow BCC	FCC	FCC
Room temperature E (GPa)	115	215	200	72
Yield stress level (MPa)	1000	1000	1000	500
Density (g/cm³)	4.5	7.9	8.9	2.7
Comparative corrosion resistance	Very high	Low	Medium	High
Comparative reactivity with oxygen	Very high	Low	Low	High
Comparative price of metal	Very high	Low	High	Medium

Source: LEYENS, PETERS (2003)

Figure 1 – Unit cells of a) α and b) β phases of pure titanium.



Source: LÜTJERING, WILLIAMS (2007)

The self-diffusion rate in the high-temperature BCC β phase is about three orders of magnitude higher than in the low-temperature HCP α phase. In addition, the self-diffusion rate in β shows a non-Arrhenius plot with an upward curvature, which is best described using two exponential terms:

$$D_{\text{Ti}}^{\beta} = A_1 \exp\left(-\frac{Q_1}{RT}\right) + A_2 \exp\left(-\frac{Q_2}{RT}\right) \quad (1)$$

where $A_1 = 3.58 \times 10^{-4} \text{ cm}^2/\text{s}$, $A_2 = 1.09 \text{ cm}^2/\text{s}$, $Q_1 = 130 \text{ kJ/mol}$, $Q_2 = 251 \text{ kJ/mol}$ and $R = 8.314 \text{ J/K.mol}$. This implies that the self-diffusion in the β phase is controlled by two or more mechanisms. Zirconium and hafnium are examples of metals that present the same behavior. In contrast, the self-diffusion rate in the α phase shows an Arrhenius plot (POLMEAR et al., 2017).

The diffusion rates of transition metals such as iron, nickel, cobalt, manganese and chromium in α titanium are three to five orders of magnitude higher than the self-diffusion rate of titanium. These transition metals diffuse even one to three orders of magnitude faster than interstitial oxygen, carbon, and nitrogen in the α phase. Their diffusion rates in the β phase are also higher than the self-diffusion rate of titanium, but the difference is less prominent (about one order of magnitude faster). Diffusion rates of these elements parallel to the c -axis of α titanium are higher than those perpendicular to this axis. Aluminum is a slow diffuser in both α and β phases, and its Arrhenius plot of diffusion coefficient in β titanium also exhibits an upward curvature. Zirconium is also a slow diffuser in α phase, but its diffusion rate is similar to the self-diffusion rate of titanium in the β phase. Vanadium, molybdenum, niobium, tantalum, tungsten and tin are slow diffusers in both α and β phases. Hydrogen, on the other hand, exhibits very high diffusion rates in both phases, which can lead to hydrogen embrittlement, stress-corrosion cracking and corrosion fatigue in titanium alloys that are exposed to humid environments. The very high diffusion rate of hydrogen in the α phase is desired only when titanium is hydrogenated for the production of titanium hydride (TiH_2) powder or hydride-dehydride titanium powder (POLMEAR et al., 2017).

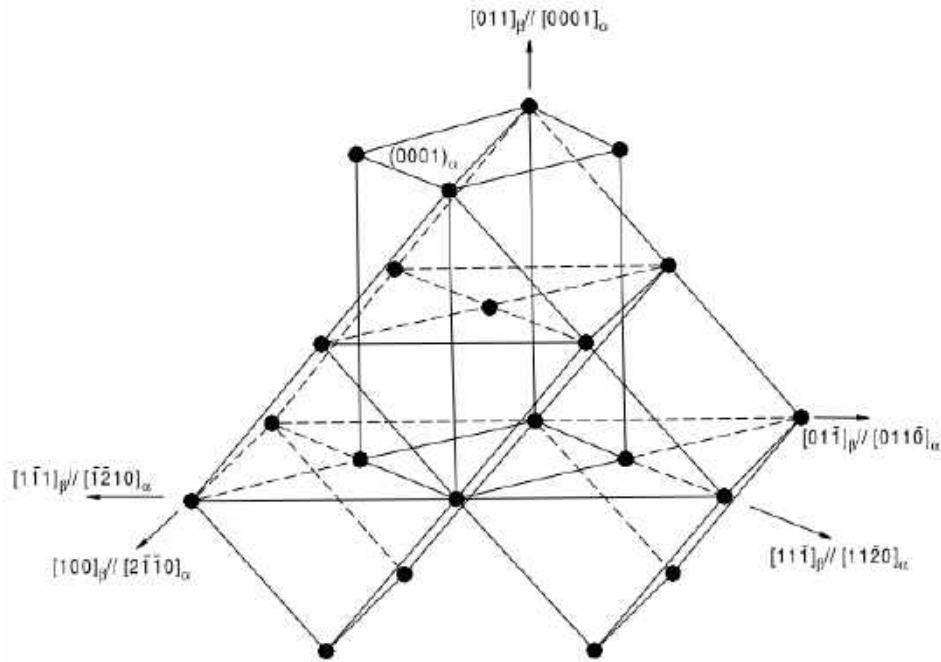
Because of the densely packed atoms in HCP α titanium, diffusion is considerably lower than in BCC β titanium, which means that the diffusion coefficient of α titanium is orders of magnitude smaller than that of β titanium. The different diffusion coefficients of α and β are influenced by the microstructure and thus influence the mechanical behavior of both phases, e.g. creep performance, hot workability, and superplasticity. The limited volume diffusion in α titanium translates into a superior creep performance of α titanium and α -containing Ti alloys compared to β titanium (LEYENS; PETERS, 2003).

Empirical rules of diffusion suggest that the addition of a faster diffusing solute tends to enhance diffusion rates of both the solvent and other solute atoms, while the opposite effect occurs with the addition of a slower diffusing element. Of the four transition metals mentioned above, iron exists as an impurity in all titanium-based materials and is also introduced as an alloying element to a number of titanium alloys. Chromium is a common alloying element. A small amount of nickel can be found in several commercial titanium

alloys. The effects of these fast diffusing impurities or alloying elements can be significant on the diffusion phenomena in both α and β phases during heat treatment or in service at elevated temperatures. Consequently, they are avoided in creep-resistant or high-temperature titanium alloys (POLMEAR et al., 2017).

The existence of two different crystal structures and the corresponding allotropic transformation temperature is of vital importance, since they are the basis for the large variety of properties achieved by titanium alloys. Plastic deformation is closely connected with the respective crystal structure. In addition, the HCP lattice causes anisotropy of mechanical behavior in α titanium, being the elastic anisotropy particularly pronounced. The Young's modulus of titanium single crystals varies between 145 GPa for a load vertical to the basal plane (parallel to the c-axis) and 100 GPa for a load parallel to this plane (perpendicular to the c-axis). The shear modulus presents similar variations, ranging from 34 GPa to 46 GPa for shear stresses applied in $\langle 11\bar{2}0 \rangle$ direction in $\{10\bar{1}0\}$ and (0002) planes, respectively (LEYENS; PETERS, 2003).

The crystallographic relationship between α and β phases is given by the so-called Burgers orientation relationship (BOR): $\{0001\}_\alpha \parallel \{110\}_\beta$ and $\langle 1120 \rangle_\alpha \parallel \langle 111 \rangle_\beta$. This lattice relationship corresponds to the one involving minimum distortion and rotation of lattice vectors. The relationship shows that the basal plane of α derives from a $\{011\}_\beta$ plane and that $[01\bar{1}]_\beta$ and $[100]_\beta$ directions transform into $[01\bar{1}0]_\alpha$ and $[2\bar{1}\bar{1}0]_\alpha$ directions, respectively. The close-packed directions $[1\bar{1}1]_\beta$ and $[\bar{1}1\bar{1}]_\beta$ lying on the $\{110\}_\beta$ plane transform into two close-packed $\langle 11\bar{2}0 \rangle_\alpha$ directions. The other $\langle 11\bar{2}0 \rangle_\alpha$ directions derive from $\langle 100 \rangle_\beta$ directions (BANERJEE; MUKHOPADHYAY, 2007). **Figure 2** illustrates these relationships. Accordingly, the six slip planes and the two slip directions of the β phase unit cell give a maximum of 12 variants of orientation to the α phase. In other words, a BCC crystal can transform into 12 hexagonal variants, having different orientations with regard to the parent β crystal. These variants are depicted in **Table 3**. This Burgers relationship is closely obeyed for both the conventional diffusional process and the martensitic transformation (LEYENS; PETERS, 2003; LÜTJERING; WILLIAMS, 2007).

Figure 2 – The distorted HCP cell derived from the parent BCC cell.

Source: BANERJEE, MUKHOPADHYAY (2007)

Table 3 – All twelve possible variants of the $\beta \rightarrow \alpha$ transformation according to the BOR.

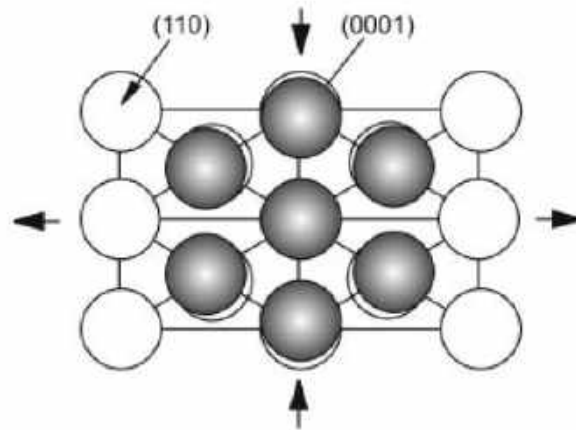
Variant	Parallel planes	Parallel directions	Rotation angle/axis from V1
V1	$(1\bar{1}0)\beta \parallel (0001)\alpha$	$[111]\beta \parallel [11\bar{2}0]\alpha$	-
V2	$(10\bar{1})\beta \parallel (0001)\alpha$	$[111]\beta \parallel [11\bar{2}0]\alpha$	$60^\circ/[11\bar{2}0]$
V3	$(01\bar{1})\beta \parallel (0001)\alpha$	$[111]\beta \parallel [11\bar{2}0]\alpha$	$60^\circ/[11\bar{2}0]$
V4	$(110)\beta \parallel (0001)\alpha$	$[\bar{1}11]\beta \parallel [11\bar{2}0]\alpha$	$90^\circ/[1\ 2.38\ 1.38\ 0]$
V5	$(101)\beta \parallel (0001)\alpha$	$[\bar{1}11]\beta \parallel [11\bar{2}0]\alpha$	$63.26^\circ/[\bar{1}0\ 5\ 5\ \bar{3}]$
V6	$(01\bar{1})\beta \parallel (0001)\alpha$	$[\bar{1}11]\beta \parallel [11\bar{2}0]\alpha$	$60.83^\circ/[\bar{1}.337\ \bar{1}\ 2.377\ 0.359]$
V7	$(110)\beta \parallel (0001)\alpha$	$[1\bar{1}1]\beta \parallel [11\bar{2}0]\alpha$	$90^\circ/[1\ 2.38\ 1.38\ 0]$
V8	$(10\bar{1})\beta \parallel (0001)\alpha$	$[1\bar{1}1]\beta \parallel [11\bar{2}0]\alpha$	$60.83^\circ/[\bar{1}.337\ \bar{1}\ 2.377\ 0.359]$
V9	$(011)\beta \parallel (0001)\alpha$	$[1\bar{1}1]\beta \parallel [11\bar{2}0]\alpha$	$63.26^\circ/[\bar{1}0\ 5\ 5\ \bar{3}]$
V10	$(1\bar{1}0)\beta \parallel (0001)\alpha$	$[11\bar{1}]\beta \parallel [11\bar{2}0]\alpha$	$10.53^\circ/[0001]$
V11	$(101)\beta \parallel (0001)\alpha$	$[11\bar{1}]\beta \parallel [11\bar{2}0]\alpha$	$60.83^\circ/[\bar{1}.337\ \bar{1}\ 2.377\ 0.359]$
V12	$(011)\beta \parallel (0001)\alpha$	$[11\bar{1}]\beta \parallel [11\bar{2}0]\alpha$	$60.83^\circ/[\bar{1}.337\ \bar{1}\ 2.377\ 0.359]$

Source: BELADI, CHAO, ROHRER (2014)

As mentioned, the most densely packed planes of the BCC β phase, $\{110\}$, transform into the basal planes, $\{0001\}$, of the hexagonal α phase. The distance between the basal planes in α is slightly larger than the corresponding distance between the $\{110\}$ planes in β . Therefore, the $\beta \rightarrow \alpha$ transformation causes an atomic distortion, as shown in **Figure 3**. This leads to a slight contraction of the c -axis relative to the a -axis in α , and explains the reduction of the c/a ratio to values below the ideal one for close-packed hexagonal structures. A slight

increase in volume is observed macroscopically during cooling through the β -transus temperature.

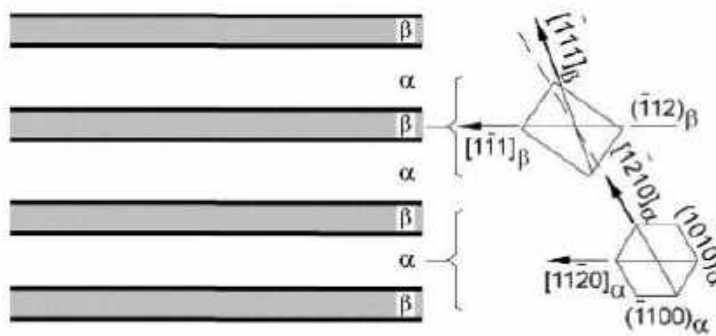
Figure 3 – Distortion of the $(110)\beta$ plane to form the $(0001)\alpha$ plane during the $\beta \rightarrow \alpha$ transformation according to the Burgers orientation relationship.



Source: LEYENS, PETERS (2003)

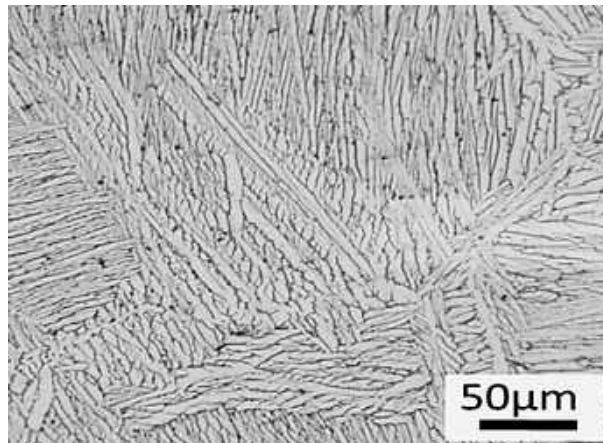
When titanium alloys are cooled at sufficiently low rates from the β phase field into the $\alpha+\beta$ field, the α phase, which is incoherent with respect to β , nucleates preferentially at β grain boundaries, leading to a somewhat continuous α layer along prior β grain boundaries. As cooling proceeds, α plates nucleate either at the interface of this α layer or at the grain boundary itself and grow into the β grain in the form of parallel plates with the same variant of the Burgers relationship, forming the so-called α colony. **Figure 4** represents schematically the crystallographic relationship between α plates and β matrix in a colony (LÜTJERING; WILLIAMS, 2007). Colonies continue to grow into the β grain until they meet other α colonies nucleated at other grain boundary areas and belonging to other variants of the Burgers relationship. This process is called sympathetic nucleation and growth. Individual α plates are separated within colonies by the retained β phase. Due to the lamellar morphology of these colonies, the resulting microstructure is also named lamellar. An example of such microstructure obtained by slow cooling from the β phase field is shown in **Figure 5** for Ti-6Al-4V alloy. In such slowly cooled material, the size of α colonies can be as large as half of the β grain size.

Figure 4 – Schematic representation of the crystallographic relationship between α and β phases within α colonies.



Source: LÜTJERING, WILLIAMS (2007)

Figure 5 – Lamellar microstructure of Ti-6Al-4V alloy.



Source: POLMEAR et al. (2017)

Below the β -*transus* temperature, time- and temperature-dependent diffusion processes are substantially slower. With increasing cooling rate, the size of α colonies, as well as the thickness of the individual α plates, become smaller. Therefore, fast cooling leads to a very fine lamellar structure, whereas upon slow cooling a coarse lamellar structure is obtained (LEYENS; PETERS, 2003; LÜTJERING; WILLIAMS, 2007). In this case, colonies nucleated at β grain boundaries cannot fill the whole grain interior anymore and colonies start to nucleate also on boundaries of other colonies. To minimize the overall elastic strains, new α plates nucleating by “point” contact on the broad face of an existing α plate tend to grow nearly perpendicular to that plate. This selective nucleation and growth mechanism, in combination with the smaller number of α plates within the colonies, leads to a characteristic microstructure called “basketweave” or Widmanstätten structure. For a given cooling rate, this basketweave structure is observed more often in alloys with higher contents of β -stabilizing elements, especially with slow diffusing elements. It is important to emphasize

that, during continuous cooling from the β phase field, the incoherent α plates do not nucleate homogeneously throughout the β matrix (LÜTJERING; WILLIAMS, 2007).

The α phase is significantly hardened by interstitial oxygen. Following the increase in oxygen content, the yield stress is increased from 170 MPa in CP titanium grade 1 to 480 MPa in CP titanium grade 4. In commercial titanium alloys, oxygen content varies between about 0.08% and 0.20%, depending on the alloy type. Substitutional solid solution hardening of the α phase is caused mainly by the elements Al, Sn, and Zr, which have fairly large atomic size differences to titanium and also large solubility in the α phase. With compositions above about 5% Al, precipitation hardening of the α phase can occur by the precipitation of coherent Ti_3Al particles (see **Section 2.2.5**) (LÜTJERING; WILLIAMS, 2007).

As for the β phase, one way to estimate the solid solution strengthening of the β stabilizing elements Mo, V, Nb, Cr, and Fe is to examine the slope of the lattice parameters *versus* solute content curves for binary alloys, which points out in a qualitative way the size misfit parameter. The steepest slope is seen in the Ti-Fe system, followed by Ti-Cr and Ti-V, while Nb and Mo have the smallest effect on the lattice parameter. Precipitation hardening of the β phase is the most effective way to increase the yield stress of commercial β titanium alloys. Two metastable phases, ω and β' , are observed in β titanium alloys (see **Section 2.2.3** and **Section 2.2.4**) (LÜTJERING; WILLIAMS, 2007).

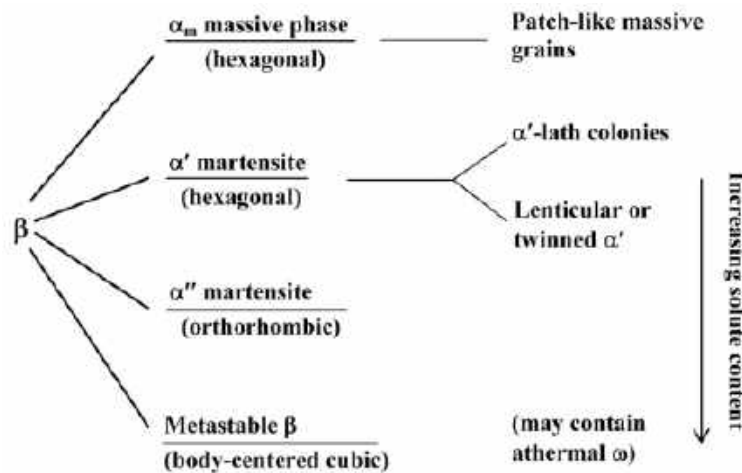
Both ω and β' are coherent and sheared by moving dislocations. This results in the formation of intense, localized slip bands leading to early crack nucleation and low ductility. Therefore, microstructures containing these precipitates are usually avoided in commercial β titanium alloys. Instead, commercial β titanium alloys are aged at slightly higher temperatures to induce the precipitation of incoherent α phase particles using ω or β' particles as precursors and nucleation sites. Using these precursors, it is possible to obtain a fairly homogeneous distribution of small α platelets. These α platelets also obey the Burgers relationship and the flat surface of the platelets is parallel to one of the $\{112\}$ planes of the β matrix. However, not all twelve possible variants are nucleated statistically; instead, in order to minimize the overall elastic strains, only two or three variants nearly perpendicular to each other are predominant in a given volume of a β grain. Since these incoherent α platelets are too small to deform plastically, they act as hard, undeformable particles. Consequently, high yield stresses can be obtained in β titanium alloys with these microstructures. The yield stress in these alloys can be easily lowered by applying a two-stage heat treatment. In this case, the first annealing step is done at high temperatures in the $(\alpha+\beta)$ phase field to precipitate a desired volume fraction of large α plates and reducing thereby the volume fraction of small α platelets in the second

aging step at lower temperatures. These large α plates contribute less to the yield stress than the small platelets because they are large enough to be plastically deformed; thus, only boundary hardening is present as a hardening mechanism for these larger plates. Nevertheless, in all microstructures with α precipitates the dislocation density increases in the β matrix during α precipitation. Therefore, dislocation hardening is also contributing to the yield stress (LÜTJERING; WILLIAMS, 2007).

2.2.2 Martensitic phases: α' and α''

Depending on the composition, titanium alloys can present different transformations of the BCC β phase upon fast cooling (**Figure 6**) (POLMEAR et al., 2017). In the case of martensitic transformation, β transforms completely by a diffusionless transformation process, forming a metastable fine plate-like, or acicular, martensitic microstructure. The martensitic microstructure is characterized by a very fine basketweave structure with needle-like character due to its diffusionless nucleation (LEYENS; PETERS, 2003).

Figure 6 – Possible reactions from the β phase in titanium alloys upon quenching.



Source: POLMEAR et al. (2017)

Titanium can form two types of martensite: the hexagonal α' martensite and the orthorhombic α'' martensite (LEYENS; PETERS, 2003). The most common titanium martensite is the α' type. It usually forms as colonies of parallel-sided plates or laths in two-dimensional morphology, the boundaries of which consist of dislocation walls. The orientation relationship between the β phase and α' -martensite is: $(110)\beta \parallel (0001)\alpha'$; $[111]\beta \parallel [1120]\alpha'$ (POLMEAR et al., 2017). It is a supersaturated solid solution of elements in α and is

formed during fast cooling from the β field, by plastic deformation or during aging in zones of the β phase depleted in β stabilizing elements. The α' phase is a typical martensitic phase similar to corresponding phases in steels and other non-iron-based alloys. However, there are some features of α' phase that are not common to iron martensite: it is a supersaturated substitutional solid solution, whereas steel martensite is an interstitial solid solution; it provides low strengthening effect when compared to steel martensite; and it does not hinder the alloy's plasticity, differently from martensite in steels (LEYENS; PETERS, 2003). Martensite in titanium is much softer than in Fe-C alloys because the interstitial oxygen atoms only cause small elastic distortion of the hexagonal lattice in the first. This is in sharp contrast to carbon and nitrogen, that cause severe tetragonal distortion of the BCC lattice in ferrous martensite (LÜTJERING; WILLIAMS, 2007).

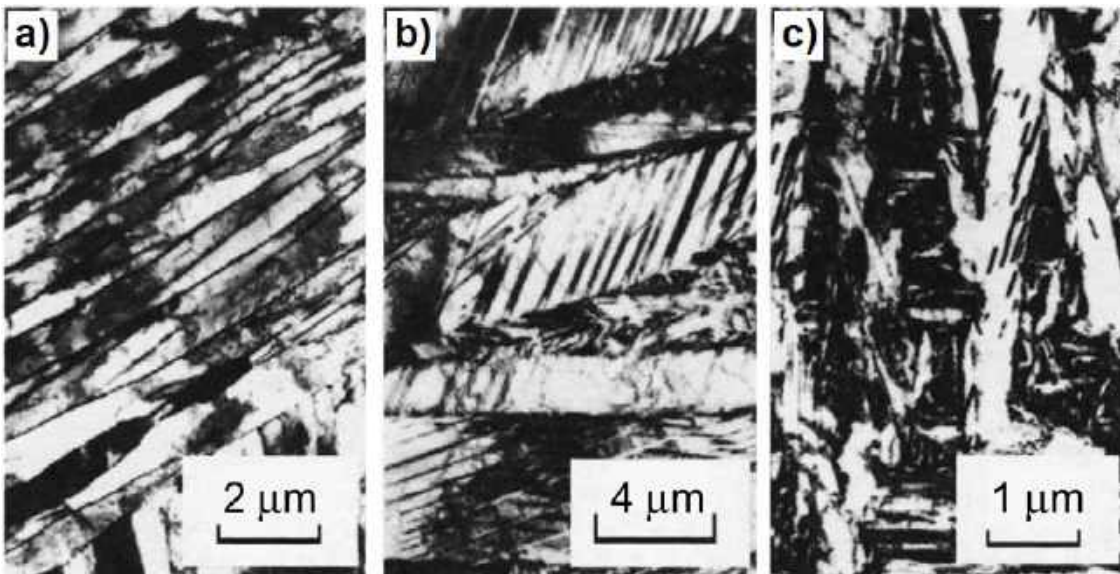
The martensitic transformation involves the cooperative movement of atoms by a shear-type process, resulting in a microscopically homogeneous transformation of the BCC into the HCP crystal lattice over a given volume. The transformed volume is usually plate- or disk-shaped for most titanium alloys. The entire shear transformation process can be reduced to the activation of the following shear systems: $[111]\beta (11\bar{2})\beta + [111]\beta (\bar{1}01)\beta$ and $[2\bar{1}\bar{1}3]\alpha (\bar{2}112)\alpha + [2\bar{1}\bar{1}3]\alpha (\bar{1}011)\alpha$.

The hexagonal martensite is observed in two morphologies: massive martensite (lath martensite) and acicular martensite. Massive martensite occurs only in pure titanium, very dilute alloys, and in alloys with a high martensitic transformation temperature. It consists of large irregular regions (size about 50-100 μm) containing near-parallel arrays of much smaller α plates or laths about 0.5-1 μm thick, belonging to the same variant of the Burgers relationship. Acicular martensite, on the other hand, occurs in alloys with higher solute content and lower martensitic transformation temperature, and consists in a mixture of individual plates, each having a different variant of the Burgers relationship, presenting also a much broader size distribution than lath martensite (HASHMI, 2014; LÜTJERING; WILLIAMS, 2007; POLMEAR et al., 2017). The transition between lath and acicular martensites is not abrupt, and the two morphologies may coexist over a certain composition range (HASHMI, 2014).

Typically, martensitic plates contain a high dislocation density and are internally twinned along $\{10\bar{1}1\}$ planes (**Figure 7a** and **Figure 7b**) (POLMEAR et al., 2017). Since the hexagonal α' martensite is supersaturated in β stabilizers, upon annealing in the $(\alpha+\beta)$ phase field it decomposes into $\alpha+\beta$ by precipitating incoherent β particles at dislocations or β layers at plate boundaries (LÜTJERING; WILLIAMS, 2007). When the solute concentration is

sufficiently high, the martensitic transformation may be incomplete, and some β phase may be retained between platelets. This arrangement is similar to the Widmanstätten one, which consists of groups of α phase needles with their long axes parallel to the $\{110\}$ planes of the retained β phase (BANERJEE; MUKHOPADHYAY, 2007).

Figure 7 – TEM images showing the structure of titanium alloy martensites: **a)** HCP α' laths in Ti-1.8Cu quenched from 900°C, **b)** HCP lenticular α' containing twins in Ti-12V quenched from 900°C and **c)** orthorhombic α'' in Ti-8.5Mo-0.5Si quenched from 950°C.



Source: POLMEAR et al. (2017)

The martensitic α' phase is normally subjected to a subsequent aging treatment. Precipitation in the retained β phase may also occur in the same process when the retained β phase exists. The aging temperature is alloy dependent. For water-quenched Ti-6Al-4V, it is recommended to be 480-595°C for 4-8 h, followed by air cooling. In β -isomorphous alloys, α' decomposes into α and β through the formation of fine precipitates at martensite plate boundaries, or at internal substructures, such as twins. In β -eutectoid alloys, α' may decompose into α phase plus an intermetallic compound, although the formation of this compound may take place in several stages. However, in systems such as Ti-Fe and Ti-Mn, where the normal eutectoid reaction is sluggish, the martensite decomposes first by forming β and α , with the intermetallic compound appearing slowly at a later stage (POLMEAR et al., 2017).

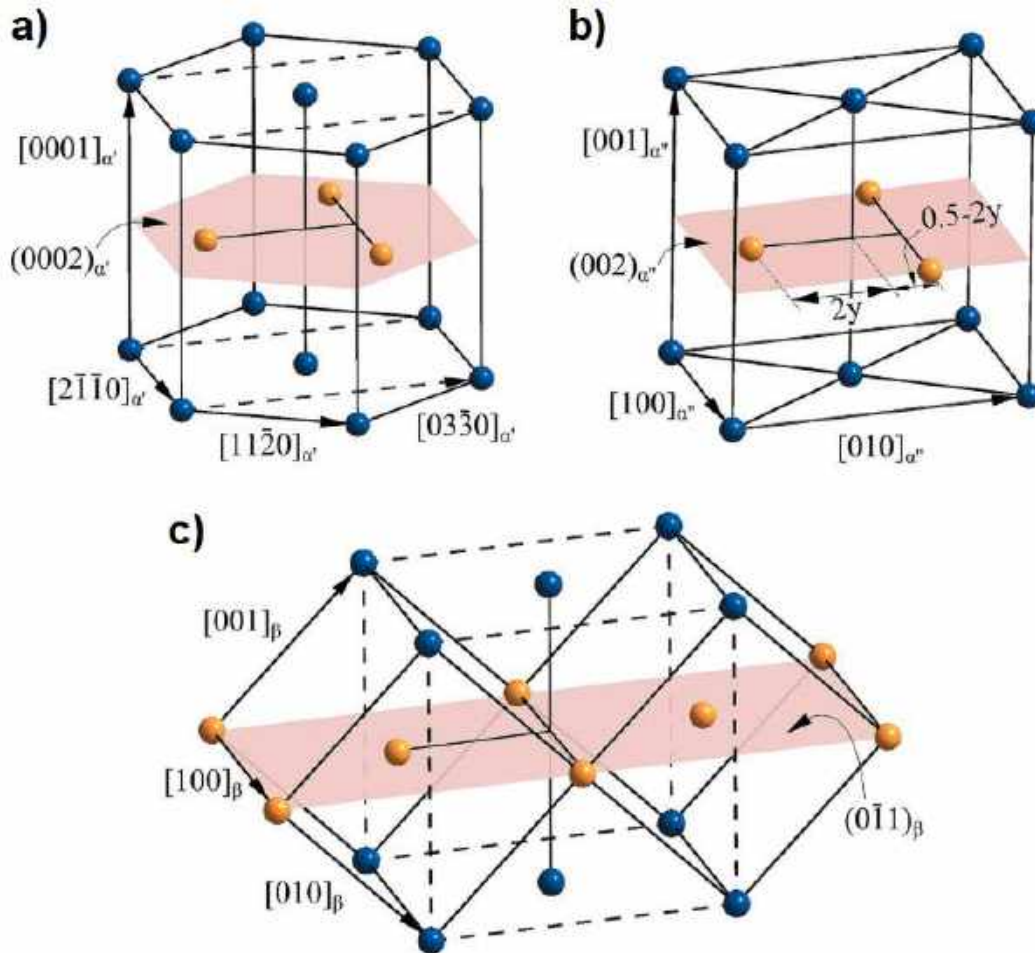
With increasing solute content, the structure of the martensite becomes distorted, losing its hexagonal symmetry and being better defined as orthorhombic. This orthorhombic martensite is designated α'' (LÜTJERING; WILLIAMS, 2007). It presents a similar lattice

correspondence with the β phase and is also internally twinned, with twins forming on the $\{111\}$ planes (**Figure 7c**) (POLMEAR et al., 2017). Different from α' , which can form in all titanium alloys in which martensitic transformation occurs, α'' is present in alloys containing specific alloying elements and high alloying elements content. It is also a supersaturated solid solution, and its crystal structure is shown in **Figure 8**. Its needlelike morphology is similar to that of α' , but it is usually composed of smaller laths. There are several hypotheses to explain α'' phase formation in titanium alloys, being the most often mentioned atomic volumes, concentration of electrons and valence (in this regard, α'' forms only in alloys containing elements with valence higher than that of titanium) (HASHMI, 2014). Orthorhombic α'' martensite is characterized by its good deformability (LEYENS; PETERS, 2003).

Depending on the heat treatment or manufacturing process, α'' martensite can be formed in the following three ways: by decomposition of metastable β during quenching, following the reaction $\beta \rightarrow \alpha''$; by decomposition of retained β by intermediate transformation during isothermal aging, e.g. through $\beta \rightarrow \beta_{\text{lean}} + \beta_{\text{rich}} \rightarrow \alpha'' + \beta_{\text{rich}}$; or by stress-induced transformation of retained β , i.e. $\beta \rightarrow \alpha'' + \text{twinned } \beta$ (POLMEAR et al., 2017). The martensitic start temperature (M_S) of pure titanium depends on the impurity level, but lies around 800-850°C, increases with increasing amounts of α -stabilizing elements, such as aluminum and oxygen, and decreases with increasing content of β stabilizers (LÜTJERING; WILLIAMS, 2007). If M_S and M_F (martensitic finish temperature) fall above and below room temperature, respectively, then a mixed microstructure containing lenticular α' or α'' martensite may be formed together with retained β (POLMEAR et al., 2017). The α'/α'' boundary in terms of solute content for some binary Ti systems is defined in **Table 4**.

Aging of α'' martensite may occur by two mechanisms. In alloy compositions in which the $M_S(\alpha'')$ lies in a relatively high temperature, decomposition of α'' may proceed by both spinodal decomposition and reverse martensitic transformation (POLMEAR et al., 2017). Spinodal decomposition consists in a separation between solute lean and solute rich α'' regions, forming a characteristically modulated microstructure before the β phase is finally precipitated ($\alpha''_{\text{lean}} + \alpha''_{\text{rich}} \rightarrow \alpha + \beta$) (LÜTJERING; WILLIAMS, 2007). The resulting microstructure consists of α and β phases. Further aging might lead to the formation of α phase particles at the prior β grain boundaries and lamellar $\alpha+\beta$ in the matrix. In alloys having a $M_S(\alpha'')$ temperature close to room temperature, α'' reverts to the β phase, which then decomposes by a mechanism that is characteristic of the particular aging temperature (POLMEAR et al., 2017).

Figure 8 – **a)** The HCP lattice of the α' martensite., where the (0002) plane is shaded in pink and dashed lines delineate the edges of an equivalent C-centered orthorhombic unit cell, **b)** the unit cell of the C-centered orthorhombic α'' martensite where the (002) α'' plane is shaded in pink and **c)** two unit cells of the BCC β phase where one $\{110\}_\beta$ plane is shaded in pink and dashed lines delineate the edges of an equivalent C-centered orthorhombic unit cell. The magnitude of y determines the position of atoms on the (002) α'' plane along the $[010]_{\alpha''}$ direction.



Source: BÖNISCH et al. (2014)

Table 4 – Composition of the α'/α'' martensite boundary in some binary titanium alloy systems with transition metals.

α'/α'' boundary	Ti-V	Ti-Nb	Ti-Ta	Ti-Mo	Ti-W
wt%	9.4	10.5	26.5	4.0	8.0
at%	8.9	5.7	8.7	2.0	2.2

Source: LÜTJERING, WILLIAMS (2007)

In terms of mechanical behavior, aging of the modulated microstructure resulting from the spinodal decomposition of the orthorhombic α'' martensite leads to a drastic increase in yield stress. In this case, the disordered, solute rich zones become stronger obstacles to dislocation movement as their size and misfit increase with aging. Due to the large volume

fraction of these zones in those modulated microstructures, the material becomes brittle on a macroscopic scale. The reason is the intense strain localization that occurs because the modulated zones are destroyed within the slip bands. This means that the first slip band in the largest α'' martensite plate develops sufficient strain to cause crack nucleation at the plate boundary. Fracture occurs by microvoid coalescence and growth, not by cleavage (LÜTJERING; WILLIAMS, 2007).

Whereas α'' tended to be neglected in earlier studies, its importance is now recognized, especially in the development of shape memory and superelastic β -titanium alloys. Both properties are associated with the reversible transformation between β and α'' . The presence of α'' lowers tensile ductility in titanium alloys, although it does have the advantage of being a favorable precursor in producing a very uniform distribution of the α phase following subsequent heat treatment (POLMEAR et al., 2017).

In addition to martensitic transformations, the other composition-invariant transformation, $\beta \rightarrow \alpha_m$ massive transformation, may also occur in $\alpha+\beta$ alloys at slower quenching rates from the β phase field. Limited diffusional activities are involved at the advancing interfaces. The resulting α_m grains are patch-like and can form at different locations, e.g. at or across β grain boundaries or inside β grains. It should be pointed out that martensite laths often form together with the α_m grains due to local fast cooling rates (POLMEAR et al., 2017).

2.2.3 Omega (ω) phase

Decomposition of the β phase that is retained upon quenching into the equilibrium α phase occurs only at relatively high temperatures, probably because of the difficulty of nucleation of the HCP α phase from the BCC β matrix. Accordingly, intermediate decomposition products are usually formed and the possible reactions are: $\beta \rightarrow \beta + \omega \rightarrow \beta + \alpha$ for medium alloy content aged at temperatures between 100°C and 500°C; $\beta \rightarrow \beta + \beta' \rightarrow \beta + \alpha$ for concentrated alloys aged at temperatures between 200 and 500°C; and $\beta \rightarrow \beta + \omega \rightarrow \beta + \alpha$ for concentrated alloys aged at temperatures above 500°C (POLMEAR et al., 2017).

Metastable omega phase was discovered in 1954 in aged β titanium alloys which presented abnormal fragility (FROST et al., 1954). Since then, it has been extensively studied, especially because of its deleterious effects on mechanical properties of β titanium alloys, its influence on physical properties such as superconductivity and because of the mechanisms

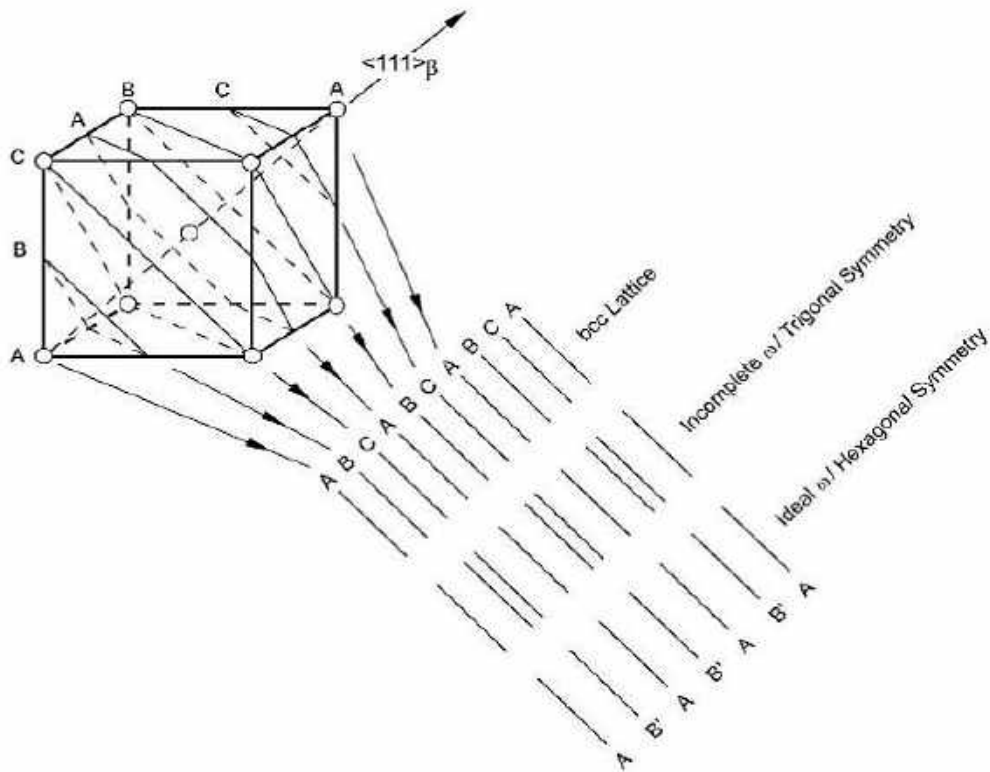
behind the $\beta \rightarrow \omega$ transformation (BANERJEE; TEWARI; DEY, 2006). It occurs mostly under three conditions:

1. When the amount of β -stabilizing elements is high enough to retain β phase during rapid cooling, avoiding martensitic transformation. In this case, the so called athermal ω is formed by a displacive, diffusionless reaction that cannot be suppressed, no matter how rapid the cooling (BANERJEE; MUKHOPADHYAY, 2007; HICKMAN, 1969a; SIKKA; VOHRA; CHIDAMBARAM, 1982).
2. With higher contents of alloying elements, a phase called isothermal ω can form during aging at temperatures between 100 and 500°C. It differentiates itself from athermal ω by its larger particle size and by the existence of a compositional gradient in the interface with the β matrix, being leaner in β -stabilizing elements than the matrix, while athermal ω presents very similar composition to that of the matrix (BANERJEE; MUKHOPADHYAY, 2007; HICKMAN, 1968, 1969a, 1969b).
3. Under certain conditions of room temperature deformation and high pressure application (KUAN; AHRENS; SASS, 1975). In these cases, ω can form from the α phase as well (BANERJEE; TEWARI; DEY, 2006).

Omega forms rapidly as homogeneously nucleated, coherent precipitates (POLMEAR et al., 2017) and presents hexagonal structure ($P6/mmm$ space group) with $c/a = 0.613$. However, it can present a trigonal structure ($P\bar{3}m1$ space group) in the early stages of the transformation and in alloys with higher concentration of alloying elements (DUERIG; TERLINDE; WILLIAMS, 1980; SASS, 1972; SASS; BORIE, 1972; SIKKA; VOHRA; CHIDAMBARAM, 1982). The equivalent atomic sites in the ω unit cell are A (0, 0, 0) and B ($\frac{2}{3}$, $\frac{1}{3}$, $\frac{1}{2} - z$; $\frac{2}{3}$, $\frac{1}{3}$, $\frac{1}{2} + z$), where $z = 0$ defines an ideal structure with hexagonal symmetry, $0 < z < \frac{1}{6}$ defines a non-ideal trigonal symmetry and $z = \frac{1}{6}$ defines the cubic symmetry (BANERJEE; TEWARI; DEY, 2006). Its orientation relationship with the β phase is defined as: $\{111\}\beta \parallel (0001)\omega$ and $\langle 1\bar{1}0 \rangle\beta \parallel \langle 1\bar{2}10 \rangle\omega$. This orientation relationship is valid for both athermal and isothermal phases, and it implies that there are four possible crystallographic variants of the ω structure, depending on which of the $\{111\}\beta$ planes is parallel to the $(0001)\omega$ plane. For the same variant of the ω structure, there are three $\langle 110 \rangle\beta$ directions, so that a total of 12 variants of the ω structure are possible. However, since the basal plane of this structure has a six-fold symmetry, the three variants for a given $\{111\}\beta$ plane will appear identical and, therefore, the contribution from only four variants will be seen in selected area diffraction patterns (BANERJEE; MUKHOPADHYAY, 2007).

The athermal ω phase has been suggested to be a precursor to the martensitic reaction because the athermal transformation involves a shear displacement in the $\langle 111 \rangle_{\beta}$ direction of the BCC lattice, as shown in **Figure 9**, which also relates the trigonal structure that ω phase may present.

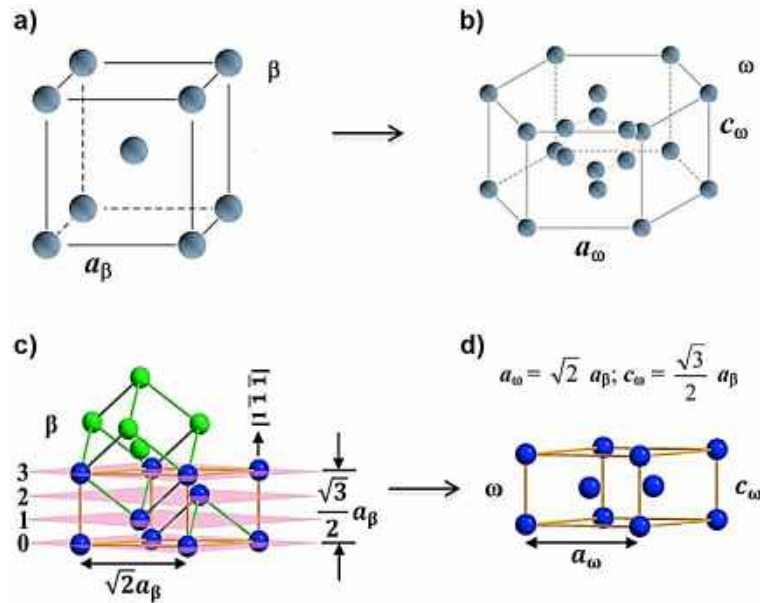
Figure 9 – Representation of the $\beta \rightarrow \omega$ transformation showing the $\{222\}$ planes of the BCC lattice.



Source: LÜTJERING, WILLIAMS (2007)

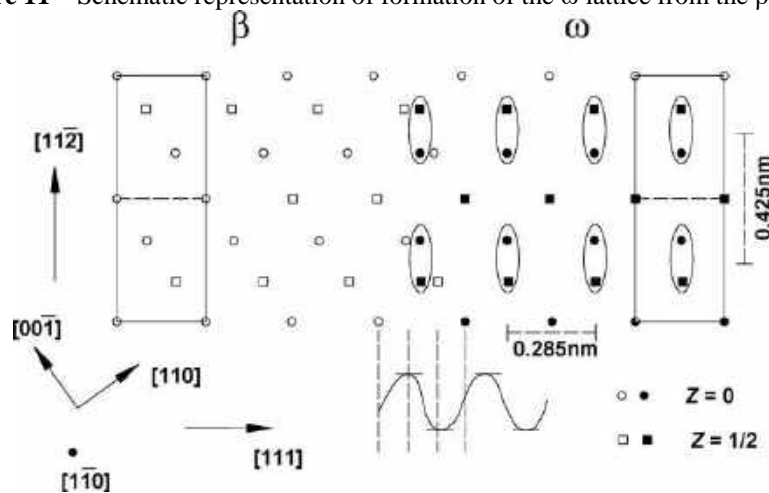
Changes in the lattice structure from β to ω are schematically illustrated in **Figure 10**. The unit cell of the ω phase can be regarded as originating from four adjacent layers of $\{222\}_{\beta}$ (d-spacing = $\frac{\sqrt{3}}{6} a_{\beta}$) after a small shuffle along the $\langle 111 \rangle_{\beta}$ direction. Hence, the d-spacing of $(0001)_{\omega}$ is equal to three times the d-spacing of $\{222\}_{\beta}$, ($c_{\omega} = \frac{\sqrt{3}}{2} a_{\beta}$) (BANERJEE; MUKHOPADHYAY, 2007; POLMEAR et al., 2017). The presence of ω phase precipitates in β matrix can be found by electron diffraction patterns along $\langle 113 \rangle_{\beta}$ and $\langle 110 \rangle_{\beta}$ zone axes (POLMEAR et al., 2017). **Figure 11** shows another schematic representation of the development of the ω phase from the β matrix using crystallographic relationships between both phases. The short spacing (0.285 nm) is along $[111]$ or $[11\bar{1}]$ directions and the long spacing (0.425 nm) is along $[112]$ or $[11\bar{2}]$ directions.

Figure 10 – a) BCC lattice of β , b) hexagonal lattice of ω , c) relationship between β and ω prior to shuffle along $[1\bar{1}\bar{1}]$ direction and d) unit cell of ω after shuffle (represents a third of the hexagonal lattice of ω shown in a).



Source: LAI et al. (2015); POLMEAR et al. (2017)

Figure 11 – Schematic representation of formation of the ω lattice from the β lattice

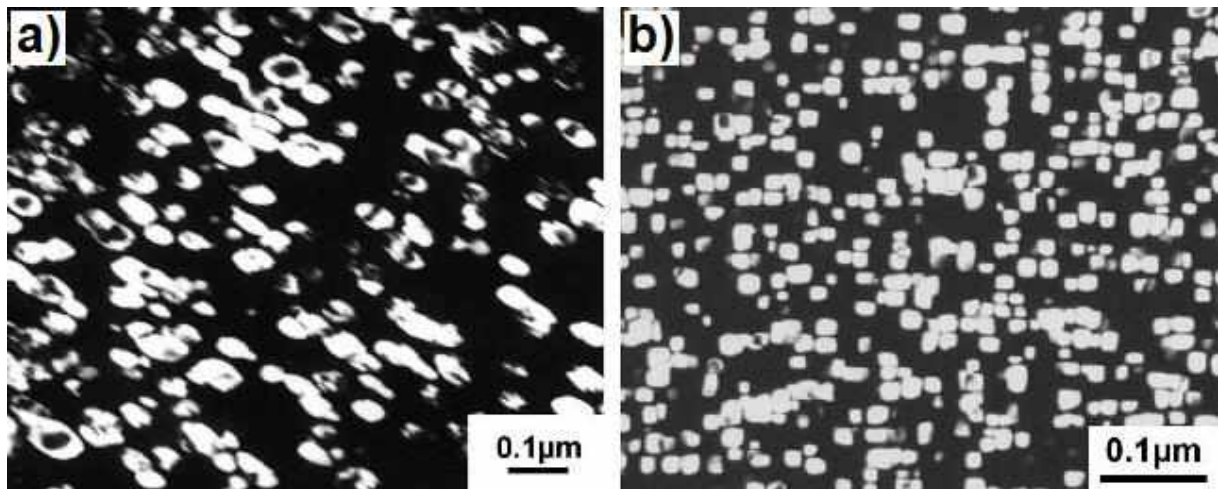


Source: BANERJEE, TEWARI, DEY (2006)

Typically, its morphology can be either ellipsoidal or cuboidal (BANERJEE; TEWARI; DEY, 2006; BLACKBURN; WILLIAMS, 1968; BRAMMER; RHODES, 1967; HICKMAN, 1968; WILLIAMS; BLACKBURN, 1969), although rod-like ω particles have also been observed (CROUTZEILLES; MIRAND; SAULNIER, 1961). In cuboidal particles, the cube face is parallel to $\{100\}_\beta$, and in ellipsoidal particles the long axis is parallel to $\langle 111 \rangle_\beta$. Precipitates of athermal ω are usually difficult to have their shape defined due to their reduced size (2-10 nm) and to their tendency to be aligned along $\langle 111 \rangle_\beta$ directions. The

shapes of isothermal ω (10-20 nm) are more distinguishable (BANERJEE; MUKHOPADHYAY, 2007). The variation of morphology justifies itself by the lattice deformation caused by the coherence of particles, $(V_{\omega} - V_{\beta})/3V_{\beta}$: in systems with low misfit ($< 0.5\%$), the shape is defined by minimization of surface energy, resulting in ellipsoidal particles, whereas systems with higher misfit strains ($> 1\%$) present cuboidal-shaped particles in order to minimize elastic strains in the matrix (BANERJEE; MUKHOPADHYAY, 2007; WILLIAMS; BLACKBURN, 1969). There are several hypotheses to explain the $\beta \rightarrow \omega$ transformation, and two factors appear to play a key role: electron density and atomic volume (ω forms in alloys in which the lattice parameter of β phase ranges between 0.3255 and 0.3260 nm). **Figure 12** present examples of ellipsoidal and cuboidal ω .

Figure 12 – a) TEM dark field micrograph of ellipsoidal ω precipitates in Ti-16Mo aged 48h at 450°C and b) TEM dark field micrograph of cuboidal ω precipitates in Ti-8Fe aged 4h at 400°C.



Source: LÜTJERING, WILLIAMS (2007)

As previously stated, the presence of the ω phase can cause severe embrittlement of the alloy, caused by the poor mobility of dislocations along ω particles. It is interesting to note, however, that even in alloys displaying no macroscopic ductility, the fracture surfaces show exceedingly small dimples, which are indicative of some ductility at a microscopic scale. Thus, the possibility exists that the potent hardening associated with ω may be used to practical advantage, although no progress has been made in this regard. On the other hand, strengthening of Ti-10Al-2Fe-3Al (Ti-1023) alloy through ω phase precipitation instead of α phase precipitation has been found to retard fatigue crack propagation significantly. This retardation has been attributed to changes in slip character. In addition, ω particles have been

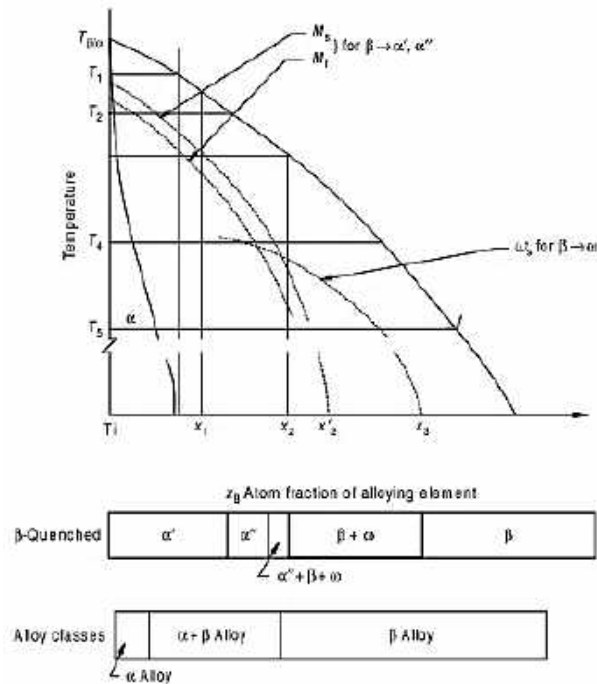
beneficial in the specialized field of superconducting titanium-niobium alloys (POLMEAR et al., 2017).

Omega phase is not easily encountered in the “workhorse” Ti-6Al-4V alloy due to its high Al content. Williams, Hickman and Leslie (WILLIAMS; HICKMAN; LESLIE, 1971) have observed that additions of Al to Ti-V alloys continuously reduced the maximum volume fraction of ω in the alloy after aging, as well as its temperature and time of stability, and maximum particle size. With a composition of Ti-20V-10Al, ω formation was completely suppressed during aging between 300°C and 400°C. In the case of Ti-6Al-4V, the presence of oxygen also contributes to ω suppression. However, if the β phase is sufficiently enriched with vanadium, ω phase might precipitate during low temperature aging (BOYER; ELSCH; COLLINS, 1994). Lasalmonie and Loubradou (LASALMONIE; LOUBRADOU, 1979) have reported the formation of ω in the alloy during aging at 360°C after annealing at 800°C followed by water quenching. This has been attributed to a V enrichment of the β phase with more than 10 wt%. Omega phase was also observed in rapidly solidified Ti-6Al-4V alloy and can also be attributed to the occurrence of a highly V-enriched β phase. TEM analysis of the alloy showed a diffuse ω scattering, characteristic of the initial stage of the $\beta \rightarrow \omega$ transformation (FAN, 1994), and after room temperature aging for one year the transformation advanced (FAN; MIODOWNIK, 1994).

The range of compositions over which the different athermal products, namely α' , α'' and ω , can be formed, are illustrated in **Figure 13**, with indication of the start (M_S) and finish (M_F) temperatures of martensite formation, as well as the temperature of ω formation (ω_S) as function of the concentration of β -stabilizing elements. In the same figure, the resulting microstructures obtained upon quenching from the β field and the corresponding alloy classification, which will be discussed ahead, are also depicted. On quenching, alloys of different compositions exhibit different athermal transformation products. Alloys in the composition range $0 < x_B < x_1$ produce α' (HCP) martensite, while those in the range $x_1 < x_B < x_2$ transform into orthorhombic α'' martensite, being x_1 the level of supersaturation at which orthorhombic distortion occurs. The curves corresponding to M_F and ω_S intersect at $x_B = x_2$. This means that, for alloy compositions with $x_B > x_2$, the martensitic transformation reaches completion before the ω_S temperature and therefore the product is fully martensitic. The temperature gap between M_S and M_F in most of the Ti-based alloys is very small (in the range of 25°C), and, as consequence, incomplete martensitic transformation is not frequently observed. In the composition range $x'_1 < x_B < x'_2$, the quenched structure consists of martensitic plates along with some untransformed β phase in which ω is finely distributed. In

the composition range of $x'_2 < x_B < x'_3$, the quenched product contains a distribution of athermal ω particles in the β matrix (BANERJEE; MUKHOPADHYAY, 2007).

Figure 13 – Basis for the classification of commercial Ti and alloys into α alloys, $\alpha+\beta$ alloys and β alloys.



Source: BANERJEE, MUKHOPADHYAY (2007)

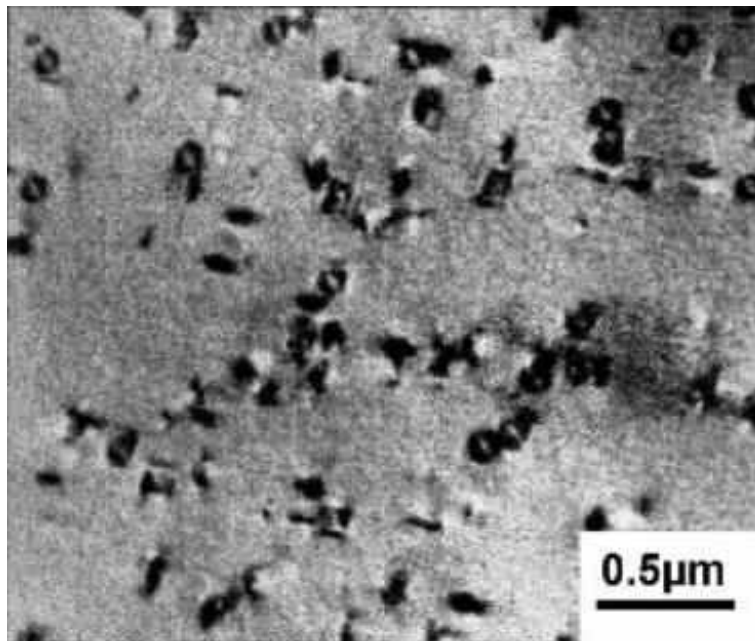
Solute partitioning occurs during aging, leading to depletion of ω and enrichment of the β matrix. The terminal composition of ω in aged binary titanium alloys is related to the group number of the solute in the periodic table because the electron-to-atom ratios of all ω phases have been found close to 4.2:1. Thus, the possibility exists that ω is an electron compound (POLMEAR et al., 2017).

2.2.4 Beta phase separation

Separation of the β phase into two BCC phases with different compositions is favored in alloys that contain sufficient β -stabilizers to prevent ω formation during low temperature aging, and which transform slowly to the equilibrium α phase under these conditions. This transformation is thought to occur during aging of a wide range of alloys but has received only limited attention, because it is not considered to be important in commercial alloys. The phases that form correspond to the β matrix (β_{rich}) and to uniformly dispersed, coherent precipitates designated as β' (β_{lean}). (POLMEAR et al., 2017). As ω phase, this case represents

a miscibility gap between two BCC phases, β_{lean} and β_{rich} , the major difference being the magnitude of distortion of the BCC lattice in the coherent disordered precipitates (β_{lean}) with respect to the BCC lattice of the matrix (β_{rich}). In highly concentrated alloys, the magnitude of distortion is very small and the metastable particles are called β' having a BCC crystal structure. In some cases, a tetragonal lattice can be obtained (AFONSO et al., 2010). In case of less concentrated alloys, the distortion of the BCC lattice is much higher and the metastable particles are called isothermal ω , having an hexagonal crystal structure (LÜTJERING; WILLIAMS, 2007). The β' precipitates have a morphology which varies from spheres or cuboids in Ti-Nb and Ti-V-Zr alloys to plates in Ti-Cr alloys, depending on the magnitude of misfit and coherency strains, as is the case of ω precipitates. One example for the solute lean β' precipitates is shown in **Figure 14** for Ti-15Zr-20V alloy aged during 6 h at 450°C (LÜTJERING; WILLIAMS, 2007).

Figure 14 – TEM image of coherent β' particles in Ti-15Zr-20V aged 6 h at 450°C.



Source: LÜTJERING, WILLIAMS (2007)

2.2.5 Ordered intermetallic phase: Ti_3Al

Ti_3Al , also known as α_2 (alpha-2) is one of the three stable intermetallic phases formed in the Ti-Al system, along with $TiAl$ and $TiAl_3$ (BANERJEE; MUKHOPADHYAY, 2007). Alpha-2 is an ordered hexagonal solid solution. It occurs mainly due to the addition of high amounts of α stabilizers and is seen in alloys containing more than 6 wt% Al (FROES, 2015;

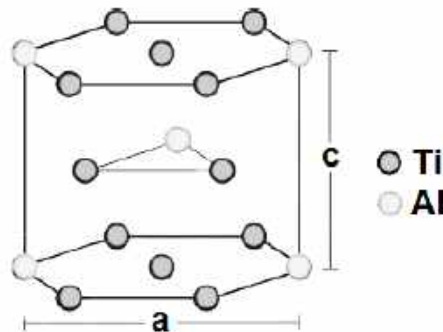
NAG, 2008). Its crystallographic properties are described in **Table 5**. Alloys based on intermetallic phases are interesting for structural applications, but are difficult to be processed because intermetallics are normally brittle (BANERJEE; MUKHOPADHYAY, 2007). **Figure 15** presents its crystal structure, which is characterized by an atomic arrangement on the close-packed (0001) planes, ensuring that Al atoms have only Ti atoms as their neighbors. An hexagonal ABABAB... stacking sequence of these planes forms the ordered structure of α_2 .

Table 5 – Crystallographic properties of the Ti_3Al phase.

System	HCP
Prototype	Ni_3Sn
Strukturbericht	D0_{19}
Space group	$\text{P6}_3/\text{mmc}$
Number	194
Pearson symbol	hP8
Lattice parameters	
a	0.577 nm
c	0.465 nm

Source: VILLARS, CALVERT (1986)

Figure 15 – Crystal structure of the Ti_3Al phase.

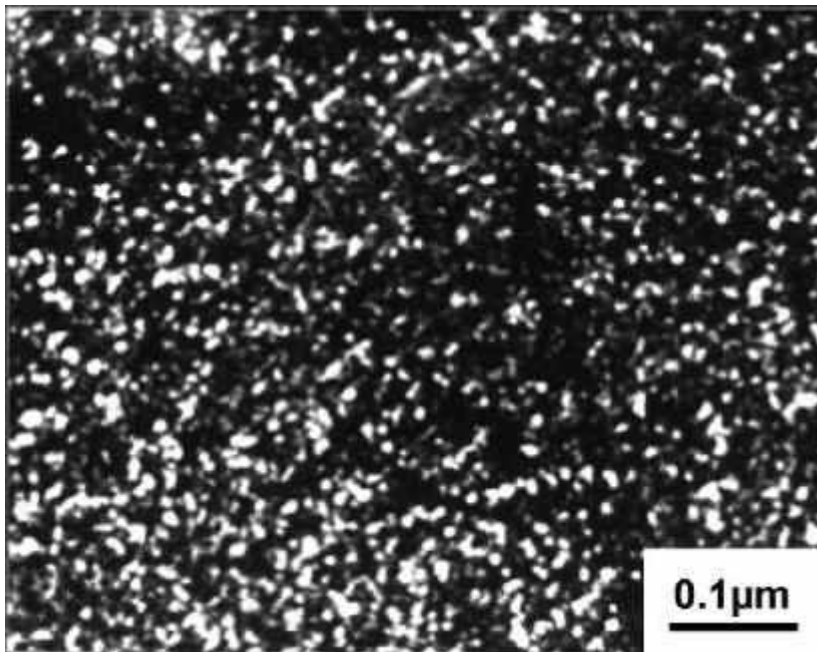


Source: ZAMBALDI (2010)

Since α_2 particles are coherent, they can be sheared by moving dislocations, resulting in planar slip and extensive dislocation pile-up against boundaries. With increasing size, these α_2 particles become ellipsoidal in shape, the long axis being parallel to the c-axis of the hexagonal lattice. This phase is further stabilized by oxygen and tin. In such cases, Sn substitutes for Al whereas oxygen remains as an interstitial. Upon annealing of $\alpha+\beta$ alloys in the two phase region ($\alpha+\beta$), significant alloy element partitioning takes place and the α phase is enriched with α stabilizing elements (Al, O, Sn). Substantial volume fractions of coherent

α_2 particles can then be precipitated in the α phase by aging for example at 500°C (Ti-6Al-4V, IMI 550), at 550°C (IMI 685), at 595°C (Ti-6242), or even at 700°C (IMI 834). The very high density of these homogeneously distributed α_2 particles in the α phase is shown in the dark field transmission electron micrograph in **Figure 16** for the IMI 834 alloy (LÜTJERING; WILLIAMS, 2007).

Figure 16 – TEM dark field micrograph of α_2 particles in IMI 834 alloy aged 24h at 700°C.

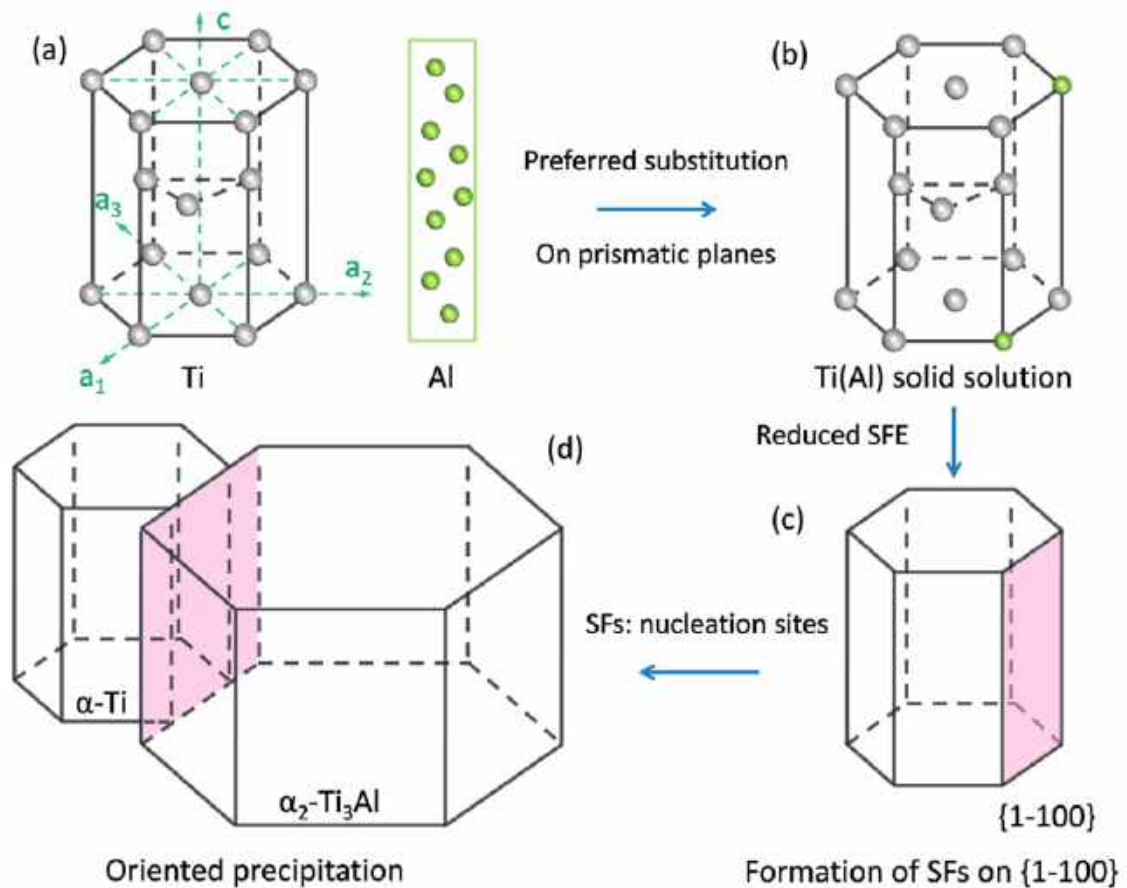


Source: LÜTJERING, WILLIAMS (2007)

The $\alpha \rightarrow \alpha_2$ transformation fulfills the so-called first Landau-Lifshitz condition, which defines that symmetry elements of the product phase must have a subset of the symmetry elements of the parent phase. This means that replacement of atoms in the HCP α lattice can produce the $D0_{19}$ lattice of α_2 . It also fulfills the second Landau-Lifshitz condition, since the $D0_{19}$ can be formed by introducing and amplifying a concentration wave with vector star of $\vec{k} \langle \frac{1}{2}00 \rangle$, and this wave vector terminates at the special point M of the reciprocal space (Brillouin zone). However, the third Landau-Lifshitz is not satisfied, as the sum of the three variants of the wave vector star that form the structure ($\vec{k}_1 + \vec{k}_2 + \vec{k}_3 = [\frac{1}{2}00] + [0\frac{\sqrt{3}}{2}0] + [\frac{\sqrt{3}}{2}\frac{1}{2}0]$) results in a reciprocal lattice vector of the parent HCP structure. Therefore, the transformation is a first order ordering process (BANERJEE; MUKHOPADHYAY, 2007). The precipitation from the α phase takes place according to the following orientation

relationship: $[\bar{4}223]\alpha \parallel [2\bar{1}\bar{1}\bar{3}]\alpha_2$ and $(01\bar{1}0)\alpha \parallel (01\bar{1}0)\alpha_2$ (WU et al., 2016). This relationship is shown in **Figure 17**.

Figure 17 – **a)** Configuration of α -Ti lattice and Al atoms before annealing. **b)** During annealing, Al atoms solubilize in Ti and a Ti-Al substitutional solid solution is formed. **c)** During cooling, the formation of stacking faults on $\{1\bar{1}00\}\alpha$ planes is observed. **d)** Precipitation of α_2 -Ti₃Al near stacking faults and relative positions of α -Ti and α_2 -Ti₃Al.



Source: WU et al. (2016)

The low ductility of α alloys containing the α_2 phase has been a disappointment, as the strengthening of nickel-based superalloys is essentially dependent on microstructures containing a rather similar coherent phase Ni₃(Ti, Al). The only element reported to improve the ductility of α_2 in titanium alloys is gallium, an α -stabilizer. Although some gallium-containing alloys have been produced, the high cost of this element and problems with melting make their applications impractical. In α -alloys with complex compositions, the misfit between α and α_2 can be larger than in Ti-Al alloys. Therefore, nucleation of α_2 becomes more difficult and it tends to form heterogeneously. This non-uniform dispersion appears to have a less deleterious effect on ductility (POLMEAR et al., 2017).

2.3 Alloying elements of titanium alloys

Properties of titanium alloys are essentially determined by two factors: chemical composition and microstructure. The chemical composition primarily determines the properties and volume fractions of α and β phases. On this basis, they can be classified into α alloys, $\alpha+\beta$ alloys and β alloys, and alloying elements can be divided into α stabilizers or β stabilizers, depending on their contribution to the stabilization of one phase or another (LEYENS; PETERS, 2003). Elements that dissolve preferentially in the α phase expand the α phase field, thereby raising the β -*transus* temperature. There are only six elements, known as α -stabilizing elements, that behave in this way: aluminum, oxygen, nitrogen, carbon, gallium and germanium (DONACHIE JR., 2000; POLMEAR et al., 2017). Beta-stabilizing elements further divide into two groups: the beta isomorphous group, which consists of elements that are miscible in the β phase, including molybdenum, vanadium, tantalum, and columbium, and the beta eutectoid group, which includes elements that form eutectoid systems with titanium, having eutectoid temperatures as much as 333°C below the transformation temperature of unalloyed titanium, such as manganese, iron, chromium, cobalt, nickel, copper, and silicon (DONACHIE JR., 2000). It should be noted, however, that eutectoid reactions in a number of titanium alloys (e.g., Ti-Fe, Ti-Mn) are sluggish; for this reason, no eutectic reactions are observed in practice, even under slow furnace cooling conditions. These alloys behave as if they conformed to the β -isomorphous phase diagram (POLMEAR et al., 2017).

Neutral elements, which do not strongly promote phase stability, can also be added for other purposes, such as strengthening effects, for example (DONACHIE JR., 2000). Tin and silicon, for example, do not strongly affect the stability of either the α or β phase at low addition levels and are often regarded as neutral (POLMEAR et al., 2017). **Table 6** lists alloying elements for titanium and their respective stabilization effect and **Figure 18** shows schematic representations of binary Ti-X diagrams according to the classification of alloying elements.

Research has revealed that the intense hardening effect of oxygen atoms in pure α titanium is attributed to the interaction between oxygen and the core of screw dislocations that mainly glide on prismatic planes. However, increasing oxygen lowers ductility so that its content is often limited to $\sim 0.25\%$. In particular, oxygen promotes the formation of Ti_3Al phase, into which it partitions preferentially in Ti-Al-based alloys. In the $\alpha+\beta$ alloy Ti-6Al-4V, doubling the oxygen content from 0.25% to 0.5% was found to promote the formation of the Ti_3Al when slowly cooled from the β phase field (POLMEAR et al., 2017). Besides

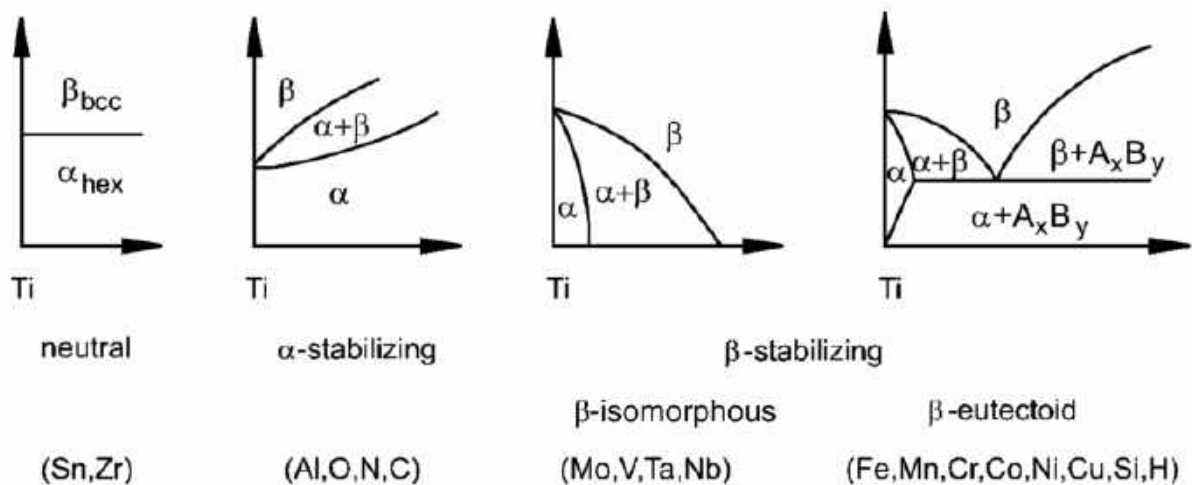
oxygen, interstitial elements nitrogen and carbon also stabilize the α phase, i.e. they raise the β -*transus* temperature (DONACHIE JR., 2000). Hydrogen, on the other hand, strongly promotes the formation of the β phase, lowering the β -*transus* temperature (POLMEAR et al., 2017).

Table 6 – Effect of alloying elements on phase stabilization of titanium.

Classification	Elements
Alpha stabilizer	Aluminum, carbon, gallium, germanium, nitrogen, oxygen
Beta isomorphous stabilizer	Molybdenum, niobium, rhenium, tantalum, vanadium
Beta eutectoid stabilizer	Bismuth, chromium, cobalt, copper, gold, hydrogen, indium, iron, lead, manganese, nickel, palladium, silicon, silver, tungsten, uranium
Neutral	Hafnium, tin, zirconium

Source: DONACHIE JR. (2000); FROES (2015)

Figure 18 – Schematic influence of alloying elements on phase diagrams of Ti alloys.



Source: LEYENS, PETERS (2003)

Substitutional alloying elements, such as tantalum and vanadium, also play an important role in controlling the microstructure and properties of titanium alloys. As mentioned above, they are β isomorphous (i.e., have similar phase relations) with BCC titanium. Titanium does not form intermetallic compounds with β isomorphous elements. Eutectoid elements are usually added to alloys in combination with one or more of the β isomorphous elements to stabilize the β phase and prevent or minimize formation of intermetallic compounds that can occur during service at elevated temperature (DONACHIE JR., 2000).

Zirconium and hafnium are isomorphous with both alpha and beta phases. Tin and aluminum have significant solubility in both α and β phases, with aluminum increasing the transformation temperature significantly and tin lowering it slightly. Aluminum, tin, and zirconium are commonly used together in α and near- α alloys. In $\alpha+\beta$ alloys, these elements are distributed approximately equally between the α and β phases. Almost all commercial titanium alloys contain one or more of these three elements because they are soluble in both phases, and particularly because they improve creep resistance of the α phase (DONACHIE JR., 2000). Zirconium is usually regarded as neutral. However, the Ti-Zr binary phase diagram produced using thermodynamic databases suggests that zirconium should be treated as a β -stabilizer as the β -*transus* decreases with increasing zirconium on the titanium-rich side. Research has confirmed that zirconium plays the role of a β -stabilizer in Ti-Nb based alloys (POLMEAR et al., 2017).

Iron, chromium, manganese, and other compound formers are used sometimes in β -rich $\alpha+\beta$ alloys or in β alloys because they are strong β stabilizers and improve hardenability and response to heat treatment. Nickel, molybdenum, and palladium improve the corrosion resistance of unalloyed titanium in certain media (DONACHIE JR., 2000). Silicon atoms tend to segregate to dislocations and thus effectively prevent dislocation climb, which improves creep behavior. Zirconium tends to homogenize fine silicide precipitates. Molybdenum, vanadium and niobium are moderate solid solution strengtheners of β . Niobium is known to improve the oxidation behavior of titanium alloys, while small additions of palladium substantially improve their corrosion resistance (LEYENS; PETERS, 2003).

Among the substitutional β -stabilizing elements, molybdenum, vanadium, and chromium are commonly used, while tungsten is little used because of its high density and tendency to segregate during alloy preparation. Iron addition is typically limited to 2% due to its tendency to segregate during ingot solidification. An addition of more than 6% of chromium can cause similar problems. The potency of each element in stabilizing the β phase is defined according to the approximate critical minimum addition of each element needed to retain 100% β on water quenching, as will be discussed ahead (POLMEAR et al., 2017).

2.4 Classification of titanium alloys

As stated before, titanium alloys can be mainly classified into α alloys, $\alpha+\beta$ alloys and β alloys, depending on their composition, which, in turn, defines the amount of α and β phases they contain. Metastable β alloys are included in the β class. A fourth class, the so-called the

near- α alloys, and the commercially pure (CP) titanium, also exist. However, because the alloys studied in this work belong to the $\alpha+\beta$ and β classes, these will be the only ones hereby discussed. But firstly, an insight into the methods for classification of titanium alloys will be provided.

2.4.1 Al and Mo equivalents and the $\overline{Bo} \times \overline{Md}$ method

The standard α -stabilizing and β -stabilizing elements are Al and Mo, respectively. For this reason, it is usual to describe a multicomponent Ti-based alloy in terms of its equivalent Al and Mo contents. There are different acceptable equations for the calculation of the equivalent values. The classical expressions for [Al]eq (ROSENBERG, 1970) and Mo[eq] (BOYER; ELSCH; COLLINS, 1994) are:

$$[\text{Al}]_{\text{eq}} = [\text{Al}] + [\text{Zr}]/6 + [\text{Sn}]/3 + 10[\text{O} + \text{N}] \quad (2)$$

$$[\text{Mo}]_{\text{eq}} = [\text{Mo}] + 0.20 [\text{Ta}] + 0.28 [\text{Nb}] + 0.40 [\text{W}] + 0.67 [\text{V}] + 1.25 [\text{Cr}] + 1.25 [\text{Ni}] + 1.70 [\text{Mn}] + 1.70 [\text{Co}] + 2.50 [\text{Fe}] \quad (3)$$

where [X] indicates the concentration of the element X, in weight percent, in the alloy. However, another equation for the calculation of [Mo]eq has been proposed by Bania (BANIA, 1994), which takes into account the amount of Al in the alloy with a negative value to reinforce its α -stabilizing character:

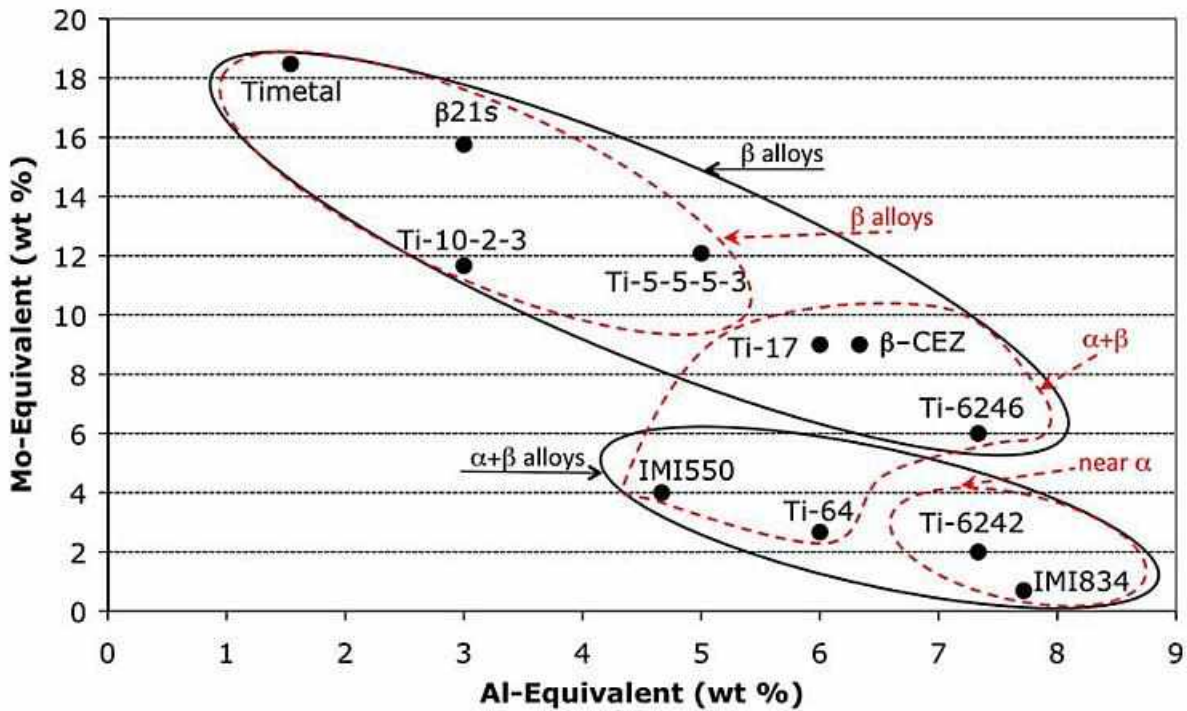
$$[\text{Mo}]_{\text{eq}} = [\text{Mo}] + 0.67 [\text{V}] + 0.44 [\text{W}] + 0.28 [\text{Nb}] + 0.22 [\text{Ta}] + 2.90 [\text{Fe}] + 1.60 [\text{Cr}] - [\text{Al}] \quad (4)$$

More recently, a new [Mo]eq formula (in at%) has been proposed by Wang, Dong and Liaw using the slopes of the $\beta/(\alpha+\beta)$ boundary lines in binary Ti-M (where “M” is a metal) phase diagrams (WANG; DONG; LIAW, 2015):

$$[\text{Mo}]_{\text{eq}} = [\text{Mo}] + 0.74 [\text{V}] + 1.01 [\text{W}] + 0.30 [\text{Ta}] + 1.23 [\text{Fe}] + 1.10 [\text{Cr}] + 1.09 [\text{Cu}] + 1.67 [\text{Ni}] + 1.81 [\text{Co}] + 1.42 [\text{Mn}] + 0.38 [\text{Sn}] + 0.34 [\text{Zr}] + 0.99 [\text{Si}] - 0.57 [\text{Al}] \quad (5)$$

Figure 19 provides a $[Mo]_{eq} \times [Al]_{eq}$ chart showing the regions corresponding to different classes of titanium alloys according Lütjering and Williams' (LÜTJERING; WILLIAMS, 2007) and to Donachie's criteria (DONACHIE JR., 2000).

Figure 19 – The $[Al]_{eq}$ and $[Mo]_{eq}$ values for some Ti alloys showing the different alloy classes based on Lütjering and Williams' classification (solid black lines) and Donachie's classification (dashed red lines).



Source: ATTALLAH et al. (2009)

Values of $[Al]_{eq}$ and $[Mo]_{eq}$ are commonly used as basis for the classification of titanium-based systems. However, another methodology for alloy classification is based on the theoretical calculation of the electronic structures of Ti alloys: the bond order (\overline{Bo}) vs. metal d-orbital energy level (\overline{Md}) method. This methodology has been developed by Morinaga et al. for the design of new titanium alloys (MORINAGA et al., 1988). The bond order describes the strength of a covalent bond between Ti and the alloying element, while the metal d-orbital energy level is correlated with the electronegativity and metallic radius of elements. This method allows the estimation of β -*transus* temperatures and, for β alloys, it is useful to define the boundary between slip and twin deformation. **Table 7** provides the values of \overline{Bo} and \overline{Md} of several alloying elements for BCC and HCP Ti, and **Figure 20** shows the $\overline{Bo} \times \overline{Md}$ diagram for the classification of titanium alloys into α , $\alpha+\beta$ and β groups.

Table 7 – List of \overline{Bo} and \overline{Md} for alloying elements in titanium.

Element	Bo		Md (eV)	
	HCP Ti	BCC Ti		
3d	Ti	3.513	2.790	2.447
	V	3.482	2.805	1.872
	Cr	3.485	2.779	1.478
	Mn	3.462	2.723	1.194
	Fe	3.428	2.651	0.969
	Co	3.368	2.529	0.807
	Ni	3.280	2.412	0.724
	Cu	3.049	2.114	0.567
	Zr	3.696	3.086	2.934
4d	Nb	3.767	3.099	2.424
	Mo	3.759	3.063	1.961
	Hf	3.664	3.110	2.975
5d	Ta	3.720	3.144	2.531
	W	3.667	3.125	2.072
Other	Al	3.297	2.426	2.200
	Si	3.254	2.561	2.200
	Sn	2.782	2.283	2.100

Source: MORINAGA et al. (1988)

For multicomponent alloys, the average \overline{Bo} and \overline{Md} values for the system are calculated based on the weighted compositional average:

$$\overline{Md} = \sum_{i=1}^n x_i Md_i \quad (6)$$

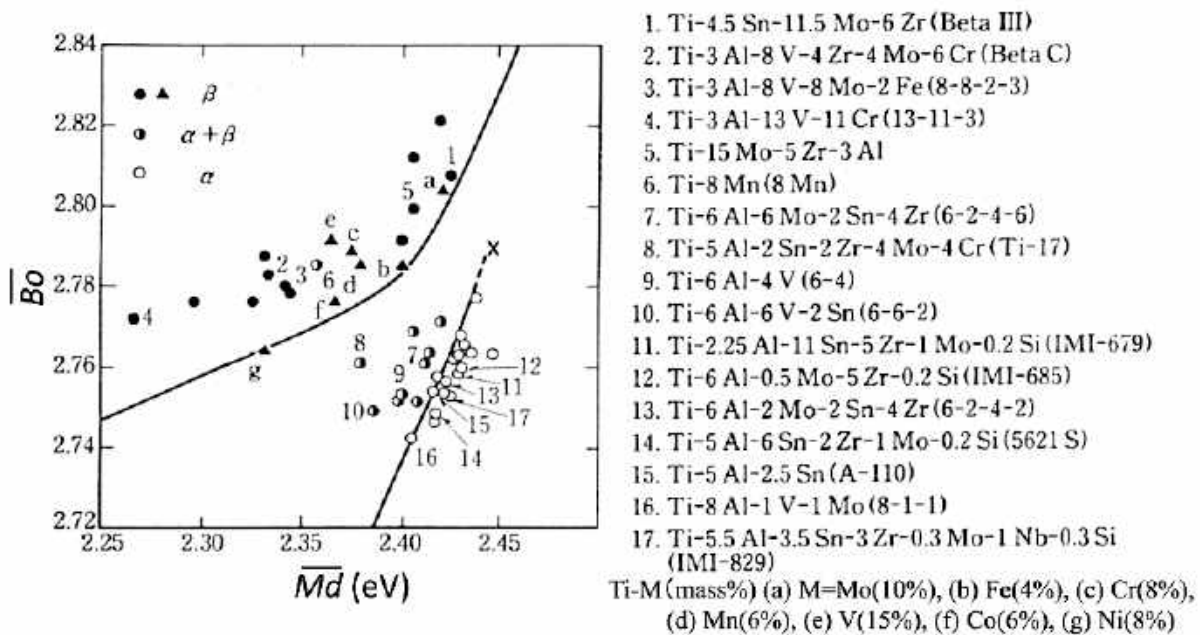
$$\overline{Bo} = \sum_{i=1}^n x_i Bo_i \quad (7)$$

where x_i is the atomic fraction of the component i in the alloy, and Md_i and Bo_i are their respective d-orbital energy level and bond order.

By this method, the correlation between both parameters and the β -transus temperature is given by:

$$\overline{Bo} = 0.326 \overline{Md} - 1.950 \times 10^{-4} T_{\beta} + 2.217 \quad (8)$$

Figure 20 – Division of commercial titanium alloys into α , $\alpha+\beta$ and β groups on the $\overline{Bo} \times \overline{Md}$ diagram.



Source: MORINAGA (2016)

2.4.2 Alpha+beta alloys

The $\alpha+\beta$ alloys' group ranges in the phase diagram from the $\alpha/\alpha+\beta$ phase boundary to the intersection of the M_s line with room temperature, meaning that $\alpha+\beta$ alloys transform martensitically upon fast cooling from the β phase field (LÜTJERING; WILLIAMS, 2007). Alloys from the $\alpha+\beta$ group contain one or more α -stabilizer (e.g. aluminum) or α -soluble elements plus one or more β -stabilizer (e.g. vanadium, molybdenum) in larger amounts than near- α alloys. By moving alloy composition away from the α solvus phase boundary, these alloys form significant amounts of β phase when heated, and they can also retain significant quantities of untransformed β after solution treatment and cooling. The formation of β to some extent allows these alloys to be strengthened by solution treatment (above the β -transus or at least producing significant β phase for subsequent transformation) and aging (heating to produce further changes in the transformed β – martensites and acicular α – and in the retained β). The specific amount of β phase available for transformation from a fixed temperature depends on the amount of β stabilizers and on processing conditions. Although the strength of $\alpha+\beta$ alloys can be significantly enhanced by subsequent aging, few compositions can sustain these levels of strength in thick sections because of the hardenability limitation upon quenching, which is aggravated by the low thermal conductivity of titanium (POLMEAR et al., 2017).

Depending on the processing route, a variety of microstructures can be achieved for $\alpha+\beta$ alloys. Several annealing treatments can be applied to these alloys, with the major purpose of increasing fracture toughness, ductility at room temperature, dimensional and thermal stability, creep resistance, or fatigue strength. **Figure 21** shows examples of the possible microstructures to be obtained, namely fully lamellar (which can be subdivided into “ β annealed” and “ β processed”), fully equiaxed, bi-modal (or duplex) and a less defined microstructure called mill-annealed (DONACHIE JR., 2000; LÜTJERING; WILLIAMS, 2007), and **Table 8** summarizes the correlation between some microstructural features of $\alpha+\beta$ alloys and their mechanical properties. The commonly used annealing treatments for $\alpha+\beta$ alloys are (POLMEAR et al., 2017):

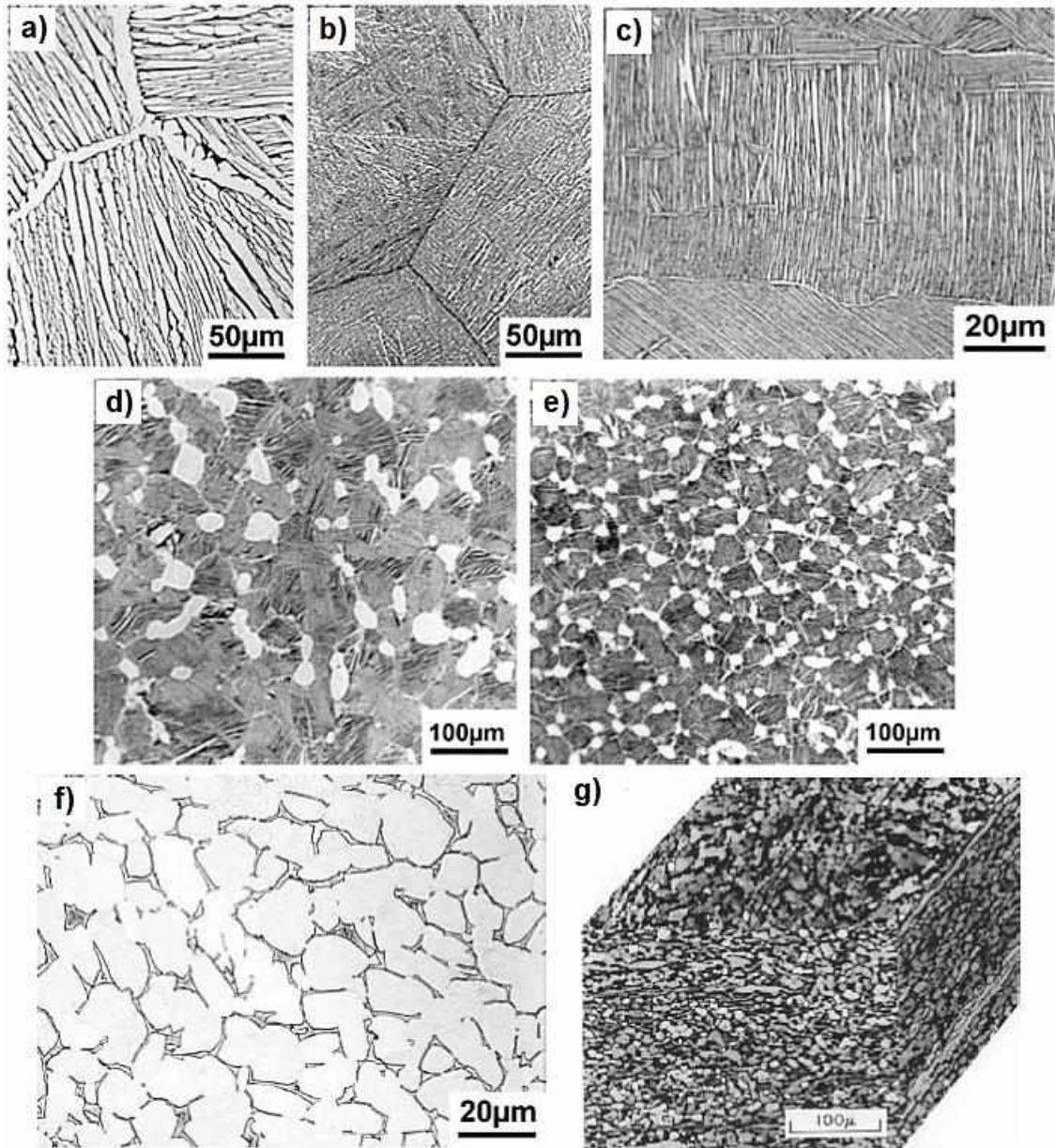
1. β -annealing: consists of heating the alloy into the β phase field for an isothermal hold, followed by furnace or air cooling, or water quenching for thicker sections, to avoid the formation of coarse α phase layers along prior β grain boundaries (α_{GB}). The purpose is to improve fracture toughness. Since β -annealing often leads to coarse prior- β grains, both annealing temperature and time should be minimized. In general, slow cooling results in coarse lamellar $\alpha+\beta$ and α_{GB} , from which α laths can also nucleate and grow inward. Increasing cooling rate promotes the formation of finer and shorter α -laths. In addition, due to the increased driving force, i.e., the increased cooling rate, α -colonies not only nucleate and grow from the prior β grain boundaries but also from the boundaries of the newly formed α colonies. Such developments lead to the formation of a basketweave microstructure. Beta-annealed $\alpha+\beta$ alloys show reduced ductility and tensile strength but improved fracture toughness. They also exhibit reduced fatigue crack growth rates. The α -colony size, α -lath width and prior- β grain size all affect mechanical properties.
2. Mill annealing: it is an incomplete annealing treatment with the purpose of retaining the wrought-state microstructure, which consists of elongated α phase and irregular β phase particles for desired strength properties. The maximum annealing temperature is determined by the stability of the β phase, which changes with temperature due to compositional variations. For Ti-6Al-4V, the critical annealing temperature is $\sim 845^\circ\text{C}$. The isothermal hold is typically carried out in the range $700\text{--}800^\circ\text{C}$ for this alloy for 1-4 h, followed by air cooling. When annealed at temperatures above 845°C , the β phase in Ti-6Al-4V is not retained during subsequent cooling, either by water quenching or furnace cooling, due to its low vanadium content and low stability.
3. Recrystallization annealing: similar to β -annealing, this treatment serves primarily to improve fracture toughness. The alloy is usually heated into the upper end of the $\alpha+\beta$

field for an isothermal hold up to 2 h, followed by furnace cooling. For Ti-6Al-4V, it is annealed at 955°C for 2 h. The resulting α and β phases are both essentially dislocation free, which gives the name recrystallization annealing. Recrystallization annealing leads to a bimodal microstructure. The process has largely replaced β -annealing as it offers similar advantages, but without causing excessive β grain growth, so that ductility can be maintained.

4. Duplex annealing: the first anneal serves to control the fraction and morphology of the α phase, while the second anneal allows for the precipitation of acicular secondary α phase within the metastable β phase. Duplex annealing also produces a bimodal microstructure, which offers improved fracture toughness and creep resistance. A typical duplex annealing schedule for Ti-6Al-4V includes 870-950°C for 0.2-1 h, air cooling, 680-730°C for 2-4 h, and air cooling again.
5. Stabilization annealing: this treatment is essentially similar to the second stage of duplex annealing. The purpose is to enhance the stability of the β phase in order to make the alloy capable of resisting further transformation during services at elevated temperatures.
6. Stress-relief annealing: the purpose is to alleviate residual stresses resulted from previous cold- or hot-forming or heat-treatment processes. For example, it is common practice to apply stress-relief annealing to fixtures to remove springback or warpage. For Ti-6Al-4V, stress-relief annealing is performed at 480-650°C in air for 1-4 h, followed by air cooling.

The $\alpha+\beta$ group is dominated by the Ti-6Al-4V alloy (LÜTJERING; WILLIAMS, 2007). The alloy was invented between 1952 and 1954 by Stanley Abkowitz in the United States (US Patent 2,906,654), motivated by the search of Ti-Al-based alloys that were both strong and ductile and by the desire from the U.S. defense industry to replace steels with lightweight titanium alloys for a variety of important applications. Vanadium was chosen because it showed little adverse effect on ductility while improving tensile strength (POLMEAR et al., 2017). Currently, more than 50% of all usage of titanium-based materials worldwide corresponds to this alloy. It is by far the most intensively developed and tested titanium alloy, which is a major advantage, especially in the aerospace industry, the largest user of Ti-6Al-4V (LEYENS; PETERS, 2003). This alloy has an exceptionally good balance of strength, ductility, fatigue, and fracture toughness, but can be used only up to temperatures of about 300°C (LÜTJERING; WILLIAMS, 2007). It is largely applied in the aerospace industry and in the medical sector, for medical prostheses, but also in the automotive, marine and chemical industries (SHA; MALINOV, 2009).

Figure 21 – Lamellar microstructures of Ti-6242 alloy cooled from β field at **a)** $1^\circ\text{C}/\text{min}$ and **b)** $8000^\circ\text{C}/\text{min}$, **c)** Ti-6242 alloy in the β -processed condition cooled at approximately $100^\circ\text{C}/\text{min}$, bi-modal microstructure of IMI 834 alloy cooled from β field at **d)** slow cooling rate and **e)** fast cooling rate, **f)** fully equiaxed microstructure of Ti-6242 alloy slowly cooled from the recrystallization annealing temperature, and **g)** mill-annealed microstructure of a Ti-6Al-4V alloy plate.



Source: LÜTJERING, WILLIAMS (2007)

Two grades of Ti-6Al-4V are produced commercially, Grade 5 and Grade 23, also called ELI (extra-low interstitials). **Table 9** lists their compositions. The alloy is fully heat treatable but it is most commonly used in the mill-annealed condition. Ti-6Al-4V is also hardenable in sections up to 25.4 mm thick and is also used in the solution-treated and aged (STA) condition for aircraft fasteners, for example. STA Ti-6Al-4V possesses superior tensile and fatigue strength. ELI Ti-6Al-4V offers better ductility but lower strength than Grade 5 Ti-

6Al-4V, and can be made into a wide variety of product forms, including coils, strands, wires, or flat wires. In particular, it is the main titanium alloy for dental and medical applications (POLMEAR et al., 2017).

Table 8 – Correlation between some microstructural features and mechanical properties of $\alpha+\beta$ alloys.

Feature	Yield strength	Ductility	High cycle fatigue life	Fracture toughness	Creep strength
Small α colonies or lamellae ^a	↑	↑	↑	↓	-
Bimodal structure ^b	↑	↑	↓	↓	↓
Small α grain size ^c	↑	↑	↑	↓	↓
Presence of α_2 (aging)	↑	↓	↑	↓	↑
Secondary α in β	↑	↓	↑	-	↑

^aCompared with coarse lamellar structure; ^bCompared with fully lamellar structure;

^cCompared with large α grain size in fully equiaxed structures.

Source: LÜTJERING, WILLIAMS (2007)

Table 9 – Ti-6Al-4V composition, in wt%, in Grade 5 and Grade 23 (ELI).

Grade	Al	V	O	Fe	C	H	N	Others*
5	5.5-6.75	3.5-4.5	≤0.20	≤0.30	≤0.08	≤0.015	≤0.05	≤0.4
ELI	5.5-6.5	3.5-4.5	≤0.13	≤0.25	≤0.08	≤0.0125	≤0.03	≤0.3

*Maximum amount per individual impurity: 0.1

Source: POLMEAR et al. (2017)

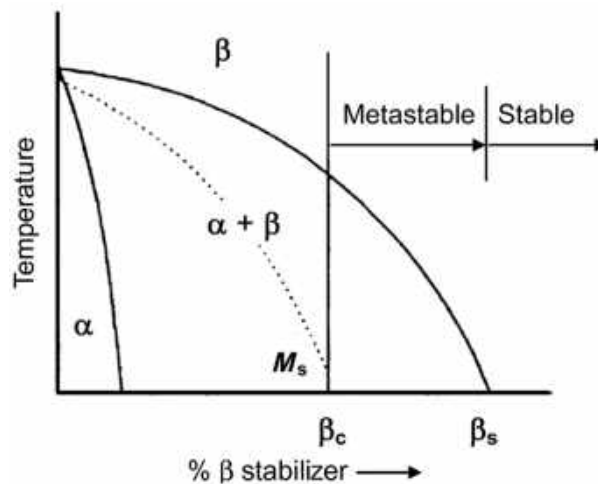
Control and optimization of the α phase morphology in Ti-6Al-4V alloy is one of the important issues in the use of the alloy. Thermomechanical processing is useful to improve microstructure by controlling the size and the aspect ratio of the lamellar α phase, optimizing the α/β phase ratio and controlling the morphology of β phase. Hot deformation of the alloy in the β phase field results in relatively large deformed β grains and possibly in dynamic or metadynamic recrystallization, while processing in the $\alpha+\beta$ phase field results in a much finer $\alpha + \beta$ structure, because the primary α phase limits the growth of β phase (SHA; MALINOV, 2009).

Other $\alpha+\beta$ alloys like Ti-6-6-2 and IMI 550 were primarily developed for high strength. High strength and high toughness is achieved with Ti-6-2-4-6. Ti- 6-2-2-2-2, Ti-55-24-S and Ti-17 alloys were primarily developed for elevated temperature applications in gas turbine engines up to about 400°C (LEYENS; PETERS, 2003).

2.4.3 Beta alloys

Beta titanium alloys are generally defined as those containing sufficient β -stabilizing elements to enable the β phase to be retained by water quenching to room temperature. This means that the amount of these elements is sufficient to avoid passing through the M_s temperature during water quenching. **Figure 22** illustrates the M_s curve, the position of the approximate critical minimum amount of the β -stabilizer needed to retain 100% β phase on water quenching (β_c), and the β -*transus* curve (β_s) on a pseudo-binary phase diagram of a Ti-X system, where X is a β -stabilizer. Highly alloyed compositions to the right of the β -*transus* curve (β_s) are considered to be stable β titanium alloys. Since these compositions are in the single β phase field, no response is expected to aging. Alloy compositions lying between β_c and β_s are commonly referred to as metastable β titanium alloys, because they are still within the $\alpha+\beta$ field, and α phase can precipitate upon aging, leading to improved mechanical properties (POLMEAR et al., 2017).

Figure 22 – Pseudo-binary β -isomorphous phase diagram showing locations of metastable and stable β titanium alloys. β_c refers to the critical minimum addition of a β -stabilizer to retain 100% β on water quenching. β_s denotes the β -*transus*.



Source: POLMEAR et al. (2017)

Table 10 lists the commonly used β -stabilizers and their β_c values. Iron is the most potent β -stabilizer by this criterion. Between the two groups of β -stabilizers considered in the table, the eutectoid stabilizers are generally stronger than the isomorphous ones. Additionally, all the five isomorphous β -stabilizers considered reduce the β -*transus* temperature of their respective Ti-X binary alloys per wt% of addition, while the eutectoid β -stabilizers have an inconsistent effect on the β -*transus* (POLMEAR et al., 2017).

Table 10 – Potency of β -stabilizers in titanium.

β -stabilizer	Type	β_c (wt%)	$\Delta\beta$ -transus ($^{\circ}\text{C}$)
Mo	Isomorphous	10.0	-8.3
V	Isomorphous	15.0	-5.5
W	Isomorphous	22.5	-13.8
Nb	Isomorphous	36.0	-10.6
Ta	Isomorphous	45.0	-15.6
Fe	Eutectoid	3.5	0
Cr	Eutectoid	6.5	-2.8
Cu	Eutectoid	13.0	-5.6
Ni	Eutectoid	9.0	4.4
Co	Eutectoid	7.0	3.3
Mn	Eutectoid	6.5	4.4
Si	Eutectoid	-	21.1

Source: POLMEAR et al. (2017)

Molybdenum is well known as a β -stabilizing element in titanium alloys. The critical minimum molybdenum content required to retain 100% β in Ti-Mo binary alloys upon water quenching is of 10% for small samples. This critical minimum molybdenum content was defined as the β phase stability parameter, molybdenum equivalent (see **Section 2.4.1**). In the [Mo]eq equation, the coefficient before each β -stabilizer reflects the ratio of the β_c value for molybdenum (10.0) divided by the β_c value for the specific β -stabilizer. The [Mo]eq value provides a simple and useful parameter for ranking the β phase stability in different titanium alloys after water quenching and predicting the microstructures to be produced. Based on the [Mo]eq values, titanium alloys with [Mo]eq > 30 are usually classified as stable β alloys, whereas alloys with $8 \leq [\text{Mo}]_{\text{eq}} \leq 30$ are defined as metastable β alloys (POLMEAR et al., 2017).

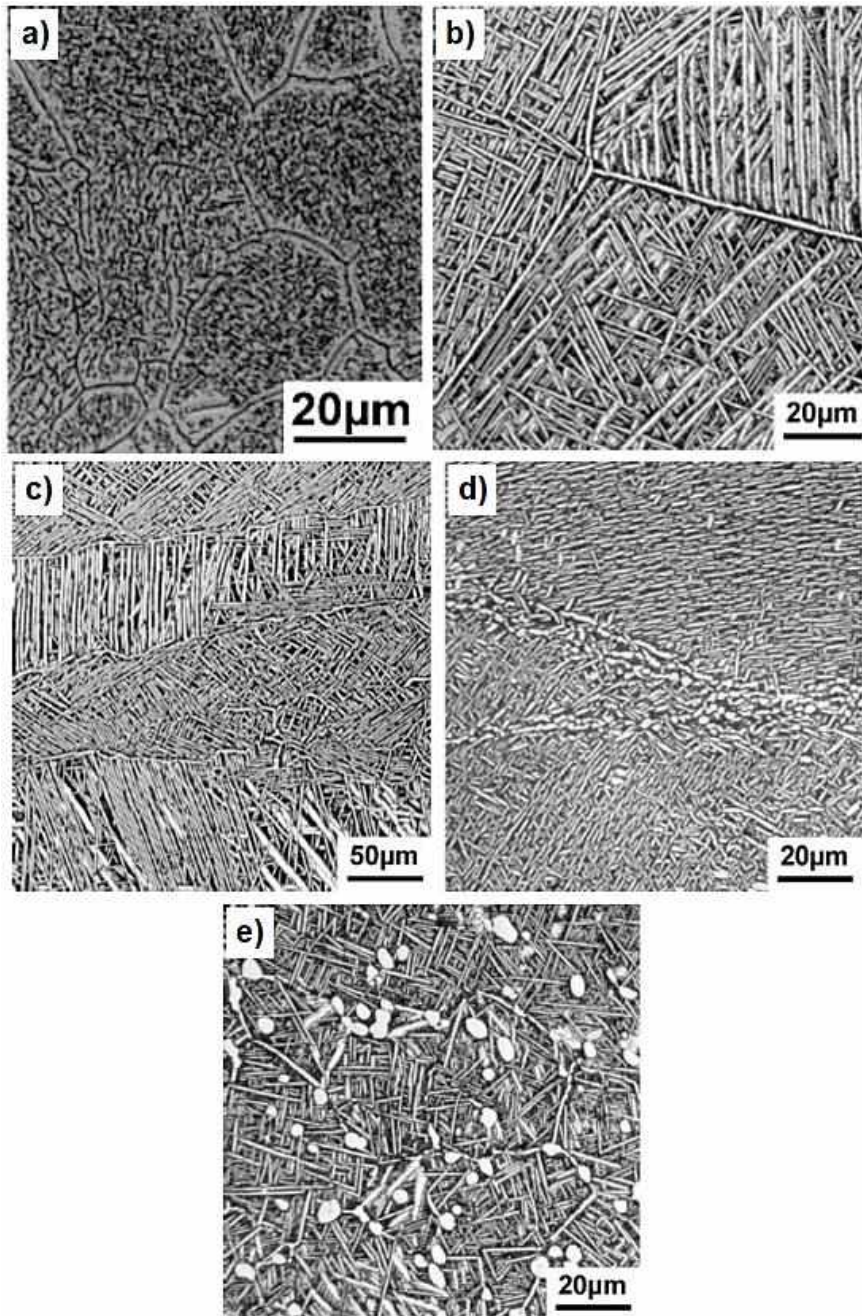
In metastable β alloys, cold working at room temperature or heating to a slightly elevated temperature can cause partial transformation to α , as the alloy reverts to the equilibrium condition. This metastability is exploited to produce exceptional structures from β alloys. Their main advantages are: extremely high hardenability, excellent forgeability and good cold formability in the solution-treated condition. Because the β phase is invariably metastable and has a long-term tendency to transform to the equilibrium $\alpha+\beta$ structure, producers rely on this tendency by aging metastable β alloys after solution treatment (DONACHIE JR., 2000). Temperatures of about 450°C to 650°C are used to partially transform the metastable microstructure, resulting in yield stress levels near 1200 MPa. This high yield stress owes itself to the homogeneous precipitation of fine α platelets from the metastable precursor phases which are formed either during the cooling process after solution-

treatment or during heating to the aging temperature. By comparison, the maximum yield stress level that can be obtained for $\alpha+\beta$ alloys, using the same cooling rates and optimum aging treatments, is only about 1000 MPa (LÜTJERING; WILLIAMS, 2007). In the solution-treated condition (100% retained β), these alloys have good ductility and toughness, relatively low strength, and excellent formability. However, solution-treated β alloys begin to precipitate α phase at slightly elevated temperatures and thus are unsuitable for elevated-temperature service without prior stabilization or over-aging treatment (DONACHIE JR., 2000).

Possible microstructures for β alloys are the so called β -annealed, β -processed, through-*transus* processed and bi-modal. In the β -annealed microstructure, continuous α layers in β grain boundaries are the key feature, since the α phase always nucleates preferentially at β grain boundaries. Since β alloys are hardened by small α platelets, these continuous α layers become deleterious to the mechanical properties. The main intention of the thermo-mechanical processing of β alloys is to eliminate or reduce this negative effect of the continuous α_{GB} layers. Beta processing and through-*transus* processing have the objective of restricting the formation of these layers, and in the bi-modal microstructure the influence of these layers on mechanical properties is limited (LÜTJERING; WILLIAMS, 2007). **Figure 23** shows examples of microstructures and **Table 11** summarizes the correlation between some microstructural features of β alloys and their mechanical properties.

In β alloys with high concentrations of β stabilizing elements it is sometimes difficult to achieve a homogeneous distribution of α platelets by normal aging treatments, especially with aging temperatures above the metastable two-phase region, because the formation of precursors (ω or β') or α nucleation at the precursors is too sluggish to occur during the heating period to the aging temperature. In such cases, a pre-aging treatment at lower temperatures might create a more homogeneous distribution of α platelets. Another possibility is to cold work prior to aging which results in a more homogeneous distribution of α platelets by nucleation at dislocations (LÜTJERING; WILLIAMS, 2007).

Figure 23 – **a)** β 21S alloy annealed and aged for 8 h at 500°C + 24 h at 725°C, **b)** β annealed microstructure of β -CEZ, **c)** β processed microstructure of Ti-6246, **d)** through-*transus* processed microstructure of Ti-6246 and **e)** bi-modal microstructure of β -CEZ alloy.



Source: LÜTJERING, WILLIAMS (2007)

The specifications of most β titanium alloys require extra low oxygen ($\leq 0.13\%$) and carbon ($\leq 0.05\%$). The former is necessary to maintain desired toughness and ductility at high strength levels; the latter arises from the high Mo, V or Nb contents, which can reduce the solubility of carbon in the β phase from 0.08% to less than 0.006%, leading to the precipitation of carbides in grain boundaries. Their hydrogen content is usually limited to $\leq 0.015\%$, although a lower hydrogen content is always preferred (POLMEAR et al., 2017).

Table 11 – Correlation between some microstructural features and mechanical properties of β alloys.

Feature	Yield strength	Ductility	High cycle fatigue life	Fracture toughness	Creep strength
GB α in β -annealed structure	-	↓	↓	↑	-
Bimodal structure	-	↑	↑	↓	-
Necklace or β -processed structure ^a	-	↑	↑	↑	-
Necklace or β -processed structure ^b	-	↓	↓	↑	-
Decreasing age-hardening	↓	↑	↓	↑	↓
Small β grain size in β -annealed structure ^c	-	↑	↑	↓	0

^aCompared with β -annealed structure; ^bCompared with bimodal structure; ^cOnly applied to heavily stabilized alloys.

Source: LÜTJERING, WILLIAMS (2007)

Beta titanium alloys attracted attention because of their superior forming characteristics arising from their BCC structure. Moreover, they offer the prospect of being cold-formed in the relatively soft β phase state with subsequent strengthening by aging. Their increased hardenability is also highly desirable for hardening of thick sections (POLMEAR et al., 2017). Over the last few decades, the importance of metastable β alloys has steadily increased. The complex microstructure of alloys like Ti-10V-2Fe-3Al and Beta C enables design optimization for both high strength and high toughness. Other alloys, like TIMETAL 15-3, can be deformed at room temperature down to thin foils. TIMETAL 21S was specially developed as an oxidation-resistant foil alloy to be used as matrix for long fiber reinforced titanium alloys. TIMETAL LCB is a low-cost alloy particularly aimed at applications beyond the aerospace sector, e.g. for the automotive industry. Beta-CEZ was developed in France for application at moderate temperatures in gas turbine engines. Due to its very fine grained bimodal microstructure, the Japanese alloy SP 700 features excellent superplastic behavior even at temperatures as low as 700°C (LEYENS; PETERS, 2003).

However, β alloys do have some disadvantages when compared to $\alpha+\beta$ alloys. They usually have higher density, lower creep strength, and lower tensile ductility in the aged condition (DONACHIE JR., 2000). Other disadvantages are limited weldability, poor oxidation behavior, and microstructural complexity (LEYENS; PETERS, 2003). Although tensile ductility is lower, the fracture toughness of an aged β alloy generally is higher than that of an aged $\alpha+\beta$ alloy of comparable yield strength. Very high yield strengths – about

1172 MPa – with excellent toughness have been achieved in the beta alloy Ti-10V-2Fe-3Al. In general, the class of β alloys serves a great need for titanium components that can be fabricated for moderate-temperature applications (DONACHIE JR., 2000). Although the number of commonly used β titanium alloys is as large as the number of $\alpha+\beta$ alloys, the percentage of β alloy usage on the total titanium market is very low. However, this percentage is increasing due to the attractive properties of this class, especially the high yield stress level and the low modulus of elasticity for some specific applications (LÜTJERING; WILLIAMS, 2007).

One of the latest additions to the β titanium alloy family was the near- β alloy Ti-5553 (Ti-5Al-5V-5Mo-3Cr-0.5Fe), developed in the late 1990s by the premier titanium producer in Russia, VSMPO, mainly for aerospace applications. It was designed on the basis of the alloy VT 22, but with improved processability and performances compared to both VT 22 and Ti-1023. Its microstructure consists of 10-20 vol% globular primary α in a matrix of aged β in the STA condition. A modification of the alloy Ti-5553 containing 1 wt% zirconium, designated Ti-55531, has reportedly been in production (POLMEAR et al., 2017). It presents properties higher specific strength and fatigue properties than Ti-5553, simplified processing routes to achieve superior strength levels than Ti-1023 and a considerably low β -*transus* temperature (BOYER; BRIGGS, 2005; COTTON et al., 2015; DURET, 2003; FAN et al., 2017; FU et al., 2008; NYAKANA; FANNING; BOYER, 2005; WARCHOMICKA; POLETTI; STOCKINGER, 2011; ZHANG et al., 2013). It is mostly used for the manufacturing of airframes and landing gears (BOYER, 2010; JONES et al., 2009b; NYAKANA; FANNING; BOYER, 2005).

2.5 Deformation of titanium alloys

In this section, the main aspects involved in the deformation of titanium alloys, i.e. deformation mechanisms (dislocation slip and twinning) and texture formation are presented.

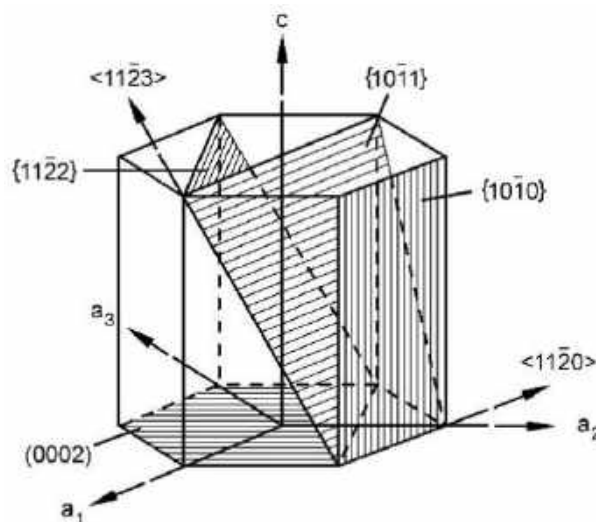
2.5.1 Slip modes

Theoretically, a slip plane in the HCP lattice, with a packing density of 91%, should be more favorable to slip than a slip plane in the BCC lattice, with a packing density of only 83%. However, the energy needed for plastic deformation is also directly dependent on the length of the minimal slip path. For HCP structures, this minimum slip path corresponds to

$b_{\min} = a$, while for BCC structures it corresponds to $b_{\min} = 0.87a$, where “a” is the lattice parameter of the respective unit cell. This, in turn, favors the plastic deformation of the BCC structure over the HCP (LEYENS; PETERS, 2003).

Compared to an ideally packed hexagonal crystal structure, the reduced c/a ratio of α titanium leads to a larger spacing between prismatic planes. This causes the packing density of the prismatic planes to increase relative to the basal plane, thus favoring slip on prismatic planes rather than on basal planes (LEYENS; PETERS, 2003). The various slip planes and slip directions for α titanium are indicated in the hexagonal unit cell in **Figure 24** and in **Table 12**. The main slip directions are the three $\langle 11\bar{2}0 \rangle$ close-packed directions. The slip planes containing this type of Burgers vector are the (0002) plane, the three $\{10\bar{1}0\}$ planes, and the six $\{10\bar{1}1\}$ planes. These three different types of slip planes combined with the possible slip directions result in a total of twelve slip systems, which can be reduced to eight independent slip systems. However, this number is further reduced to only four independent slip systems because the shape changes that are produced by the combined action of slip system types 1 and 2 are exactly the same as those of slip system type 3 (LÜTJERING; WILLIAMS, 2007). Slip on pyramidal planes does not increase the number either, since this glide is composed of a prism component and a basal component, and therefore cannot be considered an independent slip system (LEYENS; PETERS, 2003).

Figure 24 – Slip planes and slip directions in the hexagonal α phase.



Source: LEYENS, PETERS (2003)

Table 12 – Slip systems in the hexagonal α phase.

System type	Burgers vector type	Slip direction	Slip plane	Number of slip systems	
				Total	Independent
1	\vec{a}	$\langle 11\bar{2}0 \rangle$	(0002)	3	2
2	\vec{a}	$\langle 11\bar{2}0 \rangle$	{10 $\bar{1}$ 0}	3	2
3	\vec{a}	$\langle 11\bar{2}0 \rangle$	{10 $\bar{1}$ 1}	6	4
4	$\vec{c}+\vec{a}$	$\langle 11\bar{2}3 \rangle$	{11 $\bar{2}$ 2}	6	5

Source: LÜTJERING, WILLIAMS (2007)

The von Mises criterion requires at least five independent slip systems for homogenous plastic deformation of polycrystals. Thus, the operation of one of the slip systems with a so-called non-basal Burgers vector needs to be activated, either the \vec{c} type with the slip direction [0001] or the $\vec{c}+\vec{a}$ type with the slip direction $\langle 11\bar{2}3 \rangle$. The presence of $\vec{c}+\vec{a}$ type dislocations has been observed by TEM observations in a number of titanium alloys. To justify the presence of these $\vec{c}+\vec{a}$ dislocations it is not so important whether the von Mises criterion is valid or not, but rather to clarify which slip systems are activated if a grain in a polycrystalline material is oriented in such a manner that the applied stress is parallel to the c -axis. In that case, neither a slip system with an \vec{a} Burgers vector nor dislocations with a \vec{c} Burgers vector can be activated, because the Schmidt factor for both is zero. From the possible slip planes of the dislocations with a $\vec{c}+\vec{a}$ Burgers vector, the {10 $\bar{1}$ 0} slip planes cannot be activated because they are parallel to the stress axis and, from the other possible slip planes, the {11 $\bar{2}$ 2} planes are closer to 45° (higher Schmidt factor) than the {10 $\bar{1}$ 1} planes. Assuming the critical resolved shear stresses are about the same for both types of slip planes, then the slip system with a non-basal Burgers vector, which is most likely activated in α titanium, is the $\langle 11\bar{2}3 \rangle$ {11 $\bar{2}$ 2} type (slip system type 4). The slip systems in BCC β titanium alloys are {110}, {112} and {123}, all with the same $\langle 111 \rangle$ Burgers vector, in agreement with the generally observed slip modes in BCC metals (LÜTJERING; WILLIAMS, 2007).

2.5.2 Deformation twinning

Polycrystalline hexagonal α titanium is extremely difficult to deform. The limited ductility that is observed is the result of additional deformation on secondary slip systems, as well as possible mechanical twinning, especially at low temperatures (LEYENS; PETERS, 2003; LÜTJERING; WILLIAMS, 2007). These twinning modes are important for the deformation behavior of CP titanium and some α titanium alloys. Although twinning is

suppressed nearly completely in two phase $\alpha+\beta$ alloys by the small phase dimensions, high solute content, and possible presence of precipitates like Ti_3Al , these alloys are quite ductile at low temperatures. The BCC β phase also shows twinning in addition to slip, but the occurrence of twinning in β alloys is limited again to the single phase state and decreases with increasing solute content. In fully heat treated β alloys, which are hardened by the precipitation of α particles, twinning is completely suppressed. In these alloys, twinning might occur during forming operations prior to aging. Some commercial β alloys can also form deformation induced martensite, which further enhances their formability. Deformation-induced martensite formation is very sensitive to alloy composition (LÜTJERING; WILLIAMS, 2007).

The main twinning modes observed in pure α titanium are $\{10\bar{1}2\}$, $\{11\bar{2}1\}$, and $\{11\bar{2}2\}$. The crystallographic elements of these three twin systems are listed in **Table 13**. Twinning modes are especially important for plastic deformation and ductility at low temperatures if the stress axis is parallel to the c-axis and the dislocations with a basal Burgers vector cannot move. In this case, $\{10\bar{1}2\}$ and $\{11\bar{2}1\}$ twins are activated during deformation in tension leading to an extension along the c-axis. The most frequently observed twins are of the $\{10\bar{1}2\}$ type, but they have the smallest twinning shear, whereas a $\{11\bar{2}1\}$ twin has a much larger magnitude of twinning shear. Under compression loading parallel to the c-axis, $\{11\bar{2}2\}$ twins are activated, allowing a contraction along this axis. After compression loading, $\{10\bar{1}1\}$ twins are also observed, but only at relatively high deformation temperatures, above 400°C. Increasing concentrations of solute atoms in α titanium, such as oxygen or aluminum, suppresses the occurrence of twinning. Therefore, twinning as a deformation mode to allow shape changes parallel to the c-axis only plays a major role in pure titanium or in CP titanium with low oxygen concentrations (LÜTJERING; WILLIAMS, 2007).

Table 13 – Twinning elements in α titanium.

Twinning plane (first undeformed plane) (K_1)	Twinning shear direction (η_1)	Second undeformed plane (K_2)	Direction of intersection of shear plane with K_2 (η_2)	Plane of shear perpendicular to K_1 and K_2	Magnitude of twinning shear
$\{10\bar{1}2\}$	$\langle 10\bar{1}\bar{1} \rangle$	$\{\bar{1}012\}$	$\langle 10\bar{1}1 \rangle$	$\{\bar{1}\bar{2}10\}$	0.167
$\{11\bar{2}1\}$	$\langle 11\bar{2}\bar{6} \rangle$	(0002)	$\langle 11\bar{2}0 \rangle$	$\{\bar{1}100\}$	0.638
$\{11\bar{2}2\}$	$\langle 11\bar{2}\bar{3} \rangle$	$\{11\bar{2}4\}$	$\langle 2243 \rangle$	$\{\bar{1}100\}$	0.225

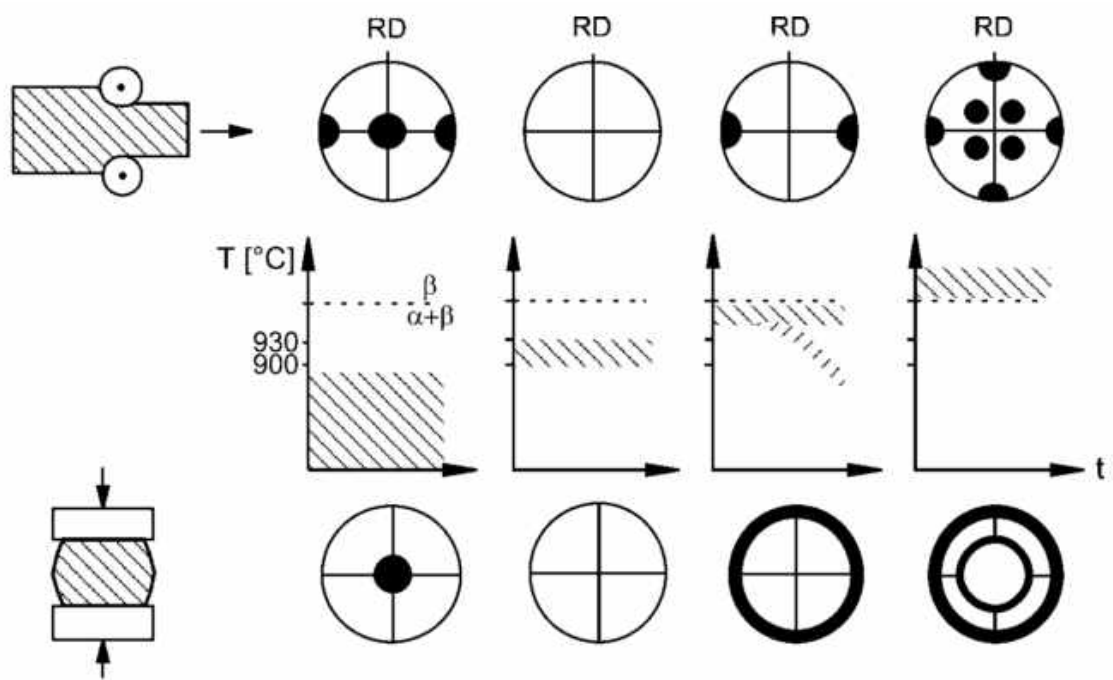
Source: LÜTJERING, WILLIAMS (2007)

2.5.3 Textures

Titanium alloys can have a pronounced anisotropy of properties, which can be directly related to the inherent anisotropy of the hexagonal crystal structure of the α phase. These crystallographic textures develop upon deformation (deformation texture) and can be further pronounced by a subsequent recrystallization annealing (recrystallization texture). Generally basal and transverse textures are distinguishable. Essentially, they describe the orientation of the (0002) planes relative to the deformation plane and deformation direction. For the two basic texture types, the (0002) planes are either parallel or perpendicular to the deformation plane, respectively. Crystallographic textures generally depend on the degree, mode, and temperature of deformation, as well as on the subsequent recrystallization annealing. Usually, the intensity of the texture increases with increasing deformation degree (LEYENS; PETERS, 2003).

In **Figure 25**, the influence of deformation mode and temperature on the (0002) α pole figure is schematically shown. Two basic deformation modes are considered: axial material flow, for example, with uniaxial rolling, and radial deformation, as is the case in upset forging or multidirectional rolling. The deformation temperature determines the texture type and deformation mode determines the texture symmetry, whereas the deformation degree determines the texture intensity. For the $\alpha+\beta$ alloy Ti-6Al-4V, four temperature regions can be distinguished. At temperatures below 900°C, where the HCP phase is mainly present, an α -deformation texture called basal/transverse develops. The extra transverse part is revealed upon uniaxial deformation. At temperatures between 900 and 930°C, almost no textures are observed, independently of deformation mode. Here, a substantial volume fraction of the BCC β is present. It is worth mentioning that this temperature window is also preferentially used to achieve maximum deformation for superplastic forming. At deformation temperatures just below the *transus* temperature, the basal component of the texture disappears. Here, a β -deformation texture develops in which, upon subsequent transformation to α , only one of the six possible variants of the Burgers relationship is selected. The (0002) pole figures are left with just a transverse pole, i.e. the resulting texture is of the transverse (T) type, which is radial after multidirectional deformation. Above the β -*transus* temperature, a classic cube texture is observed (LEYENS; PETERS, 2003; LÜTJERING, 1998).

Figure 25 – Influence of deformation temperature and mode on texture of Ti-6Al-4V (schematic (0002) pole figures).

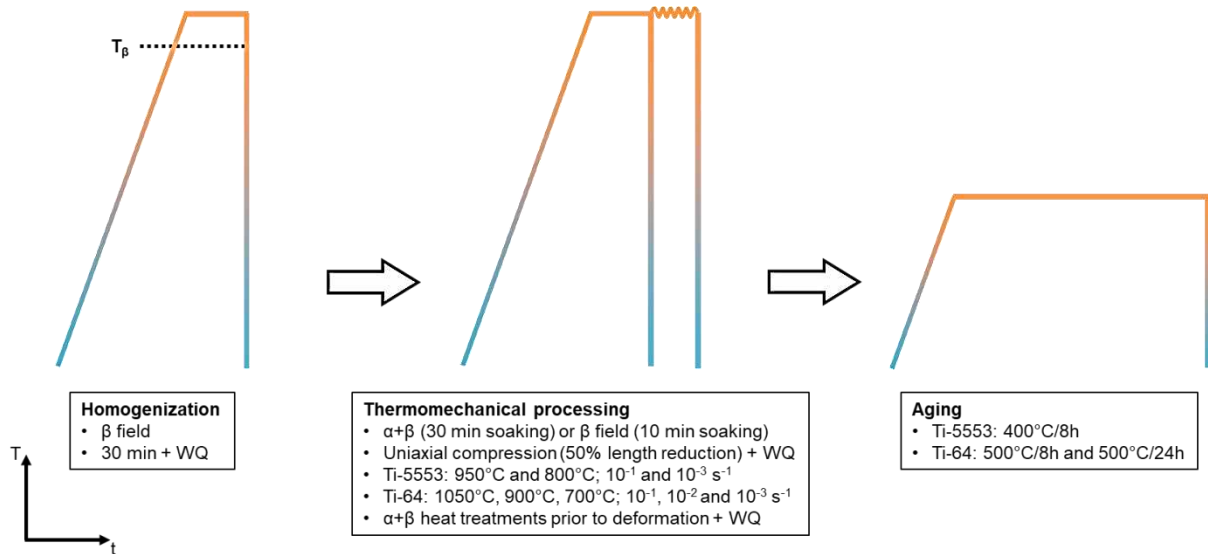


Source: SEMIATIN, SEETHARAMAN, WEISS (1997)

3 SUMMARY OF EXPERIMENTAL TECHNIQUES

The following section provides a unified and detailed description of experimental techniques and equipment used in this thesis. **Figure 26** depicts a schematic representation of the treatment route applied to the studied titanium alloys.

Figure 26 – Schematic representation of the processing routes applied to Ti-5553 and Ti-64 alloys.



3.1 Differential scanning calorimetry

Differential scanning calorimetry (DSC) has been performed to define the β -*transus* temperature of Ti-5553 and Ti-64 alloys. In both cases, three samples were heated at a constant rate of 20°C/min up to temperatures high enough to ensure systems would enter the single β phase field – 1000°C for Ti-5553 and 1100° for Ti-64 – according to reported theoretical *transus* temperatures. Real temperatures were determined as the average of the three measured endothermic peaks related to the completion of the $\alpha \rightarrow \beta$ transformation during heating. Experiments were performed in a Netzsch® 404 F3 Pegasus calorimeter located at the Department of Materials Engineering of the University of São Paulo (São Carlos, Brazil).

3.2 Chemical analyses

Chemical analyses were carried out to determine the nominal composition of Ti-5553 and Ti-64 alloys. The analysis of heavier elements, such as Ti, Al, Mo, V, Cr and Fe, were done by inductively coupled plasma atomic emission spectrometry in an Ametek® SPECTROMAXx spectrometer located at the Metals Characterization and Processing Laboratory of the Brazilian Center for Research in Energy and Materials (Campinas, Brazil). Three measurements were taken in different positions of the bulk of as-received materials and average amounts were then calculated.

Oxygen content was analyzed in a Leco® RO-400 inert gas fusion analyzer located at the Department of Materials Engineering of the University of São Paulo (São Carlos, Brazil). Carbon amount was determined by direct combustion in a Leco® CS-844 analyzer located at the Center for Characterization and Development of Materials of the Federal University of São Carlos (São Carlos, SP, Brazil). Nitrogen and hydrogen contents were obtained via infrared absorption radiation in a Leco® ONH-836 analyzer located at the Center for Characterization and Development of Materials of the Federal University of São Carlos (São Carlos, SP, Brazil). In all cases, three samples were analyzed and the average composition was calculated.

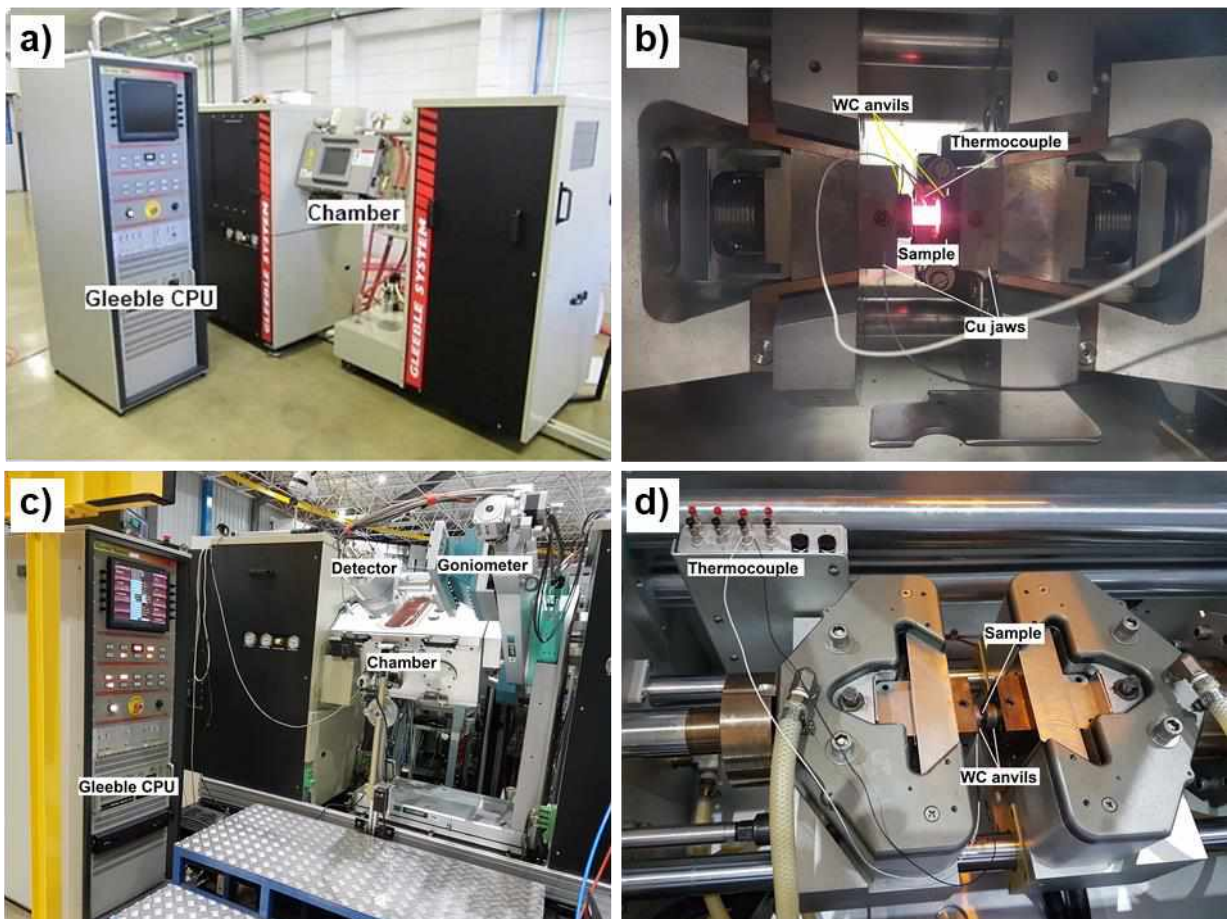
3.3 Thermomechanical processing

Cylindrical specimens with 10 mm of diameter and 15 mm of length were wire-cut from the as received bars with their length parallel to the bars' lengths. To remove effects of prior processing, specimens of both alloys underwent a homogenization treatment in the β phase field – Ti-5553 alloy at 950°C and Ti-64 alloy at 1050°C – during 30 minutes followed by quenching in water at room temperature. These treatments were done in an EDG® 10P-S furnace with vacuum and argon atmosphere located at the Department of Materials Engineering of the Federal University of São Carlos (São Carlos, Brazil).

Then, specimens were uniaxially compressed to a length reduction of 50% in a Gleeble® 3800 thermomechanical simulator located at the Metals Characterization and Processing Laboratory of the Brazilian Center for Research in Energy and Materials (Campinas, Brazil) (**Figure 27a** and **b**). Ti-5553 alloy was deformed at 950°C (β field) and 800°C ($\alpha+\beta$ field) with strain rates of 10^{-1} and 10^{-3} s⁻¹, whereas Ti-64 was deformed at 1050°C (β field), 900°C and 700°C ($\alpha+\beta$ field) with strain rates of 10^{-1} , 10^{-2} and 10^{-3} s⁻¹.

Specimens of both alloys were isothermally held at the target temperature before compression during 10 minutes in the β field and 30 minutes in the $\alpha+\beta$ field. Temperature control took place through S-type thermocouples spot-welded mid-length on samples' surfaces. Niobium foils with thickness of 0.5 mm were placed between compression anvils and the parallel faces of specimens, and conductive graphite paint was also applied to these faces to ensure lubrication and improve conductivity. Heat treatments without deformation were also performed at the same temperatures in the $\alpha+\beta$ during 30 minutes to obtain microstructures exactly before the beginning of compression. In all cases, samples were cooled by room-temperature water quenching and at least three samples were heat-treated and deformed in each condition.

Figure 27 – a) Overview and b) internal chamber view of the Gleeble® 3800 located at the Metals Characterization and Processing Laboratory at CNPEM; c) overview and d) internal chamber view of the Gleeble® 3S50 located at the XTMS beamline of the Brazilian Synchrotron Light Laboratory.



Source: “Conventional Thermomechanical Simulator – Gleeble® 3800” (a); the author (b-d)

3.4 Metallographic preparation

Samples for microstructural analyses of the as-received materials were cut in a Buehler® IsoMet 1000 cutter with a diamond disk located at the Department of Materials Engineering of the University of São Paulo (São Carlos, Brazil), embedded in bakelite in a Buehler® SimpliMet XPS1 located at the Department of Materials Engineering of the University of São Paulo (São Carlos, Brazil), manually ground on #320, #600 and #1200 sandpapers and automatically polished with a 3- μ m diamond suspension and with a 90 vol% colloidal silica + 10 vol% hydrogen peroxide in a Buehler® EcoMet 250 machine (force: 5 N; base rotation: 20 rpm; head rotation: 60 rpm; counter-rotation), located at the Department of Materials Engineering of the University of São Paulo (São Carlos, Brazil).

Samples for subsequent metallographic analyses and aging treatments, as well as aged samples, were wire cut from heat-treated and deformed specimens with dimensions of $3 \times 4 \times 6$ mm³. In addition, one deformed specimen of each condition was cut in half with the diamond disk Buehler® IsoMet 1000 cutter to expose the surface perpendicular to the compression direction for macrottexture analysis. After cutting, samples were embedded either in bakelite in a Buehler® SimpliMet XPS1 located at the Department of Materials Engineering of the University of São Paulo (São Carlos, Brazil) – for light optical microscopy, scanning electron microscopy, electron backscatter diffraction and micro-hardness measurements – or in cold-mounting resin – for texture analysis –, manually ground and automatically polished in the Buehler® EcoMet 250 machine, located at the Department of Materials Engineering of the University of São Paulo (São Carlos, Brazil), or in a Struers® TegraPol-21 machine (force: 10 N; base rotation: 50 rpm; head rotation: 50 rpm; both rotations in the same direction), located in the Chair of Functional Materials of the Saarland University (Saarbrücken, Germany).

In cases where chemical etching was necessary to reveal the microstructure for LOM and SEM, Kroll's etchant (91 vol% water, 6 vol% nitric acid and 3% hydrofluoric acid) has been used. Etching was carried out at room temperature by immersion.

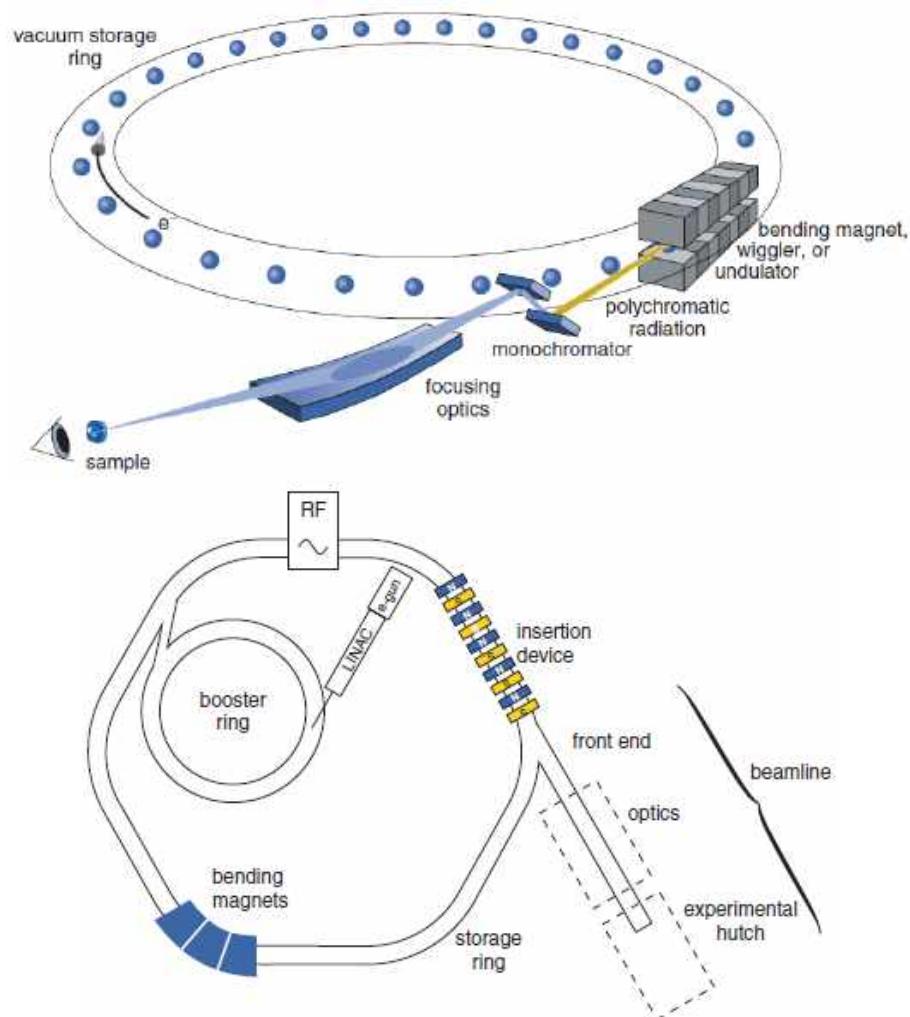
3.5 Synchrotron X-ray diffraction

Synchrotron radiation is generated in particle accelerators when charged particles are accelerated to relativistic velocities and deflected in magnetic fields, in order to keep them in a circular orbit. Due to their high charge-to-mass ratio, synchrotron radiation is particularly

pronounced for electrons and positrons (STARON et al., 2017). Synchrotron research facilities are designed and dedicated to generate tunable beams of electromagnetic radiation from the far infrared to the hard X-ray regime, with intensities, defined by their ‘flux’ or ‘brilliance’, many orders of magnitude greater than those produced by laboratory-based sources (WILLMOTT, 2011).

Synchrotron sources consist of evacuated storage rings in which high-energy electrons circulate at highly relativistic velocities, and so-called beamlines that utilize synchrotron light emitted by electrons tangentially to their orbital path at positions defined by components known as bending magnets and insertion devices (STARON et al., 2017; WILLMOTT, 2011). A storage ring with its typical main components is illustrated in **Figure 28**.

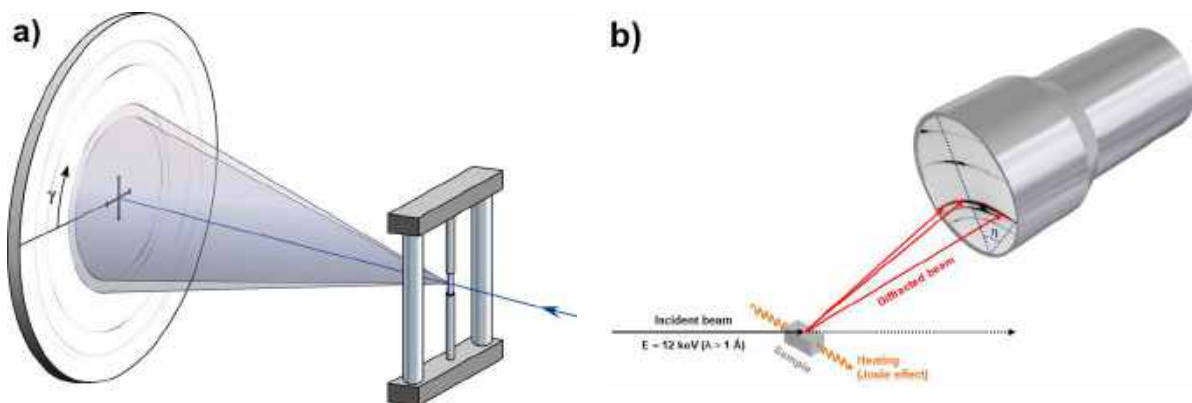
Figure 28 – Schematic representations of the most important components of a modern synchrotron radiation source.



Source: WILLMOTT (2011)

The simplest experimental technique for HEXRD experiments is the employment of a two-dimensional detector placed behind a sample in transmission mode. Different scanning techniques have been employed for careful measurements, but the simple setup with a two-dimensional detector is of great benefit with regard to the speed of data acquisition. Polycrystalline materials benefit from the registration of entire Debye-Scherrer rings with a two-dimensional detector. A typical setup is given using an image-plate detector as shown in **Figure 29a**. Here, both, the eccentricity of a ring and the azimuthal intensity distribution along the ring can be used for strain and texture measurements, respectively. In storage rings with lower beam energy (typically below 30 keV), experiments are conducted in reflection mode, since attenuation length decreases considerably, and detectors in this case acquire sections of Debye-Scherrer rings (**Figure 29b**).

Figure 29 – Schematic experimental setups for synchrotron x-ray diffraction experiments at **a)** ID15B beamline of the European Synchrotron Radiation Facility (energy: 90 keV) and **b)** XTMS experimental station of the Brazilian Synchrotron Light Laboratory (energy: 12 keV).



Source: LISS, YAN (2010) (a); adapted from FARIA et al. (2014) (b)

High-energy x-ray diffraction has been extensively used as an in situ characterization technique for microstructural evolution in titanium alloys during thermal treatments, e.g. continuous heating and cooling experiments and isothermal treatments. Examples of works on phase transformation kinetics during thermal treatments can be found in: AEBY-GAUTIER *et al.*, 2007, 2013; BARRIOBERO-VILA *et al.*, 2014; BARRIOBERO-VILA; REQUENA; BUSLAPS; *et al.*, 2015; BARRIOBERO-VILA; REQUENA; SCHWARZ; *et al.*, 2015; BRUNESEAUX *et al.*, 2008; ELMER *et al.*, 2005; GEANDIER *et al.*, 2012; JONES *et al.*, 2009; MALINOV *et al.*, 2002; SETTEFRATI; AEBY-GAUTIER; *et al.*, 2011; SETTEFRATI; DEHMAS; *et al.*, 2011; SETTEFRATI *et al.*, 2013. As examples of works focused on in situ thermomechanical treatments of titanium alloys, HÉRAUD et al., 2015;

WARCHOMICKA et al., 2019; WARWICK et al., 2013 can be cited. Elmer et al. has also studied phase transformation dynamics during welding of Ti-6Al-4V alloy (ELMER et al., 2004). Most recently, with the momentum of additive manufacturing technology, works on in situ analysis of microstructural buildup during additive processing have also started to emerge, as is the example of the work of Barriobero-Vila et al. on selective laser sintering of Ti-6Al-4V (BARRIOBERO-VILA et al., 2017).

Heat-treated and deformed samples of Ti-5553 and Ti-64 were analyzed by high energy synchrotron X-ray diffraction at the P07B beamline of the *Deutsches Elektronen Synchrotron* (Hamburg, Germany). Single shots were taken at room temperature with a beam energy of 87.1 keV (0.142 Å) and beam size of $1 \times 1 \text{ mm}^2$ in transmission mode, and complete Debye-Scherrer rings ($\Delta\eta = 360^\circ$) were acquired by a Perkin Elmer® XRD 1621 detector with pixel size of $200 \times 200 \text{ }\mu\text{m}^2$. For Ti-5553, an exposure time of 0.2 s and 5 frames/image were used, and for Ti-64, an exposure time of 0.1 s and 5 frames/image were used. Images were calibrated with a LaB₆ standard using Fit2D software and integrated in ImageJ software to generate the corresponding diffractograms.

Heat-treated and slowly (10^{-3} s^{-1}) deformed conditions of both alloys were selected for subsequent aging treatments. Samples of Ti-5553 were aged at 400°C during 8 h and of Ti-64 were aged at 500°C during 8 h using in situ synchrotron X-ray diffraction at the XTMS experimental station of the XRD1 beamline (**Figure 27c and d**), at the Brazilian Synchrotron Light Laboratory (Campinas, Brazil). Experiments were carried out in reflection mode in a Gleeble® 3S50 simulator with the acquisition of sections of Debye-Scherrer rings ($\Delta\eta \approx 30^\circ$) by a Rayonix® SX165 area detector with pixel size of $39 \times 39 \text{ }\mu\text{m}^2$ and acquisition time of 60 s. The maximum vacuum level of the chamber was of $\sim 10^{-3}$ torr, and temperature was controlled by spot-welded K-type thermocouples. The beam energy was of 12 keV, which corresponds to a wavelength of 1.032 Å and a penetration depth of approximately 10 μm in titanium with an incidence angle of $\sim 19^\circ$. A 2theta interval between 15° and 45° was acquired. Images were calibrated using an Al₂O₃ standard and integrated in the Matlab® macro Dracon, developed by the XTMS staff, to generate 2D diffraction patterns. Samples of Ti-64 were also aged at 500°C during 24 h in a Carbolite® STF15/75/450 tube furnace with a vacuum level of $\sim 10^{-4}$ mbar (7.5×10^{-5} torr) and subsequently probed at the P07B beamline at DESY.

Integrated diffractograms were analyzed using MAUD (Materials Analysis Using Diffraction) software (“MAUD - Materials Analysis Using Diffraction”, [s.d.]), to draw quantitative information such as phase fractions and lattice parameters of phases, and PeakFit

software to draw information regarding peak shape parameters, such as area and width, using a combined Gauss + Lorentz model.

3.6 Rietveld refinement

Rietveld refinement was developed by H. M. Rietveld in 1969 (RIETVELD, 1969) and consists in a complex minimization process for structural refinement, in which each individual intensity point is considered individually, including background points. The idea behind the method is to treat the diffraction pattern through a number of refinable parameters. Also, because it treats intensities point by point, and not in an integral manner, the eventual problem of peak overlapping can be overcome. Currently, the method is widely utilized in several diffraction-based fields of analysis, e. g. for phase and texture analysis (WILL, 2006). It is a powerful tool for quantitative evaluation of the evolution of parameters of interest during in situ HEXRD experiments as function of variables such as time, temperature or strain rates, allowing for kinetics analysis of these parameters.

Rietveld uses the minimum square method to minimize the weighted difference between experimental, $y(obs)$, and calculated, $y(calc)$, profiles, given by S , according to the equation (WILL, 2006):

$$S = \sum_i w_i [y_i(obs) - y_i(calc)]^2 \quad (9)$$

Through the application of the method, a variety of information can be drawn from the diffraction pattern, such as: lattice parameters and space groups, which can be deduced and refined from the positions of the peaks; amorphous fraction of the material, which can be deduced from the background; domain sizes and stress/strain states, which can be analyzed from the broadening of peaks; and quantitative and qualitative information about phases (WILL, 2006). During refinement, important parameters to be analyzed include (MCCUSKER et al., 1999):

1. Background, which can be assessed by linear interpolation or by empirical and semi-empirical functions with refinable parameters;
2. Peak shape, that depends on sample parameters (domain size, strains and stresses, defects), instrumental parameters (radiation source, geometry, slit aperture), and diffraction angle, and whose approximation is done most commonly by the pseudo-Voigt approach, which combines Gaussian and Lorentzian factors;

3. Profile parameters, such as broadening and asymmetry of the peaks, which are functions of the Bragg angle, Bragg angle correction and lattice parameters;
4. Structural parameters, such as scale factors, atom occupation sites and thermal parameters.

The best way to evaluate the convergence of refinement is by observing directly the superposition between calculated and experimental patterns and the resulting difference curve, whose profile may indicate which problem is causing mismatch between both patterns, as exemplified in **Figure 30**. Nonetheless, there are two extremely important parameters that must be observed during refinement: the reliability factor, R_{wp} , corresponding to the weighted value of the profile, and R_{exp} , corresponding to the expected value for the profile, which are given by the equations (MCCUSKER et al., 1999):

$$R_{wp} = \sqrt{\frac{\sum_i w_i [y_i(\text{obs}) - y_i(\text{calc})]^2}{\sum_i w_i [y_i(\text{obs})]^2}} \quad (10)$$

$$R_{exp} = \sqrt{\frac{N-P}{\sum_i w_i [y_i(\text{obs})]^2}} \quad (11)$$

where N is the number of observations and P is the number of parameters. The ratio between R_{wp} and R_{exp} , given by χ^2 , provides the quality of the adjustment and for this reason must be as close as possible to the unit.

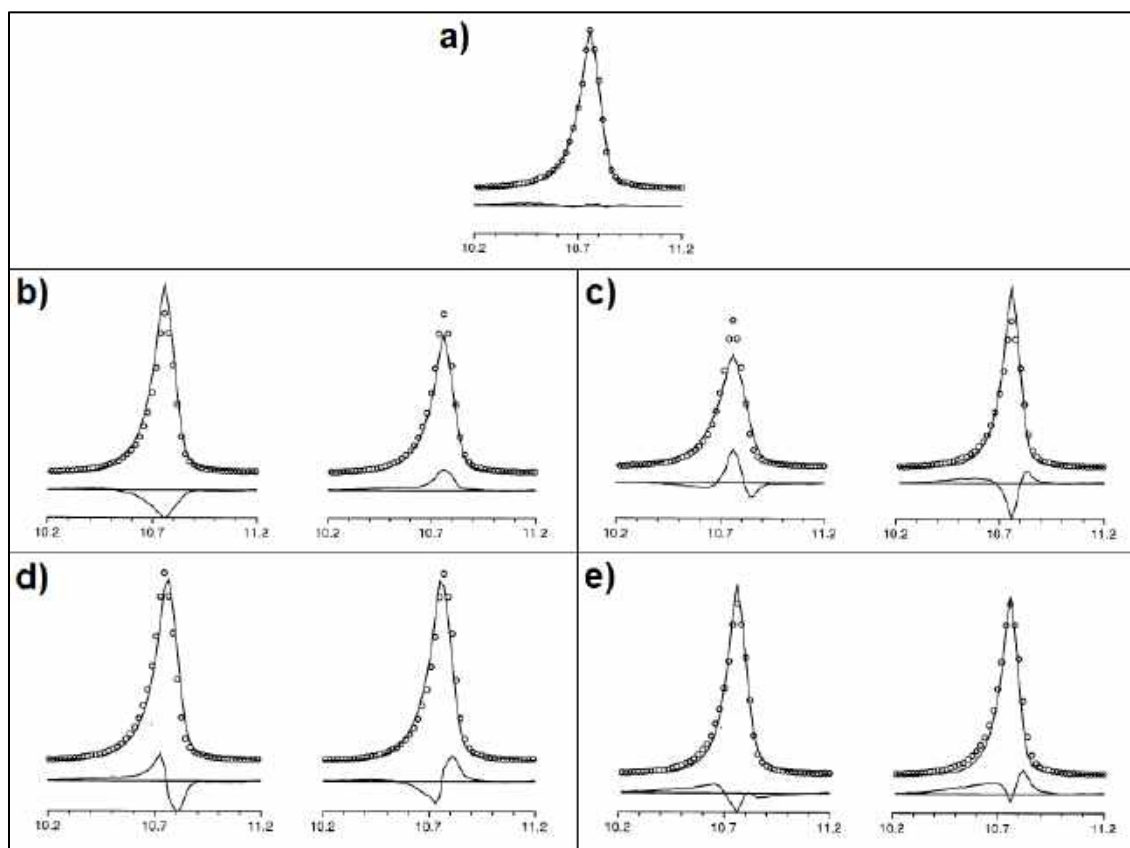
To allow for an adequate refinement of experimental data, a number of requirements need to be attended during a x-ray diffraction experiment (LUTTEROTTI; VASIN; WENK, 2014):

1. The wavelength must be well known for refinement of instrument parameters;
2. The precise location of the primary beam must be established to assure the beam is at the center of all goniometer rotations;
3. When measuring textures, the orientation of the sample relative to the diffraction instrument must be known;
4. The sample needs to be centered in the rotation axis to ensure the same volume element and sample-detector distance at all tilt angles;
5. The exact detector distance and orientation, as well as instrument peak broadening parameters, need to be calibrated at least once, by means of a powder standard, such as

LaB₆ or CeO₂. These instrumental parameters are previously refined for calibration during analysis and then kept fixed during subsequent refinement of experimental data.

6. Detector dimensions and characteristics, such as resolution and pixel size, must be known as well.

Figure 30 – Examples of difference curve behavior for **a**) a good fit between experimental (dots) and calculated (lines) profiles, **b**) too high (left) and too low (right) calculated intensities, **c**) too large (left) and too small (right) calculated FWHM, **d**) too large (left) and too small (right) 2θ and **e**) too small FWHM combined with too small peak asymmetry (left) and too small FWHM combined with too low intensity (right).



Source: MCCUSKER et al. (1999)

Rietveld refinement was carried out in version 2.55 of MAUD software (“MAUD - Materials Analysis Using Diffraction”, [s.d.]). The CIFs (crystallographic information files) of each phase were downloaded from the Inorganic Crystal Structure Database (ICSD). The instrument was refined using the aforementioned LaB₆ and Al₂O₃ standards to obtain the instrumental broadening using the Caglioti model (CAGLIOTI; PAOLETTI; RICCI, 1958). In sequence, experimental diffractograms were refined following the sequence:

1. Refinement of background function, incident intensity and phase fractions;
2. Refinement of lattice parameters and 2θ offset;

3. Refinement of crystallite size and micro-strain, using an isotropic model for the BCC β phase and the anisotropic Popa rules (POPA, 1998) for the HCP α and ω phases and the orthorhombic α'' phase;
4. Refinement of the atomic coordinate “y” of α'' , when applicable;
5. Manual background interpolation.

No specific texture model was employed and the Popa line broadening model was used. The refinement of XTMS data was conducted considering an incidence angle (ω) of 19° .

3.7 Microstructural characterization

Light optical microscopy (LOM) and scanning electron microscopy (SEM) were carried out in a Zeiss® Axio Scope.A1 optical microscope and in a FEI® Inspect F50 scanning electron microscope equipped with field emission gun (FEG). Both microscopes are located at the Department of Materials Engineering of the University of São Paulo (São Carlos, Brazil). SEM was performed using both secondary and backscattered electrons, according to necessity.

Transmission electron microscopy (TEM) was done in a JEOL® JEM 2010 microscope with a LaB₆ source, located at the Leibniz Institute for New Materials of the Saarland University (Saarbrücken, Germany), and in a FEI® TECNAI G²-F20 microscope with FEG, located at the Structural Characterization Laboratory of the Department of Materials Engineering, at the Federal University of São Carlos (São Carlos, Brazil). Both microscopes were operated at 200 kV. Samples for TEM were fabricated by lift-out using focused ion beam (FIB) in a FEI® Helios NanoLab 600 DualBeam located at the Chair of Functional Materials of the Saarland University (Saarbrücken, Germany). Electron diffraction patterns were indexed using the PTCLab software (GU; FURUHARA; ZHANG, 2016).

3.8 Macro- and micro-texture analyses

Macrotexture analyses of deformed conditions of both alloys were carried out in a PANalytical® Empyrean X-ray diffractometer located at the Chair of Functional Materials of the Saarland University (Saarbrücken, Germany) with Cu K α radiation ($\lambda = 1.54 \text{ \AA}$). Step sizes for both the φ rotation ($0\text{-}360^\circ$) and the ψ tilt ($0\text{-}85^\circ$) were of 5° . A beam size of $2 \times 2 \text{ mm}^2$ and a counting time of 10 s were used. For Ti-5553, (0002), (10 $\bar{1}$ 0), (10 $\bar{1}$ 1), (10 $\bar{1}$ 2) and (11 $\bar{2}$ 0) pole figures of the α phase and (110), (200) and (211) pole figures of the β phase were

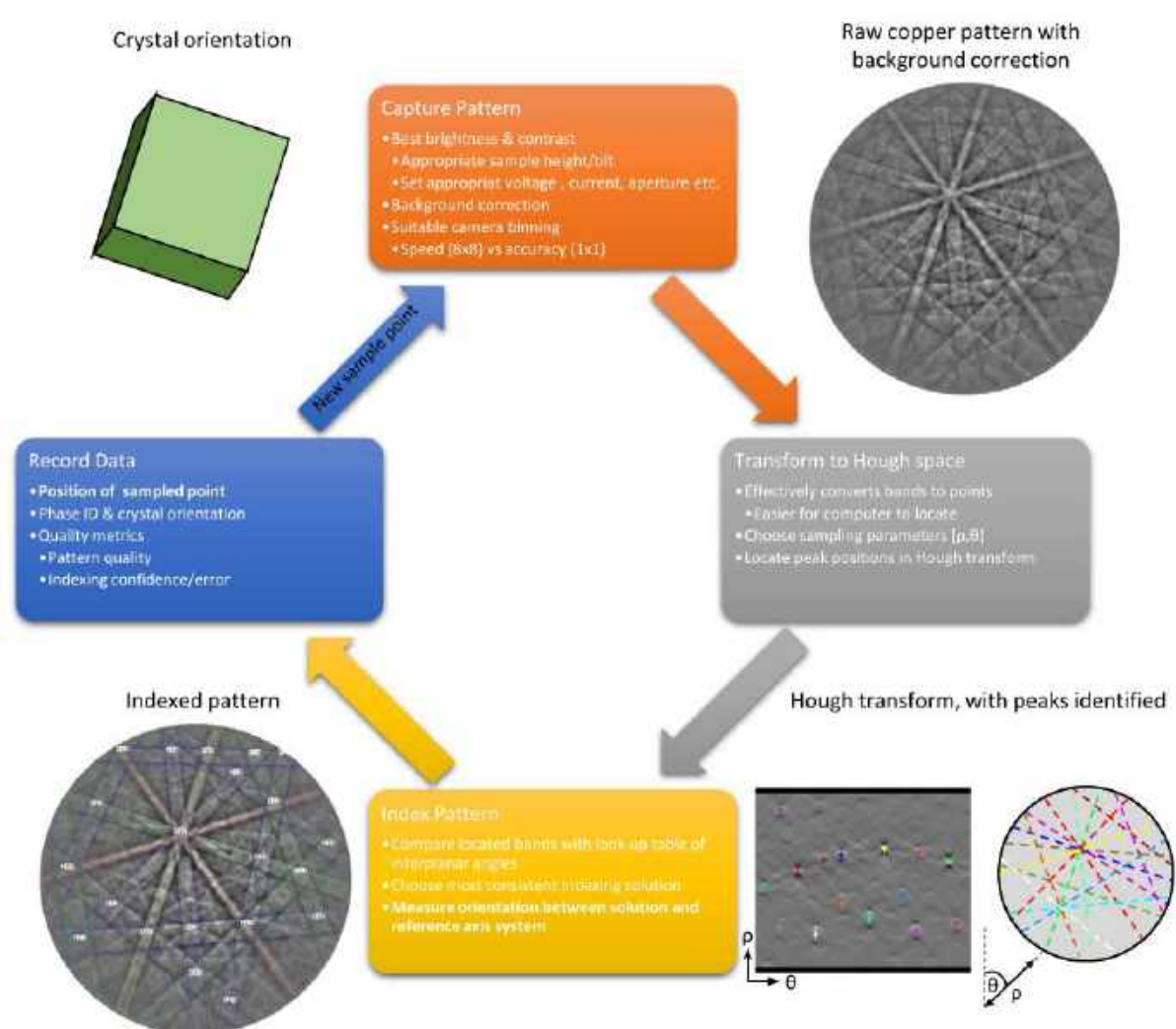
measured. For Ti-64, only the pole figures of the α phase were measured. The calculation of orientation distribution functions (ODFs) and of corrected pole figures from the acquired pole figures was performed using the MTEX toolbox for MATLAB® (BACHMANN; HIELSCHER; SCHAEBEN, 2010).

However, the aim of the conventional X-ray approach for texture measurement is to efficiently provide an overview of the texture, showing what volume fraction of the specimen (obtained from the diffraction intensity of particular planes) has a particular orientation. This texture results from numerous individual grains with their own discrete orientation, but it does not tell us how these grains are distributed in the material. An approach that deals with the orientation statistics of a population of individual grains, and usually encompasses the *spatial location* of these grains, is called *micro-texture*. This approach provides a direct connection between microstructure and crystallography, including not only the spatial components of grain orientations, but also the interface between grains. Examples of features that can be explored by micro-texture analysis include local property effects, interfacial parameters and properties, morphological and geometrical grain parameters (e.g. size, shape, and location), orientation variations within individual grains, phase relationships and direct ODF measurement (ENGLER; RANDLE, 2010). Moreover, the orientations of these crystals and relationships between them are important to help understand macroscopic properties and microstructural transformation pathways. These relationships are specified by the rotation between adjacent crystals, known as misorientation, and by the interface boundary between them. Misorientations between crystals of the same or different phases often occur repeatedly near to particular values, which is typically the result of special crystallographic orientation relationships arising due to the transformation pathway. Understanding these orientation relationships is, therefore, crucial for the study of microstructure in materials science (KRAKOW et al., 2017).

Currently, electron backscatter diffraction (EBSD) is the main tool for most of micro-texture research. The most attractive feature of EBSD is its unique capability to perform rapid, automatic diffraction analysis to provide crystallographic data and images with nanoscale spatial resolution in combination with the regular capabilities of a scanning electron microscope, such as capacity for large specimens, concurrent chemical analysis, and the ability to image rough surfaces (ENGLER; RANDLE, 2010). The emergence of EBSD follows the rapid image analysis routines developed by Yale and Risø research laboratories, which transformed the technique into the heavily automated method currently used (BRITTON et al., 2016).

The technique relies on inserting the specimen within the SEM sample chamber in a position such that a small angle ($\sim 20^\circ$) is made between the incident electron beam and the specimen surface. This enhances the amount of backscattered electrons able to undergo diffraction and escape from the specimen surface. The resulting diffraction pattern, named Kikuchi diffraction pattern, is captured and computer algorithms allow the orientation of each diffraction pattern to be obtained and stored. This raw data is then translated into micro-texture data based on the crystallographic information of the phase. **Figure 31** presents a schematic overview of the EBSD indexing procedure (ENGLER; RANDLE, 2010).

Figure 31 – Overview of EBSD indexing procedure showing pattern capture through to determination of crystal orientation.

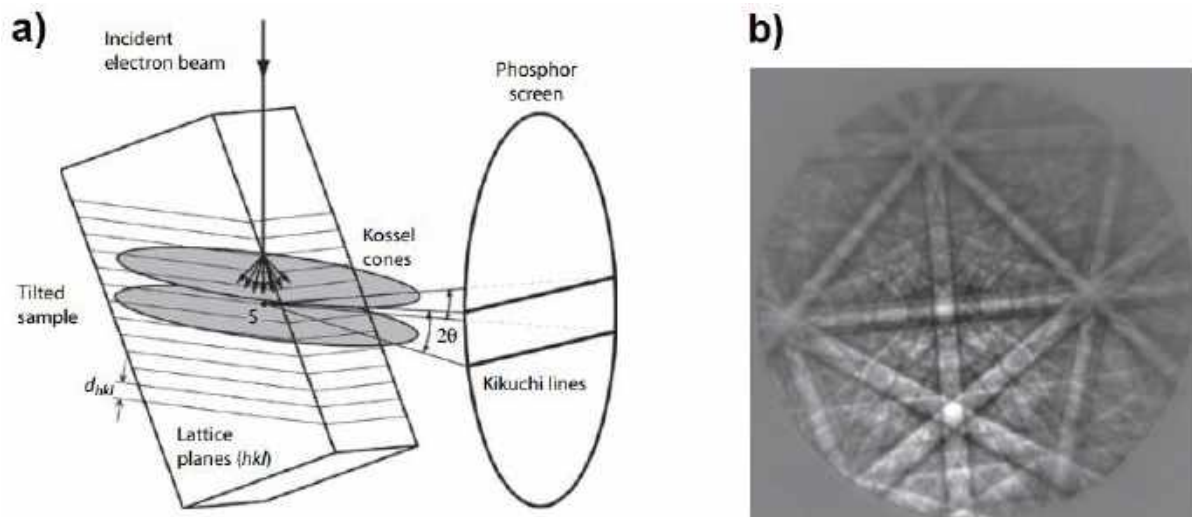


Source: BRITTON et al. (2016)

The so-called Kikuchi pattern aforementioned consists of pairs of parallel lines where each pair, or “band”, has a distinct width and corresponds to a distinct crystallographic plane.

The intersection of these bands corresponds to a zone axis (pole), and major zone axes are recognized by the intersection of several bands. Therefore, the Kikuchi pattern contains all the angular relationships in a crystal and hence contains information about crystal symmetry. In the SEM, Kikuchi diffraction occurs from the interaction of backscattered electrons with lattice planes close to the surface of the specimen (ENGLER; RANDLE, 2010). **Figure 32** presents the formation of Kikuchi lines in the EBSD geometry. The so-called Kossel cone corresponds to the resulting surface of the trajectories of diffracted electrons, since diffraction occurs in all directions.

Figure 32 – a) Origin of backscattered Kikuchi lines from the EBSD (i.e., tilted specimen) perspective, and b) EBSD pattern from copper (accelerating voltage: 15 kV).



Source: ENGLER, RANDLE (2010)

EBSD analyses of heat-treated and deformed specimens of Ti-5553 were performed in a FEI® Helios NanoLab 600 DualBeam located at the Chair of Functional Materials of the Saarland University (Saarbrücken, Germany). EBSD data were processed in the EDAX® OIM software. On the other hand, EBSD analyses of Ti-64 were done both in the FEI® Helios NanoLab 600 DualBeam and in a FEI® Quanta 650 FEG microscope located at the Electron Microscopy Laboratory of the Brazilian Center for Research in Energy and Materials (Campinas, SP, Brazil). For standardization purposes, all data of this alloy were processed in the MTEX toolbox for MATLAB®. Step sizes ranged from 0.08 μm to 1 μm , depending on the necessary resolution based on the size of microstructural features.

3.9 Micro-hardness testing

The micro-hardness of samples pre- and post-aging of Ti-5553 was measured with a Leica® VMHT-MOT tester located at the Department of Materials Engineering of the University of São Paulo (São Carlos, Brazil). Ten indentations were made on the polished surface of samples in a random manner with a load of 0.2 kgf. The average hardness value and the standard deviation were then calculated. For Ti-64, the micro-hardness of samples before and after aging during 24 h was measured with a Struers® DuraScan tester located at the Chair of Functional Materials of the Saarland University (Saarbrücken, Germany). Twenty-five measurements were taken in each sample using a load of 0.2 kgf in a 5×5 mesh with a spacing of 150 μm between indentations.

4 THERMOMECHANICAL PROCESSING OF Ti-6Al-4V ALLOY

4.1 Introduction

Titanium alloys are indispensable materials for the manufacturing of aerospace parts, and the most used forming technique is forging. Generally, titanium forgings are transformed by secondary hot working from bars, which are produced by primary hot working. The microstructure of bars has a great influence on the performance of the final products, meaning that a rigorous microstructural control during primary hot working is necessary to achieve a fine and homogeneous microstructure that attends the mechanical requirements for these parts. Typical primary processing for titanium bars involves forging both in the β phase field and in the $\alpha + \beta$ phase field (GUO et al., 2015).

Ti-6Al-4V (Ti-64, composition in weight percent) has been the main representative of $\alpha+\beta$ alloys for decades, being responsible for more than 50% of all titanium alloys' applications (POLMEAR et al., 2017). Reasons for its extensive application involve the good equilibrium of properties such as strength, ductility, toughness and fatigue resistance (FROES, 2015; LEYENS; PETERS, 2003; LÜTJERING; WILLIAMS, 2007). Properties of this alloy are a consequence of their response to thermal and thermomechanical treatments, in terms of variation of composition, morphology and fraction of existing phases (FROES, 2015). Several types of phases and morphologies in final microstructures can be obtained depending on the applied processing routes. Treatment temperature, cooling rate, and degree and mode of deformation are the most critical processing factors, influencing the type and morphology of the precipitated α phase, the formation of martensitic phases, the occurrence of texture and the possibility of subsequent age hardening (LÜTJERING; WILLIAMS, 2007).

The behavior of Ti-64 alloys under thermomechanical processing in the $\alpha+\beta$ field has been extensively studied. Important works on the evolution of lamellar and/or martensitic microstructures into globular ones have been carried out, e.g. Refs. (BIELER; SEMIATIN, 2002; MATSUMOTO et al., 2016, 2018; MOTYKA et al., 2015, 2018; MOTYKA; SIENIAWSKI; ZIAJA, 2014; SEMIATIN; BIELER, 2001; SEMIATIN; SEETHARAMAN; WEISS, 1999; SHELL; SEMIATIN, 1999). These findings are important to understand the superplastic behavior of $\alpha+\beta$ alloys in these conditions and for the continuous development of models to predict their flow behavior, aiming at the constant improvement of processing maps (HU et al., 2018; SESHACHARYULU et al., 2002). The dynamic globularization mechanism of the α phase with lamellar morphology is usually attributed to dynamic recrystallization

(splitting of lamellae into necklace strings with similar orientation), but different globularization mechanisms have been proposed, such as boundary splitting (formation of sub-boundaries within lamellae with subsequent wedging of the β phase into the α/β interface, evolving to a globular morphology) and shearing mechanism (shearing of lamellae leading to dislocation migration and interface formation along shear lines, promoting globularization) (SEMIATIN, 2020; ZHANG; LI; ZHAN, 2020). The understanding of substructure evolution in colony α is critical for the development of advanced models for texture evolution and dynamic globularization, for example (SEMIATIN, 2020). However, descriptions of these mechanisms are mostly qualitative, lacking quantitative description of microstructural features such as crystal and substructure orientation (SEMIATIN, 2020; ZHANG; LI; ZHAN, 2020). Moreover, a subject of growing interest during $\alpha+\beta$ processing is a dynamic reduction in the α phase volume fraction with respect to static conditions, whose mechanisms are not yet fully known (SEMIATIN, 2020; SEMIATIN et al., 2020).

Regarding the microstructural evolution of the alloy during processing in the β field, works are rather limited (POLETTI et al., 2016; WARCHOMICKA et al., 2019). Overall, dynamic recovery is acknowledged as the main restoration mechanism of the β phase. However, in certain conditions, deformation at β grain boundaries might lead to the generation of a “necklace” morphology consisting in fine recrystallized grains, which have been suggested to form by discontinuous dynamic recrystallization (SEMIATIN, 2020). After deformation in the β phase, the morphology of β grains becomes quite inhomogeneous, including elongated, equiaxed recrystallized and non-deformed grains. This heterogeneity impacts α precipitation upon quenching, and heterogeneous globularization can occur during subsequent $\alpha+\beta$ processing as a result. Therefore, morphology and distribution of processed β grains play a key role in microstructure evolution behavior during $\alpha+\beta$ working (GUO et al., 2015). Thus, the correlation between β processing and the precipitated α phase is of vital importance, and to our best knowledge there are no studies with such focus.

Another relevant aspect of mastering the phase evolution in titanium alloys, both during thermal and thermomechanical treatments, is related to the subsequent heat treatment steps the alloy might undergo with varied purposes, such as age hardening. According to Pederson, α plates or lamellae which form upon cooling do not respond as well to age hardening as globular α that forms during static or dynamic recrystallization due to elemental partitioning effects (PEDERSON, 2002). This means that aging of Ti-64 with globular α makes it more prone to hardening by precipitation of coherent Ti_3Al particles, for example. Furthermore, deformation-induced defects, such as dislocations and low-angle boundaries

may act as additional nucleation sites (ZHANG; LI, 2003). At the same time, supersaturated martensitic α' transforms into the stable and harder α phase upon ageing, which also improves the strength of the alloy (QAZI et al., 2003).

In this context, the present work aims to provide a deeper and concise understanding on the microstructural features arising from processing of Ti-6Al-4V alloy both in the single β phase field and in the dual $\alpha+\beta$ field, relying mainly on X-ray and backscattered electron diffraction techniques, with focus on crystallographic and morphological aspects of the α phase in final microstructures, emphasizing martensitic and globular conditions. Phase quantification was carried out to evaluate dynamic phase transformations and the influence of treatments on the stability of α and β phases. To promote microstructural variability, annealing treatments were applied prior to deformation in the $\alpha+\beta$ field, providing starting microstructures with different degrees of lamellar coarsening.

4.2 Materials and methods

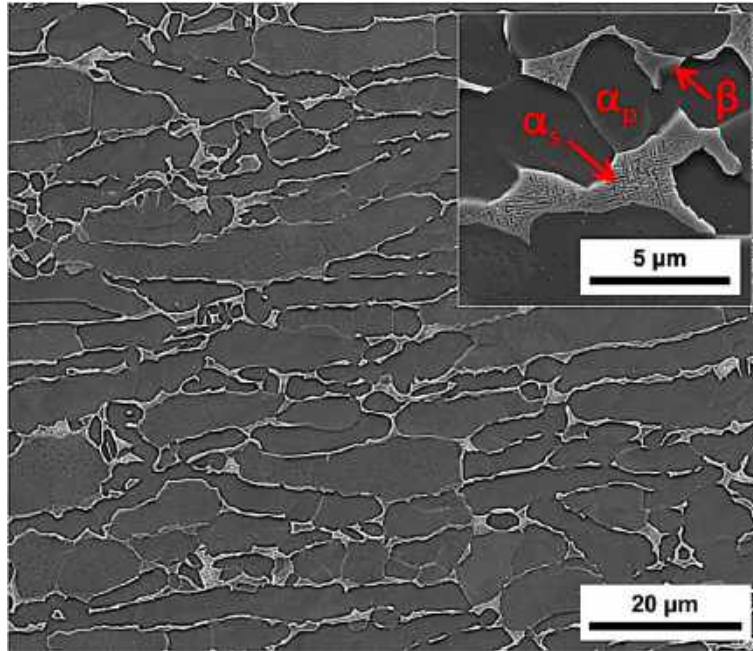
4.2.1 Material

The composition of the Ti-6Al-4V alloy (grade 23) (AMERICAN SOCIETY FOR TESTING AND MATERIALS, 2019; BOYER; ELSCH; COLLINS, 1994) used in this work is given in **Table 14**. Heavier elements, such as Ti, Al, V and Fe, were analyzed by inductively coupled plasma atomic emission spectrometry in an Ametek® SPECTROMAXx spectrometer. Interstitial elements – O, C, N and H – were quantified by direct combustion or infrared absorption using Leco® RO-400 (O), Leco® CS-844 (C) and Leco® ONH-836 (N and H) analyzers. Aluminum ([Al]eq) and molybdenum ([Mo]eq) equivalent values were calculated according to Ref. (BOYER; ELSCH; COLLINS, 1994). Its β -*transus* temperature was determined to be of $\sim 964^\circ\text{C}$ by differential scanning calorimetry with a heating rate of $20^\circ\text{C}/\text{min}$ in a Netzsch® 404 F3 Pegasus calorimeter. **Figure 33** shows the mill-annealed microstructure of the as-received, comprising the α phase with globular morphology (primary α) and lamellar morphology (secondary α) within a β matrix.

Table 14 – Composition of the Ti-64 alloy used in this work.

Element	Ti	Al	V	Fe	O	C	N	H
wt%	Bal.	6.03	4.18	0.24	0.14	0.013	0.011	0.006
[Al]eq		7.4		[Mo]eq		3.4		

Source: CALLEGARI et al. (2020a)

Figure 33 – SE-SEM image of the as-received mill-annealed microstructure of Ti-64 alloy.

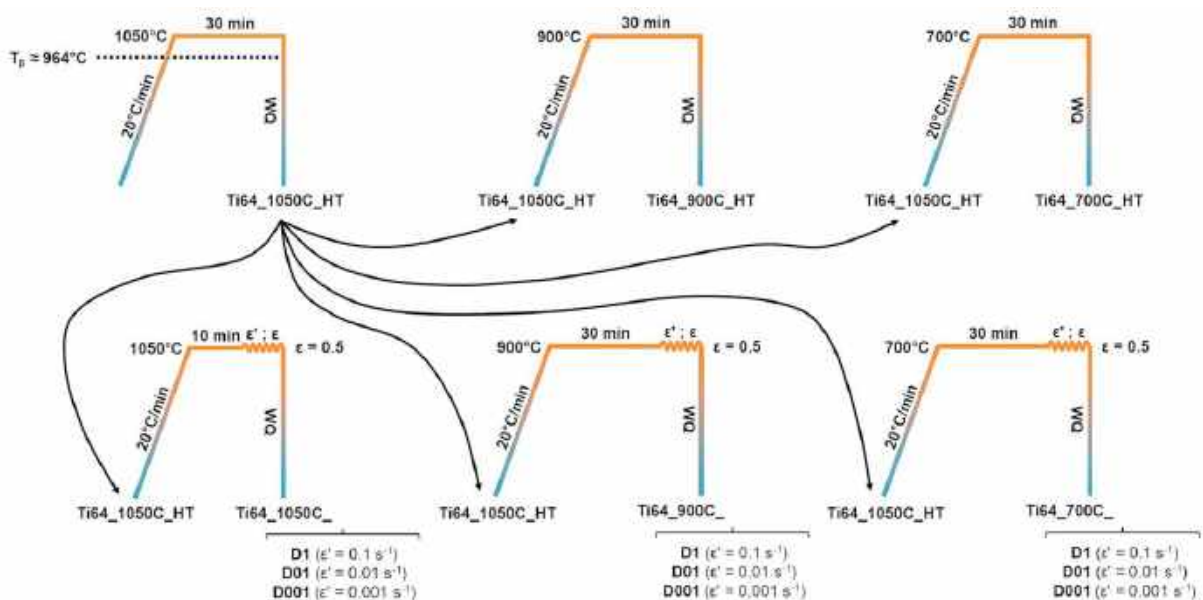
Source: the author.

4.2.2 Thermomechanical treatments

Cylindrical specimens with $\phi 10 \times 15$ mm were longitudinally wire-cut from the as-received billet and underwent an initial homogenization treatment at 1050°C during 30 minutes followed by water quenching in an EDG 10P-S furnace with vacuum and argon atmosphere protection to remove any features resulting from the prior processing of the as-received material. Then homogenized alloy was then uniaxially compressed at 1050°C (β field), 900°C and 700°C ($\alpha+\beta$ field) with strain rates of 10^{-1} , 10^{-2} and 10^{-3} s $^{-1}$ up to a compression ratio of 0.5 (true strain = 0.7). Deformation in the $\alpha+\beta$ field was carried out in a Gleeble® 3800 thermomechanical simulator after heating at 20°C/min to the target temperature and soaking for 30 minutes to induce the formation of lamellar microstructures with different degrees of lamellar coarsening. Compression at 1050°C was applied after a holding time of 10 minutes. Type-S thermocouples were spot-welded to samples in their mid-length for temperature control, and conductive silver-graphite paint was applied between

samples' faces and compression anvils to improve thermal contact and for lubrication purposes. A minimum of three samples were deformed in each condition. The maximum measured diameter of the barreled section after compression was around 16 mm, indicating a true strain of 0.94 in the cross section of specimens. Heat treatments were also carried out at 900°C and 700°C during 30 minutes followed by water quenching to obtain pre-deformation microstructures. The nomenclature was defined based on treatment temperature (“1050C” for 1050°C, “900C” for 900°C and “700C” for 700°C), type (“HT” for heat treatment and “D” for deformation) and strain rate (“1”, “01” and “001” for compressions with strain rates of 0.1, 0.01 and 0.001 s⁻¹, respectively). **Figure 34** provides a schematic framework of the processing routes applied to the alloy.

Figure 34 – Schematic representation of thermomechanical and heat treatments imposed to Ti-64 alloy.



Source: the author.

4.2.3 Microstructural characterization

Metallographic preparation of the alloy for light optical microscopy (LOM) and scanning electron microscopy (SEM) involved manual grinding on #320, #600 and #1200 sandpapers and automatic polishing in a Buehler® EcoMet 250 machine with a 3- μ m diamond suspension and with a 90 vol% colloidal silica + 10 vol% hydrogen peroxide. For LOM, samples were chemically etched with Kroll's etchant (3 vol% hydrofluoric acid + 6 vol% nitric acid + 91 vol% water). LOM images were acquired with a Zeiss® Axio Scope.A1 optical microscope and SEM analyses were carried out in a FEI® Inspect F50 microscope

with field emission gun using secondary (SE) and backscattered electrons (BSE) signal. BSE images were taken from unetched samples. Electron backscatter diffraction (EBSD) analyses were conducted in a FEI® Quanta 650 microscope and in a FEI® Helios NanoLab 600 microscope, both equipped with field emission gun. Step sizes varied from 0.08 μm to 1 μm , depending on the necessary resolution. All images were acquired on a surface parallel to the compression axis. EBSD data were processed using the MTEX toolbox for MATLAB® (BACHMANN; HIELSCHER; SCHAEUBEN, 2010).

4.2.4 Texture analysis

Pole figures of (0002), (10 $\bar{1}$ 0), (10 $\bar{1}$ 1), (10 $\bar{1}$ 2) and (11 $\bar{2}$ 0) reflections of the α phase were measured for macrotexture analysis. From the acquired pole figures, orientation distribution functions (ODFs) were calculated and pole figures were recalculated. All calculations were also done using the MTEX toolbox. Measurements were carried out in a PANalytical® Empyrean X-ray diffractometer with Cu K α radiation ($\lambda = 1.54 \text{ \AA}$), with step size of 5° for both the φ rotation and the ψ tilt. Measurements were done in the center of specimens, on the normal surface to the compression axis, which was polished following the same procedure described in **Section 4.2.3**.

4.2.5 Synchrotron high energy X-ray diffraction

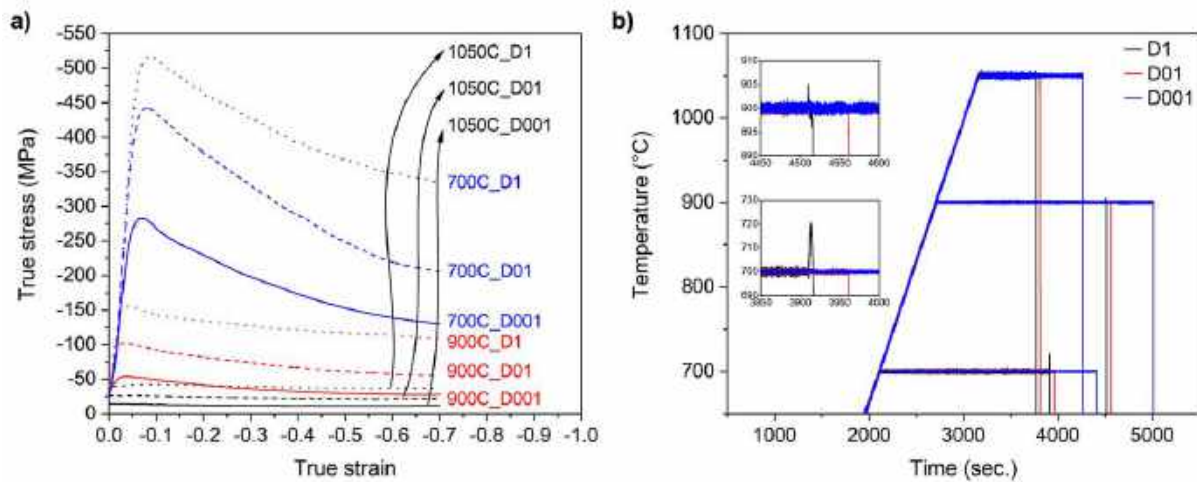
All conditions were analyzed using synchrotron high energy X-ray diffraction. Samples with $3 \times 4 \times 6 \text{ mm}^3$ were wire-cut from heat-treated and deformed specimens, with their length parallel to the compression direction. Analyses were carried out at the P07B beamline of the PETRA III facility at DESY (Hamburg, Germany). The energy of the beam was of 87.1 keV ($\lambda = 0.142 \text{ \AA}$) and experiments were conducted in transmission mode with a spot size of $1 \times 1 \text{ mm}^2$. A standard LaB $_6$ powder was used for calibration. Complete Debye-Scherrer rings were acquired by a 2D Perkin Elmer® fast detector with pixel size of $200 \times 200 \text{ }\mu\text{m}^2$ with an exposure time of 0.1 s and 5 frames per image. The corresponding diffractograms were integrated from the complete rings using ImageJ software and phase fractions were calculated via Rietveld refinement using MAUD software (LUTTEROTTI et al., 1997).

4.3 Results and discussion

4.3.1 Flow curves and adiabatic heating

Figure 35a depicts the flow curves resulting from uniaxial compression of Ti-64. These curves correspond to the average of three curves for each condition. During deformation in the β field, no significant softening is observed, contrarily to the pronounced softening seen during deformation in the $\alpha+\beta$ field. This behavior is in agreement with the one usually observed during deformation of $\alpha+\beta$ titanium alloys, with predominance of dynamic recovery of the β phase under deformation in the single phase field and dynamic softening mechanisms of the α phase under deformation in the dual phase field.

Figure 35 – a) Flow curves of Ti-64 alloy deformed at 1050°C, 900°C and 700°C with strain rates of 0.1, 0.01 and 0.001 s⁻¹; b) temperature reading with insets showing the adiabatic heating during deformation at 700°C and 900°C.



Source: the author.

During deformation at 10^{-2} and 10^{-3} s⁻¹ no adiabatic heating was detected at any of the three temperatures. During deformation at 10^{-1} s⁻¹, adiabatic heating of 20°C was observed with respect to the target temperature of 700°C and 5°C with respect to 900°C, as shown in **Figure 35b**. To verify if the adiabatic heating measured by thermocouples on the surface is representative of the heating experienced by the bulk of the sample, the theoretical temperature variation was calculated using the following equations, where ΔT is the adiabatic heating [K], η is the thermal efficiency, ρ is the density [kg/m³] (for the present alloy, the calculated density is of 4343 kg/m³), C_p is the specific heat [J/kgK], σ is the stress [Pa], ε is the strain, ε' is the strain rate [s⁻¹] and T is the temperature [K] (CHEN et al., 2015):

$$\Delta T = \frac{0.95\eta}{\rho C_p} \int_0^\varepsilon \sigma d\varepsilon \quad (12)$$

$$\eta = \begin{cases} 0, & \varepsilon' \leq 10^{-3} \text{ s}^{-1} \\ 0.316 \log \varepsilon' + 0.95, & 10^{-3} \text{ s}^{-1} < \varepsilon' < 1 \text{ s}^{-1} \\ 0.95, & \varepsilon' \geq 1 \text{ s}^{-1} \end{cases} \quad (13)$$

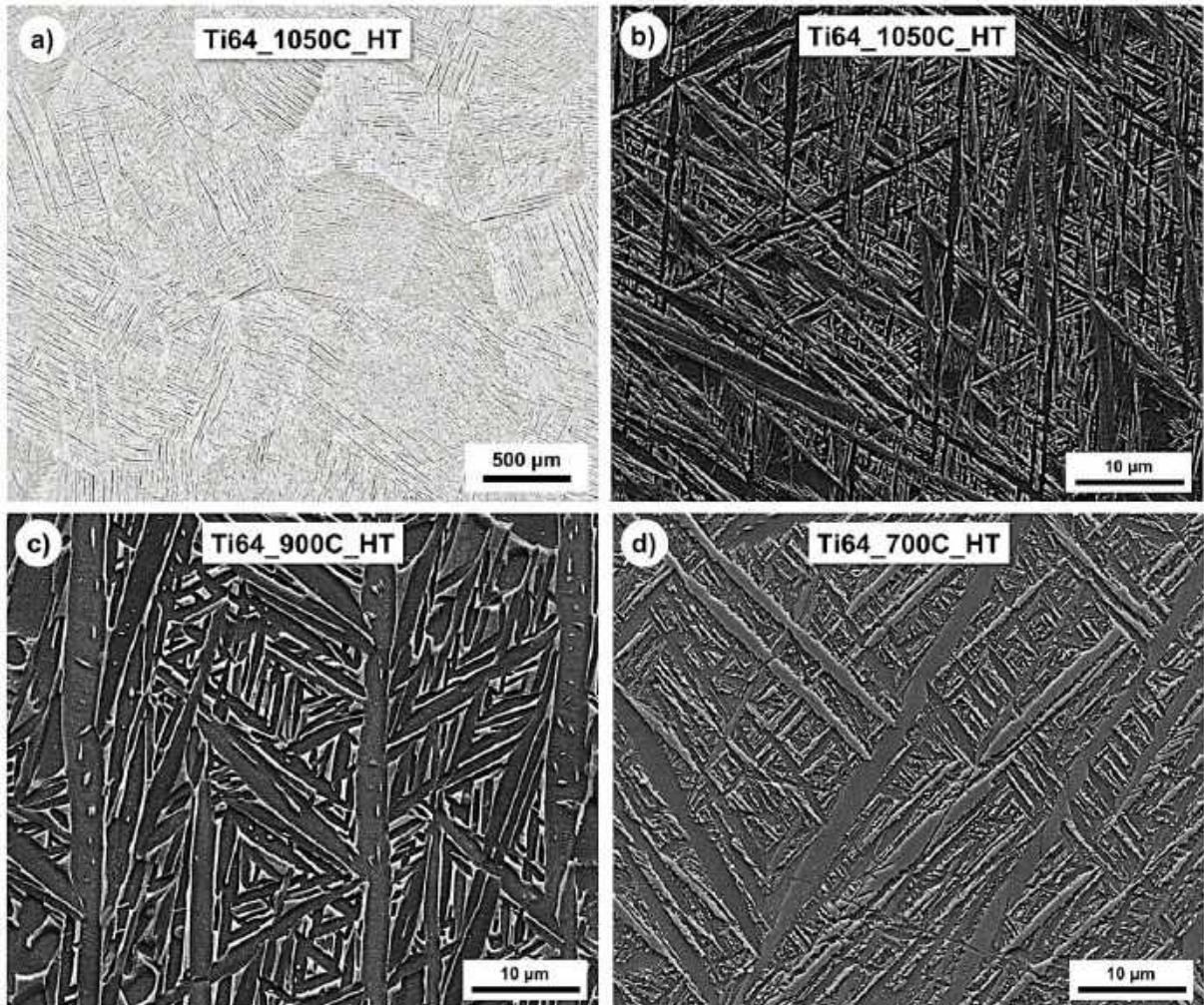
$$C_p = 559.77 - 1.473 \times 10^{-1} T + 4.27949 \times 10^{-4} T^2 \quad (278 \text{ K} < T < 1144 \text{ K}) \quad (14)$$

For the maximum heating observed, i.e. during deformation of the Ti64_700C_D1 condition, the calculated ΔT value was of 22.9 K (22.9°C), only slightly higher than the actual measured variation, 20.6°C. These levels of heating were lower than those previously observed during deformation with the same strain rate and at temperatures equal or close to the ones used in this work. Souza et al. have measured adiabatic heating of ~5-15°C during deformation of Ti-64 alloy at 920°C and 870°C at 0.1 s⁻¹, and ~30°C during deformation at 700°C with the same strain rate (SOUZA et al., 2015). Nonetheless, they have shown that in these levels of strain rate the contribution of adiabatic heating to softening is not significant.

4.3.2 Heat-treated microstructures

After the initial homogenization treatment, the resulting microstructure in Ti64_1050C_HT comprised the martensitic α' phase within equiaxed prior β grains with an average size of $742.3 \pm 175.4 \mu\text{m}$, as determined by the ASTM intercept method (AMERICAN SOCIETY FOR TESTING AND MATERIALS, 2013). In this β -quenched condition, the martensitic lamellae had an average thickness of ~0.8 μm . After heat treatment at 900°C (Ti64_900C_HT), a fully lamellar microstructure was formed with significant lamellar coarsening, reaching a thickness of ~2 μm . The annealing at 700°C (Ti64_700C_HT), in its turn, produced an intermediate microstructure containing both α lamellae and martensitic laths. After both heat treatments in the dual phase field, no significant change in prior β grain size was observed. **Figure 36** depicts these microstructures. In Ti64_900C_HT, it is possible to notice the presence of the β (brighter phase) along α lamellae (darker phase).

Figure 36 – a) LOM image of Ti64_1050C_HT condition, and SE-SEM images of the microstructures of b) Ti64_1050C_HT, c) Ti64_900C_HT and d) Ti64_700C_HT conditions.



Source: the author.

4.3.3 Deformed microstructures

Figure 37a-c shows the microstructures resulting from thermomechanical processing at 1050°C. Prior β grains are elongated, with their length perpendicular to the compression axis, within which martensitic phase resulting from rapid cooling is formed. With the variation of strain rate, it is possible to observe a change in the morphology of prior β grain boundaries. The reduction of strain rate induces the formation of the so-called “necklace” morphology. This reflects the initiation of dynamic recrystallization at grain boundaries, while dynamic recovery predominates in the bulk of β grains (DEHGHANI; KHAMEI, 2010; GUO et al., 2015; WARCHOMICKA et al., 2019; WARCHOMICKA; POLETTI; STOCKINGER, 2011).

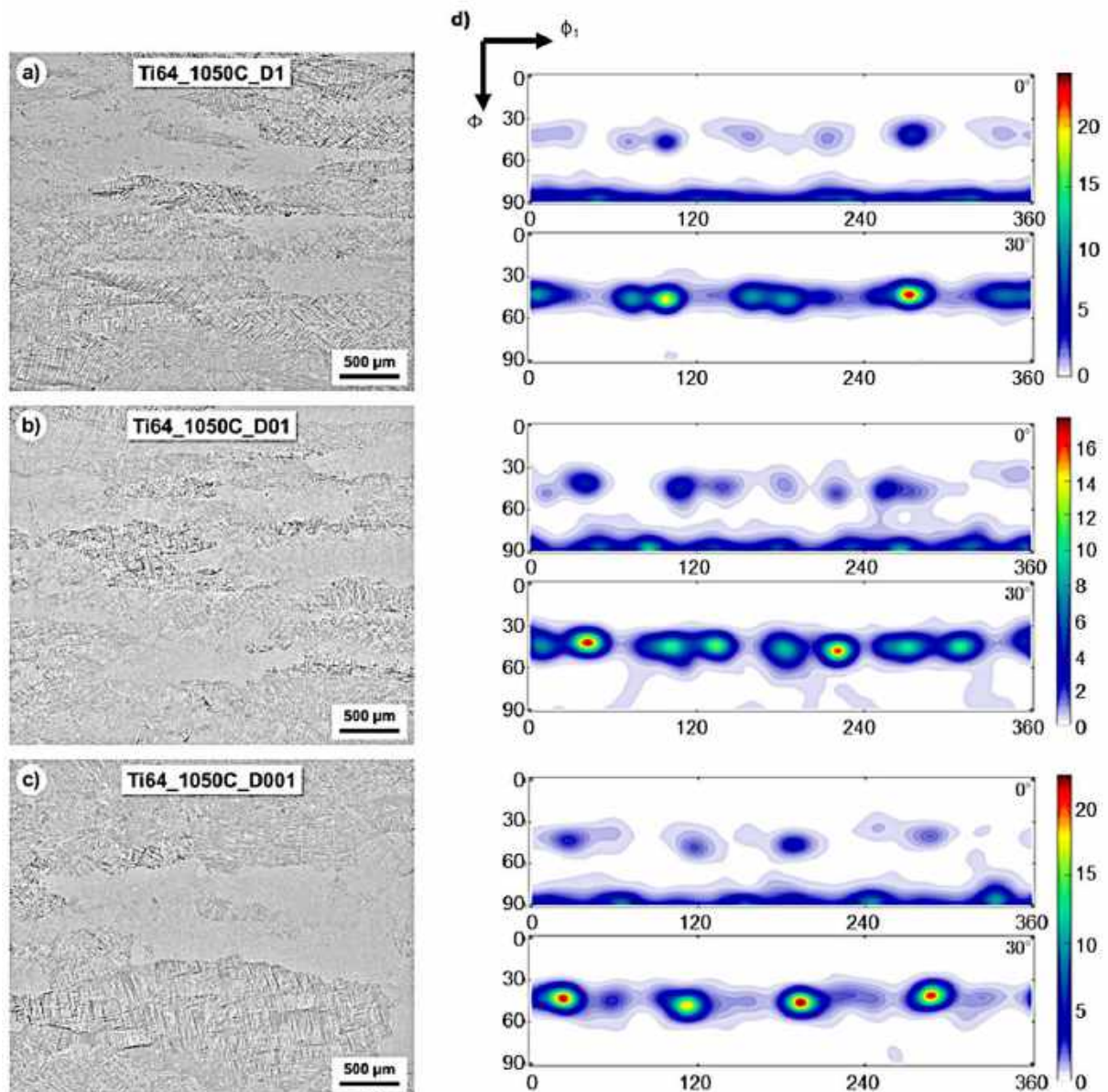
Axisymmetric hot-working methods, such as pancake forging and uniaxial compression, produce rotationally symmetric textures (fiber textures). In these cases, pole figures typically consist of circularly symmetric distributions (LÜTJERING, 1998; SEMIATIN; SEETHARAMAN; WEISS, 1997). **Figure 37d** presents the calculated orientation distribution functions for constant φ_2 sections, namely $\varphi_2 = 0^\circ$ and $\varphi_2 = 30^\circ$. A strong $\{11\bar{2}0\}$ fiber texture is seen ($\Phi = 90^\circ$, $\varphi_2 = 0^\circ$), and the second maximum at $\varphi_2 = 0^\circ$, corresponding to $\Phi \approx 45^\circ$, indicates a $\{10\bar{1}2\}$ fiber texture; at $\varphi_2 = 30^\circ$, a $\{\bar{2}113\}$ fiber texture is seen (DAVIES; GOODWILL; KALLEND, 1971; WANG; HUANG, 2003). No significant difference can be observed between the produced textures during deformation at different rates.

Figure 38 depicts the microstructures resulting from thermomechanical processing at 900°C . After deformation at this temperature, the most remarkable feature is the presence of α phase in two morphologies within the β matrix: coarse lamellar or interconnected grains (primary α) and, mainly in Ti64_900C_D001 (**Figure 38c-d**), extremely refined needles (secondary α or transformed β). No noticeable differences are seen between Ti64_900C_D1 (**Figure 38a**) and Ti64_900C_D01 (**Figure 38b**) conditions. It is also possible to observe some distorted or buckled α lamellae, especially in the microstructure produced at a higher deformation rate (**Figure 38a**). Such buckling of the α phase is not observed in the condition deformed at a lower rate (**Figure 38c**). These microstructures are in agreement with those previously reported after hot compression of Ti-64 alloy with lamellar microstructure at 815 , 900 and 955°C with strain rates of 0.001 , 0.1 , and 10 s^{-1} (SEMIATIN; SEETHARAMAN; WEISS, 1999), between 750 and 1100°C with strain rates ranging from 0.0001 to 10 s^{-1} (SESHACHARYULU et al., 2002) and after open die forging at 900°C (MOTYKA et al., 2018).

Figure 39 presents the microstructures resulting from thermomechanical processing at 700°C . All conditions present a rather homogeneous microstructure composed mainly by equiaxed α grains. However, again, microstructures resulting from deformation with the two highest rates (**Figure 39a** and **Figure 39b**) are more similar and differ from the condition with the slowest deformation rate (**Figure 39c**): in the first, it is possible to observe reminiscent coarse lamellae of the non-recrystallized α phase and a finer equiaxed α grain size, whereas in the latter virtually no α phase with remaining lamellar morphology is seen, and the globular grain size is relatively coarser (see scale bars). Nevertheless, the microstructure in all three cases is remarkably refined. The ideal deformation conditions to achieve a fully refined equiaxed microstructure from a starting martensitic microstructure range between

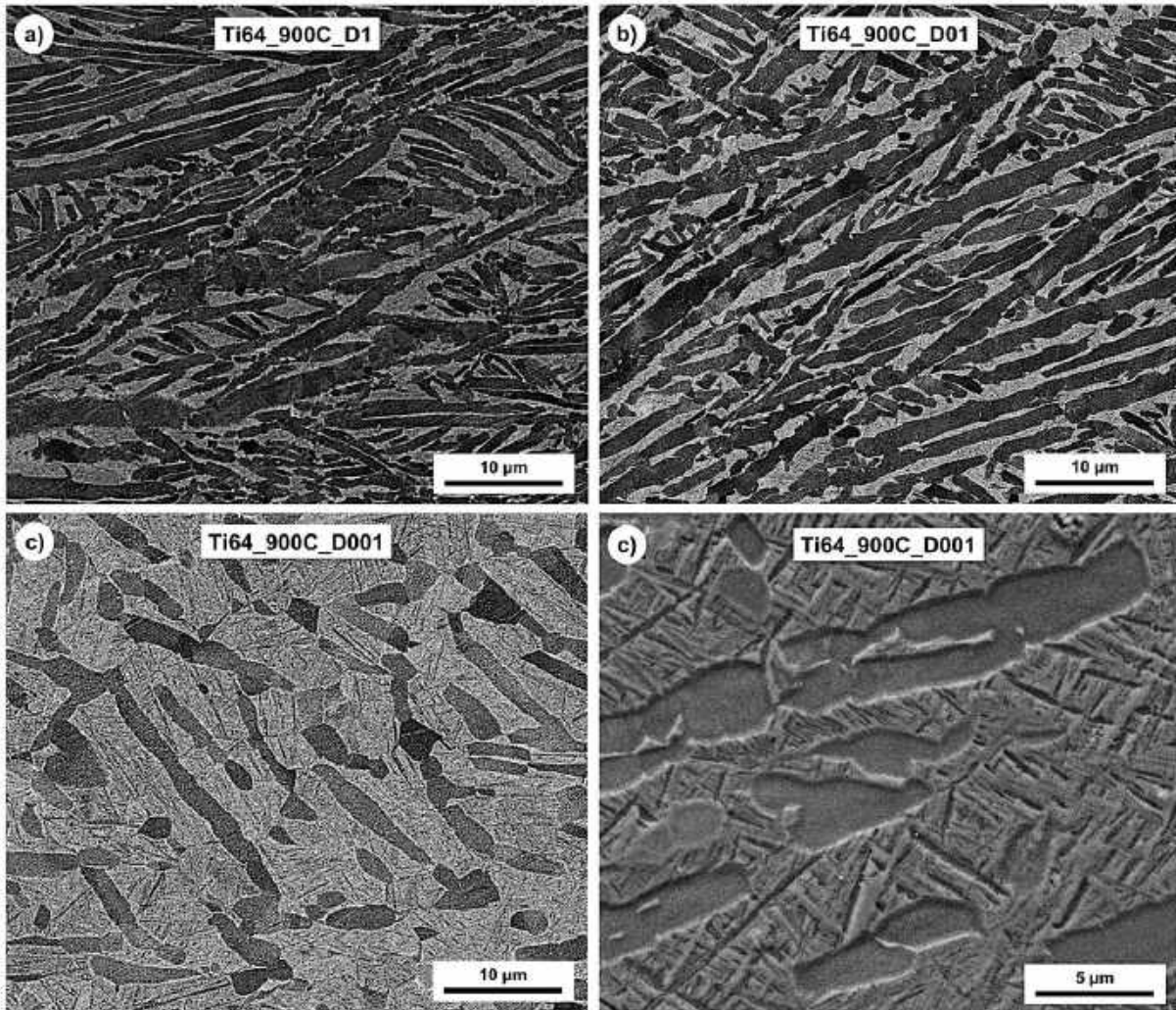
temperatures of 700°C and 800°C with low strain rates such as 0.001 or 0.01 s⁻¹ (CHAO; HODGSON; BELADI, 2014). Higher strain rates (10 s⁻¹) lead to the formation of nanosized equiaxed α (ZHANG et al., 2019), whereas low strain rates significantly facilitate grain growth (MOTYKA et al., 2018; MOTYKA; SIENIAWSKI; ZIAJA, 2014).

Figure 37 – LOM images of a) Ti64_1050C_D1, b) Ti64_1050C_D01 and c) Ti64_1050C_D001, and d) their respective calculated ODFs at $\varphi_2 = 0^\circ$ and $\varphi_2 = 30^\circ$. The compression axis is parallel to the height of images.



Source: the author.

Figure 38 – BSE-SEM images of **a)** Ti64_900C_D1, **b)** Ti64_900C_D01 and **c)** Ti64_900C_D001, and **d)** an SE-SEM image of Ti64_900C_D001 showing in detail the presence of primary α grains and secondary α laths. The compression axis is parallel to the height of images. In BSE images, the darker phase is α and the brighter phase is β .



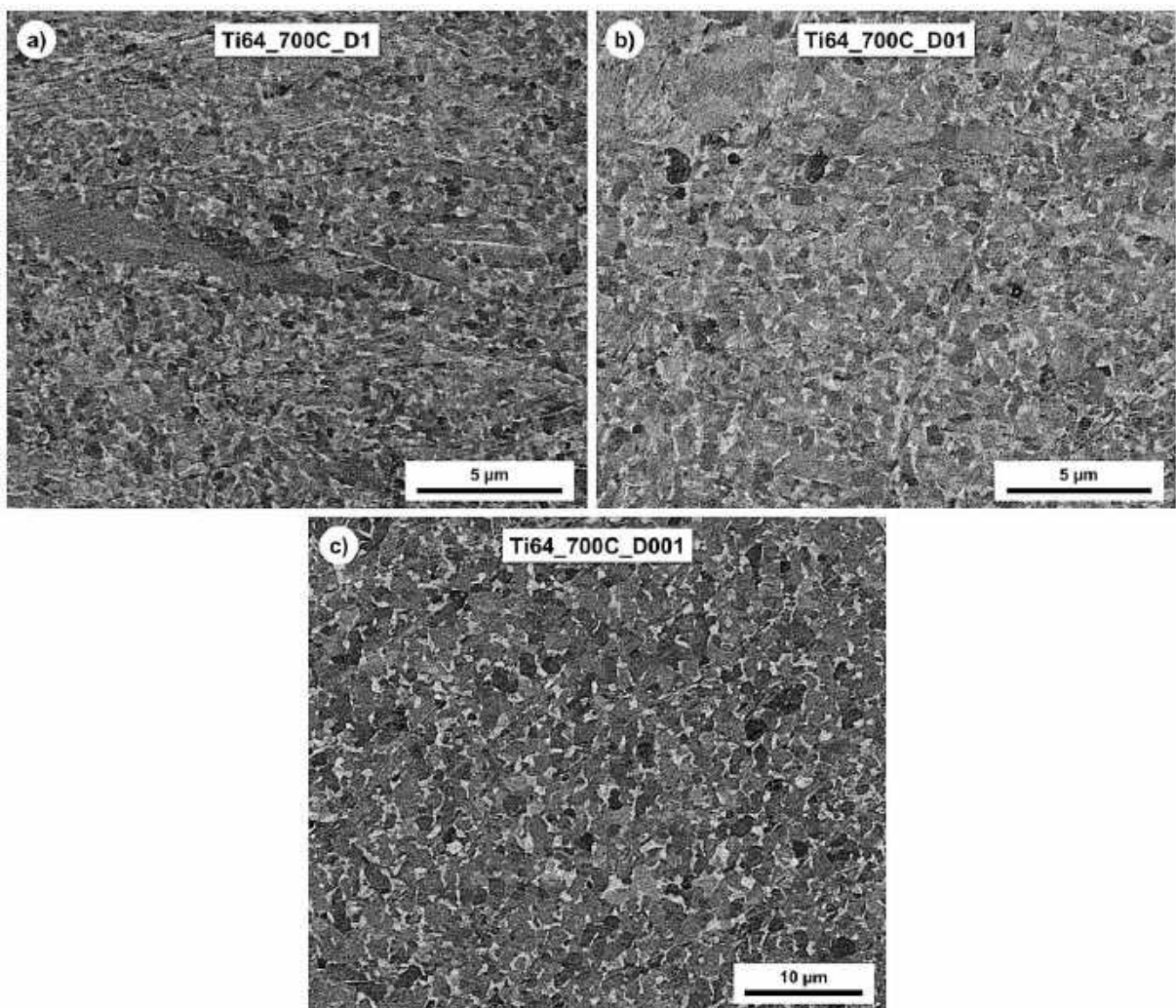
Source: the author.

Chong et al. have divided deformation temperatures of Ti-6Al-4V in two regions (CHONG et al., 2019). In the first region, between 900 and 950°C, lamellar globularization takes place by lamellae sub-division and grain growth, with the size of resulting equiaxed α grains being generally larger than the lamellar thickness before deformation. The present work shows that lamellar coarsening, or grain growth, appears not to be much a result of deformation itself, but rather of the isothermal holding before deformation. In the second region, between 700 and 900°C, dynamic recrystallization has been found to be the main globularization mechanism.

In **Figure 40**, the ODFs of conditions deformed at 900°C and 700°C are shown. The same φ_2 sections as those presented for the alloy after deformation in the β field are presented,

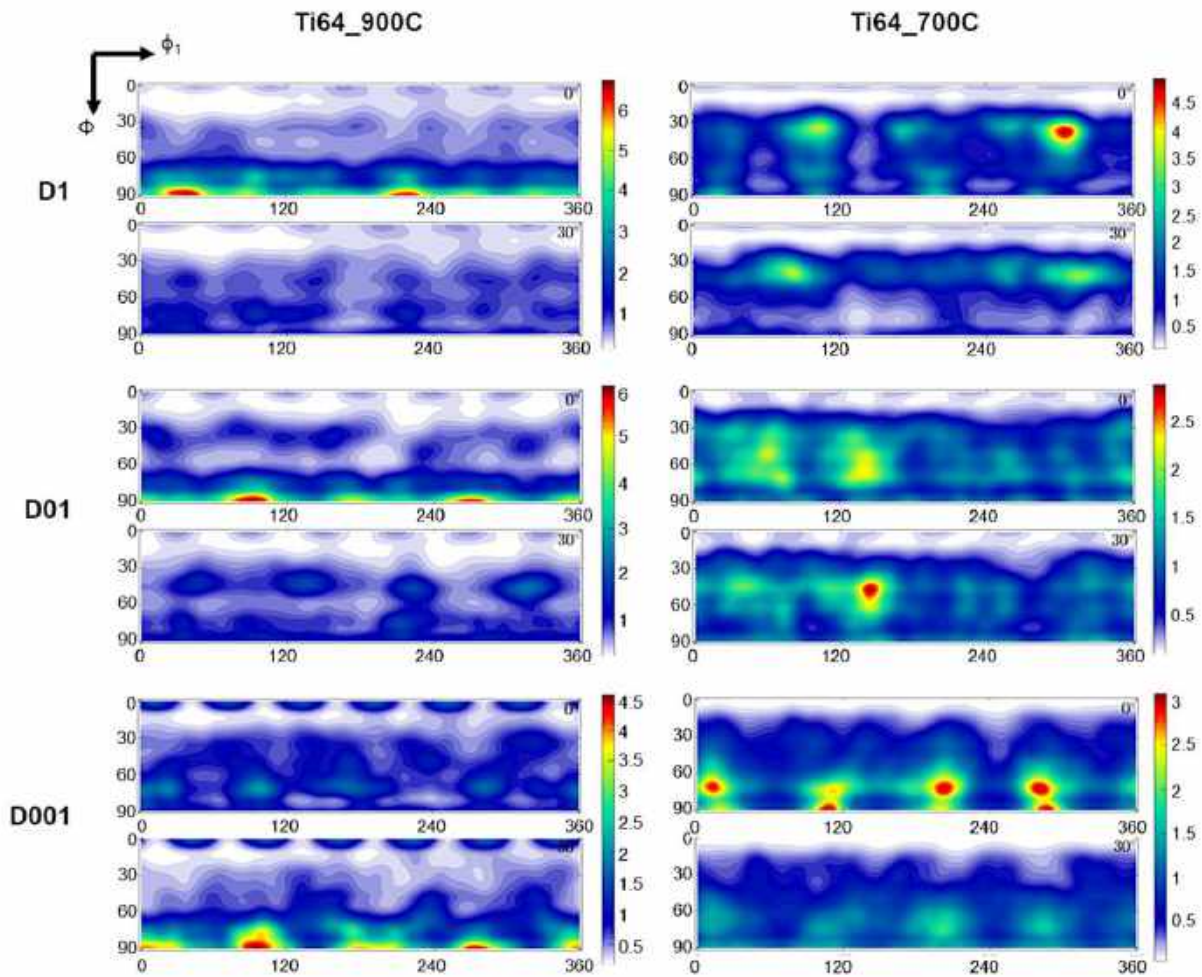
i.e. $\varphi_2 = 0^\circ$ and $\varphi_2 = 30^\circ$. A significant dispersion in orientation distribution can be seen, as opposed to the well-defined distribution seen in **Figure 37**, indicating texture weakening. This implies that recrystallization and globularization induced by thermomechanical processing lead to the weakening of α texture (WU et al., 2019). Such feature can also be denoted by the expressive reduction in the multiples of random intensity (scale bars) of ODFs when compared with those of the martensitic phase after deformation in the β field. Moreover, an additional texture component can be seen in both sections, especially after deformation at 900°C : the $\{0001\}$ basal fiber texture at $\Phi = 0^\circ$ (DAVIES; GOODWILL; KALLEND, 1971; WANG; HUANG, 2003). This component is weaker after deformation at 700°C , being inexistent in Ti64_700C_D001 condition.

Figure 39 – BSE-SEM images of a) Ti64_700C_D1, b) Ti64_700C_D01 and c) Ti64_700C_D001. The compression axis is parallel to the height of images. The darker phase is α and the brighter phase is β .



Source: the author.

Figure 40 – Calculated ODFs of Ti-64 deformed at 900°C and 700°C at $\varphi_2 = 0^\circ$ and $\varphi_2 = 30^\circ$.



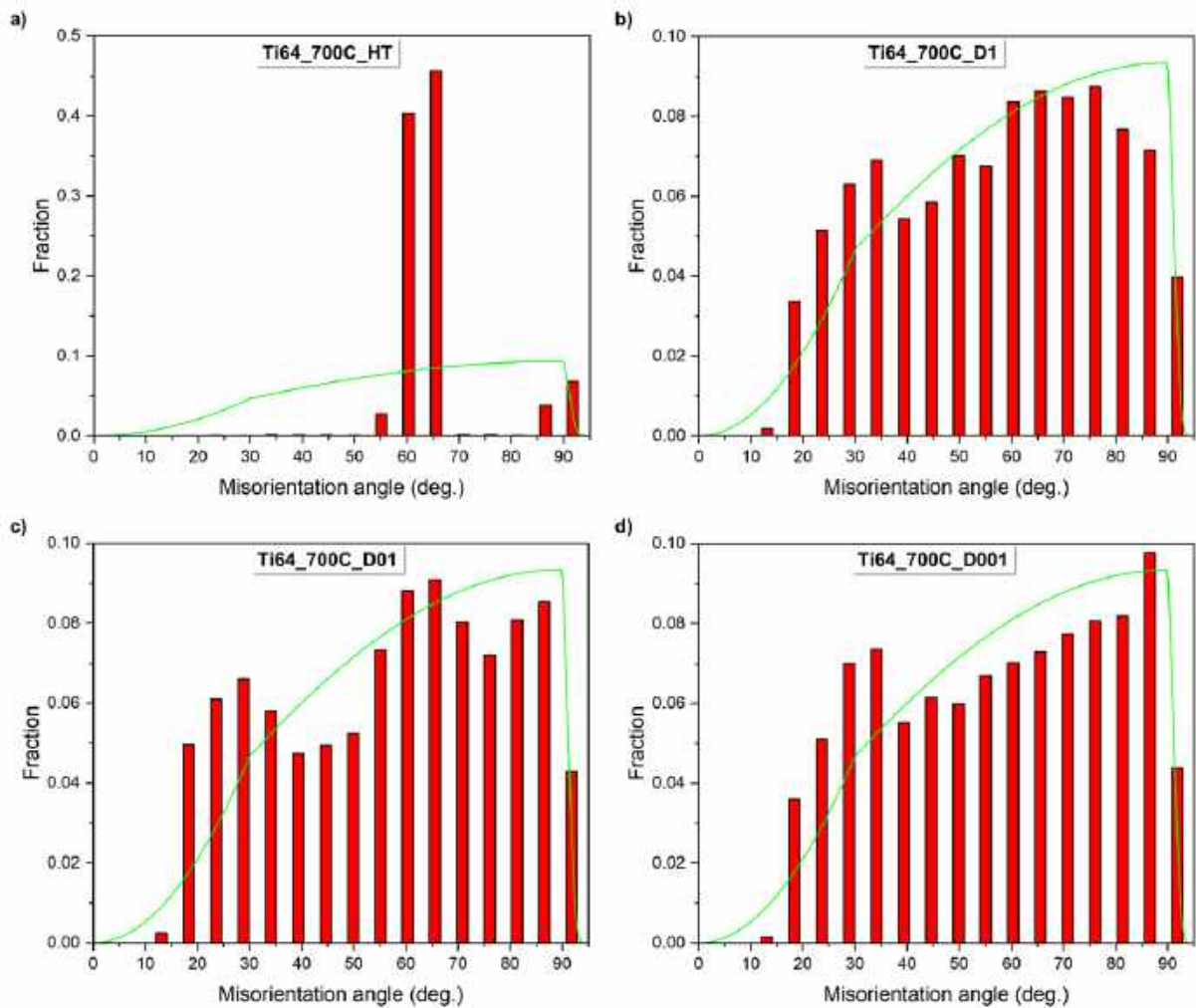
Source: the author.

4.3.4 Crystallographic aspects related to α globularization

Figure 41 depicts the misorientation distribution of the α phase after heat treatment and deformation at 700°C. Obviously, the distribution in Ti64_700C_HT corresponds to that typical of lamellar or martensitic α , which, in its turn, is a consequence of the Burger orientation relationship (BOR) between α and β and its variants (BELADI; CHAO; ROHRER, 2014; WANG; AINDOW; STARINK, 2003). All deformed conditions, on the other hand, present misorientation distributions that approach the random distribution, further indicating that recrystallization and globularization induce texture softening. **Figure 42**, which brings the misorientation axis distribution, shows it also approaches the random distribution: a stronger rotation around the $[\bar{1}2\bar{1}0]_{\alpha}$ axis is seen, but it reduces gradually with the reduction of strain rate. This maximum is associated with the $60^\circ \langle 11\bar{2}0 \rangle$ angle-axis pair variant of α precipitation from the β matrix following the BOR. The weakening of the rotation

around this angle-axis pair during deformation indicate the gradual loss of the BOR with deformation (MIRONOV et al., 2009).

Figure 41 – Misorientation angle distributions of the α phase in **a)** Ti64_700C_HT, **b)** Ti64_700C_D1, **c)** Ti64_700C_D01 and **d)** Ti64_700C_D001. The continuous curves correspond to the Mackenzie (random) distributions.

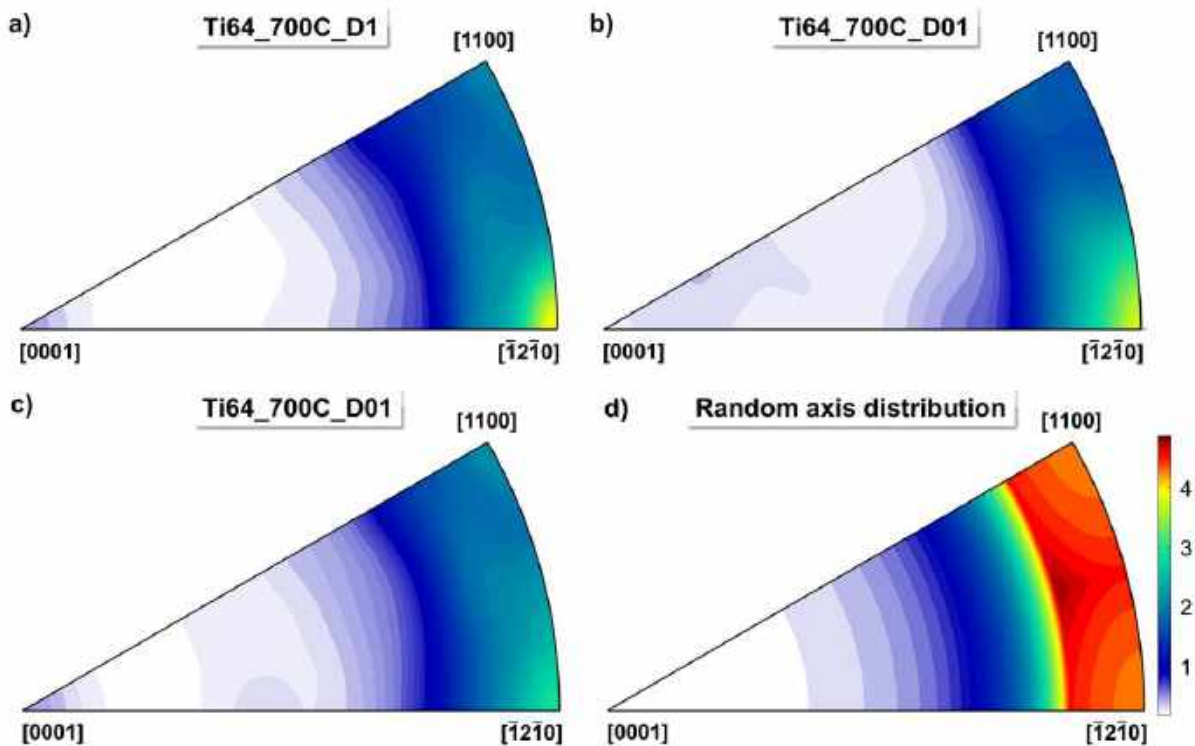


Source: the author.

Figure 43a presents the grain orientation spread (GOS) and **Figure 43b** presents the intragranular misorientation to the mean orientation of Ti64_700C_D1 condition obtained by EBSD. The grain orientation spread is the total standard deviation of crystallographic misorientation inside the grain, defined as its mean orientation. A high GOS value indicates a high degree of deformation inside the grain (MORENO et al., 2019), while a low GOS value indicates a recrystallized state (WANG et al., 2020b). In these images, a large non-recrystallized lamella with a considerably high level of internal misorientation can be seen. The white segments correspond to low-angle boundaries ($< 15^\circ$), and the presence of such

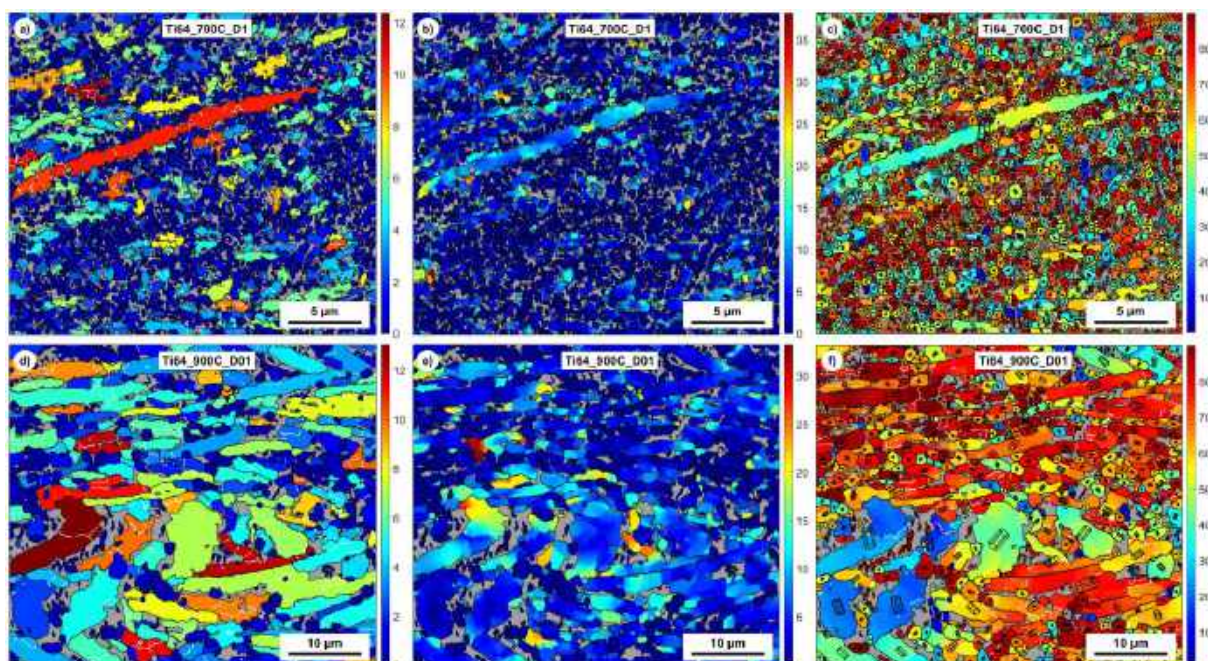
segments corroborates that fine grain formation happens through the formation of low angle boundaries that evolve to high angle boundaries inside platelets. **Figure 43c** presents maps of the c-axis tilt angle with respect to the vertical compression direction, where observation of the long unrecrystallized lamella shows that its c-axis tilt angle varies roughly between 40° and 55° . The correlation of the internal orientation spread of Ti64_700C_D1 with the BOR weakening analyzed in **Figure 41** and **Figure 42** corroborates the hypotheses of Mironov et al. (MIRONOV et al., 2009) that the orientation relationship loss during deformation is associated with the increase of internal stress in deformed lamellae. Such internal stress state, in its turn, results in the formation of recrystallized grains with the continuity of deformation. **Figure 43d** depicts the GOS map and **Figure 43e** shows the internal misorientation of Ti64_900C_D01 condition, where a heavily buckled α lamella is seen with the highest internal orientation spread. Last but not least, **Figure 43f** shows the c-axis tilt angle of this condition, where this highly buckled structure presents itself with a c-axis tilt of $\sim 25^\circ$. In both conditions, maximum GOS values observed were around 12 degrees, and the maximum deviation of the average orientation was as high as $30\text{-}35^\circ$.

Figure 42 – Misorientation axis distributions of the α phase in **a)** Ti64_700C_D1, **b)** Ti64_700C_D01 and **c)** Ti64_700C_D001, and **d)** an ideal random axis distribution. The scale bar in **(g)** applies to all plots.



Source: the author.

Figure 43 – GOS maps, internal misorientation maps and c-axis tilt maps with respect to the y-direction (compression axis), respectively, of **a-c)** Ti64_700C_D1 and **d-f)** Ti64_900C_D01 conditions. Hexagonal lattices are shown in in c-axis tilt maps to aid visualization of the α phase orientation.



Source: the author.

Grain globularization and refinement can take place through the formation of low angle boundaries inside martensitic laths, which gradually evolve into high-angle boundaries. This causes a progressive fragmentation of the microstructure into an ultrafine grained structure. Simultaneously, the supersaturated martensite partially transforms into the β phase, which locates along newly formed grain boundaries. The fact that the globularization tendency of α phase is higher at 700°C than at 900°C. i.e. globularization kinetics is accelerated at a lower temperature, can be attributed to the easier boundary formation and penetration of the β phase into finer platelets than into a coarser lamellar microstructure, which comes as result of lamellar coarsening at higher temperatures in the $\alpha+\beta$ field (KEDIA; BALASUNDAR; RAGHU, 2018). The conversion of the lamellar morphology into fine equiaxed grains can then be regarded as result of the evolution of internal misorientation in α lamellae to high angle misorientation regions that form recrystallized grain boundaries (ZHOU et al., 2019), showing that continuous dynamic recrystallization is the main globularization mechanism in α phase with lamellar morphology in this case. Non-uniform globularization in Ti64_700C_D1 can be associated with the presence of finer and coarser lamellae before deformation (**Figure 36d**), given that, as stated above, globularization

tendency is also guided by how easily the β phase can penetrate into platelets, corroborating that globularization via boundary splitting also takes place.

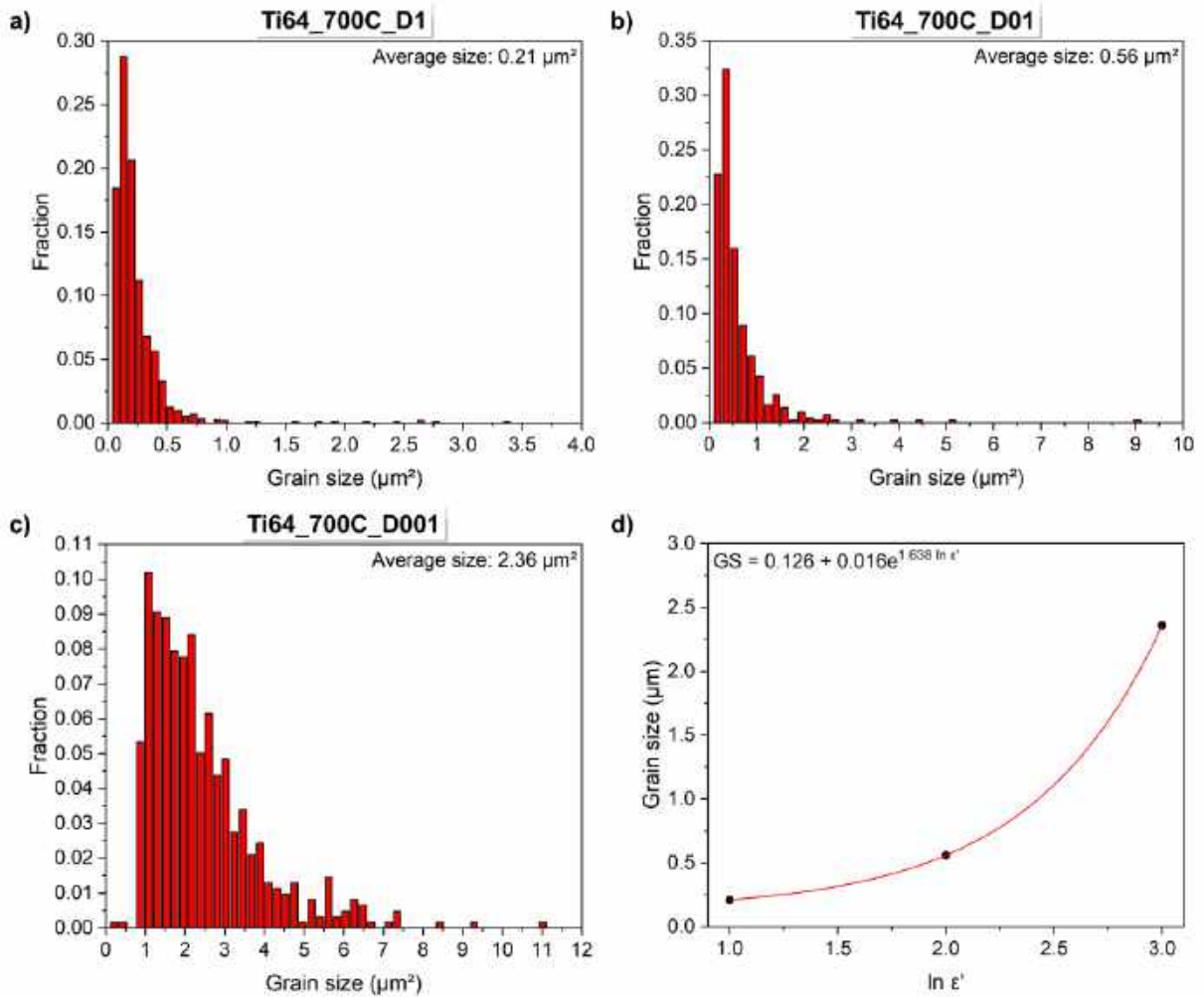
On the other hand, grooves or steps form on the surface of α lamellae either by surface tension or by internal shear localization, which serve to fragment them into nearly equiaxed grains. These kinks also serve as nucleation sites for globularization (SEMIATIN; SEETHARAMAN; WEISS, 1999). In a lamellar microstructure, flow softening is associated to the rotation of lamellae towards softer orientations with low Taylor factors. High Taylor factors are seen in regions where the c-axis is closely aligned with the compression axis, where only $\langle c+a \rangle$ prism slip is possible, and where resistance to breakdown occurs, i.e. Taylor factor is inversely related to globularization efficiency. In these regions, $\langle a \rangle$ prism or basal slip is not possible because the Schmid factor is null (ZHEREBTSOV et al., 2011). Thus, very high deformation loads and shear forces along the slip direction are required. This causes their distortion until the critical force is reached (KEDIA; BALASUNDAR; RAGHU, 2018). Bieler and Semiatin have observed globularization enhancement in a Ti-64 alloy when the c-axis is tilted between 15° and 75° from the compression axis, when both basal and prism slip systems can operate simultaneously (BIELER; SEMIATIN, 2002). One of the mechanisms that control globularization of the lamellar microstructure in the case of inclined lamellae with respect to the compression axis is the formation of substructures (WANG et al., 2020a). Favorable orientations facilitate strain partitioning, causing crystal rotation and increasing the local orientation spread, improving globularization efficiency. Therefore, present results depict the association of globularization with the shearing mechanism cited in **Section 4.1**.

4.3.5 Grain refinement evaluation

Figure 44 presents the grain size distributions in microstructures produced by thermomechanical processing at 700°C , as assessed from EBSD data. Since microstructures were mainly composed by globular grains, the calculation of the weighted average globular grain size, i.e. excluding non-recrystallized grains whose shape were too far from equiaxed, with reminiscent lamellar aspect, was done. For this purpose, a maximum threshold of 1.5 was imposed for the aspect ratio of grains. Thus, grains with an aspect ratio higher than 1.5 were excluded from calculation. In agreement with previous microstructural observations (**Figure 39**), grain sizes in conditions Ti64_700C_D1 and Ti64_700C_D01 are much smaller in comparison with Ti64_700C_D001. Fitting attempts using exponential, quadratic and

power law functions were done, and the exponential fit yielded the highest possible R^2 value, $R^2 = 1$, indicating that grain refinement has an exponential relationship with strain rate within this rate interval, as shown in **Figure 44d**.

Figure 44 – Grain size distribution in a) Ti64_700C_D1, b) Ti64_700C_D01 and c) Ti64_700C_D001 conditions, and d) the corresponding relationship between strain rate ($\dot{\epsilon}$) and grain size (GS).



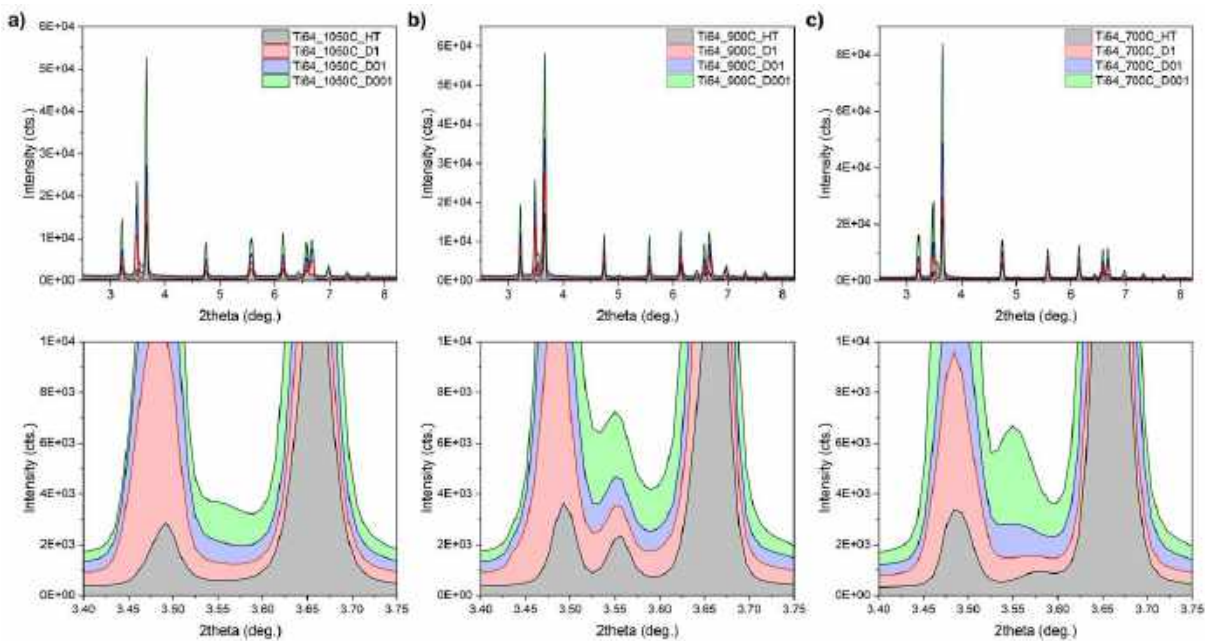
Source: the author.

4.3.6 Dynamic phase evolution

Figure 45 presents the diffractograms yielded from the integration of complete Debye-Scherrer rings. With respect to conditions deformed at 1050°C , reflections of the β phase were seen only after deformation at 10^{-2} and 10^{-3} s^{-1} . In fact, regardless of the deformation temperature, a lower strain rate has yielded a higher amount of β phase, as can be seen in **Figure 46**, that shows phase quantification results via Rietveld refinement (maximum $R_{wp} = 0.1216$). Comparing both temperatures in the dual phase field – 900°C and 700°C –,

conditions deformed at a higher temperature present a higher amount of β , which is expected due to the increase in the stability of this phase with the increase in temperature. In addition, the amount of β also increases with the decrease of strain rate, indicating that slow deformation provides a higher degree of stability to the β phase. On the other hand, the β fraction increase upon lowering of strain rate at 700°C seems to be enhanced with respect to deformation at 900°C, which can be explained by the partial transformation of β into secondary α during quenching after deformation at 900°C, as seen in **Figure 38**.

Figure 45 – Resulting diffractograms of conditions produced during deformation at **a)** 1050°C, **b)** 900°C and **c)** 700°C, with details showing the behavior of (110) β reflection between (0002) α and (10 $\bar{1}$ 1) α .

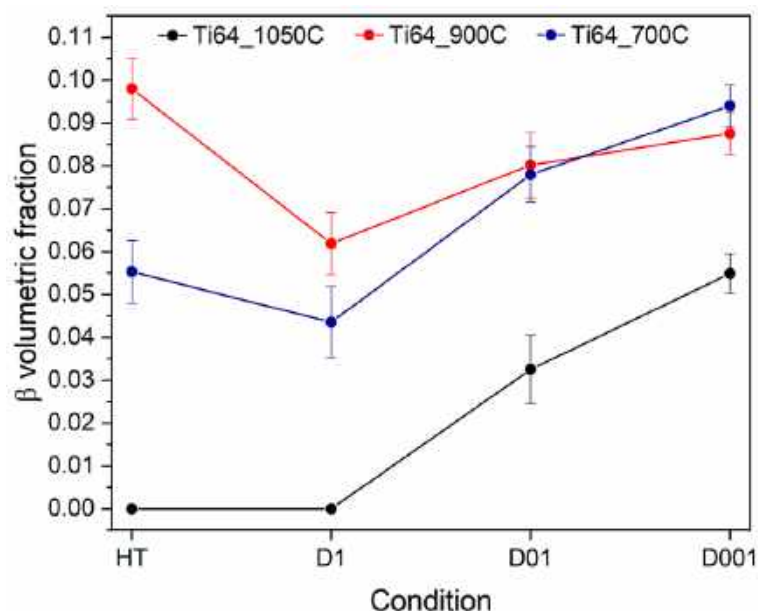


Source: the author.

Such behavior can be explained by the partitioning of vanadium between primary α and β . Deformation can accelerate the depletion of V from the supersaturated α to β or to neighboring V-enriched regions. In the first case, the existing β phase will grow; in the second, new β islands will form. Either way, this effect leads to the increase in the amount of β . This can also explain the $\beta \rightarrow \alpha_s$ transformation upon quenching in conditions deformed at 900°C, given that the stability of β phase decreases with its coarsening due to the consequent lowering of V concentration (SOUZA et al., 2015). Semiatin et al. have recently studied the static and dynamic dissolution of α in Ti-64 – starting from a fully globular microstructure – and have observed that isothermal deformation enhances dissolution by a factor of 8 in comparison with isothermal holding without deformation at a strain rate of 0.1 s⁻¹

(SEMIATIN et al., 2020). However, they found that a holding time of 900 s (15 minutes) was enough to achieve the equilibrium α phase fraction and composition before deformation, so that no significant dissolution took place during deformation. In the present work, phase fractions were significantly impacted by deformation even with the long pre-strain holding time of 30 minutes. Moreover, the tendency of β fraction increase with strain rate decrease is opposite to that observed in an equiaxed Ti-64 alloy (GUO et al., 2018). This can be attributed to the fact that isothermal holding + deformation stages came after an initial quenching from the β field, i.e. the starting microstructure was significantly supersaturated and far from equilibrium.

Figure 46 – Comparison among β phase fractions in the final microstructure of all heat-treated and deformed conditions of Ti-64 alloy.

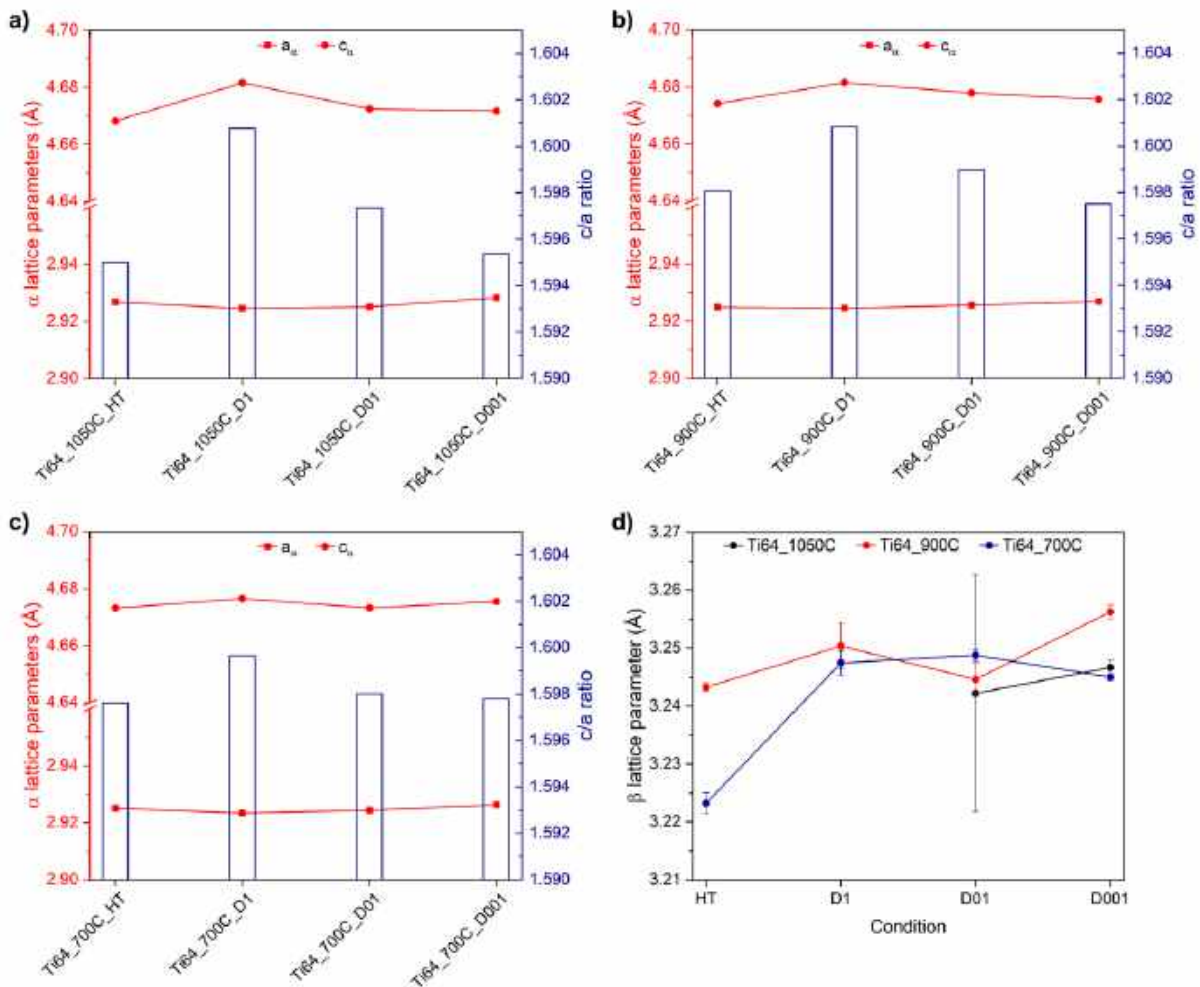


Source: the author.

Figure 47 depicts the lattice parameters of α and β phases after heat treatment and deformation. In all cases, a decrease in the c/a ratio is seen as strain rate decreases. Moreover, the c/a ratio in heat-treated conditions is lower than in deformed conditions. This decrease in c/a ratio translates into an approach to the ideal c/a ratio of Ti (1.5873) and has been previously associated with stress relaxation and texture weakening in Ti-6Al-4V alloy (WU et al., 2019). Interestingly, this trend is seen even in the martensitic phase after deformation in the β field, i.e. the influence of strain rate on the deformation of the single β phase has an influence on the crystallography of the α phase that forms only upon quenching, after deformation. This also is corroborated by the fact that post-deformation secondary α at 900°C

does not alter the lattice parameter behavior of α (**Figure 47b**). As previously stated, the change in prior β grain morphology with the variation of strain rate (**Figure 37**) is indicative of an evolution from pure dynamic recovery to dynamic recovery and recrystallization with the decrease of strain rate. Furthermore, as seen in **Figure 46**, even the amount of retained β phase after quenching from the β field is influenced by strain rate.

Figure 47 – Lattice parameters of the α phase after heat treatment and deformation at **a)** 1050°C, **b)** 900°C and **c)** 700°C; **d)** lattice parameters of the β phase in all conditions of Ti-64 alloy.



Source: the author.

In a work on the morphological control of martensite in a Ti-64 alloy additively manufactured by selective laser sintering, Yang et al. have correlated the decrease of martensitic aspect ratio in an additively manufactured Ti-64 with the decrease of hatch spacing (the distance between two neighboring scans), i.e. a smaller hatch spacing led to the limitation of martensitic growth in length (YANG et al., 2016). Aspect ratio calculation in the MTEX toolbox is carried out by fitting ellipses to the grains; the aspect ratio of a grain is then

defined as the quotient between the longest and shortest axes of the ellipse fitted to this grain. In the present work, a trend of aspect ratio decrease in martensite was observed, although high error values led to no statistical difference, as seen in **Table 15**. However, results suggest the presence of residual β could be associated with the limitation of lath growth by the commencement of β recrystallization.

Table 15 – Average aspect ratio values obtained for Ti-64 alloy deformed at 1050°C.

Condition	Arithmetic average	Geometric average	Harmonic average
Ti64_1050C_D1	7.18 ± 2.50	6.87 ± 1.32	6.63 ± 1.01
Ti64_1050C_D01	6.86 ± 1.84	6.65 ± 1.27	6.49 ± 1.02
Ti64_1050C_D001	6.75 ± 1.67	6.58 ± 1.24	6.44 ± 0.67

Source: the author.

In **Figure 47d**, the behavior of the β phase in terms of its lattice parameter does not show a direct correlation with strain rate. Although element partitioning strongly influences lattice parameter (CHAO; HODGSON; BELADI, 2017), the increase with rapid deformation might also be a result of internal strain of the material. This makes sense considering behavior of the α phase after faster deformation (**Figure 47a-c**). As strain rate decreases and time for diffusion increases, β 's lattice parameter becomes mostly affected by V enrichment. At 900°C, the discrepancy in behavior can be attributed to the secondary α precipitation within β , that might result in both straining of the matrix and V depletion to the matrix. After deformation at 1050°C, the lattice parameter of the residual β is most likely correlated with increased V content that results in enhanced stabilization.

4.4 Conclusions

Heat treatment and thermomechanical processing of a Ti-6Al-4V alloy at 1050°C (β field), 900°C and 700°C ($\alpha+\beta$ phase field) by uniaxial compression with strain rates of 0.1, 0.01 and 0.001 s⁻¹ to a compression ratio of 0.5 have been studied, with focus on the resulting morphological and crystallographic aspects of the α phase and on the dynamic phase evolution. The following conclusions can be drawn from this work:

- Significant texture of the α phase is observed after deformation in the single β phase field, where the quench-induced martensitic phase presents well-defined fiber textures. Deformation in the $\alpha+\beta$ field, on the other hand, leads to texture weakening of the α

phase and loss of the Burgers orientation relationship between α and β upon globularization.

- During deformation, the internal misorientation of lamellae increases leading to the formation of low angle boundaries that should evolve to high angle boundaries of new globularized grains, resulting in high grain orientation spread values and depicting the role of dynamic recrystallization. Non-uniform globularization indicates the occurrence of boundary splitting, and lamellar and lattice tilting evidences the role of shearing to induce globularization during deformation.
- Recrystallized equiaxed grain size presents an exponential increase with the increase of strain rate, at least within the studied strain rate range: $10^{-1} - 10^{-3} \text{ s}^{-1}$.
- Slow deformation is more effective to stabilize the β phase in the $\alpha+\beta$ field, leading to a β volume fraction increase. However, too high an amount of this phase has been shown to promote its destabilization upon quenching, which results in its transformation into secondary α during cooling. Reduction of strain rate also contributes to the approach of the c/a ratio of the α phase to the ideal ratio of titanium.
- In the β field, the reduction of strain rate also has an influence on the morphology and lattice martensitic lattice and on the stabilization of the retained β phase upon quenching, most likely due to the occurrence of dynamic recrystallization together with dynamic recovery in this phase during slow deformation.

5 AGING TREATMENTS OF Ti-6Al-4V ALLOY

Conditions of interest of Ti-64 alloy were selected from those tailored in **Chapter 4** and then submitted to aging treatments to evaluate the response of these selected microstructures to the isothermal treatment. Characterization techniques used include synchrotron X-ray diffraction, both in situ and ex situ, scanning-transmission electron microscopy and Vickers hardness testing. Results are presented in the published paper in **Annex A**. The inclusion of the published journal article in full in this thesis is supported by the sharing policies of Elsevier, which states that theses and dissertations with embedded subscription PJAs can be posted publicly by the awarding institution, as long as DOI links to the formal publications on ScienceDirect are included (“Journals article sharing”, [s.d.]). These links are present in the reference list at the end of the thesis.

6 THERMOMECHANICAL PROCESSING OF Ti-5Al-5Mo-5V-3Cr ALLOY

The work focused on the analysis of microstructures of Ti-5553 alloy produced by thermomechanical simulation via uniaxial compression is presented in the published paper in **Annex B**. Microstructural evolution in terms of substructure and texture formation, and distribution and decomposition of the α phase, was evaluated by scanning electron microscopy, electron backscatter diffraction, X-ray diffraction and synchrotron X-ray diffraction. The inclusion of the published journal article in full in this thesis is supported by the sharing policies of Elsevier, which states that theses and dissertations with embedded subscription PJAs can be posted publicly by the awarding institution, as long as DOI links to the formal publications on ScienceDirect are included (“Journals article sharing”, [s.d.]). These links are present in the reference list at the end of the thesis.

7 AGING TREATMENTS OF Ti-5Al-5Mo-5V-3Cr ALLOY

Conditions of interest of Ti-5553 alloy were selected from those tailored in **Chapter 6** and then submitted to aging treatments to evaluate the response of these selected microstructures to the isothermal treatment. Characterization techniques used include in situ synchrotron X-ray diffraction, scanning electron microscopy, transmission electron microscopy and Vickers hardness testing. Results are presented in the published paper in **Annex C**. The inclusion of the published journal article in full in this thesis is supported by the sharing policies of Elsevier, which states that theses and dissertations with embedded subscription PJAs can be posted publicly by the awarding institution, as long as DOI links to the formal publications on ScienceDirect are included (“Journals article sharing”, [s.d.]). These links are present in the reference list at the end of the thesis.

8 GENERAL CONCLUSIONS

In this thesis, the effect of different microstructural features – deformation-induced defects such as dislocations and low angle grain boundaries, α/β volume fractions, morphology, distribution and chemical composition of the α phase – on the response of a β -metastable titanium alloy, Ti-5Al-5Mo-5V-3Cr (Ti-5553), and of an $\alpha+\beta$ titanium alloy, Ti-6Al-4V (Ti-64), was evaluated. These features were introduced by different routes of heat treatment and thermomechanical processing via uniaxial compression.

The processing of Ti-64 has corroborated the versatility of the alloy in terms of microstructures that can be achieved depending on the applied route. Microstructures ranging from fully martensitic to fully globular, including lamellar and bimodal ones, were produced. Deformed lamellae of the α phase presented a high degree of internal misorientation preceding the formation of a fully globular morphology, and the final α/β fraction ratio was strongly dependent on the temperature of treatment and strain rate. These factors directly influence the stability of the retained β phase. Nonetheless, it was not possible to carry out heat treatments and uniaxial compression using in situ X-ray diffraction, to allow for a better understanding of mechanisms and kinetics of the dynamic $\alpha \leftrightarrow \beta$ transformation, and of how globularization leads to texture weakening. Globularization also leads to texture weakening.

The final composition and morphology of phases have a strong influence on the response of the alloy to subsequent aging treatments. The chemical composition of the α phase, more specifically its aluminum content, determines the possibility of Ti_3Al (α_2) precipitation, being the globular morphologies more enriched in Al than lamellar and martensitic ones, and ergo more prone to form α_2 . Aiming to achieve a thermodynamically stable state, all conditions showed a significant decomposition of the retained β phase, whose distribution directed its decomposition into the already existing primary α phase or into a newly formed refined secondary α . Moreover, in all predominantly martensitic conditions, the metastable martensite converts into the stable α phase. Overall, β decomposition and Ti_3Al precipitation provided more efficient strengthening than martensite decomposition. However, it was not possible to obtain quality dark field images of precipitates to observe their distribution. Therefore, the evaluation of the effect of dislocations and low angle boundaries on the distribution of particles was not possible. In addition, given the long aging time needed to precipitate α_2 , it is not possible to track such precipitation using in situ XRD. Thus, thermodynamic simulations using adequate databases should be useful to assess the kinetics of Ti_3Al formation in the alloy.

Ti-5553 alloy, on the other hand, undergoes mainly dynamic recovery during deformation, in the $\alpha+\beta$ phase field inclusive, due to the extremely high amount of β phase in the alloy. Deformation in the dual phase field lead to α decomposition and globularization, and the impact of strain rate on the final grain size and distribution of the phase was evidenced. Again, the in situ tracking of heat treatments and deformation to better understand the decomposition of the α phase was not possible. Upon subsequent aging, the amount of primary α phase had a remarkable impact on the isothermal precipitation, given its influence on the composition of the β phase, from which isothermal ω and α'' precipitate during this treatment. The aging temperature has shown itself not to be enough to allow the precipitation of the stable α phase, i.e. the $\alpha'' \rightarrow \alpha$ transformation is quite sluggish at this temperature. For this reason, the employed aging treatment is not adequate as a final aging step, but rather as a first step treatment in a duplex aging route, being the final step carried out at a higher temperature to promote the full precipitation of α . This must be evaluated with a more adequate experimental setup, i.e. higher vacuum levels and/or higher beam energy to enable the conduction of in situ XRD experiments in transmission mode, to minimize the effect of oxidation on the probed volume. On the other hand, a precise quantification of α'' and α amounts was difficult, given the superimposition of their X-ray diffraction reflections. Moreover, considerable high final hardness values suggest that a significant amount of α takes place, although α'' decomposition is not complete. The role of defects also appears to play a role in this transformation, given that α'' decomposition in the condition deformed in the β field was slower than that in the condition heat treated in the β field. Higher amounts of primary α suppressed the formation of isothermal ω and α'' and led to the precipitation of a coarser secondary α phase, resulting in limited hardening with respect to conditions with no or lower primary α content. Again, this needs to be further explored by TEM analyses.

9 SUGGESTIONS FOR FUTURE WORKS

1. In situ study of the microstructural evolution of Ti-5553 and Ti-64 alloy during heat treatments and thermomechanical processing in the β and $\alpha+\beta$ fields, to track texture evolution, recovery, recrystallization and dynamic phase evolution.
2. Assessment of the influence of heating rate and aging temperature on the phase transformation pathways of Ti-5553 alloy, given that these parameters influence the precipitation of metastable phases (ω and α'').
3. TEM study of the effect of microstructure on the stabilization of α'' phase in Ti-5553 alloy to enable a precise explanation of the difference between α'' decomposition rate in heat-treated and deformed conditions.
4. TEM study of the effect of microstructure on the distribution of Ti_3Al precipitates in the α phase in Ti-64 alloy, to understand if dislocations and low angle boundaries act as preferential nucleation sites.
5. Evaluation of the influence of aging treatments on the mechanical properties of heat-treated and thermomechanically processed Ti-5553 and Ti-64 alloys by tensile testing in miniature samples to give a better insight on the influence of aging treatments on the mechanical properties of the alloy, given that in the present work only a simplified evaluation based on micro-hardness values was done.
6. Thermodynamic simulations of phase and compositional evolution, including isothermal precipitation kinetics simulations, using a commercial version of ThermoCalc® software and an appropriate titanium database, for validation of experimental data.

REFERENCES

- AEBY-GAUTIER, E. et al. Microstructural formation in Ti alloys: In-situ characterization of phase transformation kinetics. **JOM**, v. 59, n. 1, p. 54–58, 2007.
- AEBY-GAUTIER, E. et al. Isothermal α'' formation in β metastable titanium alloys. **Journal of Alloys and Compounds**, v. 577, n. SUPPL. 1, p. S439–S443, 2013.
- AFONSO, C. R. M. et al. High resolution transmission electron microscopy study of the hardening mechanism through phase separation in a β -Ti-35Nb-7Zr-5Ta alloy for implant applications. **Acta Biomaterialia**, v. 6, n. 4, p. 1625–1629, 2010.
- AMERICAN SOCIETY FOR TESTING AND MATERIALS. ASTM E112-13: Standard test methods for determining average grain size. In: **Annual Book of ASTM Standards**. [s.l.] ASTM International, 2013. p. 28.
- AMERICAN SOCIETY FOR TESTING AND MATERIALS. ASTM B348/B348M-19: Standard specification for titanium and titanium alloy bars and billets. In: **Annual Book of ASTM Standards**. [s.l.: s.n.]. p. 9.
- ATTALLAH, M. M. et al. Comparative determination of the α/β phase fraction in $\alpha+\beta$ -titanium alloys using X-ray diffraction and electron microscopy. **Materials Characterization**, v. 60, n. 11, p. 1248–1256, 2009.
- BACHMANN, F.; HIELSCHER, R.; SCHAEBEN, H. Texture analysis with MTEX - Free and open source software toolbox. **Solid State Phenomena**, v. 160, p. 63–68, 2010.
- BANERJEE, S.; MUKHOPADHYAY, P. **Phase transformations: examples from titanium and zirconium alloys**. [s.l.] Elsevier, 2007.
- BANERJEE, S.; TEWARI, R.; DEY, G. K. Omega phase transformation - Morphologies and mechanisms. **International Journal of Materials Research**, v. 97, n. 7, p. 963–977, 2006.
- BANIA, P. J. Beta titanium alloys and their role in the titanium industry. **JOM**, v. 46, n. 7, p. 16–19, 1994.
- BANUMATHY, S.; GHOSAL, P.; SINGH, A. K. On the structure of the Ti₃Al phase in Ti-Al and Ti-Al-Nb alloys. **Journal of Alloys and Compounds**, v. 394, n. 1–2, p. 181–185, 2005.
- BARRIOBERO-VILA, P. et al. Phase transformation kinetics during continuous heating of a β -quenched Ti-10V-2Fe-3Al alloy. **Journal of Materials Science**, v. 50, n. 3, p. 1412–1426, 2014.
- BARRIOBERO-VILA, P. et al. Influence of phase transformation kinetics on the formation of α in a β -quenched Ti-5Al-5Mo-5V-3Cr-1Zr alloy. **Acta Materialia**, v. 95, p. 90–101,

2015a.

BARRIOBERO-VILA, P. et al. Role of element partitioning on the α - β phase transformation kinetics of a bi-modal Ti-6Al-6V-2Sn alloy during continuous heating. **Journal of Alloys and Compounds**, v. 626, p. 330–339, 2015b.

BARRIOBERO-VILA, P. et al. Inducing stable $\alpha + \beta$ microstructures during selective laser melting of Ti-6Al-4V using intensified intrinsic heat treatments. **Materials**, v. 10, n. 268, p. 1–14, 2017.

BELADI, H.; CHAO, Q.; ROHRER, G. S. Variant selection and intervariant crystallographic planes distribution in martensite in a Ti-6Al-4V alloy. **Acta Materialia**, v. 80, p. 478–489, 2014.

BIELER, T. R.; SEMIATIN, S. L. The origins of heterogeneous deformation during primary hot working of Ti-6Al-4V. **International Journal of Plasticity**, v. 18, n. 9, p. 1165–1189, 2002.

BLACKBURN, M. J.; WILLIAMS, J. C. Phase transformations in Ti-Mo and Ti-V alloys. **Transactions of the Metallurgical Society of AIME**, v. 242, p. 2461–2469, 1968.

BÖNISCH, M. et al. Composition-dependent magnitude of atomic shuffles in Ti-Nb martensites. **Journal of Applied Crystallography**, v. 47, n. 4, p. 1374–1379, 2014.

BOYER, R.; ELSCH, G.; COLLINS, E. W. **Materials property handbook: titanium alloys**. [s.l.] ASM International, 1994.

BOYER, R. R. Attributes, characteristics, and applications of titanium and its alloys. **JOM**, v. 62, n. 5, p. 21–24, 2010.

BOYER, R. R.; BRIGGS, R. D. The use of β titanium alloys in the aerospace industry. **Journal of Materials Engineering and Performance**, v. 14, n. 6, p. 680–684, 2005.

BRAMMER, W. G.; RHODES, C. G. Determination of omega phase morphology in Ti-35% Nb by transmission electron microscopy. **Philosophical Magazine**, v. 16, n. 141, p. 477–486, 1967.

BRITTON, T. B. et al. Tutorial: Crystal orientations and EBSD - Or which way is up? **Materials Characterization**, v. 117, p. 113–126, 2016.

BRUNESEAU, F. et al. In situ characterizations of phase transformations kinetics in the Ti17 titanium alloy by electrical resistivity and high temperature synchrotron X-ray diffraction. **Materials Science and Engineering A**, v. 476, n. 1–2, p. 60–68, 2008.

CAGLIOTI, G.; PAOLETTI, A.; RICCI, F. P. Choice of collimators for a crystal spectrometer for neutron diffraction. **Nuclear Instruments**, v. 3, p. 223–228, 1958.

CALLEGARI, B. et al. In-situ synchrotron radiation study of the aging response of Ti-6Al-4V

alloy with different starting microstructures. **Materials Characterization**, v. 165, p. 110400, 2020a.

CALLEGARI, B. et al. New insights into the microstructural evolution of Ti-5Al-5Mo-5V-3Cr alloy during hot working. **Materials Characterization**, v. 162, n. February, p. 110180, 2020b.

CALLEGARI, B. et al. In situ evaluation of the low-temperature aging response of Ti-5Al-5Mo-5V-3Cr alloy as influenced by starting microstructure. **Journal of Alloys and Compounds**, v. 835, p. 155331, 2020c.

CHAO, Q.; HODGSON, P. D.; BELADI, H. Ultrafine grain formation in a Ti-6Al-4V alloy by thermomechanical processing of a martensitic microstructure. **Metallurgical and Materials Transactions A**, v. 45, n. 5, p. 2659–2671, 2014.

CHAO, Q.; HODGSON, P. D.; BELADI, H. Thermal stability of an ultrafine grained Ti-6Al-4V alloy during post-deformation annealing. **Materials Science & Engineering A**, v. 694, n. March, p. 13–23, 2017.

CHEN, F. et al. Exploring the phase transformation in β -quenched Ti-55531 alloy during continuous heating via dilatometric measurement, microstructure characterization, and diffusion analysis. **Metallurgical and Materials Transactions A**, v. 47, n. 11, p. 5383–5394, 2016.

CHEN, F. et al. Isothermal kinetics of $\beta \leftrightarrow \alpha$ transformation in Ti-55531 alloy influenced by phase composition and microstructure. **Materials & Design**, v. 130, n. January, p. 302–316, 2017.

CHEN, G. et al. Temperature dependent work hardening in Ti-6Al-4V alloy over large temperature and strain rate ranges: Experiments and constitutive modeling. **Materials & Design**, v. 83, p. 598–610, 2015.

CHONG, Y. et al. Investigation on the hot deformation behaviors and globularization mechanisms of lamellar Ti-6Al-4V alloy within a wide range of deformation temperatures. **Materialia**, v. 8, n. July, p. 100480, 2019.

COAKLEY, J. et al. Precipitation processes in the Beta-Titanium alloy Ti-5Al-5Mo-5V-3Cr. **Journal of Alloys and Compounds**, v. 646, p. 946–953, 2015.

CONTREPOIS, Q.; CARTON, M.; LECOMTE-BECKERS, J. Characterization of the β phase decomposition in Ti-5Al-5Mo-5V-3Cr at slow heating rates. **Open Journal of Metal**, v. 1, n. 1, p. 1–11, 2011.

Conventional Thermomechanical Simulator – Gleeble® 3800. Disponível em: <<https://Innano.cnpem.br/laboratories/cpm/facilities/gleeble/>>. Acesso em: 13 set. 2020.

- COTTON, J. D. et al. State of the art in beta titanium alloys for airframe applications. **JOM**, v. 67, n. 6, p. 1281–1303, 2015.
- CROUTZEILLES, M.; MIRAND, P.; SAULNIER, A. Elektronenmikroskopische Untersuchungen und direkte Elektronendurchstrahlung der ω -Phase von Ti-Legierungen. **Comptes Rendus de l'Académie des Sciences**, v. 253, n. 2685–2687, 1961.
- DAVIES, G. J.; GOODWILL, D. J.; KALLEND, J. S. Charts for analysing crystallite orientation distribution function plots for hexagonal materials. **Journal of Applied Crystallography**, v. 4, p. 193–196, 1971.
- DEHGHANI, K.; KHAMEI, A. A. Hot deformation behavior of 60Nitinol (Ni60 wt%-Ti40 wt%) alloy: Experimental and computational studies. **Materials Science and Engineering A**, v. 527, n. 3, p. 684–690, 2010.
- DONACHIE JR., M. J. **Titanium: a technical guide**. 2nd. ed. [s.l.] ASM International, 2000.
- DUERIG, T. W.; TERLINDE, G. T.; WILLIAMS, J. C. **The ω -phase reaction in titanium alloy**. Titanium '80 Science & Technology - Proceedings of the 4th International Conference on Titanium. **Anais...**1980
- DURET, N. **Titanium for damage tolerance applications on A380**. Proceedings of the 10th World Conference on Titanium. **Anais...**2003
- ELMER, J. W. et al. Phase transformation dynamics during welding of Ti-6Al-4V. **Journal of Applied Physics**, v. 95, n. 12, p. 8327–8339, 2004.
- ELMER, J. W. et al. In situ observations of lattice expansion and transformation rates of α and β phases in Ti-6Al-4V. **Materials Science and Engineering A**, v. 391, n. 1–2, p. 104–113, 2005.
- ENGLER, O.; RANDLE, V. **Introduction to texture analysis: microtexture, microtexture, and orientation mapping**. [s.l.] CRC Press, 2010.
- FAN, X. G. et al. Deformation behavior and microstructure evolution during hot working of a coarse-grained Ti-5Al-5Mo-5V-3Cr-1Zr titanium alloy in beta phase field. **Materials Science & Engineering A**, v. 694, p. 24–32, 2017.
- FAN, Z. The $\beta \rightarrow \omega$ transformation during room temperature aging in rapidly solidified Ti-6Al-4V alloy. **Scripta Metallurgica et Materialia**, v. 31, n. 11, p. 1519–1524, 1994.
- FAN, Z.; MIODOWNIK, A. P. TEM study of metastable β -phase decomposition in rapidly solidified Ti-6Al-4V alloy. **Journal of Materials Science**, v. 29, p. 6403–6412, 1994.
- FANNING, J. C. Properties of TIMETAL 555 (Ti-5Al-5Mo-5V-3Cr-0.6Fe). **Journal of Materials Engineering and Performance**, v. 14, n. 6, p. 788–791, 2005.
- FARIA, G. et al. Advanced facility for parallel thermo-mechanical simulation and

- synchrotron x-ray diffraction. In: KANNENGIESSER, T. et al. (Eds.). . **In-situ Studies with Photons, Neutrons and Electrons Scattering II**. [s.l.] Springer, 2014. p. 245–259.
- FROES, F. H. (ED.). **Titanium: Physical metallurgy, processing and applications**. [s.l.] ASM International, 2015.
- FROST, P. D. et al. Isothermal transformation in titanium-chromium alloys. **Transactions of the American Society for Metals**, v. 46, p. 231–256, 1954.
- FU, Y. -Y. et al. Optimization on the heat treatment process of VST55531 titanium alloy with orthogonal test. **Heat Treatment of Metals**, v. 33, p. 66–68, 2008.
- GEANDIER, G. et al. Study of diffusive transformations by high energy X-ray diffraction. **Comptes Rendus Physique**, v. 13, n. 3, p. 257–267, 2012.
- GIL MUR, F. X.; RODRÍGUEZ, D.; PLANELL, J. A. Influence of tempering temperature and time on the α' -Ti-6Al-4V martensite. **Journal of Alloys and Compounds**, v. 234, n. 2, p. 287–289, 1996.
- GU, X. F.; FURUHARA, T.; ZHANG, W. Z. PTCLab: free and open-source software for calculating phase transformation crystallography. **Journal of Applied Crystallography**, v. 49, p. 1099–1106, 2016.
- GUO, B. et al. Dynamic transformation of Ti–6Al–4V during torsion in the two-phase region. **Journal of Materials Science**, v. 53, n. 12, p. 9305–9315, 2018.
- GUO, L. et al. Microstructure control techniques in primary hot working of titanium alloy bars: A review. **Chinese Journal of Aeronautics**, v. 29, n. 1, p. 30–40, 2015.
- HASHMI, M. S. J. (ED.). **Comprehensive materials processing**. [s.l.] Elsevier, 2014.
- HÉRAUD, L. et al. In situ synchrotron X-ray diffraction of the martensitic transformation in superelastic Ti-27Nb and NiTi alloys: A comparative study. **Materials Today: Proceedings**, v. 2, p. S917–S920, 2015.
- HICKMAN, B. S. Precipitation of the omega phase in titanium-vanadium alloys. **Journal of the Institute of Metals**, v. 96, p. 330–337, 1968.
- HICKMAN, B. S. The formation of omega phase in titanium and zirconium alloys: A review. **Journal of Materials Science**, v. 4, n. 6, p. 554–563, 1969a.
- HICKMAN, B. S. Omega phase precipitation in alloys of titanium with transition metals. **Transactions of the Metallurgical Society of AIME**, v. 245, p. 1329–1335, 1969b.
- HU, M. et al. A novel computational method of processing map for Ti-6Al-4V alloy and corresponding microstructure study. **Materials**, v. 11, n. 9, p. 1599, 2018.
- JONES, N. G. et al. The flow behavior and microstructural evolution of Ti-5Al-5Mo-5V-3Cr during subtransus isothermal forging. **Metallurgical and Materials Transactions A**, v. 40, n.

8, p. 1944–1954, 2009a.

JONES, N. G. et al. β Phase decomposition in Ti-5Al-5Mo-5V-3Cr. **Acta Materialia**, v. 57, n. 13, p. 3830–3839, 2009b.

Journals article sharing. Disponível em: <<https://www.elsevier.com/about/policies/sharing>>. Acesso em: 13 set. 2020.

KEDIA, B.; BALASUNDAR, I.; RAGHU, T. Globularisation of α lamellae in titanium alloy: effect of strain, strain path and starting microstructure. **Transactions of the Indian Institute of Metals**, v. 71, n. 7, p. 1791–1801, 2018.

KRAKOW, R. et al. On three-dimensional misorientation spaces. **Proceedings of the Royal Society A: Mathematical, Physical and Engineering Sciences**, v. 473, n. 2206, 2017.

KUAN, T. S.; AHRENS, R. R.; SASS, S. L. The stress induced omega phase transformation in Ti-V alloys. **Metallurgical Transactions A**, v. 6, p. 1767–1774, 1975.

LAI, M. J. et al. Origin of shear induced β to ω transition in Ti-Nb-based alloys. **Acta Materialia**, v. 92, p. 55–63, 2015.

LASALMONIE, A.; LOUBRADOU, M. The age hardening effect in Ti-6Al-4V due to ω and α precipitation in the β grains. **Journal of Materials Science**, v. 14, n. 11, p. 2589–2595, 1979.

LEYENS, C.; PETERS, M. (EDS.). **Titanium and titanium alloys**. [s.l.] Wiley-VCH, 2003.

LI, T. et al. The influence of partitioning on the growth of intragranular α in near- β Ti alloys. **Journal of Alloys and Compounds**, v. 643, p. 212–222, 2015.

LISS, K. D.; YAN, K. Thermo-mechanical processing in a synchrotron beam. **Materials Science and Engineering A**, v. 528, n. 1, p. 11–27, 2010.

LÜTJERING, G. Influence of processing on microstructure and mechanical properties of (α + β) titanium alloys. **Materials Science and Engineering A**, v. 243, n. 1, p. 32–45, 1998.

LÜTJERING, G.; WILLIAMS, J. C. **Titanium**. 2nd. ed. [s.l.] Springer, 2007.

LUTTEROTTI, L. et al. Combined texture and structure analysis of deformed limestone from time-of-flight neutron diffraction spectra. **Journal of Applied Physics**, v. 81, n. 2, p. 594, 1997.

LUTTEROTTI, L.; VASIN, R.; WENK, H.-R. Rietveld texture analysis from synchrotron diffraction images. I. Calibration and basic analysis. **Powder Diffraction**, v. 29, n. 01, p. 76–84, 2014.

MALINOV, S. et al. Synchrotron X-ray diffraction study of the phase transformations in titanium alloys. **Materials Characterization**, v. 48, n. 4, p. 279–295, 2002.

MANDA, P. et al. Development of α precipitates in metastable Ti-5Al-5Mo-5V-3Cr and

- similar alloys. **Materials Characterization**, v. 120, p. 220–228, 2016.
- MATSUMOTO, H. et al. Microstructural evolution and deformation mode under high-temperature-tensile-deformation of the Ti-6Al-4V alloy with the metastable α' martensite starting microstructure. **Materials Science & Engineering A**, v. 661, p. 68–78, 2016.
- MATSUMOTO, H. et al. Superplastic property of the Ti-6Al-4V alloy with ultrafine-grained heterogeneous microstructure. **Advanced Engineering Materials**, v. 20, n. 1, p. 1–6, 2018.
- MAUD - Materials Analysis Using Diffraction**. Disponível em: <<http://maud.radiographema.com/>>. Acesso em: 30 jun. 2020.
- MCCUSKER, L. B. et al. Rietveld refinement guidelines. **Journal of Applied Crystallography**, v. 32, n. 1, p. 36–50, 1999.
- MIRONOV, S. et al. Microstructure evolution during warm working of Ti-6Al-4V with a colony- α microstructure. **Acta Materialia**, v. 57, n. 8, p. 2470–2481, 2009.
- MORENO, M. et al. Real-time investigation of recovery, recrystallization and austenite transformation during annealing of a cold-rolled steel using high energy X-ray diffraction (HEXRD). **Metals**, v. 9, n. 8, p. 1–13, 2019.
- MORINAGA, M. et al. **Theoretical design of titanium alloys**. Proceedings of the 6th World Conference on Titanium. **Anais...1988**
- MORINAGA, M. Alloy design based on molecular orbital method. **Materials Transactions**, v. 57, n. 3, p. 213–226, 2016.
- MOTYKA, M. et al. Microstructural characterization of quenched and plastically deformed two-phase $\alpha+\beta$ titanium alloys. **Archives of Metallurgy and Materials**, v. 60, n. 3, p. 2033–2038, 2015.
- MOTYKA, M. et al. Dynamic fragmentation and spheroidization of α phase grains during hot deformation of Ti-6Al-4V alloy. **International Journal of Materials Research**, v. 109, n. 8, p. 685–693, 2018.
- MOTYKA, M.; SIENIAWSKI, J.; ZIAJA, W. Microstructural aspects of superplasticity in Ti-6Al-4V alloy. **Materials Science & Engineering A**, v. 599, p. 57–63, 2014.
- NAG, S. **Influence of beta instabilities on the early stages of nucleation and growth of alpha in beta titanium alloys**. [s.l.] The Ohio State University, 2008.
- NAG, S. et al. Elemental partitioning between α and β phases in the Ti-5Al-5Mo-5V-3Cr-0.5Fe (Ti-5553) alloy. **Philosophical Magazine**, v. 89, n. 6, p. 535–552, 2009.
- NYAKANA, S. L.; FANNING, J. C.; BOYER, R. R. Quick reference guide for β titanium alloys in the 00s. **Journal of Materials Engineering and Performance**, v. 14, n. 6, p. 799–811, 2005.

- PEDERSON, R. **Microstructure and phase transformation of Ti-6Al-4V**. [s.l.] Luleå University of Technology, 2002.
- POLETTI, C. et al. Unified description of the softening behavior of beta-metastable and alpha+beta titanium alloys during hot deformation. **Materials Science & Engineering A**, v. 651, p. 280–290, 2016.
- POLMEAR, I. et al. **Light alloys: Metallurgy of the light metals**. 5. ed. [s.l.] Elsevier, 2017.
- POPA, N. C. The (hkl) dependence of diffraction-line broadening caused by strain and size for all Laue groups in Rietveld refinement. **Journal of Applied Crystallography**, v. 31, p. 176–180, 1998.
- QAZI, J. I. et al. Kinetics of martensite decomposition in Ti-6Al-4V-xH alloys. **Materials Science and Engineering A**, v. 359, n. 1–2, p. 137–149, 2003.
- RIETVELD, H. M. A profile refinement method for nuclear and magnetic structures. **Journal of Applied Crystallography**, v. 2, n. 2, p. 65–71, 1969.
- ROSENBERG, H. W. Titanium alloying in theory and practice. In: JAFFEE, R. I.; PROMISEL, N. E. (Eds.). **The Science, Technology and Application of Titanium**. [s.l.] Pergamon, 1970. p. 851–859.
- SASS, S. L. The structure and decomposition of Zr and Ti b.c.c. solid solutions. **Journal of The Less-Common Metals**, v. 28, n. 1, p. 157–173, 1972.
- SASS, S. L.; BORIE, B. The symmetry of the structure of the ω phase in Zr and Ti alloys. **Journal of Applied Crystallography**, v. 5, p. 236–238, 1972.
- SEMIATIN, S. L. An overview of the thermomechanical processing of α/β titanium alloys: current status and future research opportunities. **Metallurgical and Materials Transactions A**, n. Figure 1, 2020.
- SEMIATIN, S. L. et al. Transient plastic flow and phase dissolution during hot compression of α/β titanium alloys. **Metallurgical and Materials Transactions A**, 2020.
- SEMIATIN, S. L.; BIELER, T. R. The effect of alpha platelet thickness on plastic flow during hot working of Ti-6Al-4V with a transformed microstructure. **Acta Materialia**, v. 49, p. 3565–3573, 2001.
- SEMIATIN, S. L.; SEETHARAMAN, V.; WEISS, I. The thermomechanical processing of alpha/beta titanium alloys. **JOM**, v. 49, n. 6, p. 33–39, 1997.
- SEMIATIN, S. L.; SEETHARAMAN, V.; WEISS, I. Flow behavior and globularization kinetics during hot working of Ti-6Al-4V with a colony alpha microstructure. **Materials Science and Engineering A**, v. 263, p. 257–271, 1999.
- SESHACHARYULU, T. et al. Microstructural mechanisms during hot working of

commercial grade Ti-6Al-4V with lamellar starting structure. **Materials Science and Engineering A**, v. 325, p. 112–125, 2002.

SETTEFRATI, A. et al. Precipitation in a near β titanium alloy on ageing: Influence of heating rate and chemical composition of the beta-metastable phase. **Solid State Phenomena**, v. 172–174, p. 760–765, 2011.

SETTEFRATI, A. et al. Precipitation sequences in beta metastable phase of Ti-5553 alloy during ageing. **Proceedings of the 12th World Conference on Titanium**, p. 468–472, 2012.

SETTEFRATI, A. et al. Low temperature transformation in the β -metastable Ti 5553 alloy. **Materials Science Forum**, v. 738–739, n. July 2015, p. 97–102, 2013.

SHA, W.; MALINOV, S. **Titanium alloys: Modelling of microstructure, properties and applications**. [s.l.] Woodhead Publishing, 2009.

SHELL, E. B.; SEMIATIN, S. L. Effect of initial microstructure on plastic flow and dynamic globularization during hot working of Ti-6Al-4V. **Metallurgical and Materials Transactions A**, v. 30, n. 12, p. 3219–3229, 1999.

SIKKA, S. K.; VOHRA, Y. K.; CHIDAMBARAM, R. **Omega phase in materials**. [s.l.: s.n.]. v. 27

SOUZA, P. M. et al. Constitutive analysis of hot deformation behavior of a Ti6Al4V alloy using physical based model. **Materials Science & Engineering A**, v. 648, p. 265–273, 2015.

STARON, P. et al. (EDS.). **Neutrons and synchrotron radiation in engineering materials science**. 2nd. ed. [s.l.] Wiley-VCH, 2017.

TEIXEIRA, J. C. et al. Modeling of the effect of the β phase deformation on the α phase precipitation in near- β titanium alloys. **Acta Materialia**, v. 54, n. 16, p. 4261–4271, 2006.

Titanium Alloys Market - Global Industry Analysis, Size, Share, Growth, Trends and Forecast 2017 - 2025. [s.l.: s.n.]. Disponível em: <<https://www.transparencymarketresearch.com/titanium-alloys-market.html>>.

VILLARS, P.; CALVERT, L. D. **Pearson's handbook of crystallographic data for intermetallic phases**. [s.l.] ASM International, 1986.

WANG, L. et al. The heterogeneous globularization related to crystal and geometrical orientation of two-phase titanium alloys with a colony microstructure. **Materials and Design**, v. 186, p. 108338, 2020a.

WANG, Q.; DONG, C.; LIAW, P. K. Structural stabilities of β -Ti alloys studied using a new Mo equivalent derived from $[\beta/(\alpha + \beta)]$ phase-boundary slopes. **Metallurgical and Materials Transactions A**, v. 46, n. 8, p. 3440–3447, 2015.

WANG, S. C.; AINDOW, M.; STARINK, M. J. Effect of self-accommodation on α/α

- boundary populations in pure titanium. **Acta Materialia**, v. 51, p. 2485–2503, 2003.
- WANG, X. X. et al. Deformation mode dependent mechanism and kinetics of dynamic recrystallization in hot working of titanium alloy. **Materials Science & Engineering A**, v. 772, p. 138804, 2020b.
- WANG, Y. N.; HUANG, J. C. Texture analysis in hexagonal materials. **Materials Chemistry and Physics**, v. 81, p. 11–26, 2003.
- WARCHOMICKA, F. et al. In-situ synchrotron X-ray diffraction of Ti-6Al-4V during thermomechanical treatment in the beta field. **Metals**, v. 9, n. 8, p. 1–14, 2019.
- WARCHOMICKA, F.; POLETTI, C.; STOCKINGER, M. Study of the hot deformation behaviour in Ti-5Al-5Mo-5V-3Cr-1Zr. **Materials Science and Engineering A**, v. 528, n. 28, p. 8277–8285, 2011.
- WARWICK, J. L. W. et al. In situ observation of texture and microstructure evolution during rolling and globularization of Ti-6Al-4V. **Acta Materialia**, v. 61, n. 5, p. 1603–1615, 2013.
- WILL, G. **Powder diffraction: The Rietveld Method and the Two Stage Method to determine and refine crystal structures from powder diffraction data**. [s.l.] Springer, 2006.
- WILLIAMS, J. C.; BLACKBURN, M. J. The influence of misfit on the morphology and stability of the omega phase in titanium-transition metal alloys. **Transactions of the Metallurgical Society of AIME**, v. 245, n. 10, p. 2352–2355, 1969.
- WILLIAMS, J. C.; HICKMAN, B. S.; LESLIE, D. H. The effect of ternary additions on the decomposition of metastable beta-phase titanium alloys. **Metallurgical Transactions**, v. 2, n. 2, p. 477–484, 1971.
- WILLMOTT, P. **An introduction to synchrotron radiation: Techniques and applications**. [s.l.] John Wiley & Sons, 2011.
- WU, H. et al. Nanoscale origins of the oriented precipitation of Ti₃Al in Ti-Al systems. **Scripta Materialia**, v. 125, n. October 2017, p. 34–38, 2016.
- WU, Z. et al. The influence of precipitation of alpha₂ on properties and microstructure in TIMETAL 6-4. **Metallurgical and Materials Transactions A**, v. 44, n. 4, p. 1706–1713, 2013.
- WU, Z. H. et al. Stress relaxation induced morphological evolution and texture weakening of α phase in Ti-6Al-4V alloy. **Materials Letters**, v. 236, p. 148–151, 2019.
- YANG, J. et al. Formation and control of martensite in Ti-6Al-4V alloy produced by selective laser melting. **Materials and Design**, v. 108, p. 308–318, 2016.
- ZAMBALDI, C. R. **Micromechanical modeling of γ -TiAl based alloys**. [s.l.] Rheinisch-

Westfälischen Technischen Hochschule Aachen, 2010.

ZHANG, J.; LI, D. Preferred precipitation of ordered α_2 phase at dislocations and boundaries in near- α titanium alloys. **Materials Science and Engineering A**, v. 341, n. 1–2, p. 229–235, 2003.

ZHANG, J.; LI, H.; ZHAN, M. Review on globularization of titanium alloy with lamellar colony. **Manufacturing Review**, v. 7, p. 18, 2020.

ZHANG, X. et al. Microstructural evolution and precipitation mechanism of α -phase in Ti-55531 alloy aged at high temperature. **Materials Science Forum**, v. 747–748, p. 912–918, 2013.

ZHANG, Z. et al. Achieving ultrafine grained structure in Ti-6Al-4V alloy by high strain rate deformation with a martensitic microstructure. **Materials Letters**, v. 250, p. 46–50, 2019.

ZHENG, Y. et al. The indirect influence of the ω phase on the degree of refinement of distributions of the α phase in metastable β -Titanium alloys. **Acta Materialia**, v. 103, p. 165–173, 2016a.

ZHENG, Y. et al. Role of ω phase in the formation of extremely refined intragranular α precipitates in metastable β -titanium alloys. **Acta Materialia**, v. 103, p. 850–858, 2016b.

ZHENG, Y.; CLARK, W. A. T.; FRASER, H. L. Characterization of the interfacial structure of coarse α precipitates in a metastable β -Ti Alloy Ti-5Al-5Mo-5V-3Cr. **JOM**, v. 71, n. 7, p. 2291–2295, 2019.

ZHEREBTSOV, S. et al. Spheroidization of the lamellar microstructure in Ti-6Al-4V alloy during warm deformation and annealing. **Acta Materialia**, v. 59, n. 10, p. 4138–4150, 2011.

ZHOU, D. et al. Evolution of equiaxed and lamellar α during hot compression in a near alpha titanium alloy with bimodal microstructure. **Materials Characterization**, v. 151, n. February, p. 103–111, 2019.

APPENDIX A – Example of MTEX macro for the calculation of pole figures

%% Specifying Crystal and Specimen Symmetries

% Crystal symmetry

```
CS = crystalSymmetry('6/mmm', [2.95 2.95 4.686], 'X||a*', 'Y||b', 'Z||c*', 'mineral',
'Titanium', 'color', 'cyan');
```

% Specimen symmetry

```
SS = specimenSymmetry('1');
```

% Plotting convention

```
setMTEXpref('xAxisDirection','east');
setMTEXpref('zAxisDirection','outOfPlane');
```

%% Specifying File Names

% Path to files

```
pname = 'C:\Users\bruna\Documents\USP\Doutorado\Projeto\Ti5553\Solubilizações e
deformações\DRX\Arquivos';
```

% Experimental files

```
fname1 = {...
 [pname '\20190731_BrunaCallegari_Ti5553_alpha_800C_10-1_S_002.xrdml'],...
 [pname '\20190731_BrunaCallegari_Ti5553_alpha_800C_10-1_S_100.xrdml'],...
 [pname '\20190731_BrunaCallegari_Ti5553_alpha_800C_10-1_S_101.xrdml'],...
 [pname '\20190731_BrunaCallegari_Ti5553_alpha_800C_10-1_S_102.xrdml'],...
 [pname '\20190731_BrunaCallegari_Ti5553_alpha_800C_10-1_S_110.xrdml'],...
};
```

```
fname2 = {...
```

```
 [pname '\20190731_BrunaCallegari_Ti5553_alpha_800C_10-3_S_002.xrdml'],...
 [pname '\20190731_BrunaCallegari_Ti5553_alpha_800C_10-3_S_100.xrdml'],...
 [pname '\20190731_BrunaCallegari_Ti5553_alpha_800C_10-3_S_101.xrdml'],...
 [pname '\20190731_BrunaCallegari_Ti5553_alpha_800C_10-3_S_102.xrdml'],...
 [pname '\20190731_BrunaCallegari_Ti5553_alpha_800C_10-3_S_110.xrdml'],...
};
```

% Background files

```
pname = 'C:\Users\bruna\Documents\USP\Doutorado\Projeto\Ti5553\Solubilizações e
deformações\DRX\Arquivos';
```

```
fname1_bg = {...
```

```
 [pname '\20190731_BrunaCallegari_Ti5553_alpha_800C_10-1_B_002.xrdml'],...
 [pname '\20190731_BrunaCallegari_Ti5553_alpha_800C_10-1_B_100.xrdml'],...
 [pname '\20190731_BrunaCallegari_Ti5553_alpha_800C_10-1_B_101.xrdml'],...
 [pname '\20190731_BrunaCallegari_Ti5553_alpha_800C_10-1_B_102.xrdml'],...
```

```
[pname '\20190731_BrunaCallegari_Ti5553_alpha_800C_10-1_B_110.xrdml'],...
};
```

```
fname2_bg = { ...
```

```
[pname '\20190731_BrunaCallegari_Ti5553_alpha_800C_10-3_B_002.xrdml'],...
[pname '\20190731_BrunaCallegari_Ti5553_alpha_800C_10-3_B_100.xrdml'],...
[pname '\20190731_BrunaCallegari_Ti5553_alpha_800C_10-3_B_101.xrdml'],...
[pname '\20190731_BrunaCallegari_Ti5553_alpha_800C_10-3_B_102.xrdml'],...
[pname '\20190731_BrunaCallegari_Ti5553_alpha_800C_10-3_B_110.xrdml'],...
};
```

%% Specifying Miller Indices

```
h = { ...
```

```
Miller(0,0,0,2,CS),...
Miller(1, 0,-1, 0,CS),...
Miller(1, 0,-1, 1,CS),...
Miller(1, 0,-1, 2,CS),...
Miller(1, 1,-2, 0,CS),...
};
```

%% Importing the Data

% Experimental files

```
pf1 = loadPoleFigure(fname1,h,CS,SS,'interface','xrdml');
pf2 = loadPoleFigure(fname2,h,CS,SS,'interface','xrdml');
```

% Background files

```
pf1_bg = loadPoleFigure(fname1_bg,h,CS,SS,'interface','xrdml');
pf2_bg = loadPoleFigure(fname2_bg,h,CS,SS,'interface','xrdml');
```

%% Correcting PF Data

```
pf1 = correct(pf1,'bg',pf1_bg);
pf2 = correct(pf2,'bg',pf2_bg);
```

%% Normalizing PF

```
pf1_normalized = normalize(pf1);
pf2_normalized = normalize(pf2);
```

%% Calculating ODF from PF

```
odf1 = calcODF(pf1_normalized,'silent');
odf2 = calcODF(pf2_normalized,'silent');
```

%% Plotting recalculated PF from ODF

```
mtexFig = newMtexFigure('layout',[2,1]);  
plotPDF(odf1,pf1.h,'antipodal')  
nextAxis  
plotPDF(odf2,pf2.h,'antipodal')  
CLim(gcm,'equal')  
mtexColorbar
```


APPENDIX B – Example of MTEX macro for EBSD data processing 1

%% Specifying Crystal and Specimen Symmetries

% Crystal symmetry

```
CS = { ...
  crystalSymmetry('m-3m', [3.3065 3.3065 3.3065], 'mineral', 'Ti-beta', 'color', 'red'),...
  crystalSymmetry('6/mmm', [2.95 2.95 4.686], 'X||a*', 'Y||b', 'Z||c*', 'mineral', 'Ti-
alpha', 'color', 'green'),...
  'notIndexed'};
```

% Plotting convention

```
setMTEXpref('xAxisDirection','east');
setMTEXpref('zAxisDirection','intoPlane');
```

%% Specifying File Names

% Path to files

```
pname = 'C:\Users\bruna\Documents\USP\Doutorado\Projeto\Ti64\Solubilizações e
deformações\EBSD\FuWe\Ti64_1050C_10-1';
```

% Experimental file

```
fname = [pname '\20190804_Ti64_1050_10-1_100x400um_Step_400nm_2.osc'];
```

%% Importing the Data

% Create an EBSD variable containing the data

```
ebsd = loadEBSD(fname,CS,'interface','osc',...
  'convertEuler2SpatialReferenceFrame');
```

%% Plotting Uncorrected Grain Map

```
plot(grains_high.boundary)
set(gca,'color','w')
print('C:\Users\bruna\Documents\USP\Doutorado\Projeto\Ti64\Solubilizações e
deformações\EBSD\MTEX\Ti64_1050C_10-1_FuWe\GrainMap','-dtiff')
```

%% Smoothing the Data

% Compute grains

```
[grains,ebsd.grainId,ebsd.mis2mean] = calcGrains(ebsd);
```

% Remove excessively small grains

```
ebsd(grains(grains.grainSize < 10)) = [];
```

% Repeat grain computation

```
[grains,ebsd.grainId,ebsd.mis2mean] = calcGrains(ebsd);
```

```
% Smooth the data
```

```
F = halfQuadraticFilter;
ebds_smoothed = smooth(ebsd('indexed'),F,'fill',grains);
```

```
% Compute grain boundaries
```

```
[grains,ebds_smoothed.grainId,ebds_smoothed.mis2mean] =
calcGrains(ebsd_smoothed('indexed'));
smgrains_high = calcGrains(ebsd_smoothed,'angle',15*degree);
```

```
%% Plotting Corrected Grain Map
```

```
plot(grains.boundary)
set(gca,'color','w')
print('C:\Users\bruna\Documents\USP\Doutorado\Projeto\Ti64\Solubilizações e
deformações\EBSD\MTEX\Ti64_1050C_10-1_FuWe\GrainMap_smoothed','-dtiff')
```

```
%% Analyzing Aspect Ratio
```

```
x = grains('Ti-alpha').id;
y = grains('Ti-alpha').aspectRatio;
threshold = 5;
moreThanThreshold = y >= 5;
over_x = x(moreThanThreshold);
over_y = y(moreThanThreshold);
scatter(over_x,over_y)
aratio = findobj(gca,'Type','scatter');
aratio_y = get(aratio,'Ydata');
T_y = table(aratio_y);
writetable(T_y,'C:\Users\bruna\Documents\USP\Doutorado\Projeto\Ti64\Solubilizações e
deformações\EBSD\MTEX\Ti64_1050C_10-1_FuWe\AspectRatio.xlsx')
```

APPENDIX C – Example of MTEX macro for EBSD data processing 2

%% Specifying Crystal and Specimen Symmetries

% Crystal symmetry

```
CS = { ...
    'notIndexed',...
    crystalSymmetry('6/mmm', [2.95 2.95 4.686], 'X||a*', 'Y||b', 'Z||c*', 'mineral', 'Ti-
alpha', 'color', 'green'),...
    crystalSymmetry('m-3m', [3.3065 3.3065 3.3065], 'mineral', 'Ti-beta', 'color', 'red')};
```

% Plotting convention

```
setMTEXpref('xAxisDirection','east');
setMTEXpref('zAxisDirection','intoPlane');
```

%% Specifying File Names

% Path to file

```
pname = 'C:\Users\bruna\Documents\USP\Doutorado\Projeto\Ti64\Solubilizações e
deformações\EBSD\LME\Ti64_700C_10-1';
```

% Experimental file

```
fname = [pname '\Ti64_700C_10-1.crc'];
```

%% Importing the Data

% Create an EBSD variable containing the data

```
ebsd = loadEBSD(fname,CS,'interface','crc',...
    'convertEuler2SpatialReferenceFrame');
```

%% Smoothing the Data

% Compute grains

```
[grains,ebsd.grainId,ebsd.mis2mean] = calcGrains(ebsd);
```

% Remove excessively small grains

```
ebsd(grains(grains.grainSize < 10)) = [];
```

% Repeat grain computation

```
[grains,ebsd.grainId,ebsd.mis2mean] = calcGrains(ebsd);
```

% Smooth the data

```
F = halfQuadraticFilter;
ebsd_smoothed = smooth(ebsd('indexed'),F,'fill',grains);
```

% Compute grain boundaries

```
[grains,ebbsd_smoothed.grainId,ebbsd_smoothed.mis2mean] =
calcGrains(ebbsd_smoothed('indexed'));
smgrains_high = calcGrains(ebbsd_smoothed,'angle',15*degree);
smgrains_low = calcGrains(ebbsd_smoothed,'angle',1*degree);
```

%% Plotting Inverse Pole Figure Legend

```
ipfKey = ipfColorKey(ebbsd_smoothed('Ti-alpha'));
plot(ipfKey,'resolution',0.25*degree)
print('C:\Users\bruna\Documents\USP\Doutorado\Projeto\Ti64\Solubilizações e
deformações\EBSD\MTEX\Ti64_700C_10-1_LME\IPF_legend','-dtiff')
```

%% Plotting Inverse Pole Figure

```
% Set inverse pole figure direction
ipfKey = ipfHSVKey(ebbsd_smoothed('Ti-alpha'));
ipfKey.inversePoleFigureDirection = yvector;
color = ipfKey.orientation2color(ebbsd_smoothed('Ti-alpha').orientations);
```

% Plot corrected inverse pole figure

```
plot(ebbsd_smoothed('Ti-alpha'),color,'micronbar','off')
hold on
plot(smgrains_low.boundary,'linecolor','w','linewidth',1)
plot(smgrains_high.boundary,'linecolor','k','linewidth',1)
hold off
set(gca,'color',[160/255, 160/255, 160/255])
print('C:\Users\bruna\Documents\USP\Doutorado\Projeto\Ti64\Solubilizações e
deformações\EBSD\MTEX\Ti64_700C_10-1_LME\IPF-y','-dtiff')
```

%% Plotting Grain Orientation Spread Map

```
plot(smgrains_high('Ti-alpha'),smgrains_high('Ti-
alpha').GOS./degree,'micronbar','off')
mtexColorMap jet
mtexColorbar
hold on
plot(smgrains_low.boundary,'linecolor','w','linewidth',1)
plot(smgrains_high.boundary,'linecolor','k','linewidth',1)
hold off
set(gca,'color',[160/255, 160/255, 160/255])
print('C:\Users\bruna\Documents\USP\Doutorado\Projeto\Ti64\Solubilizações e
deformações\EBSD\MTEX\Ti64_700C_10-1_LME\GOS','-dtiff')
```

%% Plotting Misorientation to Mean Orientation

```
plot(ebbsd_smoothed('Ti-alpha'),ebbsd_smoothed('Ti-
alpha').mis2mean.angle./degree,'micronbar','off')
```

```

mtexColorMap jet
mtexColorbar
hold on
plot(smgrains_high.boundary,'linecolor','k','linewidth',1)
hold off
set(gca,'color',[160/255, 160/255, 160/255])
print('C:\Users\bruna\Documents\USP\Doutorado\Projeto\Ti64\Solubilizações e
deformações\EBSD\MTEX\Ti64_700C_10-1_LME\Mis2mean','-dtiff')

%% Plotting Misorientation Distributions - Angles

% Correlated misorientation
plotAngleDistribution(grains.boundary('Ti-alpha','Ti-alpha').misorientation,...
'DisplayName','Correlated','FaceColor','r','EdgeColor','k','BarWidth',0.5)
hold on

% Random orientation
odf_Tialpha = calcODF(ebsd_smoothed('Ti-alpha').orientations,'Fourier');
plotAngleDistribution(odf_Tialpha.CS,odf_Tialpha.CS,'color','g')
hold off
legend('show','Location','Northwest')
savefig('C:\Users\bruna\Documents\USP\Doutorado\Projeto\Ti64\Solubilizações e
deformações\EBSD\MTEX\Ti64_700C_10-1_LME\MisorientationAngle.fig')

correlated = findobj(gca,'Type','bar');
correlated_x = get(correlated,'Xdata')
correlated_y = get(correlated,'Ydata')
random = findobj(gca,'Type','line');
random_x = get(random,'Xdata')
random_y = get(random,'Ydata')

%% Plotting Misorientation Distributions - Axis

plotAxisDistribution(grains.boundary('Ti-alpha','Ti-alpha').misorientation,'smooth')
mtexTitle('Correlated boundary axis distribution')
nextAxis
plotAxisDistribution(ebsd_smoothed('Ti-alpha').CS,ebsd_smoothed('Ti-
alpha').CS,'antipodal')
mtexTitle('Random boundary axis distribution')
mtexColorMap WhiteJet
setColorRange('equal')
mtexColorbar('Multiples of random distribution')
print('C:\Users\bruna\Documents\USP\Doutorado\Projeto\Ti64\Solubilizações e
deformações\EBSD\MTEX\Ti64_700C_10-1_LME\MisorientationAxis','-dtiff')

%% Analyzing Grain Size

```

```
% Calculate grains
```

```
[grains,ebbsd_smoothed('Ti-alpha').grainId] = calcGrains(ebbsd_smoothed('Ti-alpha'));
```

```
% Set aspect ratio threshold
```

```
grain_AR = grains.aspectRatio;
```

```
condition = grain_AR <= 1.5;
```

```
grain_area = grains(condition).area;
```

```
histogram(grain_area,50)
```

```
savefig('C:\Users\bruna\Documents\USP\Doutorado\Projeto\Ti64\Solubilizações e  
deformações\EBSD\MTEX\Ti64_700C_10-1_LME\GrainSize.fig')
```

```
garea = findobj(gca,'Type','histogram');
```

```
garea_x = get(garea,'BinEdges')
```

```
garea_y = get(garea,'Values')
```

```
%% C-axis orientation
```

```
ori = ebbsd_smoothed('Ti-alpha').orientations;
```

```
c_axis = Miller({0,0,0,1},cs,'uvtw');
```

```
CD = ori\yvector;
```

```
dev_ang = angle(CD,c_axis)./degree;
```

```
plot(ebbsd_smoothed('Ti-alpha'),dev_ang,'micronbar','off')
```

```
hold on
```

```
plot(smgrains_low.boundary,'linecolor','w','linewidth',1)
```

```
plot(smgrains_high.boundary,'linecolor','k','linewidth',1)
```

```
set(gca,'color',[160/255, 160/255, 160/255])
```

```
mtexColorMap jet
```

```
mtexColorbar
```

```
print('C:\Users\bruna\Documents\USP\Doutorado\Projeto\Ti64\Solubilizações e  
deformações\EBSD\MTEX\Ti64_700C_10-1_LME\C-axis','-dtiff')
```

```
cS = crystalShape.hex(ebbsd_smoothed('Ti-alpha').CS);
```

```
plot(smgrains_high('Ti-alpha'),0.4*cS,'FaceColor','none','linewidth',1)
```

```
hold off
```

```
print('C:\Users\bruna\Documents\USP\Doutorado\Projeto\Ti64\Solubilizações e  
deformações\EBSD\MTEX\Ti64_700C_10-1_LME\C-axis_crystal','-dtiff')
```

ANNEX A – Paper on aging treatments of Ti-6Al-4V alloy



RightsLink[®]


Home


Help


Email Support


Sign in


Create Account



In-situ synchrotron radiation study of the aging response of Ti-6Al-4V alloy with different starting microstructures

Author:
B. Callegari, J.P. Oliveira, K. Aristizabal, R.S. Coelho, P.P. Brito, L. Wu, N. Schell, F.A. Soldera, F. Mücklich, H.C. Pinto

Publication: Materials Characterization

Publisher: Elsevier

Date: July 2020

© 2020 Elsevier Inc. All rights reserved.

Please note that, as the author of this Elsevier article, you retain the right to include it in a thesis or dissertation, provided it is not published commercially. Permission is not required, but please ensure that you reference the journal as the original source. For more information on this and on your other retained rights, please visit: <https://www.elsevier.com/about/our-business/policies/copyright#Author-rights>

BACK

CLOSE WINDOW

© 2020 Copyright - All Rights Reserved | Copyright Clearance Center, Inc. | [Privacy statement](#) | [Terms and Conditions](#)
Comments? We would like to hear from you. E-mail us at customer-care@copyright.com



Contents lists available at ScienceDirect

Materials Characterization

journal homepage: www.elsevier.com/locate/matchar

In-situ synchrotron radiation study of the aging response of Ti-6Al-4V alloy with different starting microstructures

B. Callegari^{a,b}, J.P. Oliveira^{c,d}, K. Aristizabal^b, R.S. Coelho^e, P.P. Brito^f, L. Wu^g, N. Schell^h, F.A. Soldera^b, F. Mücklich^b, H.C. Pinto^{a,*}

^a University of São Paulo, São Carlos School of Engineering, Department of Materials Engineering, Av. João Dagnone 1100, 13563-120 São Carlos, Brazil

^b Saarland University, Department of Materials Science and Engineering, Campus D3-3, 66123 Saarbrücken, Germany

^c UNIDEMI, Department of Mechanical and Industrial Engineering, NOVA School of Science and Technology, Universidade NOVA de Lisboa, 2829-516 Caparica, Portugal

^d CENIMAT/IDN, Department of Materials Science, NOVA School of Science and Technology, Universidade NOVA de Lisboa, 2829-516 Caparica, Portugal

^e SENAI CIMATEC, Institute SENAI of Innovation for Forming and Joining of Materials, Av. Orlando Gomes 1845, 41650-010 Salvador, Brazil

^f Pontifical Catholic University of Minas Gerais, Av. Dom José Gaspar 500, 30535-901 Belo Horizonte, Brazil

^g Brazilian Synchrotron Light Laboratory, Brazilian Center for Research in Energy and Materials, Rua Giuseppe Maximo Solfaro, 10000, 13083-970 Campinas, Brazil

^h Institute of Materials Research, Helmholtz-Zentrum Geesthacht, Max-Planck-Str. 1, D-21502 Geesthacht, Germany



ARTICLE INFO

Keywords:

Titanium alloys
Aging
Hardening
Phase transformation
Secondary precipitation
Synchrotron X-ray diffraction

ABSTRACT

The aging behavior of a Ti-6Al-4V alloy with different starting microstructures was evaluated by means of synchrotron X-ray diffraction, scanning transmission electron microscopy and micro-hardness measurements. Initial microstructures were produced by thermal and thermomechanical treatments and comprised different morphologies of α phase (martensitic, lamellar, bimodal and globular), as well as the presence or absence of the β phase. Results show that one or more of the following phenomena can take place during aging and contribute to the hardening of the alloy: β decomposition into fine secondary α laths; transformation of the metastable martensitic α' into the equilibrium α phase; and precipitation of the intermetallic Ti_3Al . The composition and distribution of the β phase was shown to affect the precipitation of secondary α during aging, while the composition of the α phase plays a key role on the formation of Ti_3Al . In situ X-ray diffraction studies of the early stages of aging show the kinetics of the $\alpha' \rightarrow \alpha$ conversion by the reduction in FWHM of XRD reflections, indicate the contribution to hardening by the increase of the c/a ratio and the consequent limitation of active slip systems and depict the chemical homogenization and decomposition of the β phase.

1. Introduction

Ti-6Al-4V alloy (Ti-64; composition in wt%) is the main representative of $\alpha + \beta$ alloys, responsible for > 50% of all titanium alloys' applications [1]. Reasons for its intensive application involve the equilibrium of properties such as strength, ductility, toughness and fatigue properties [2–4]. These properties are consequence of the composition, morphology and ratio of present phases, which come as result of the alloy's response to heat treatments and thermomechanical processing [4]. Treatment temperature, cooling rate and degree and mode of deformation are the main processing parameters, influencing the morphology of the α phase, the formation of martensite, the occurrence of texture and the age hardening potential of the alloy [3].

In titanium alloys, solution treatments produce a relatively high amount of β phase, and this condition can be entirely or partially maintained upon quenching. The subsequent hardening and strength

increase attained after aging comes as consequence of the decomposition of this metastable β phase and of any martensitic phase that might form during quenching into dispersed phases [5,6]. Morita et al. attribute the strengthening of Ti-6Al-4V alloy during aging after quenching to the precipitation of a refined α phase from the retained β phase [7]. Stephen et al. state that water quenching after solution treatment provides more degrees of freedom for microstructure and mechanical properties optimization during aging than air or furnace cooling because the water quenched microstructure can consist of a variety of metastable phases, e.g. α' , α'' and β , which have good response to aging treatments [8]. Hardening of Ti-6Al-4V alloy due to martensite decomposition was investigated by Qazi et al. [9] and by Gil Mur, Rodríguez and Planell [10]. On the other hand, Pederson states that the primary α phase responds better to aging by the precipitation of intermetallic phase Ti_3Al (α_2) due to its enrichment in aluminum and oxygen, which promote the formation of this phase, in comparison with

* Corresponding author.

E-mail address: haroldo@sc.usp.br (H.C. Pinto).

<https://doi.org/10.1016/j.matchar.2020.110400>

Received 10 February 2020; Received in revised form 19 May 2020; Accepted 21 May 2020

Available online 22 May 2020

1044-5803/ © 2020 Elsevier Inc. All rights reserved.

secondary α phase, that precipitates directly from the β phase upon cooling, lean in these said elements [11].

The vast majority of works related to the aging response of Ti-6Al-4V alloys focuses on the effects of solution treatment and aging on the mechanical properties of the alloy. In the work of Venkatesh et al., water quenching after solution treatment followed by aging has led to higher yield strength and ultimate tensile strength, and lower ductility when compared to air cooling + aging [12]. Hémy and Villechaise evaluated the effect of aging on the plastic deformation of Ti-6Al-4V alloy and found that short range ordering and precipitation of Ti_3Al affects the activation of slip systems: before aging, basal systems are activated first and prismatic systems are subsequently activated, whereas after aging both systems are activated simultaneously [13]. The precipitation of Ti_3Al has been acknowledged to increase the alloy's strength and decrease its ductility [14].

Very few studies focused on tracking the alloy's microstructural behavior under aging treatments exist in the literature. Carreon et al. have studied the response of the microstructure of a Ti-64 alloy to isothermal treatments using thermoelectric methods and hardness measurements, and have attributed the behavior of the alloy to the precipitation of Ti_3Al particles [15]. El-Hadad et al. studied microstructural changes in a solution-treated Ti-6Al-4V alloy after aging at 550 °C for 6 h and have observed very few precipitates and no significant hardness evolution in the aged samples, indicating that this aging condition is not enough to induce any relevant microstructural changes in the alloy [16]. Ji et al. have applied thermodynamic simulations to the Ti-6Al-4V alloy and have proposed that, depending on the temperature range in which the isothermal treatment is conducted, different transformation sequences can occur. Between 423 K (−150 °C) and 895 K (−620 °C), the suggested transformation pathway is $\beta \rightarrow \alpha/\alpha' \rightarrow \alpha + \beta + Ti_3Al$, where the first transformation is diffusionless and the second has a diffusional nature [17].

Given the relevance of Ti-64 alloy for structural applications, the present study aims to understand its microstructural evolution during aging treatments for a better correlation of such evolution with the final properties of the aged alloy in a concise manner. Different thermal and thermomechanical treatments were imposed to the alloy to produce microstructural variability in terms of α phase morphology and ratio between α and β fractions in order to evaluate the response of each microstructure to subsequent treatments. All conditions underwent aging at 500 °C for 24 h and post-aging samples were analyzed by means of high energy X-ray diffraction, transmission electron microscopy and micro-hardness measurements. Shorter aging treatments at 500 °C with 8 h of duration were carried out using in situ synchrotron X-ray diffraction for a better understanding of the alloy's response to the isothermal treatment based on their behavior in the initial stages of aging.

2. Materials and methods

2.1. Material

The composition of the Ti-64 alloy (grade 23) used in this work is given in Table 1. Contents of heavier elements (Al, V and Fe) were determined by inductively coupled plasma atomic emission spectrometry in an Ametek® SPECTROMAXx analyzer, and amounts of interstitial elements (O, C, N and H) were analyzed using Leco® RO-400, Leco® ONH-836 and Leco® CS-844 analyzers. Its β -transus temperature

Table 1
Composition of Ti-64 alloy used in this work.

Element wt%	Ti Bal.	Al 6.03	V 4.18	Fe 0.24	O 0.14	C 0.013	N 0.011	H 0.006
[Al] eq		7.4						
				[Mo] eq			3.4	

was determined to be of approximately 963 °C with a Netzsch® 404 F3 Pegasus differential scanning calorimeter during continuous heating at 20 °C/min.

2.2. Tailoring of initial microstructures

The alloy was thermally treated and thermomechanically processed by means of uniaxial compression at 1050 °C (β field), 900 °C and 700 °C ($\alpha + \beta$ field). Specimens with dimensions of $\phi 10 \times 15$ mm were machined from the as-received bar with their length parallel to the bar's length. To remove any effects of prior processing, specimens initially underwent a homogenization treatment at 1050 °C during 30 min in an EDG 10P-S furnace with vacuum and argon atmosphere protection followed by water quenching to room temperature. From this condition, compressive deformation was imposed to specimens in a Gleeble® 3800 thermomechanical simulator with strain rate of 10^{-3} s^{-1} up to a compression ratio of 0.5 (true strain = 0.7). Before compression, except for deformation at 1050 °C, samples were soaked at the target temperature for 30 min. Type-S thermocouples were spot-welded to samples in their mid-length for temperature control, and a conductive silver-graphite paint was applied between specimens' parallel faces and compression anvils to improve thermal contact and lubrication. Heat-treatments at 900 °C and 700 °C during 30 min followed by water quenching were also done after the initial homogenization at 1050 °C. For standardization purposes, each condition was identified based on treatment temperature ("1050C" for 1050 °C, "900C" for 900 °C and "700C" for 700 °C) and type ("HT" for heat treatment and "D" for compression). Fig. 1 summarizes the processing routes imposed to the alloy.

2.3. Microstructural characterisation

The alloy was metallographically prepared for scanning electron microscopy (SEM) according to the following procedure: manual grinding on sandpapers with #320, #600 and #1200 grits, automated pre-polishing with a 3- μm diamond suspension and automated polishing using a solution composed by 90 vol% 0.04 μm OP-S and 10 vol% H_2O_2 in a Buehler® EcoMet 250 machine (force: 5 N; base rotation: 20 rpm; head rotation: 60 rpm; counter-rotation). SEM analyses were conducted in a FEI® Inspect F50 microscope with field emission gun using secondary (SE) and backscattered electrons (BSE) imaging modes. For BSE analyses, samples were unetched, and for SE analyses samples were chemically etched with Kroll's etchant (3 mL hydrofluoric acid, 6 mL nitric acid and 91 mL water).

2.4. Aging treatments using synchrotron X-ray diffraction

All conditions were aged at 500 °C and analyzed using synchrotron X-ray diffraction. The aging temperature was chosen based on the following criteria: it should be high enough to allow for diffusion but it stands below the solvus temperature of Ti_3Al , to allow its precipitation. A simplified verification of the solvus temperature was done on ThermoCalc® software using COST 507 database [18] and the procedure developed by Zhang et al. to describe a pseudo-ternary Ti-Al-V system based on the composition of the multicomponent Ti-64 alloy given in Table 1 [19]. By this procedure, the obtained solvus temperature was of ~548 °C. In addition, the chosen temperature should not cause excessive oxidation of the material. Samples with $3 \times 4 \times 6 \text{ mm}^3$ were wire-cut from the previously heat-treated and deformed specimens. In the case of deformed conditions, samples were machined with their length parallel to the compression direction. Aging treatments with holding time of 24 h were done in a Carbolite STF 15/75/450 tube furnace with vacuum level of $\sim 10^{-4}$ mbar followed by furnace cooling and samples pre- and post-aging were analyzed in the P07B beamline of the PETRA III facility at DESY (Hamburg, Germany). The energy of the beam was 87.1 keV ($\lambda = 0.142 \text{ \AA}$). Complete Debye-Scherrer rings

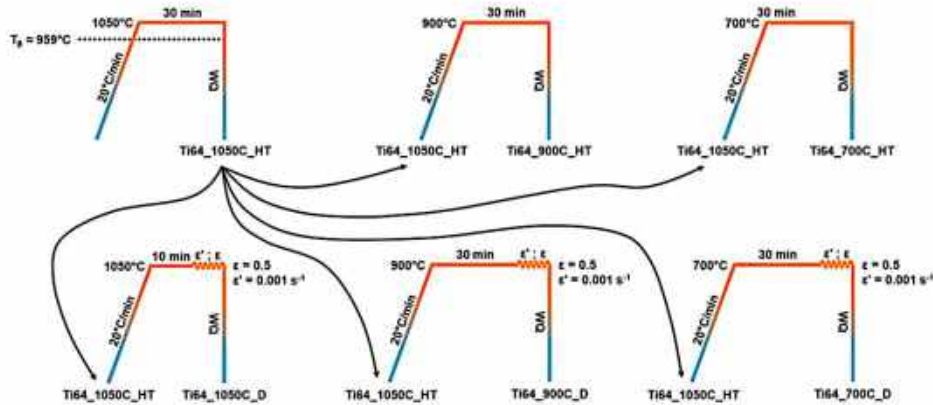


Fig. 1. Schematic representation of thermal and thermomechanical treatments imposed to Ti-64 alloy.

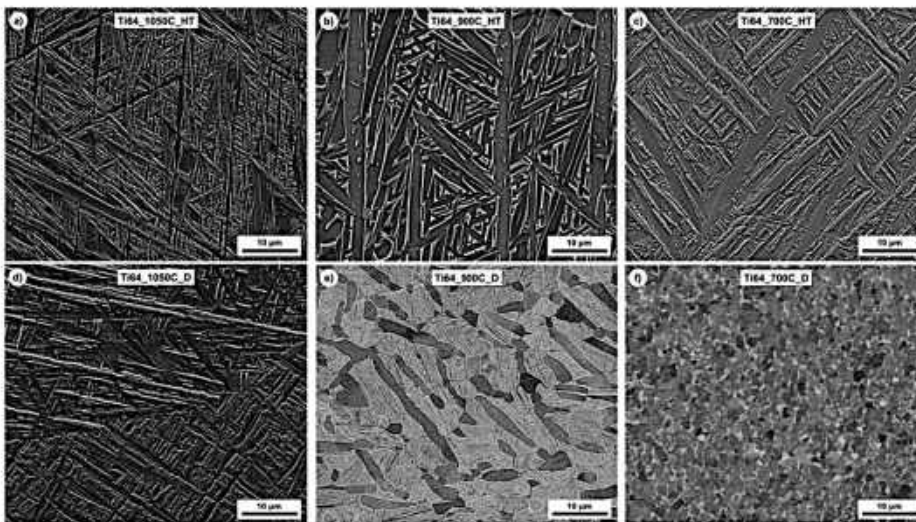


Fig. 2. SEM images of a) Ti64_1050C_HT (SE), b) Ti64_900C_HT (SE), c) Ti64_700C_HT (SE), d) Ti64_1050C_D (SE), e) Ti64_900C_D (BSE) and f) Ti64_700C_D (BSE). In deformed conditions, the compression axis is parallel to the height of images. The α phase is darker and the β phase is brighter.

were acquired in transmission mode using a Perkin Elmer* XRD 1621 flat panel detector with $200 \times 200 \mu\text{m}^2$ pixel size with an exposure time of 0.1 s and 5 frames/image and a spot size of $1 \times 1 \text{ mm}^2$. A standard LaB_6 powder was used for calibration on FIT2D software. The corresponding diffractograms were integrated from the images using an ImageJ software macro.

Shorter aging treatments with holding time of 8 h using in situ synchrotron X-ray diffraction were done in the XTMS experimental station of the XRD1 beamline at the Brazilian Synchrotron Light Laboratory equipped with an adapted Gleeble* 3550 thermomechanical simulator. The energy of the beam was of 12 keV ($\lambda = 1.033 \text{ \AA}$). Temperature control was done using spot-welded K-type thermocouples. The experiment was conducted in reflection mode with a spot size of $1 \times 2 \text{ mm}^2$. Sections of Debye-Scherrer rings were acquired with 60 s of exposure time using a Rayonix* SX165 area detector with pixel size of $39 \times 39 \mu\text{m}^2$. Calibration was done using a standard Al_2O_3

powder [20]. Acquired images were processed on Dracon software, a MATLAB* macro developed by the XTMS staff, for the integration of diffractograms.

X-ray diffraction data were analyzed quantitatively using Rietveld refinement on MAUD software [21] for the withdrawal of information such as phase fractions and lattice parameters. Calculation of the full width at half maximum (FWHM) of peaks was done on PeakFit software using a Lorentz + Gauss profile.

2.5. (Scanning) transmission electron microscopy

Samples Ti64_900C_HT, Ti64_900C_D and Ti64_700C_D aged at 500 °C during 24 h were selected for transmission (TEM) and scanning-transmission (STEM) electron microscopy analyses. TEM lamellae were prepared by lift-out in a FEI* Helios NanoLab 600 DualBeam microscope. Analyses were carried out in a FEI* Tecnai G²-F20 transmission

electron microscope with field emission gun operated at 200 kV. Indexing of selected area diffraction patterns was done using PTCI Lab software [22].

2.6. Micro-hardness measurements

The Vickers hardness of samples before and after aging at 500 °C for 24 h was measured in a Struers® DuraScan with load of 0.2 kgf. Twenty-five measurements were done with a spacing of 150 µm between each indentation in a 5 × 5 matrix in the center of samples. For the hardness testing, specimens were metallographically prepared as described in Section 2.3.

3. Results

3.1. Initial microstructures

Fig. 2 shows the microstructures produced via thermal treatment and thermomechanical processing to compose the initial conditions used for subsequent aging treatments. In some cases, backscattered electrons' signal was used for a better visualization of α and β phases based on chemical contrast. The applied processing pathways achieved all typical microstructures of titanium alloys in terms of α phase morphology, namely martensitic, lamellar, globular and bimodal. Both heat treatment and deformation at 1050 °C produced martensitic microstructures. Heat-treatment at 900 °C, on the other hand, resulted in coarsening of the α phase, producing a Widmanstätten-like microstructure with a lamellar width of approximately 2 µm, against a width of 0.8 µm in martensitic laths. Hot working at 900 °C produced the so-called bimodal microstructure, comprising a coarse globularized α phase formed during deformation (primary α) and colonies of fine laths of α precipitated within the β matrix during rapid cooling (secondary α). With respect to heat treatment at 700 °C, a partially martensitic microstructure is seen, with the presence of relatively coarse α lamellae when compared to those seen in Ti64_1050C_HT. Finally, deformation at 700 °C yielded a fully globular α microstructure embedded in a β matrix.

3.2. Microstructure and hardness evolution

Fig. 3 presents the diffractograms resulting from the complete integration of Debye-Scherrer rings for all conditions before and after aging at 500 °C/24 h. The initial diffractogram of Ti64_900C_HT is shown in Fig. 3g as a support to identify reflections from α and β phases. No new reflections belonging to phases other than the allotropic ones were seen. The most outstanding difference between non-aged and aged conditions lies on the absence of visible reflections of the β phase after 24 h of aging in all conditions where it was initially present.

The initial volume fractions of β phase ($R_{\beta_0} \leq 0.121$) are shown in Table 2. It is worth pointing out that Ti64_1050C_D condition contained some remaining metastable β after quenching, differently from Ti64_1050C_HT condition, which has shown a fully martensitic microstructure. As consequence, its hardness was relatively lower, as can be seen in Fig. 4. Another contribution to the lower hardness might have its origins on the softening of the alloy caused by dynamic recrystallization of the β phase during deformation [23]. Overall, initial hardness values result from the combination of the amount of the soft β phase and the size and morphology of the α phase.

During aging, all conditions underwent a hardness increase. It is important to notice that the highest hardness value after aging is presented by Ti64_1050C_HT, which is in agreement with the literature regarding the strength of the alloy with an aged martensitic microstructure [12]. However, results show that the response of the alloy to aging is maximized in microstructures containing a high amount of β and primary α phases. The most significant hardness raises occurred in Ti64_700C_D, Ti64_900C_HT and Ti64_900C_D conditions. This is in

agreement with the decomposition of β phase observed in Fig. 3, given that these conditions were the ones with the highest initial contents of this phase, whose stabilization upon quenching after solution treatment is useful to enhance the alloy's response to subsequent aging treatments by its decomposition [4]. Thermodynamic simulations as described in Section 2.4 show that the equilibrium amount of β phase at 500 °C is ~2.5 wt%. It is known that, during aging, the alloy tends to reach the equilibrium microstructure for the treatment temperature in terms of phase fractions, and present phases tend to reach their stable chemical composition [4]. Thus, it is reasonable to assume that, in all conditions studied which contained the β phase in their initial microstructure, the amount of β has decreased during aging aiming to achieve thermodynamic stability. Regarding martensitic microstructures, i.e. Ti64_1050C_HT, Ti64_1050C_D and Ti64_700C_HT, the increase in hardness comes as a result of the transformation of the metastable α' into the stable α phase [9,10,12,24]. In the last two conditions, there is the additional effect of decomposition of the remaining metastable β phase.

4. Discussion

4.1. Secondary α precipitation and β decomposition

In order to evaluate microstructural evolution in detail and identify additional hardening mechanisms other than α' and β decomposition, the three conditions with the highest hardness increases mentioned above were analyzed by (S)TEM. Fig. 5 shows bright field (BF) detail images of the aged microstructures of Ti64_900C_HT, Ti64_900C_D and Ti64_700C_D conditions for 24 h. Overall, no noticeable differences can be seen in comparison with the starting microstructures shown in Fig. 2. However, in Ti64_900C_HT condition (Fig. 5a), it is possible to observe a β island with extremely refined precipitates between primary α grains.

Fig. 6 shows a BF STEM image of Ti64_900C_HT condition after aging during 24 h accompanied by energy dispersive spectroscopy (EDS) maps, which indicate that these refined precipitates are lean in β -stabilizing elements V and Fe and enriched with Ti and Al, therefore consisting of extremely refined secondary α laths. Such features were not observed in the microstructure of Ti64_900C_HT condition before aging. These results show that β decomposition into secondary α occurs during aging, similarly to what has already been observed during annealing of the alloy after hot isostatic pressing [25]. It is important to emphasize that these precipitates were not observed in Ti64_700C_D condition after aging. This difference can be a consequence of the difference in morphology and distribution of the β phase in both conditions, which appears to play a key role, since this phase presents itself continuous along the α laths in the Widmanstätten structure, whereas in the globular structure it is concentrated in triple α boundaries, in a non-uniform manner.

Fig. 7 shows a high angle annular dark field (HAADF) image of a secondary α colony in Ti64_900C_D condition. It is possible to notice the presence of the β phase (bright) in the interfaces between adjacent α laths (dark). The qualitative EDS line scan of a region between two adjacent laths shows the enrichment of these regions with β -stabilizing elements V and Fe. As previously discussed, the amount of β decreases towards its equilibrium value during aging. The amount of α increases at the expense of β dissolution. At the end of the aging treatment, extremely thin layers of β remain among α laths.

4.2. Precipitation of Ti_3Al (α_2)

In Fig. 8 are shown selected area electron diffraction (SAED) patterns of the $\langle 110 \rangle$ α zone axis of Ti64_900C_D and Ti64_700C_D conditions after aging. In both cases, the selected area was inside an α grain. With respect to the first, the selected area was inside a primary α grain. In the SAED, in addition to the α spots belonging to the zone axis,

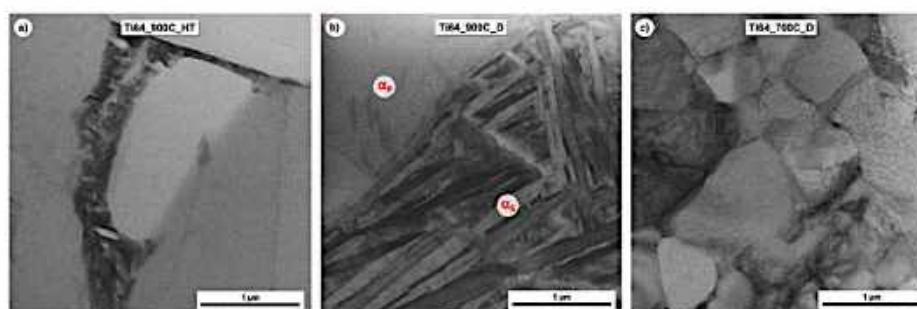


Fig. 5. Bright field image details of the aged microstructures of a) Ti64_900C_HT, b) Ti64_900C_D, where α_1 denotes the primary α phase and α_2 , the secondary α phase, and c) Ti64_700C_D.

which promote the precipitation of coherent Ti_3Al particles and the consequent age hardening. As a result, secondary α lamellae, which form from the β phase upon cooling, do not respond as well as primary α to aging [11]. The precipitation of Ti_3Al is known to increase the tensile strength of Ti-64 alloy, but, on the other hand, it lowers its ductility and fatigue resistance [14,26,32].

It is worth mentioning that these reflections were not seen in SAED patterns of the α phase in the Ti64_900C_HT condition, which shows that the globular α phase produced by thermomechanical treatment is richer in α -stabilizing elements than the α lamellae obtained by annealing. The explanation for this behavior most likely lies in the fact that the imposition of deformation has been shown to significantly enhance diffusive activity in the alloy in comparison with sheer thermal treatment [33]. Furthermore, the total holding time during annealing was of 30 min, whereas the thermomechanically processed specimen has undergone an isothermal holding of 30 min plus 8.3 min to complete the 50% compression with a strain rate of 0.001 s^{-1} . In other words, deformed conditions have experienced an expressively higher diffusional activity than heat-treated conditions at 700 °C and 900 °C.

In fact, EDS analyses carried out within α grains and laths in the three conditions have yielded the Al contents presented in Table 3, which show that the α phase is richer in Al in the Ti64_700C_D

condition and leaner in the Ti64_900C_HT condition. These results are also helpful to understand the precipitation of secondary α in the β phase in the Ti64_900C_HT condition against the absence of such precipitation in Ti64_700C_D, as previously discussed. In the latter, the α phase is richer in α -stabilizing elements, thus making β lean in these elements and hindering secondary α precipitation in these conditions. Furthermore, oxygen is known to promote the precipitation of Ti_3Al phase by decreasing the solubility of Al in the α phase [34]. In a study of Ti-64 alloy with 0.07 and 0.19 wt% O, Welsch and Bunk have observed the presence of α_2 after aging at 550 °C for 115 h only in the alloy with the highest oxygen content [35]. Lim et al. have found that the increase of oxygen content in a Ti-8 wt% Al alloy not only increases the volume fraction of α_2 after aging, but also changes its distribution from heterogeneous (concentrated at dislocations) to uniform. In their work, the phase has precipitated even with oxygen concentrations as low as 580 ppm (0.058 wt%) after aging at 695 °C during 200 h [36], which reinforces the cooperative effect of Al and O concentrations and aging temperature on the precipitation of this phase. However, so far, no systematic correlation between the $\alpha + \alpha_2$ solvus line and the oxygen content has been established. Overall, studies focused on Ti-64 alloy with oxygen concentrations up to 0.22 wt% have observed the formation of Ti_3Al [14,26,35]. Therefore, the amount of oxygen in the

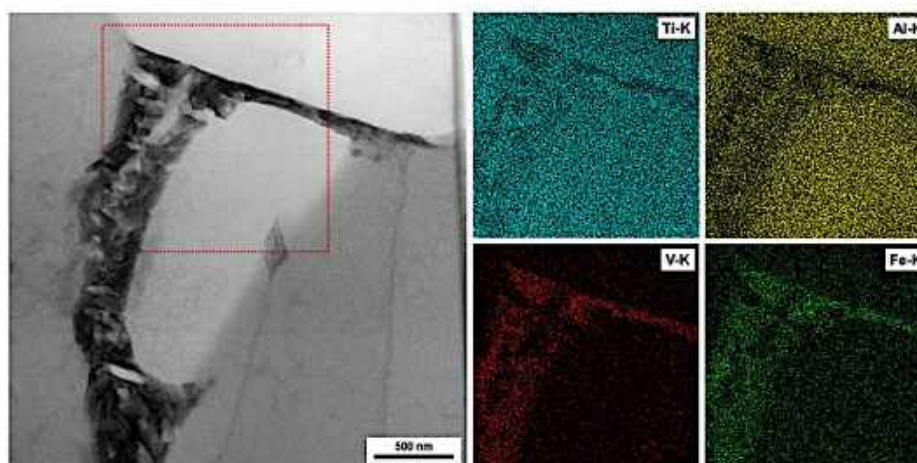


Fig. 6. A bright field STEM image of aged Ti64_900C_HT condition with the EDS maps of Ti, Al, V and Fe of the area delimited by the red square with preserved scale. (For interpretation of the references to colour in this figure legend, the reader is referred to the web version of this article.)

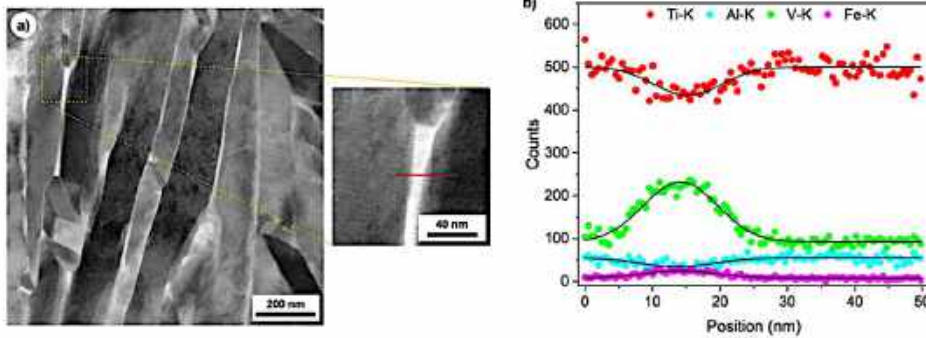


Fig. 7. a) STEM-HAADF image of a secondary α colony in aged Ti64_900C_D condition, with indication of the line scan region, and b) the resulting spectra of the line scan.

present alloy, 0.14 wt%, is enough to aid the formation of the inter-metallic phase. In the present work, EDS results have shown that the β phase contains no detectable amount of oxygen and therefore one can assume that this element partitions in its totality to the α phase.

4.3. Early stages of aging treatment

Shorter aging treatments with soaking time of 8 h were carried out in situ to enable the tracking of the alloy's behavior with its different initial microstructures in the early stages of aging. Fig. 9 shows the behavior of the α/α' phase in conditions where martensite was majorly present in the initial microstructure. In X-ray diffraction, peak broadening might be a result of chemical inhomogeneity and lattice distortions, and lattice parameters are also sensitive to chemical composition [37,38]. Because α' is a supersaturated substitutional phase [6], it can be assumed that its reflections present themselves broader than the reflections of the chemically stable α phase. Furthermore, its consequently strained state also contribute to the broadening of their reflections [31]. Taking this into account, the full width at half maximum (FWHM) of (1011) α , the most intense reflection of the α phase, was calculated ($R^2 \geq 0.9892$), and results are shown in Fig. 9a, while Fig. 9b presents the evolution of the lattice parameters of α/α' , obtained via Rietveld refinement ($Rwp \leq 0.1194$ and standard error $\leq 9.32 \times 10^{-4}$ Å), in the form of the c/a aspect ratio.

In all conditions, a decrease in the FWHM values is seen. The lower initial FWHM value of Ti64_700C_HT indicated that this condition presents a lower degree of chemical inhomogeneity and internal strain,

Table 3
Al contents of the α phase in different conditions of the Ti-64 alloy.

Condition	Al content (wt%)
Ti64_700C_D	7.3 ± 0.1
Ti64_900C_D (α_0)	6.2 ± 0.1
Ti64_900C_D (α_2)	3.8 ± 0.3
Ti64_900C_HT	5.2 ± 0.4

which is in agreement with its lamellar/martensitic microstructure. The decrease is more accentuated within the first hour of aging and in the remaining time this parameter tends to stabilize. This implies that, in all these systems, the α' phase undergoes chemical and lattice homogenization and such homogenization is intensified in the beginning of the treatment. Results are in good agreement with previous studies on the martensite decomposition in Ti-64 alloys tracked by the increase in hardness values [9,10].

Regarding the ratio between the lengths of c and a parameters of the hexagonal lattice, it is noticeable that Ti64_1050C_HT and Ti64_1050C_D follow the same tendency, with the increase of the c/a ratio during aging, while Ti64_700C_HT follows the opposite tendency, i.e. its c/a ratio decreases during the isothermal treatment. Both a and c parameters decrease in length; however, the percent decrease of the a -axis is larger than the decrease of the c -axis for Ti64_1050C_D and Ti64_1050C_HT, whereas the decrease of c -axis is larger in Ti64_700C_HT. The variation of lattice parameters is a direct

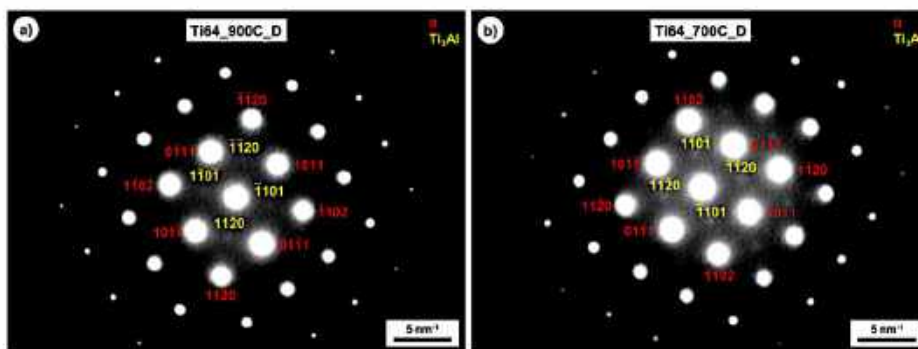


Fig. 8. SAED patterns of the $\langle 1101 \rangle \alpha \parallel \langle 1102 \rangle \alpha_2$ zone axis of a) Ti64_900C_D and b) Ti64_700C_D aged conditions with indication of α and Ti_3Al reflections.

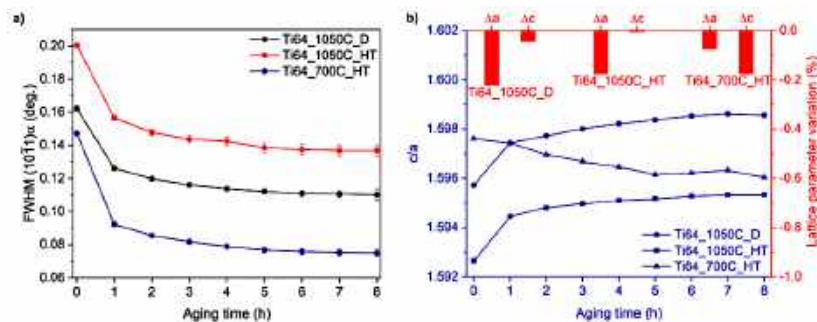


Fig. 9. a) (101) FWHM and b) lattice parameters evolution of the α/α' phase during aging of Ti64_1050C_D, Ti64_1050C_HT and Ti64_700C_HT conditions.

consequence of the diffusion of interstitial and substitutional atoms; since martensite, in this case, is a supersaturated substitutional solution, the variation is mostly affected by the diffusion of substitutional atoms. The increase in c/a ratio is known to harden and strengthen the alloy due to the restriction in the number of activated slip systems in the hexagonal structure [35,39]. Thus, this is a plausible explanation for the hardening of the alloy upon conversion of the α' phase into α . Regarding Ti64_700C_HT, the reduction in the c/a ratio might be related to the early presence of the stable α phase, in contrast with the martensitic microstructure present in both conditions produced at 1050 °C, which results in different chemical distributions between α and α' phases and between the α/α' set and β . Because no deconvolution between α and α' peaks is possible, their behavior comes as a sum of the behavior of each component alone.

Fig. 10 depicts the behavior of the β phase during the first eight hours of aging in conditions where the phase was present with a higher fraction, namely Ti64_900C_HT, Ti64_900C_D and Ti64_700C_D. Such behavior is exemplified by the main β reflection, (110). In all cases, a decrease in the cell length of β , which causes an increase in the 2θ position of the reflections of the phase, is seen. This decrease is more easily seen in the Ti64_700C_D condition. Such behavior can be explained by the partitioning of solute, most specifically V, in the β phase. Elmer et al. [40] have observed a decrease in the lattice parameter of β at temperatures near 500 °C, and Barriobero-Vila et al. [41] have observed the same behavior of the β phase in a Ti-6Al-6V-2Sn alloy also at temperatures close to the one used in this work. They have attributed this behavior to the enrichment of V in the β phase with a simultaneous depletion of Ti by this phase, basically driven by an attempt of the system to reach thermodynamic equilibrium. In this regard, the contraction owes itself to the smaller atomic radius of V, and also of Fe, in comparison to that of Ti. Elmer et al. further proposes that the decrease in the lattice parameter of β can be a consequence of the relaxation of

internal stresses created by the different lattice expansion rates of α and β phases during heating [40].

In Ti64_900C_HT condition, a sharp increase in intensity and decrease in width can be noticed. ThermoCalc® simulations described in Section 2.4 show that the equilibrium weight fraction of the β phase at 900 °C is of approximately 62%, against 5.5 wt% at 700 °C. The volume fraction shown in Table 2, equivalent to a weight fraction of ~10%, deviates significantly from this value. This indicates that the thermal/thermomechanical treatments imposed to the alloy in these conditions, in addition to the rapid cooling to room temperature, induce the formation of a metastable system. Thus, the behavior of the β phase might be, again, a consequence of an attempt to achieve equilibrium in the beginning of the subsequent isothermal treatment. The absence of this behavior in the Ti64_900C_D might be explained by the fact that the β phase remaining after deformation transforms almost completely into secondary α colonies, as can be seen in Fig. 2. In this case, the final β phase is enriched in β -stabilizing elements due to depletion from the secondary α phase in comparison with the isolated β islands between primary α lamellae seen in Ti64_900C_HT condition [42].

5. Conclusions

The response of Ti-6Al-4V alloy with different starting microstructures to aging treatment has been evaluated. From this study, the following conclusions can be drawn:

- A wide variety of microstructures, ranging from martensitic to globular morphologies of the α phase with different amounts of the β phase, can be achieved by an adequate selection of thermal and thermomechanical processing routes.
- All produced microstructures have shown some degree of hardening after aging at 500 °C/24 h. The conditions with the highest hardness

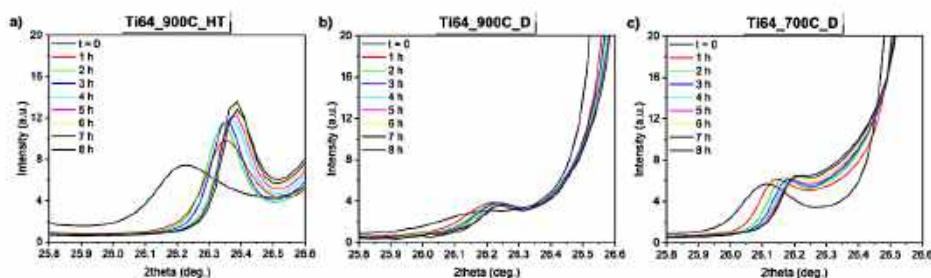


Fig. 10. Behavior of the (110) β reflection during aging of a) Ti64_900C_HT, b) Ti64_900C_D and c) Ti64_700C_D conditions.

values after aging were those with a predominantly martensitic microstructure, but the best response to aging in terms of hardness increase was shown in conditions with globular, Widmanstätten and bimodal microstructures with a higher content of β phase.

- In conditions with martensitic microstructure, the main contribution to the hardening of the alloy arises from the transformation of the martensitic α' phase into α , whereas in conditions with a high amount of β phase, hardening takes place by the decomposition of this phase into fine α platelets, and the precipitation of Ti_3Al also contributes to hardening when a high amount of primary α sufficiently enriched in Al and O is present.
- The distribution of the remaining β phase influences the precipitation of secondary α during aging, favoring such precipitation when it presents itself continuous along the boundaries of the α phase and hindering the precipitation when it is discontinuous and concentrated in triple boundaries.
- In situ analysis of the early stages of aging treatments show that the decomposition of the metastable α' phase is intensified in the beginning of the treatment. The reduction of the FWHM of reflections indicates homogenization by the conversion into the stable α phase and the increase of the c/a ratio indicates a contribution to hardening by the reduction in the number of active slip systems.
- In situ analysis of the early stages of aging treatments also show that the β undergoes chemical homogenization and shrinkage, which is caused by the difference in atomic radii of the partitioning elements.

Declaration of competing interest

No conflicts of interest exist.

Acknowledgements

The Materials Department of the Federal University of São Carlos (DEMa – UFSCar, São Carlos, Brazil) and the Metals Characterization and Processing Laboratory of the Brazilian Center for Research in Energy and Materials (CNPEM, Campinas, Brazil) are acknowledged for granting access to their facilities for the conduction of thermal and thermomechanical treatments and for TEM and EBSD analyses. The Deutsches Elektronen Synchrotron (Hamburg, Germany) is acknowledged for the use of P07B beamline and the Brazilian Synchrotron Light Laboratory is acknowledged for the use of XTMS experimental station of the XRD1 beamline for the (HE)XRD experiments hereby presented.

Funding

This work was supported by the National Council for Scientific and Technological Development – CNPq (grant number 161959/2015-6), by the Coordination for the Improvement of Higher Education Personnel – CAPES (grant number 88887.302880/2018-00 and PROBRAL project 88881.143948/2017-01), by the German Academic Exchange Service – DAAD (project DAAD PPP-Brazil 2018 – ID 57390937), by Fundação para a Ciência e Tecnologia (FCT – MCTES) via the project UIDB/00667/2020 (UNIDEMI) and by the CALIPSOplus project under the Grant Agreement 730872 from the EU Framework Programme for Research and Innovation HORIZON 2020 (project reference I-20190492 EC). H. C. Pinto is CNPq fellow. The funding source had no involvement in the development of the research or in the preparation of the article.

Data availability

The raw/processed data required to reproduce these findings cannot be shared at this time due to technical or time limitations.

References

- [1] J. Polunear, D. StJohn, J.-F. Nie, M. Qian, *Light Alloys: Metallurgy of the Light Metals*, 5th ed., Elsevier, 2017.
- [2] C. Leyens, M. Peters (Eds.), *Titanium and Titanium Alloys*, Wiley-VCH, 2003.
- [3] G. Lonzjering, J.C. Williams, *Titanium*, 2nd ed., Springer, 2007.
- [4] J.I. Proc, *Titanium: Physical Metallurgy, Processing and Applications*, ASM International, 2015.
- [5] M.J. Donachie Jr., *Titanium: A Technical Guide*, 2nd ed., ASM International, 2006.
- [6] M. Motyka, A. Baran-Sadłaja, J. Sienkiewicz, M. Wierzbinska, K. Gancarczyk, Decomposition of deformed α' martensitic phase in Ti-6Al-4V alloy, *Mater. Sci. Technol. (United Kingdom)*, 35 (2019) 260–272, <https://doi.org/10.1080/02670836.2018.1466418>.
- [7] T. Morita, K. Hataoka, T. Inaka, K. Kawasaki, Strengthening of Ti-6Al-4V alloy by short-time duplex heat treatment, *Mater. Trans.* 46 (2005) 1681–1686, <https://doi.org/10.2320/matertrans.46.1681>.
- [8] M. Stephen, M. Kalenda, S. Charles, S. Waldo, Effect of ageing treatment on the microstructure and hardness of the Ti6Al4V alloy, *Mater. Sci. Forum* 829 (2015) 194–199, <https://doi.org/10.4028/www.scientific.net/MSF.829-829.194>.
- [9] J.I. Qazi, O.N. Senkov, J. Rahim, F.H. Froese, Kinetics of martensite decomposition in Ti-6Al-4V-xHf alloys, *Mater. Sci. Eng. A* 359 (2003) 137–149, [https://doi.org/10.1016/S0921-5093\(03\)00350-2](https://doi.org/10.1016/S0921-5093(03)00350-2).
- [10] F.K. Gil Mor, D. Rodríguez, J.A. Planell, Influence of tempering temperature and time on the α' -Ti-6Al-4V martensite, *J. Alloys Compd.* 234 (1996) 287–289, [https://doi.org/10.1016/0925-8388\(95\)02057-8](https://doi.org/10.1016/0925-8388(95)02057-8).
- [11] R. Pedersen, *Microstructure and Phase Transformation of Ti-6Al-4V*, Luleå University of Technology, 2002.
- [12] B.D. Venkatesh, D.L. Chen, S.D. Bhole, Effect of heat treatment on mechanical properties of Ti-6Al-4V ELI alloy, *Mater. Sci. Eng. A* 506 (2009) 117–124, <https://doi.org/10.1016/j.msea.2008.11.018>.
- [13] S. Hémyry, F. Villerchaise, On the influence of ageing on the onset of plastic slip in Ti-6Al-4V at room temperature: insight on dwell fatigue behavior, *Scr. Mater.* 130 (2017) 157–160, <https://doi.org/10.1016/j.scriptamat.2016.11.042>.
- [14] Z. Wu, C. Qiu, V. Venkatesh, H.L. Fraser, R.E.A. Williams, G.B. Viswanathan, M. Thomas, S. Nag, R. Banerjee, M.H. Loreto, The influence of precipitation of α_2 on properties and microstructure in Ti6Al-6-4, *Mater. Trans. A* 44 (2013) 1706–1713, <https://doi.org/10.1007/s11661-012-1530-9>.
- [15] H. Carreon, A. Ruiz, B. Santoveña, Study of aging effects in a Ti-6Al-4V alloy with Widmanstätten and equiaxed microstructures by non-destructive means, *Adv. Conf. Proc.* 2014, pp. 739–745, <https://doi.org/10.1063/1.4864894>.
- [16] S. El-Hadad, M. Nady, W. Khalifa, A. Shashi, Influence of heat treatment conditions on the mechanical properties of Ti-6Al-4V alloy, *Can. Metall. Q.* 57 (2018) 186–193, <https://doi.org/10.1080/00084433.2017.1412557>.
- [17] Y. Ji, T.W. Hoa, F. Zhang, L.Q. Chen, Theoretical assessment on the phase transformation kinetic pathways of multi-component Ti alloys: application to Ti-6Al-4V, *J. Phase Equilibria Diffus.* 37 (2016) 53–64, <https://doi.org/10.1007/s11669-015-0436-9>.
- [18] I. Ansara, T. Dinsdale, M.H. Rand, COST 507 - Thermomechanical Database for Light Metal Alloys, (1998).
- [19] F. Zhang, S. Chen, Y.A. Chang, N. Ma, Y. Wang, Development of thermodynamic description of a pseudo-ternary system for multicomponent Ti64 alloy, *J. Phase Equilibria Diffus.* 28 (2007) 115–120, <https://doi.org/10.1007/s11669-006-9006-5>.
- [20] L.G. Martínez, R.U. Ichikawa, K. Inakuma, M.T.D. Orlando, X. Turrillas, Synchrotron diffraction characterization of alternative powder diffraction standards, *An. Do V. Encontro Científico Física Apl.* (2014) 115–117, <https://doi.org/10.5151/phyppc-efca-051>.
- [21] L. Lutterotti, S. Marchisio, H.-R. Wenk, A.S. Schultz, J.W. Richardson, Combined texture and structure analysis of deformed limestone from time-of-flight neutron diffraction spectra, *J. Appl. Phys.* 81 (1997) 594, <https://doi.org/10.1063/1.364220>.
- [22] X.F. Gu, T. Furuhara, W.Z. Zhang, PTCLab: free and open-source software for calculating phase transformation crystallography, *J. Appl. Crystallogr.* 49 (2016) 1099–1106, <https://doi.org/10.1107/S1600576716006075>.
- [23] L. Guo, X. Fan, G. Yu, H. Yang, Microstructure control techniques in primary hot working of titanium alloy bars: a review, *Chinese J. Aeronaut.* 29 (2015) 30–40, <https://doi.org/10.1016/j.cja.2015.07.011>.
- [24] A. Gheysarian, M. Abbasi, The effect of aging on microstructure, formability and springback of Ti-6Al-4V titanium alloy, *J. Mater. Eng. Perform.* 26 (2017) 374–382, <https://doi.org/10.1007/s11665-016-2431-7>.
- [25] K. Sofinowski, M. Šmíd, I. Kuběna, S. Virbò, N. Casati, S. Godet, H. Van Swygenhoven, In situ characterization of a high work hardening Ti-6Al-4V prepared by electron beam melting, *Acta Mater.* 179 (2019) 224–236, <https://doi.org/10.1016/j.actamat.2019.08.037>.
- [26] A. Kadecka, P.A.J. Bagot, T.L. Martin, J. Coakley, V.A. Vorontsov, M.P. Moody, H. Ishii, D. Rugg, D. Dye, The formation of ordered clusters in Ti-7Al and Ti-6Al-4V, *Acta Mater.* 112 (2016) 141–149, <https://doi.org/10.1016/j.actamat.2016.03.050>.
- [27] J.C. Williams, R.G. Baggerly, N.E. Paton, Deformation behavior of HCP Ti-Al alloy single crystals, *Mater. Trans. A* 33 (2002) 837–850, <https://doi.org/10.1007/s11661-002-1016-2>.
- [28] M.J. Slackburn, The ordering transformation in titanium-aluminum alloys containing up to 25 at. pct. Al, *Trans. Metall. Soc. AIME* 239 (1967) 1200–1208.
- [29] T.K.G. Nambodhiri, C.J. McMahon Jr., H. Herman, Decomposition of the α -phase in titanium-rich Ti-Al alloys, *Mater. Trans. A* 4 (1973) 1323–1331, <https://doi.org/10.1007/BF02644528>.

- [30] H. Wu, G. Fan, L. Geng, X. Cai, M. Huang, Nanoscale origins of the oriented precipitation of Ti₃Al in Ti-Al systems, *Scr. Mater.* 125 (2016) 34–38, <https://doi.org/10.1016/j.scriptamat.2016.07.037>.
- [31] P. Barralero-Vila, J. Gussone, J. Haubrich, S. Sandlöbes, J. Da Silva, P. Cloetens, N. Schell, G. Requena, Inducing stable $\alpha + \beta$ microstructures during selective laser melting of Ti-6Al-4V using intensified intrinsic heat treatments, *Materials (Basel)* 10 (2017) 1–14, <https://doi.org/10.3390/ma10030268>.
- [32] A. Radecka, J. Czakley, V.A. Voronin, T.L. Martín, P.A.J. Bago, M.P. Moody, D. Rugg, D. Eyo, Precipitation of the ordered α_2 phase in a near- α titanium alloy, *Scr. Mater.* 177 (2018) 81–85, <https://doi.org/10.1016/j.scriptamat.2018.02.015>.
- [33] S.L. Semiatin, N.C. Leikalich, C.A. Heck, A.E. Mann, N. Bozzolo, A.L. Pilchak, J.S. Tilley, Transient plastic flow and phase dissolution during hot compression of α/β titanium alloys, *Metall. Mater. Trans. A.* (2020), <https://doi.org/10.1007/s11661-020-05673-0>.
- [34] R. Boyer, G. Elsch, E.W. Collins, *Materials Property Handbook: Titanium Alloys*, ASM International, 1994.
- [35] G. Welsch, W. Bunk, Deformation modes of the α -phase of Ti-6Al-4V as a function of oxygen concentration and aging temperature, *Metall. Trans. A.* 13 (1982) 889–899, <https://doi.org/10.1007/BF02642403>.
- [36] J.Y. Lim, C.J. McMahon, D.P. Pope, J.C. Williams, The effect of oxygen on the structure and mechanical behavior of aged Ti-8 Wt pct Al, *Metall. Trans. A.* 7 (1976) 139–144, <https://doi.org/10.1007/BF02644050>.
- [37] E. Aeby-Gautier, P. Bruneseaux, J. Da Costa Teixeira, B. Appolaire, G. Geandier, S. Denis, Microstructural formation in Ti alloys: in-situ characterization of phase transformation kinetics, *JOM* 59 (2007) 54–58, <https://doi.org/10.1007/s11837-007-0011-x>.
- [38] T. Ungár, Microstructural parameters from X-ray diffraction peak broadening, *Scr. Mater.* 51 (2004) 777–781, <https://doi.org/10.1016/j.scriptamat.2004.05.007>.
- [39] J.M. Oh, B.G. Lee, S.W. Cho, S.W. Lee, G.S. Choi, J.W. Lim, Oxygen effects on the mechanical properties and lattice strain of Ti and Ti-6Al-4V, *Met. Mater. Int.* 17 (2011) 733–736, <https://doi.org/10.1007/s12540-011-1006-2>.
- [40] J.W. Elmer, T.A. Palmer, S.S. Babu, E.D. Specht, In situ observations of lattice expansion and transformation rates of α and β phases in Ti-6Al-4V, *Mater. Sci. Eng. A* 391 (2005) 104–113, <https://doi.org/10.1016/j.msea.2004.08.084>.
- [41] P. Barralero-Vila, G. Requena, T. Bulupe, M. Alford, U. Bossenborg, Role of element partitioning on the α/β phase transformation kinetics of a bi-modal Ti-6Al-6V-2Sn alloy during continuous heating, *J. Alloys Compd.* 626 (2015) 330–339, <https://doi.org/10.1016/j.jallcom.2014.11.176>.
- [42] G. Geandier, E. Aeby-Gautier, A. Settefrati, M. Dehmas, B. Appolaire, Study of diffusive transformations by high energy X-ray diffraction, *Comptes Rendus Phys* 13 (2012) 257–267, <https://doi.org/10.1016/j.crdp.2011.12.001>.

ANNEX B – Paper on thermomechanical processing of Ti-5Al-5Mo-5V-3Cr alloy



RightsLink[®]


Home


Help


Email Support


Sign in


Create Account



New insights into the microstructural evolution of Ti-5Al-5Mo-5V-3Cr alloy during hot working

Author:
B. Callegari, J.P. Oliveira, R.S. Coelho, P.P. Brito, N. Scheil, F.A. Soldera, F. Mücklich, M.I. Sadik, J.L. Garcia, H.C. Pinto

Publication: Materials Characterization

Publisher: Elsevier

Date: April 2020

© 2020 Elsevier Inc. All rights reserved.

Please note that, as the author of this Elsevier article, you retain the right to include it in a thesis or dissertation, provided it is not published commercially. Permission is not required, but please ensure that you reference the journal as the original source. For more information on this and on your other retained rights, please visit: <https://www.elsevier.com/about/our-business/policies/copyright#Author-rights>

BACK

CLOSE WINDOW

© 2020 Copyright - All Rights Reserved | Copyright Clearance Center, Inc. | [Privacy statement](#) | [Terms and Conditions](#)
Comments? We would like to hear from you. E-mail us at customercare@copyright.com



Contents lists available at ScienceDirect

Materials Characterization

journal homepage: www.elsevier.com/locate/matchar

New insights into the microstructural evolution of Ti-5Al-5Mo-5V-3Cr alloy during hot working

B. Callegari^{a,b}, J.P. Oliveira^c, R.S. Coelho^d, P.P. Brito^e, N. Schell^f, F.A. Soldera^b, F. Mücklich^b, M.I. Sadik^g, J.L. García^g, H.C. Pinto^{h,*}

^a University of São Paulo, São Carlos School of Engineering, Department of Materials Engineering, Av. João Dagnone 1100, 13563-120 São Carlos, Brazil

^b Saarland University, Department of Materials Science and Engineering, Campus D3.3, 66123 Saarbrücken, Germany

^c UNIDEMI, Department of Mechanical and Industrial Engineering, NOVA School of Science and Technology, Universidade NOVA de Lisboa, 2829-516 Caparica, Portugal

^d SENAI CIMATIC, Institute of Innovation for Forming and Joining of Materials, Av. Orlando Gomes 1845, 41650-010 Salvador, Brazil

^e Pontifical Catholic University of Minas Gerais, Av. Dom José Gaspar 500, 30535-901 Belo Horizonte, Brazil

^f Institute of Materials Research, Helmholtz-Zentrum Geesthacht, Max-Planck-Str. 1, D-21502 Geesthacht, Germany

^g AB Sandvik Coromant R&D, Lerkrogsvägen 19, SE 12680, Stockholm, Sweden



ARTICLE INFO

Keywords:

Titanium alloys
Thermomechanical processing
Microstructure evolution
Electron backscattered diffraction
Synchrotron X-ray diffraction

ABSTRACT

Microstructural features resulting from thermomechanical treatment of the β -metastable Ti-5Al-5Mo-5V-3Cr (Ti-5553) alloy were studied by means of electron backscatter diffraction and X-ray diffraction. The alloy was deformed at 950 °C (β field) and 800 °C ($\alpha + \beta$ field) with strain rates of 0.001 s^{-1} and 0.1 s^{-1} in compression mode up to a compression ratio of 0.5 (true ratio = 0.7). It was concluded that β phase undergoes dynamic recovery both above and below its β -transus temperature, and recovery is more dominant at lower strain rates, which was corroborated by EBSD misorientation measurements. Meanwhile, α phase undergoes not only a process of breakage and globalization, but also decomposition, which contributes to flow softening. The increase in strain rate caused non-uniform recovery at 950 °C and a more intense refinement of α precipitates at 800 °C. Macrotexture evaluation after deformation indicates that β 's texture is much stronger than that of α , with its (200) component being the strongest one.

1. Introduction

The advantages of β titanium alloys arise from their excellent combination of physical and mechanical properties, generally including good corrosion properties too. Additionally, these alloys have good processability, which can be attained by a wide range of routes. According to Nyakana, Fanning and Boyer [1], one feature that makes β -type Ti alloys genuinely unique is the possibility of tuning their elastic modulus within a fairly wide range by altering processing parameters.

Ti-5Al-5Mo-5V-3Cr (Ti-5553) alloy, commercially known as TIMETAL® 555, is a high-strength β titanium alloy that was designed as an improved version of the Russian alloy VT22 (Ti-5Al-5Mo-5V-1Cr-1Fe). The alloy possesses better combination of strength, ductility, and toughness than VT22, and a final part can be achieved through more simplified processing approaches. According to Nyakana et al., the Ti-5553 alloy is capable of achieving strengths levels as high as 1517 MPa

[1]. Besides improved processability and excellent mechanical properties, Ti-5553 alloy is also deeply hardenable [2]. As of 2005, the alloy was under evaluation to be employed in several major airframe components on new programs [1].

Ti-5553 is also frequently compared to Ti-10V-2Fe-3Al (Ti-1023), another widely used β alloy. Forging of both alloys is quite similar, but the higher β -transus of Ti-5553 enables forging operations in the $\alpha + \beta$ to be performed at temperatures approximately 56 °C higher [2]. Another processing feature that differentiates both alloys is that, for Ti-5553, primary forging can be conducted either in the β or $\alpha + \beta$ fields prior to the final $\alpha + \beta$ forging [3]. Both routes can achieve similar strength levels, but primary β forging promotes higher ductility and fracture toughness [4]. Another difference between Ti-5553 and Ti-1023 is that the first one can be air cooled after ageing with no deterioration of properties, whereas the latter needs to be water quenched to obtain the same results [5]. According to Fanning and Boyer [4], this limits the section thickness of parts produced with Ti-1023 to 76 mm,

* Corresponding author at: University of São Paulo, São Carlos School of Engineering, Department of Materials Engineering, Av. João Dagnone, 1100, 13563-120 São Carlos, SP, Brazil.

E-mail address: haroldo@sc.usp.br (H.C. Pinto).

<https://doi.org/10.1016/j.matchar.2020.110180>

Received 18 November 2019; Received in revised form 8 January 2020; Accepted 2 February 2020

Available online 04 February 2020

1044-5803/© 2020 Elsevier Inc. All rights reserved.

while sections 152 mm thick are attainable in parts fabricated using Ti-5553. An additional advantage of Ti-5553 over Ti-2013 is that it exhibits a more robust processability. Typically, new suppliers of Ti-1023 forgings must go through a learning curve to attain the desired levels of strength, ductility and toughness, whereas Ti-5553's forging suppliers have been able to supply products which meet the requirements at their first attempt. Similarly to Ti-1023, its highest recommended service temperature is around 315 °C [1].

Several works have been developed in order to understand Ti-5553 alloy's response to thermomechanical processing in terms of microstructural evolution and resulting mechanical properties. Jones et al. [5] have proposed that the initial flow behavior and the dominating deformation mechanism of the alloy depends on the morphology and fraction of α precipitates. They have also suggested that the flow softening observed is caused by the fragmentation of high aspect ratio α laths due to local strains resulting from the accumulation of dislocations. However, they have pointed out that the volume fraction of grain boundary α , for example, also affects the flow softening, but have not evaluated this contribution. Jones and Jackson [6] have reinforced that α plates become fragmented during the forging process and, depending on strain rate, they can transform into a well distributed globular microstructure. They also show that adiabatic heating effects are minimal during forging of small samples at low strain rates, thus attributing the flow softening solely to the fragmentation of α platelets. Finally, they have also confirmed what had been suggested in previous studies regarding accumulation of dislocations surrounding α platelets and their resulting role as barriers to deformation. Matsumoto et al. [7] have tested the alloy in a wide range of temperatures and deformation rates. They affirm that the behavior of stress-strain curves, with continuous flow softening at lower temperatures and higher strain rates and with achievement of a steady state at higher temperatures and lower strain rates, indicates that dynamic recovery becomes dominant with increasing temperature and decreasing strain rate, which has been corroborated by the calculation of activation energies of the β phase deformation. In microstructures deformed at and above 800 °C, they proposed the activation of continuous dynamic recrystallization in the vicinity of prior β grain boundaries at lower strain rates. There appears to be a general agreement that dynamic recovery of β phase governs deformation, and that the main softening mechanism is due to break-up and globularization of the α phase. This has also been proposed for Ti-1023 alloy [8,9]. Poletti et al. [10] also attribute softening to the coarsening of β subgrains.

A relevant aspect of studying the deformation behavior of β alloys arises from the need of understanding how deformation affects subsequent heat treatments, given that these alloys generally undergo ageing treatments to promote strengthening by precipitation of a refined α phase. It is well known that β alloys need nucleation sites to allow for α precipitation during ageing [11]. In this context, lattice defects such as dislocations and low-angle grain boundaries (LAGBs) may act as additional nucleation sites for phase precipitation. Furuhashi and Maki have reported on the crystallography of heterogeneous nucleation on defects during phase transformations in β titanium alloys and ferrous alloys, and have pointed out the role of dislocations and sub-grain boundaries as preferential nucleation sites [12]. This role has been reinforced in the review of Kolli and Devaraj on metastable β titanium alloys [13]. Teixeira et al. have modelled the effect of β phase plastic deformation on α precipitation during subsequent cooling and proposed that LAGBs act as nucleation sites for grain boundary α (α_{GB}) allotriomorph. They have also assessed the likelihood of Widmanstätten α colonies growth from α_{GB} (α_{WGS}) [14]. In a later work also involving modelling of α precipitation as influenced by deformation of the β phase, the same authors highlighted the importance of accurate information on the misorientation distributions of the β phase for the success of the developed model [15].

The present work provides a study on the microstructural evolution of the β -metastable alloy Ti-5553 subjected to deformation at different

Table 1
Composition of Ti-5553 alloy used in this work.

Element wt%	Ti Bal.	Al 5.36	Mo 4.42	V 5.01	Cr 2.93	Fe 0.48	O 0.16	C 0.03	N 0.005	H 0.002
[Al]eq		6.9			[Mo]eq			12.6		

strain rates both at β and $\alpha + \beta$ fields starting from a fully β condition. It complements works previously developed on the subject, providing a microtexture evaluation following deformation and evidences of the occurrence of phenomena such as non-uniform recovery and dynamic phase transformation, as well as relying on high energy X-ray diffraction as an additional tool to study the effects of deformation on the microstructure.

2. Materials and methods

2.1. Material

The composition of the Ti-5553 alloy used in this work is given in Table 1. Amounts of heavier elements, i.e. Al, Mo, V, Cr and Fe, were measured by inductively coupled plasma atomic emission spectrometry using an Ametek® SPECTROMAXx analyzer. Oxygen amount was analyzed via inert gas fusion using a Leco® RO-400 analyzer; nitrogen and hydrogen were analyzed with a Leco® ONH-836 equipment; and carbon was analyzed in a Leco® CS-844 analyzer. Its β -*transus* temperature, measured by differential scanning calorimetry in a Netzsch® 404 F3 Pegasus calorimeter with heating rate of 20 °C/min, is of approximately 875 °C. The as-received alloy presented the bimodal microstructure shown in Fig. 1, which comprises the α phase with globular morphology (primary α , α_p) and lamellar morphology (secondary α , α_s) within a β matrix. It is also possible to observe some remaining α phase at prior β grain boundaries (α_{GB}).

2.2. Thermomechanical treatments

The Ti-5553 alloy was thermomechanically treated by means of uniaxial compression at 950 °C (β field) and 800 °C ($\alpha + \beta$ field). Specimens with dimensions of $\phi 10 \times 15$ mm were cut from the as-received bar with their length parallel to the bar's length. To remove any effects of prior processing, specimens initially underwent a homogenization treatment at 950 °C during 30 min, followed by water quenching in an EDG 10P-S furnace with vacuum and argon atmosphere protection. Compressions were imposed in a Gleeble® 3800 thermomechanical simulator with strain rates of 10^{-1} s^{-1} and

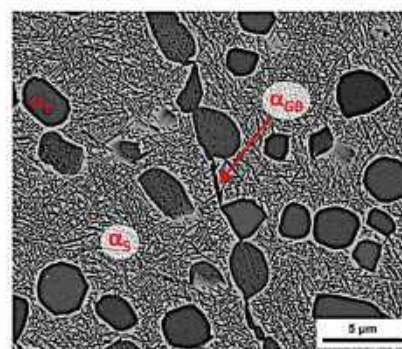


Fig. 1. Bimodal microstructure of the as-received Ti-5553 alloy with indication of the different α morphologies: α_p , α_s and α_{GB} .

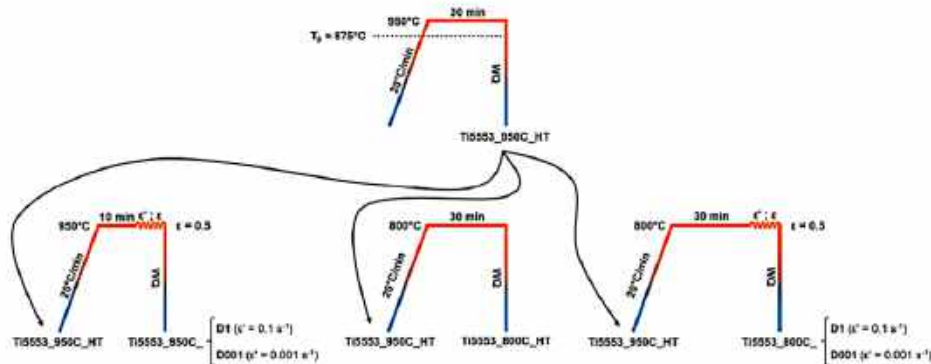


Fig. 2. Schematic representation of thermomechanical and heat treatments imposed to Ti-5553 alloy.

10^{-3} s^{-1} up to a compression ratio of 50% (true strain = 0.7). The alloy was also heat-treated at 800 °C without deformation for microstructural comparison between heat-treated and deformed conditions. Fig. 2 represents schematically the framework of treatments imposed to the alloy as well as the names given to each condition based on the treatment temperature (“950C” for 950 °C and “800C” for 800 °C) and type (“HT” for heat treatment and “D1” and “D001” for compressions with strain rates of 10^{-1} or 0.1 and 10^{-3} or 0.001 s^{-1} , respectively).

2.3. Microstructural characterization

The alloy was metallographically prepared for light optical microscopy (LOM) and scanning electron microscopy (SEM) according to the following procedure: manual grinding steps using #320, #600 and #1200 sandpapers, automated pre-polishing with a 3 μm diamond suspension and final automated polishing using a solution composed by 90 vol% 0.04 μm OP-S and 10 vol% H_2O_2 . Automated steps were carried out in a Buehler® EcoMet 250 machine (force: 5 N; base rotation: 20 rpm; head rotation: 60 rpm; counter-rotation). For the electron backscatter diffraction analyses (EBSD), the alloy was prepared following the same steps using a Struers® TegraPol-21 machine (force: 10 N; base rotation: 50 rpm; head rotation: 50 rpm; both rotations in the same direction). A final light manual polishing with the OP-S – H_2O_2 solution during 5 min. was added to ensure the removal of residual scratches from the surface. Samples were not chemically etched for microscopy.

LOM analyses were done in a Zeiss® Axio Scope.A1 optical microscope. SEM analyses were carried out in a FEI® Inspect F50 microscope with field emission gun using backscattered electrons’ (BSE) signal. EBSD analyses were conducted in a FEI® Helios NanoLab 600 microscope also equipped with field emission gun. Step sizes were 1 μm for maps with lower magnification and 200 nm for maps with higher magnification. In the case of compressed specimens, all images were done on the plane parallel to the compression axis.

2.4. Texture analysis

To evaluate the macrotexture evolution upon deformation, pole figures of (110) β , (200) β and (211) β reflections were measured for all deformed specimens. In the case of specimens deformed in the $\alpha + \beta$ field, pole figures of (0002) α , (10 $\bar{1}$ 0) α , (10 $\bar{1}$ 1) α , (10 $\bar{1}$ 2) α and (11 $\bar{2}$ 0) α reflections were also measured. Orientation distribution functions (ODFs) were calculated using all reflections and pole figures were re-calculated from calculated ODFs. Calculations were carried out using the MTEX toolbox for MATLAB® [16]. Measurements were done in a PANalytical® Empyrean X-ray diffractometer using Cu K α ($\lambda = 1.54 \text{ \AA}$)

radiation. The step size for both φ (0–360°) and ψ (0–85°) coordinates was 5°. In this case, measurements were done on the surface normal to the compression axis, which was polished following the same procedure adopted for EBSD analyses described in Section 2.3.

2.5. Synchrotron high energy X-ray diffraction

Produced conditions were analyzed using synchrotron high energy X-ray diffraction (HEXRD). Samples with $3 \times 4 \times 6 \text{ mm}^3$ were wire cut from the specimens. In the case of deformed conditions, samples were cut with their length parallel to the compression axis. Experiments were done in the P07B beamline of the PETRA III facility at DESY (Hamburg, Germany). The energy of the beam was 87.1 keV ($\lambda = 0.142 \text{ \AA}$). Complete Debye-Scherrer rings were acquired in transmission mode using a Perkin Elmer® 2D fast detector with $200 \times 200 \mu\text{m}^2$ pixel size. An exposure time of 0.2 s was used, and 5 frames/image were acquired using a spot size of $1 \times 1 \text{ mm}^2$. Acquired images were treated using ImageJ software to obtain the corresponding diffractograms.

Quantitative analyses were carried out on PeakFit and MAUD [17] softwares to obtain parameters such as phase fractions and width and area of peaks. The calculation of peak parameters on PeakFit was done using a combined Gauss + Lorentz profile and Rietveld refinement was done on MAUD after instrument calibration using a standard LaB $_6$ powder.

3. Results

Fig. 3 depicts the microstructures resulting from heat treatments and deformation. For specimens heat-treated and deformed at 950 °C, only LOM images are shown because the microstructure was composed solely by β phase grains. No precipitates were detectable even by SEM. It is possible to observe that both Ti5553_950C_HT and Ti5553_800C_HT samples present a microstructure composed by coarse equiaxed β grains. In the case of the Ti5553_800C_HT sample, a considerable amount of α phase is present both within grains and along grain boundaries. On the other hand, deformed conditions present elongated β grains with their longer axis perpendicular to the compression direction. With respect to the presence of the α phase, a significantly lower amount is present in comparison to the heat-treated condition. Moreover, comparing both deformed conditions, Ti5553_800C_D001 presents coarser α precipitates, with approximately the same size as those seen dispersed within β grains in Ti5553_800C_HT condition.

Fig. 4 presents the flow curves of Ti-5553 alloy upon deformation at both temperatures and strain rates. As expected, the lower the temperature and the higher the strain rate, the higher the peak stress. Also,

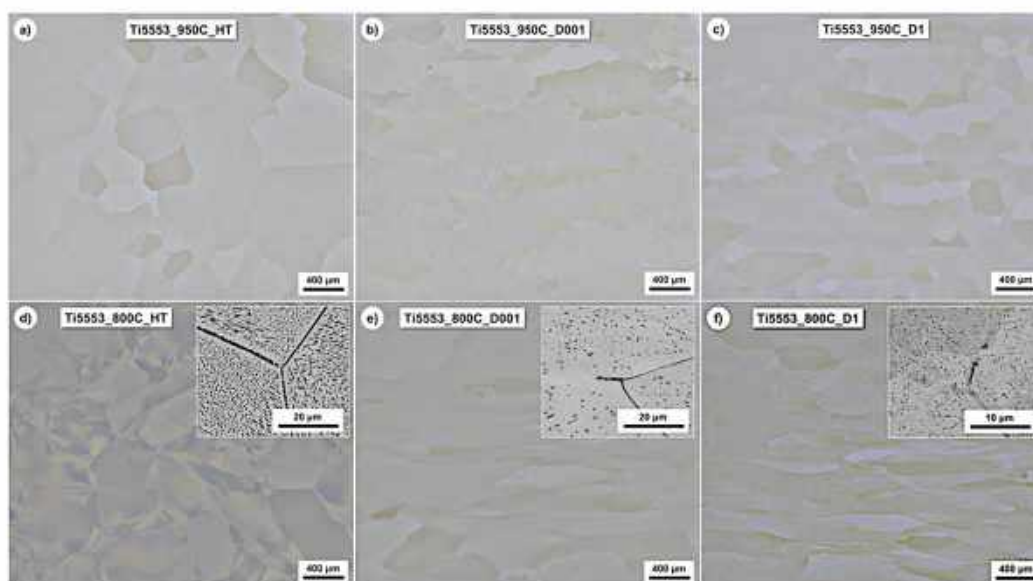


Fig. 3. Microstructures of a) Ti5553_950C_HT (LOM), b) Ti5553_950C_D001 (LOM), c) Ti5553_950C_D1 (LOM), d) Ti5553_800C_HT (LOM with a BSE-SEM image in the inset), e) Ti5553_800C_D001 (LOM with a BSE-SEM image in the inset) and f) Ti5553_800C_D1 (LOM with a BSE-SEM image in the inset). The compression axis is parallel to the height of images. The dark phase is α and the bright phase is β .

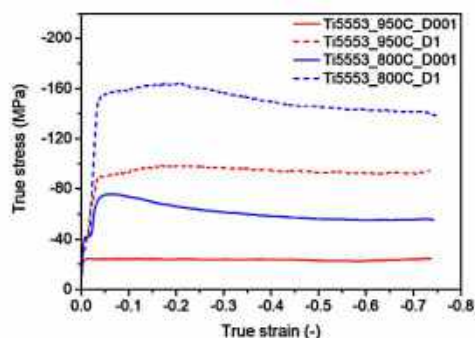


Fig. 4. Flow curves of Ti-5553 alloy upon uniaxial compression at 950 °C and 800 °C with strain rates of 0.001 s^{-1} and 0.1 s^{-1} .

In all cases it is possible to observe a steady state after the peak curve, without significant softening, indicating the dominance of dynamic recovery over recrystallization, especially during deformation in the β field. The occurrence of softening during compression in the $\alpha + \beta$ field further confirms that β phase undergoes solely dynamic recovery. Softening is thus attributed to the change in morphology of the α phase, i.e. its break-up and globularization. This is evidenced in this Ti-5553 alloy and also in other β alloys, such as Ti-1023, where α laths break up into a necklace of small α particles [8]. Jones and Jackson [6] have proposed that, during forging of Ti-5553 alloy with acicular α precipitates, the initial work hardening up to the peak stress is dominated by the pile-up of dislocations at α particles causing work hardening to a peak stress, point at which the local strain is sufficient to trigger the fragmentation of the α phase, removing dislocation barriers and

causing the flow stress drop.

Due to microstructural coarseness, a conventional XRD macrotexture analysis was carried out in order to maximize the probed area, hence increasing the amount of probed grains and consequently improving statistics for texture evaluation. Fig. 5 presents the calculated pole figures for Ti-5553 alloy deformed at 950 °C. It is possible to notice that (110) β texture does not vary significantly between both strain rates and is not expressive in neither of both cases, presenting the expected fiber texture with its highest intensity around $\psi = 45^\circ$. However, (200) β and (211) β textures vary considerable between both strain rates. The first is much more intense in Ti5553_950C_D001 with a strong fiber component, whereas it presents itself weaker in Ti5553_950C_D1, with the appearance of three additional poles around $\psi = 60^\circ$. The latter does not present intensity variation between both strain rates, but, in a similar manner as for (200) β reflection, it presents three additional poles at lower ψ values. The stronger (200) texture is in good agreement with previous works showing the strengthening of $\langle 100 \rangle$ fiber texture with decreasing strain rate in β alloys [18]. The formation of a strong $\langle 100 \rangle$ texture at low strain rates during compression is mainly attributed to dynamic strain-induced boundary migration, as proposed by Li et al. for the deformation of a Ti-5Al-5Mo-5V-1Cr-1Fe alloy [19].

Fig. 6 depicts the calculated pole figures of α and β reflections for when the material was deformed at 800 °C. No significant texture differences can be seen in the α phase with variation of strain rate. The most noticeable difference occurs for the (0002) α reflection, which presents a more defined fiber texture in Ti5553_800C_D001. With respect to the β phase, the most noticeable variation is seen between (200) β reflections, being the texture in the Ti5553_800C_D1 condition weakened, in a similar manner as for deformation in the single β field. In comparison with samples deformed at 950 °C, the texture of β is weakened. It is interesting to notice the difference in intensity distributions of (0002) α and (110) β pole figures in both conditions, given by the well-defined fiber aspect of the (110) β texture that is not strictly accompanied by the (0002) α texture, which shows slight deviations

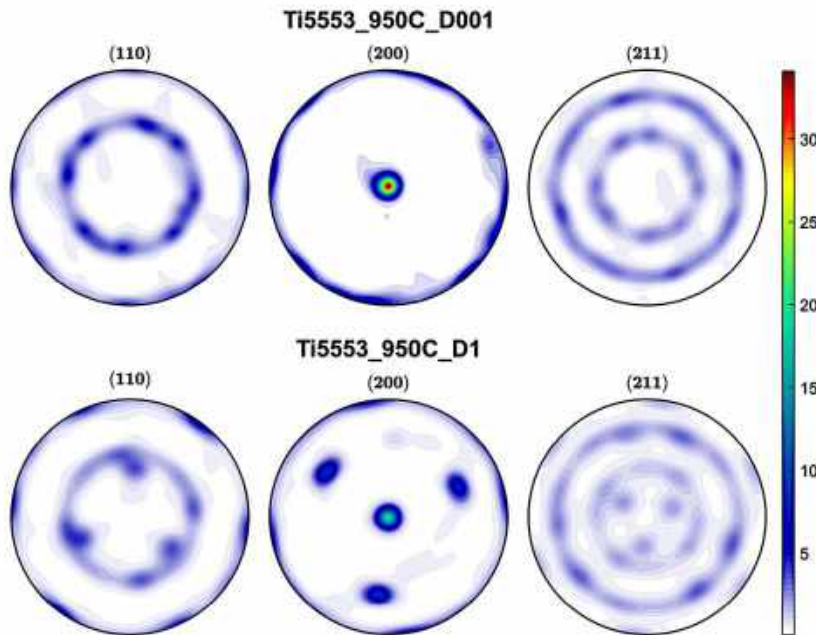


Fig. 5. Calculated pole figures of (110) β , (200) β and (211) β reflections of Ti-5553 alloy deformed at 950 °C.

from the Burgers orientation relationship (BOR) $\{0001\}\alpha||\{110\}\beta$ between α and β phases. Such deviations from the BOR after hot deformation have been observed in other alloys, such as Ti-7Mo-3Al-3Nb-3Cr [20] and Ti-5Al-5Mo-5V-1Cr-1Fe [21].

4. Discussion

4.1. Processing in the single β field

Fig. 7 shows the inverse pole figures (IPF) of the Ti-5553 alloy deformed at 950 °C. The compression direction lies in the vertical axis for all images. Additionally, plots of grain boundaries with indication of misorientation angles are shown in Fig. 7b and e. A misorientation angle of 15° was defined as the threshold to separate high-angle (HAB) and low-angle boundaries (LAB). In addition, it is possible to observe regions with different orientations inside prior grains in Fig. 7a and d, which indicate the presence of subgrains whose boundaries have not been outlined. Since the minimum software-defined threshold angle defined to identify boundaries is of 2°, the non-indexed regions represent boundaries with a misorientation lower than 2°, i.e. in the early stages of recovery. These are more clearly seen in the Kernel average misorientation (KAM) maps in Fig. 7c and f. Kernel average misorientation is useful to analyze dislocation density, being areas with low KAM values (blue) the leanest in dislocations and areas with high KAM values (red) the richest in dislocations [22]. As expected, the highest dislocation densities are concentrated along boundaries, and it is possible to observe that the average KAM is higher in the sample deformed with a higher rate. Given the absence of refined grains with high angle boundaries, no evidence of dynamic recrystallization was found. In Ti5553_950C_D1, it is also possible to observe coarse prior β grains without any apparent substructure formation, indicated by the arrows in Fig. 7d, which can also be seen in Fig. 3c. This non-uniform microstructure has been observed in the β -metastable Ti-5Al-5Mo-5V-1Cr-

1Fe titanium alloy after recrystallization in the β field following an $\alpha + \beta$ forging [23]. The difference in formation of substructures, which would form new grains with high angle boundaries during a subsequent recrystallization treatment, is given by the difference in interfacial energy of grains as function of their crystallographic orientation. During recrystallization, substructured grains can either evolve or be consumed by non-substructured grains. It is a phenomenon to be considered, since this heterogeneous restoration leads to a heterogeneous microstructure, which can be deleterious for the mechanical properties of the material.

The misorientation distribution of the β phase for both deformed conditions is given in Fig. 8. A higher fraction of low angle misorientations is seen in Ti5553_950C_D001, in accordance to the calculation of LABs' fractions carried out based on Fig. 7b and e, which yielded values of 48.9% for Ti5553_950C_D1 and 56.4% for Ti5553_950C_D001. This indicates the intensification of dynamic recovery with the reduction of strain rate. These results go against those typically observed during hot working of β titanium alloys in the β field, with the dominance of dynamic recovery at higher strain rates [7,18,24]. This can be explained by the heterogeneous deformation of grains that has already been discussed for Fig. 7. Not all grains have experienced the formation of substructures and therefore the resulting fraction of LABs is lower.

4.2. Processing in the $\alpha + \beta$ field

Fig. 9 shows the IPF maps of Ti-5553 alloy deformed at 800 °C. Due to the coarse step size used in comparison to the size of α precipitates as seen in SEM images (see Fig. 3), smaller areas were chosen within the larger maps to be scanned with a finer step size. In these conditions, it is possible to observe that α precipitates are more homogeneously distributed within the β matrix and also on grain boundaries in Ti5553_800C_D001 condition, whereas for Ti5553_800C_D1 condition they are highly concentrated along grain boundaries, being present in a

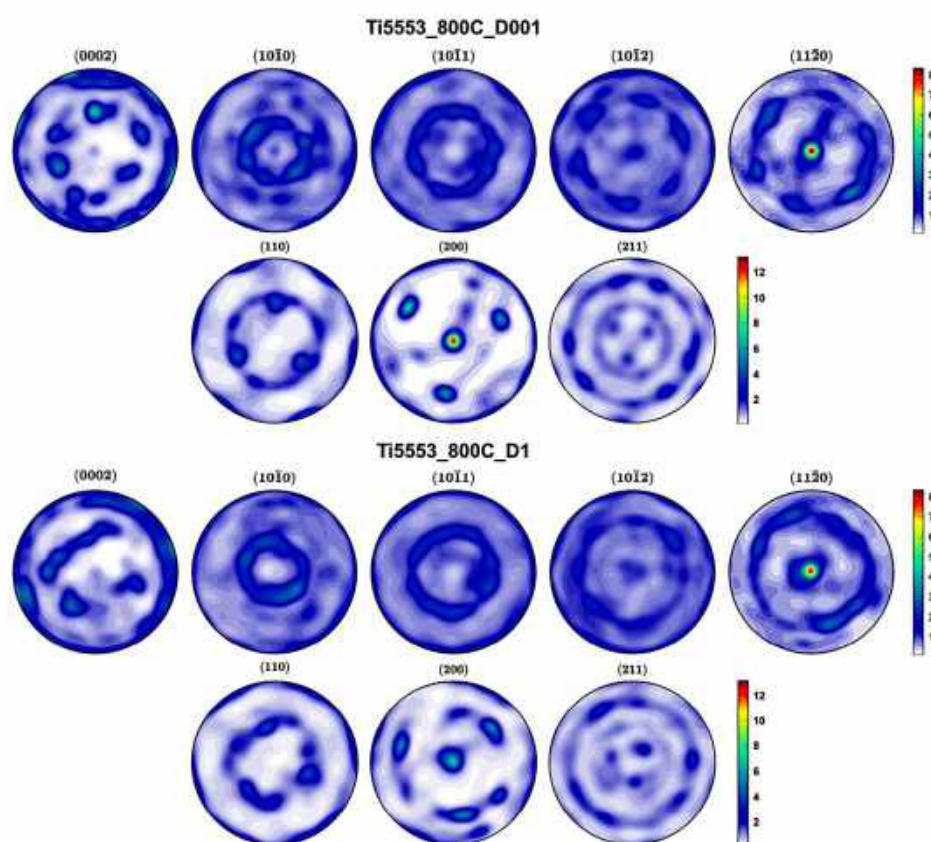


Fig. 6. Calculated pole figures of (0002) α , (10 $\bar{1}$ 0) α , (10 $\bar{1}$ 1) α , (10 $\bar{1}$ 2) α and (11 $\bar{2}$ 0) α , (110) β , (200) β and (211) β reflections of Ti-5553 alloy deformed at 800 °C.

much lower amount inside β grains. Also, the Ti5553.800C.D001 sample shows a typical feature of dynamic recovery: elongated grains with serrated primary boundaries. Additionally, one can notice the degree of fragmentation of α particles upon faster deformation. Finally, it is also possible to notice a more intense substructure formation within prior β grains with resulting coarser sub-grains in the slowly deformed condition in comparison with the one deformed with higher strain rate, in which the formation of finer sub-grains is more restricted to the boundaries of prior β grains. The distribution of the α phase seen in this work after deformation in the $\alpha + \beta$ field further exemplifies the role of boundaries on the preferred precipitation of α [20,25].

4.2.1. Behavior of β phase

The substructure distribution can be seen more clearly in the maps of grain boundaries for both conditions shown in Fig. 10a and b, whose threshold was defined in the same manner as for conditions deformed at 950 °C. Fractions of LABs for Ti5553.800C.D001 and Ti5553.800C.D1 were 44.0% and 37.6%, respectively. Here, again, it is possible to observe adjacent regions with different orientations that indicate the presence of sub-grains whose boundaries were not indexed. These also correspond to boundaries in the early stages of recovery with a misorientation lower than 2°. In Ti5553.800C.D001, it is also possible to notice the presence of recrystallized grains decorating prior β grain boundaries in a necklace structure, indicating the occurrence of

discontinuous dynamic recrystallization as well [26]. The Kernel average misorientation maps of each condition are shown in Fig. 10c and d. Again, the rapidly deformed condition presents a higher dislocation density and therefore a higher KAM value. In comparison to conditions deformed at 950 °C, the average KAM is higher, being the highest values concentrated in boundaries with the presence of α , indicating a higher dislocation density in the vicinities of α precipitates.

Fig. 11 summarizes the misorientation distribution of β phase for the conditions deformed at 800 °C. In this case, the higher fraction of low angle misorientations is evident, indicating that in the dual phase field, dynamic recovery becomes dominant with decreasing strain rate [7].

4.2.2. Fragmentation and decomposition of a phase during deformation

As seen in the SEM insets in Fig. 3, the amount of α phase has decreased considerably in both deformed conditions with respect to the heat-treated condition. Fig. 12 presents the temperature read by thermocouples during treatment, where a slight temperature variation of ± 7 °C can be seen. Earlier studies have shown that adiabatic heating effects are negligible when forging small samples at strain rates of the order of the ones used in this study [6]. This demonstrates that a dynamic decomposition of α phase occurs, presenting itself as an additional softening mechanism. These findings go against those from Jones et al. [27] during thermomechanical processing of the same alloy with

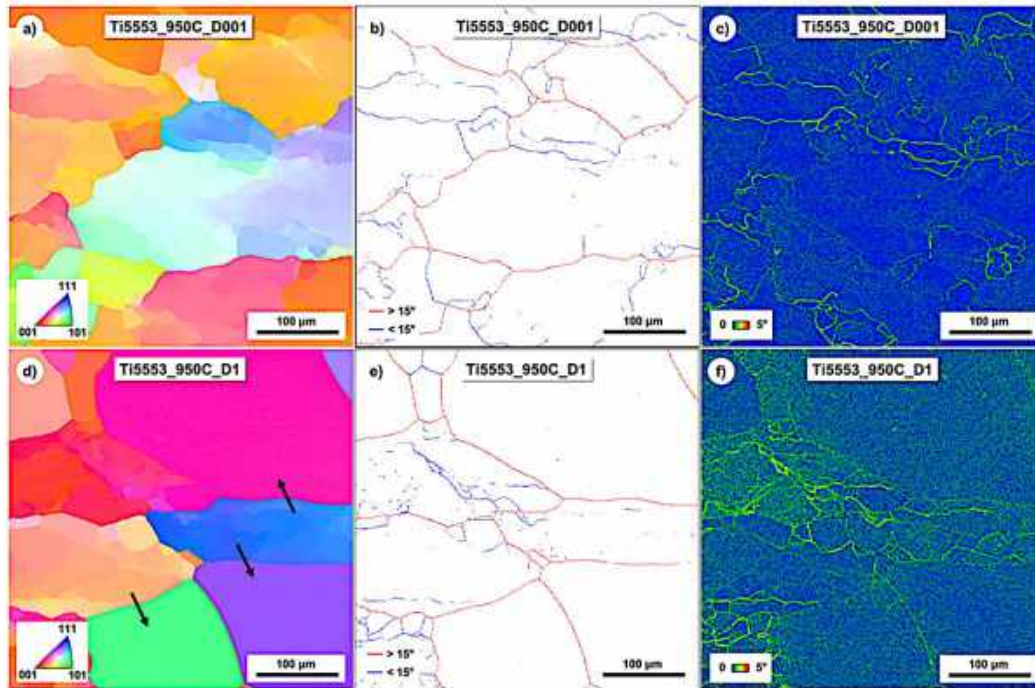


Fig. 7. a) IPF, b) grain boundary and c) Kernel average misorientation maps of Ti5553_950C_D001 condition, and d) IPF, e) grain boundary and f) Kernel average misorientation maps of Ti5553_950C_D1 condition. The compression axis is parallel to the height of images.

an initial microstructure composed by globular α dispersed in a β matrix, in which the initial globular α morphology was maintained with little or no alteration, and the α size distribution showed almost no deviation among strain rates, indicating there was no effect of strain rate on particle size. On the other hand, it agrees well with the results from Matsumoto et al. [7], who observed a decrease in α fraction with the increase of strain rate. Nonetheless, Matsumoto et al. propose a dynamic precipitation of α , with an increase in precipitation with the decrease in strain rate, and the present results show that what occurs, in fact, is a dynamic decomposition of α into β that intensifies with the

increase in strain rate.

The dissolution of α during deformation has been observed for Ti-5553 [10,28] and Ti-5Al-5Mo-5V-3Cr-1Zr (Ti-55531) [29] alloys at moderate strain rates. In the latter, α dissolution at low strain rates is attributed to a modification of equilibrium conditions due to deformation or to a non-equilibrium condition of the alloy before deformation. Nevertheless, because the volume fraction of α is even lower after deformation at higher strain rate, dissolution due to the aforementioned adiabatic heating might be a hypothesis. However, thermodynamic simulations are necessary to confirm this assumption.

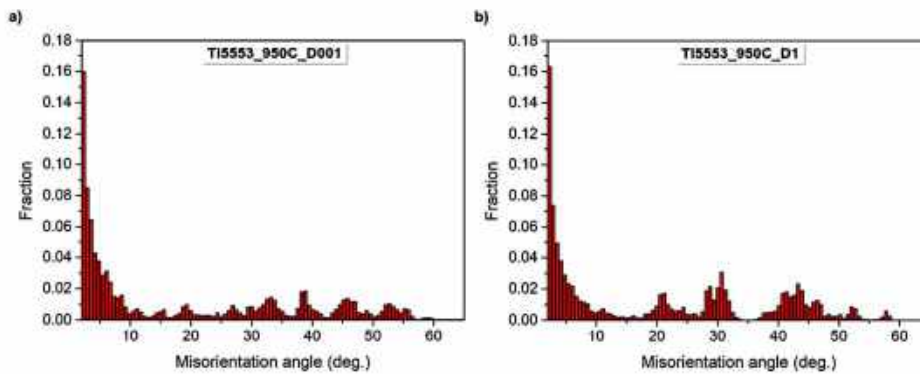


Fig. 8. Misorientation distributions of the β phase in a) Ti5553_950C_D001 and b) Ti5553_950C_D1 conditions.

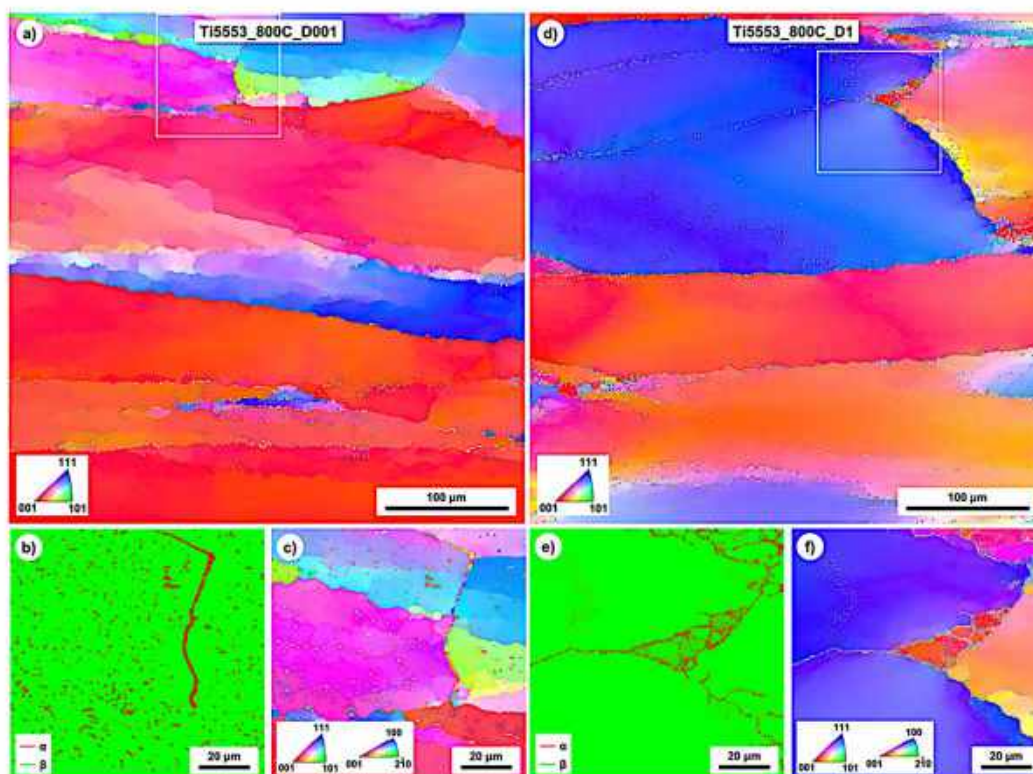


Fig. 9. a) Low magnification IPF, b) high magnification phase map and c) high magnification IPF of Ti5553_800C_D001 condition, and d) low magnification IPF, e) high magnification phase map and f) high magnification IPF of Ti5553_800C_D1 condition. The white squares indicate the chosen areas for the higher magnification mapping, and the compression axis is parallel to the height of images.

Given the difference between the size of α precipitates between deformed conditions, ImageJ color thresholding was used to calculate size and distribution of particles. The calculations were done using the phase maps in Fig. 9b and e. Because of the irregular shape of precipitates in Ti5553_800C_D001 condition, the size was calculated based on the area, not on the diameter of particles (for which an assumption of spherical particles would need to be made). Fig. 13 presents the plots of size distribution with the resulting weighted average size for each case. As expected from microstructure images, the average size of precipitates in Ti5553_800C_D001 is considerably larger than in Ti5553_800C_D1.

In Fig. 14, the misorientation distribution of the α phase can be observed. The distribution in the Ti5553_800C_HT condition is similar to that previously verified for strain-free α phase in a quenched Ti-6Al-4V alloy [30,31]. The peaks at $\sim 60^\circ$ and $\sim 90^\circ$ correspond to different variants of the Burgers orientation relationship selected during the $\beta \rightarrow \alpha$ transformation ($60^\circ/[111\ 20]$; $60.83^\circ/[1337\ 1\ 2.377\ 0.359]$; $63.26^\circ/[10\ 5\ 5\ 3]$; $90^\circ/[1\ 238\ 1.38\ 0]$). In the deformed condition, α 's misorientation behavior is remarkably different. However, in both cases a tendency is seen to follow the so-called Mackenzie distribution [32], which is the theoretical misorientation distribution for a perfectly random polycrystal, i.e. without preferential orientation [33]. This tendency is significantly more evident in the Ti5553_800C_D1 condition. These results are in good agreement with the pole figures in Fig. 6, which show a weak α texture. Also, misorientation results show that the

more fragmented the α phase is, the more random its orientation becomes.

High energy synchrotron X-ray diffraction data was used for phase quantification. Given the coarse microstructure, the possibility of running the experiment in transmission mode and the relatively large spot size enabled the acquisition of significant data volume from the bulk of samples. This makes phase quantification following this route more reliable with respect to EBSD, given the fact that α is not homogeneously distributed and the probed area might not be representative enough. Diffractograms were integrated from the complete Debye-Scherrer rings acquired and Fig. 15 presents the resulting patterns for all conditions. In Fig. 15a, the main β reflections are identified for clarification, and α and β reflections are indicated in Fig. 15b. In Table 2 are shown the volume fractions obtained in all conditions produced at 800 °C ($R_{wp} \leq 0.1040$). An expressive difference between heat-treated and deformed conditions can be observed, in accordance with previously discussed results.

The average values of full width at half maximum (FWHM) and area of the three main β peaks, i.e. (110), (200) and (211) were measured ($R^2 \geq 0.9578$). Results are shown in Fig. 16. It is possible to observe that (110) β and (211) β follow the same tendency regardless of temperature: their areas and FWHM increase as strain rate decreases, and heat-treated conditions present the highest FWHM and lowest area values. However, (200) β follows opposite tendencies: at 950 °C, both FWHM and area increase with decreasing strain rate, while at 800 °C

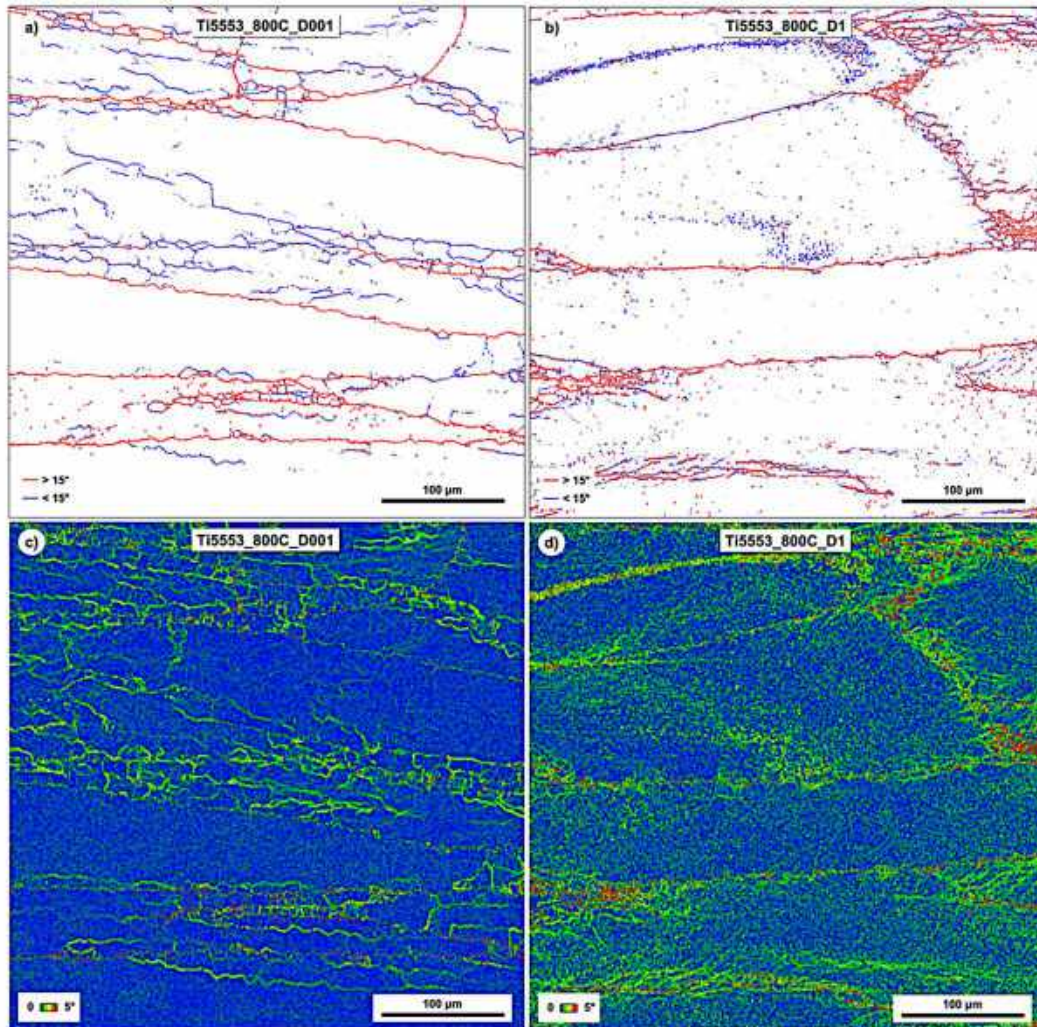


Fig. 10. Grain boundary maps of a) Ti5553_800C_D001 and b) Ti5553_800C_D1 conditions, and Kernel average misorientation maps of c) Ti5553_800C_D001 and d) Ti5553_800C_D1 conditions. The compression axis is parallel to the height of images.

the values of both parameters decrease. This can be correlated with results discussed above: dynamic recovery is associated with the formation of strong $\langle 100 \rangle$ textures, but dynamic recovery dominance increases with increasing temperature and strain rate. Therefore, the behavior of $(200)\beta$ reflection is mostly affected, with the intensification of dynamic recovery causing a decrease in its FWHM and area.

5. Conclusions

The microstructure of the β -metastable Ti-5Al-5Mo-5V-3Cr (Ti-5553) alloy after isothermal compression at 950 °C (β field) and 800 °C ($\alpha + \beta$ field) with strain rates of 10^{-1} s^{-1} and 10^{-3} s^{-1} up to a compression ratio of 50% has been evaluated. From this study, the

following conclusions can be drawn:

- β undergoes dynamic recovery in all cases. Recovery is more dominant at lower strain rates in the $\alpha + \beta$ field, as shown by the evolution of the phase's misorientation. In the single β field, misorientation analyses also imply that recovery is more dominant at lower strain rates, due to non-uniform deformation of grains during rapid deformation.
- During deformation in the β field with a higher strain rate, the occurrence of non-uniform recovery has been observed. This is critical to industrial processing, since the phenomenon causes a microstructural inhomogeneity that can affect mechanical properties of the alloy.

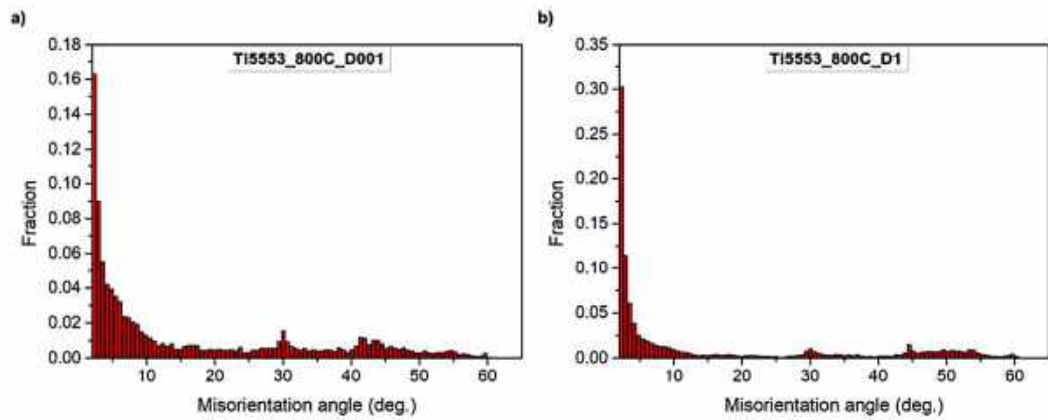


Fig. 11. Misorientation distribution of the β phase for a) Ti5553_800C_D001 and b) Ti5553_800C_D1 conditions.

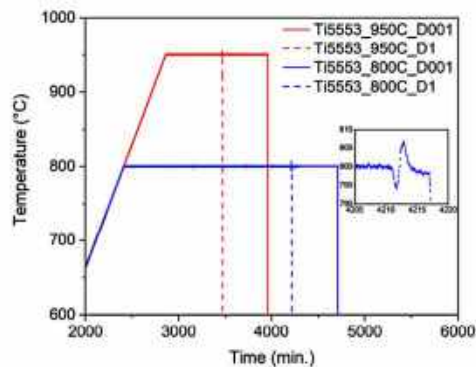


Fig. 12. Temperature evolution during treatments with an inset showing temperature variation during deformation of Ti5553_800C_D1 condition.

- When the alloy is deformed in the $\alpha + \beta$ field, α undergoes breakage and globularization during deformation. In addition, the amount of α has varied significantly between heat-treated and deformed conditions, indicating that α also decomposes during deformation.
- Upon deformation with higher strain rates, α has shown itself to suffer a more intense globularization and refinement with respect to deformation at lower strain rates.
- Macrotecture evaluation has shown that only the texture of the β phase is significantly affected by deformation, more specifically the (200) component, whereas α phase's texture presents itself relatively weak. This is in agreement with misorientation evaluation, since deformation causes a misorientation distribution which approaches the random distribution.

Acknowledgements

The Materials Department of the Federal University of São Carlos (DEMa – UFSCar, São Carlos, Brazil) and the Metals Characterization and Processing Laboratory of the Brazilian Center for Research in

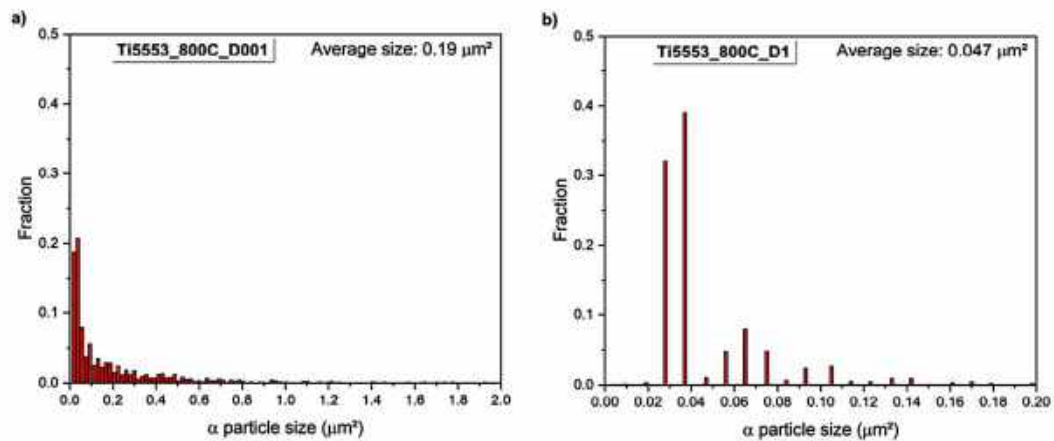


Fig. 13. Size distribution of α particles in a) Ti5553_800C_D001 and b) Ti5553_800C_D1 conditions.

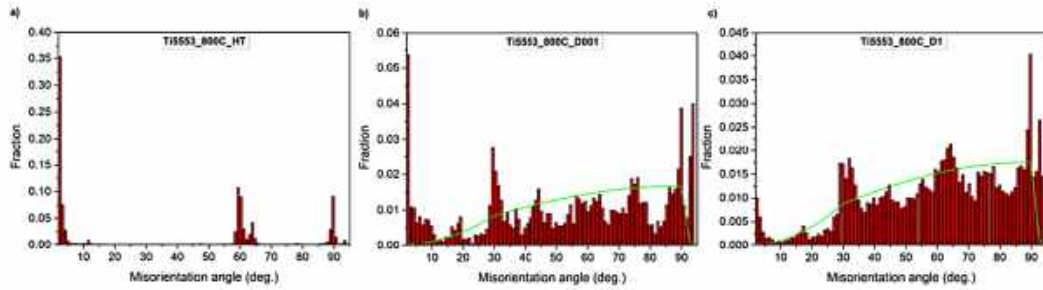


Fig. 14. Misorientation distribution of α phase in a) Ti5553_800C_HT, b) Ti5553_800C_D001 and c) Ti5553_800C_D1 conditions. The green curves are the corresponding Mackenzie (random) distributions. (For interpretation of the references to color in this figure legend, the reader is referred to the web version of this article.)

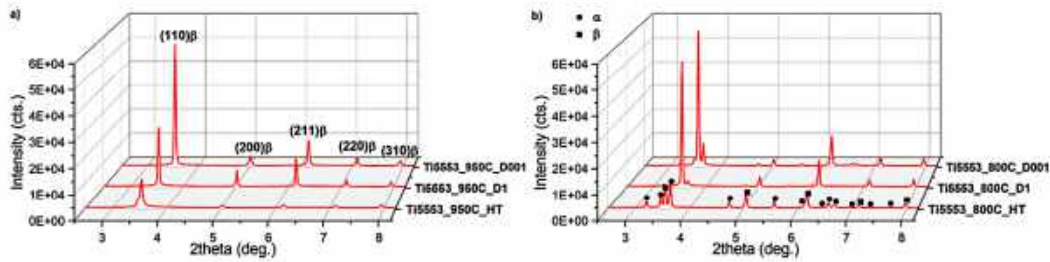


Fig. 15. Resulting diffractograms of conditions produced at a) 950 °C and b) 800 °C with identification of β reflections and differentiation between α and β reflections.

Table 2

Volume fractions of α phase obtained for all conditions of Ti-5553 alloy at 800 °C.

Condition	Ti5553_800C_HT	Ti5553_800C_D1	Ti5553_800C_D001
α fraction (%)	67.4 ± 0.7	8.4 ± 0.6	24.3 ± 0.5

thermomechanical treatments. The *Deutsches Elektronen Synchrotron* (Hamburg, Germany) is acknowledged on the use of P07B beamline for the HEXRD experiments hereby presented. AB Sandvik Coromant R&D (Stockholm, Sweden) is also acknowledged for the provision of the studied material.

Funding

This work was supported by the National Council for Scientific and Technological Development – CNPq (grant number 161959/2015-6).

Energy and Materials (CNPEM, Campinas, Brazil) are acknowledged for opening their facilities for the conduction of thermal and

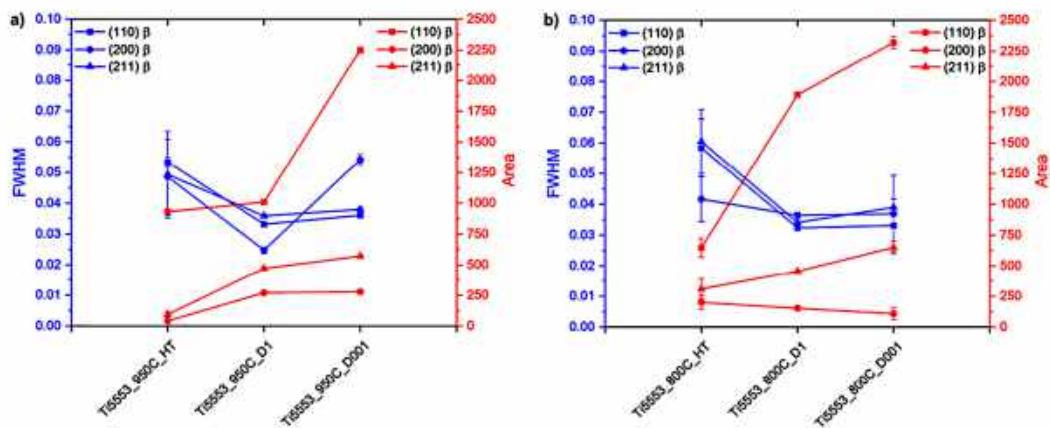


Fig. 16. Average full width at half maximum (FWHM) and area evolution of (110) β , (200) β and (211) β peaks for conditions produced at a) 950 °C and b) 800 °C.

by the Coordination for the Improvement of Higher Education Personnel – CAPES (grant number 88887.302880/2018-00 and PROBRAL project 88881.143948/2017-01), by the German Academic Exchange Service – DAAD (project DAAD PPP-Brazil 2018 – ID 57390937), by Fundação para a Ciência e Tecnologia (FCT – MCTES) via the project UIDB/00667/2020 (UNIDEMI) and by the CALIPSOplus project under the Grant Agreement 730872 from the EU Framework Programme for Research and Innovation HORIZON 2020 (project reference I-20190492 EC). H. Pinto is CNPq fellow. The funding source had no involvement in the development of the research or in the preparation of the article.

Data availability

The raw/processed data required to reproduce these findings cannot be shared at this time due to technical or time limitations.

Declaration of competing interest

The authors declare that they have no known competing financial interests or personal relationships that could have appeared to influence the work reported in this paper.

References

- [1] S.L. Nyakana, J.C. Fanning, R.R. Boyer, Quick reference guide for β titanium alloys in the 0s, *J. Mater. Eng. Perform.* 14 (2005) 799–811, <https://doi.org/10.1361/105994905X75646>.
- [2] J.C. Fanning, Properties of TIMETAL 555 (Ti-5Al-5Mo-5V-3Cr-0.6Fe), *J. Mater. Eng. Perform.* 14 (2005) 788–791, <https://doi.org/10.1361/105994905X75628>.
- [3] R.R. Boyer, R.D. Briggs, The use of β titanium alloys in the aerospace industry, *J. Mater. Eng. Perform.* 14 (2005) 680–684, <https://doi.org/10.1007/s11665-013-0728-3>.
- [4] J.C. Fanning, R.R. Boyer, Properties of TIMETAL 555 – a new near-beta titanium alloy for airframe components, Proc. 10th World Conf. Titan, 2003, pp. 2643–2650.
- [5] N.G. Jones, R.J. Dashwood, D. Dye, M. Jackson, The flow behavior and microstructural evolution of Ti-5Al-5Mo-5V-3Cr during subtransus isothermal forging, *Metall. Mater. Trans. A* 40 (2009) 1944–1954, <https://doi.org/10.1007/s11661-009-9966-5>.
- [6] N.G. Jones, M. Jackson, On mechanism of flow softening in Ti-5Al-5Mo-5V-3Cr, *Mater. Sci. Technol.* 27 (2010) 1025–1032, <https://doi.org/10.1179/026708310x12668415533720>.
- [7] H. Matsumoto, M. Kitamura, Y. Li, Y. Koizumi, A. Chiba, Hot forging characteristic of Ti-5Al-5V-5Mo-3Cr alloy with single metastable β microstructure, *Mater. Sci. Eng. A* 611 (2014) 337–344, <https://doi.org/10.1016/j.msea.2014.06.006>.
- [8] M. Jackson, N.G. Jones, D. Dye, R.J. Dashwood, Effect of initial microstructure on plastic flow behaviour during isothermal forging of Ti-10V-2Fe-3Al, *Mater. Sci. Eng. A* 501 (2009) 248–254, <https://doi.org/10.1016/j.msea.2008.09.071>.
- [9] M. Jackson, R. Dashwood, I. Christodoulou, H. Flower, The microstructural evolution of near beta alloy Ti-10V-2Fe-3Al during subtransus forging, *Metall. Mater. Trans. A* 36 (2005) 1317–1327, <https://doi.org/10.1007/s11661-005-0223-z>.
- [10] M.C. Poletti, R. Buzolin, S. Kumar, P. Wang, T.F.J. Simoes-Foto, Microstructure evolution of Ti-5Al-5V-5Mo-3Cr after hot deformation at large and moderate strains, *Mater. Sci. Forum* 941 (2018) 1443–1449, <https://doi.org/10.4028/www.scientific.net/MSF.941.1443>.
- [11] J. Coakley, V.A. Vorontsov, N.G. Jones, A. Radecka, P.A.J. Bagot, K.C. Littrell, R.K. Heenan, F. Hu, A.P. Magyari, D.C. Bell, D. Dye, Precipitation processes in the beta-titanium alloy Ti-5Al-5Mo-5V-3Cr, *J. Alloys Compd.* 646 (2015) 945–953, <https://doi.org/10.1016/j.jallcom.2015.05.251>.
- [12] T. Furuhara, T. Maki, Variant selection in heterogeneous nucleation on defects in diffusional phase transformation and precipitation, *Mater. Sci. Eng. A* 312 (2001) 145–154, [https://doi.org/10.1016/S0921-5093\(00\)01904-3](https://doi.org/10.1016/S0921-5093(00)01904-3).
- [13] R.P. Kollá, A. Devaraj, A review of metastable beta titanium alloys, *Metals (Basel)* 8 (2018) 506–546, <https://doi.org/10.3390/met8070506>.
- [14] J.C. Teixeira, E. Appolaire, E. Acby-Gautier, S. Denis, F. Bruneseaux, Modeling of the effect of the β phase deformation on the α phase precipitation in near- β titanium alloys, *Acta Mater.* 54 (2006) 4261–4271, <https://doi.org/10.1016/j.actamat.2006.05.019>.
- [15] J.C. Teixeira, E. Appolaire, E. Acby-Gautier, S. Denis, L. Hélicher, Modeling of the phase transformations in near- β titanium alloys during the cooling after forging, *Comput. Mater. Sci.* 42 (2008) 266–280, <https://doi.org/10.1016/j.commatsci.2007.07.056>.
- [16] F. Bachmann, R. Hielscher, H. Schaeben, Texture analysis with MTEX – free and open source software toolbox, *Solid State Phenom.* 160 (2010) 63–68, <https://doi.org/10.4028/www.scientific.net/ssp.160.63>.
- [17] L. Lutterotti, S. Mathies, H.-R. Wenk, A.S. Schultz, J.W. Richardson, Combined texture and structure analysis of deformed limestone from time-of-flight neutron diffraction spectra, *J. Appl. Phys.* 81 (1997) 594, <https://doi.org/10.1063/1.364220>.
- [18] J.K. Fan, H.C. Kou, M.J. Lai, B. Tang, H. Chang, J.S. Li, Hot deformation mechanism and microstructure evolution of a new near β titanium alloy, *Mater. Sci. Eng. A* 584 (2013) 121–132, <https://doi.org/10.1016/j.msea.2013.07.019>.
- [19] K. Li, P. Yang, The formation of strong (100) texture by dynamic strain-induced boundary migration in hot compressed Ti-5Al-5Mo-5V-1Cr-1Fe alloy, *Metals (Basel)* 7 (2017) 1–8, <https://doi.org/10.3390/met7100412>.
- [20] K. Hua, J. Li, H. Kou, J. Fan, M. Sun, B. Tang, Phase precipitation behavior during isothermal deformation in β -quenched near beta titanium alloy Ti-7333, *J. Alloys Compd.* 671 (2016) 381–388, <https://doi.org/10.1016/j.jallcom.2016.02.102>.
- [21] M. Klimova, S. Zherebtsov, G. Salishchev, S.I. Semiatin, Influence of deformation on the Burgers orientation relationship between the α and β phases in Ti-5Al-5Mo-5V-1Cr-1Fe, *Mater. Sci. Eng. A* 645 (2015) 292–297, <https://doi.org/10.1016/j.msea.2015.08.008>.
- [22] Q. Zhao, F. Yang, R. Torrens, I. Bolzoni, Comparison of hot deformation behaviour and microstructural evolution for Ti-5Al-5V-5Mo-3Cr alloys prepared by powder metallurgy and ingot metallurgy approaches, *Mater. Des.* 169 (1–16) (2019) 107682, <https://doi.org/10.3390/ma12030457>.
- [23] S. Huang, Y. Ma, S. Zhang, S.S. Youssef, J. Qin, H. Wang, B.Y. Zeng, J. Lei, B. Yang, Nonuniform recrystallization and growth behavior of β grains dominated by grain misorientation and interfacial energy in metastable β titanium alloy, *Metall. Mater. Trans. A Phys. Metall. Mater. Sci.* 49 (2018) 6390–6400, <https://doi.org/10.1007/s11661-018-4933-4>.
- [24] X. Liu, D. Yu, Q. Fan, R. Shi, Influence of hot rolling and heat treatment on the microstructural evolution of β 20C titanium alloy, *Materials (Basel)* 10 (2017) 1071, <https://doi.org/10.3390/ma10091071>.
- [25] T. Liu, L. Germain, J. Teixeira, E. Acby-Gautier, N. Gey, Hierarchical criteria to promote fast and selective $\alpha\beta$ precipitation at β grain boundaries in β -metastable Ti-alloys, *Acta Mater.* 141 (2017) 97–108, <https://doi.org/10.1016/j.actamat.2017.08.063>.
- [26] X.G. Fan, Y. Zhang, P.F. Gao, Z.N. Lei, M. Zhan, Deformation behavior and microstructure evolution during hot working of a coarse-grained Ti-5Al-5Mo-5V-3Cr-1Zr titanium alloy in beta phase field, *Mater. Sci. Eng. A* 694 (2017) 24–32, <https://doi.org/10.1016/j.msea.2017.03.095>.
- [27] N.G. Jones, R.J. Dashwood, D. Dye, M. Jackson, Thermomechanical processing of Ti-5Al-5Mo-5V-3Cr, *Mater. Sci. Eng. A* 490 (2008) 369–377, <https://doi.org/10.1016/j.msea.2008.01.055>.
- [28] Q. Zhao, F. Yang, R. Torrens, I. Bolzoni, Effect of processing parameters on hot deformation behaviour and microstructural evolution of PM Ti-5553 alloy at a moderate-high strain rate, *Mater. Res.* 22 (2019), <https://doi.org/10.1590/1980-5373-MR-2018-0738>.
- [29] M. Dikovits, C. Poletti, F. Worzchecka, Deformation mechanisms in the near- β titanium alloy Ti-55531, *Metall. Mater. Trans. A* 45 (2014) 1586–1596, <https://doi.org/10.1007/s11661-013-2073-4>.
- [30] Q. Chao, P.D. Hodgson, H. Beladi, Ultrafine grain formation in a Ti-6Al-4V alloy by thermomechanical processing of a martensitic microstructure, *Metall. Mater. Trans. A* 45 (2014) 2659–2671, <https://doi.org/10.1007/s11661-014-2295-5>.
- [31] H. Beladi, Q. Chao, G.S. Rohrer, Variant selection and invariant crystallographic planes distribution in martensite in a Ti-6Al-4V alloy, *Acta Mater.* 80 (2014) 478–489, <https://doi.org/10.1016/j.actamat.2014.05.004>.
- [32] J.K. Mackenzie, Second paper on statistics associated with the random disorientation of cubes, *Biometrika* 45 (1958) 229–240, <https://doi.org/10.1093/biomet/45.1-2.229>.
- [33] V. Randle, “Five-parameter” analysis of grain boundary networks by electron backscatter diffraction, *J. Microsc.* 222 (2006) 69–75, <https://doi.org/10.1111/j.1365-2818.2006.01573.x>.

ANNEX C – Paper on aging treatments of Ti-5Al-5Mo-5V-3Cr alloy



RightsLink[®]


Home


Help


Email Support


Sign in


Create Account



In situ evaluation of the low-temperature aging response of Ti-5Al-5Mo-5V-3Cr alloy as influenced by starting microstructure

Author:
B. Callegari, K. Aristizabal, S. Suarez, L. Wu, R.S. Coelho, P.P. Brito, J.L. Garcia, F.A. Soldera, F. Mücklich, H.C. Pinto

Publication: Journal of Alloys and Compounds

Publisher: Elsevier

Date: 15 September 2020

© 2020 Elsevier B.V. All rights reserved.

Please note that, as the author of this Elsevier article, you retain the right to include it in a thesis or dissertation, provided it is not published commercially. Permission is not required, but please ensure that you reference the journal as the original source. For more information on this and on your other retained rights, please visit: <https://www.elsevier.com/about/our-business/policies/copyright#Author-rights>

BACK

CLOSE WINDOW

© 2020 Copyright - All Rights Reserved | Copyright Clearance Center, Inc. | [Privacy statement](#) | [Terms and Conditions](#)
Comments? We would like to hear from you. E-mail us at customer-care@copyright.com



Contents lists available at ScienceDirect

Journal of Alloys and Compounds

journal homepage: <http://www.elsevier.com/locate/jalcom>

In situ evaluation of the low-temperature aging response of Ti–5Al–5Mo–5V–3Cr alloy as influenced by starting microstructure

B. Callegari^{a,b}, K. Aristizabal^b, S. Suarez^b, L. Wu^c, R.S. Coelho^d, P.P. Brito^e, J.L. García^f, F.A. Soldera^b, F. Mücklich^b, H.C. Pinto^{a,*}

^a University of São Paulo, São Carlos School of Engineering, Department of Materials Engineering, Av. João Dagnone 1100, 13563-120, São Carlos, SP, Brazil

^b Saarland University, Department of Materials Science and Engineering, Campus D3.3, 66123, Saarbrücken, Germany

^c Brazilian Synchrotron Light Laboratory, Brazilian Center for Research in Energy and Materials, R. Giuseppe Maximo Scalfaro 10000, 13083-970, Campinas, Brazil

^d SENAI CIMATEC, Institute of Innovation for Forming and Joining of Materials, Av. Orlando Gomes 1845, 41650-010, Salvador, Brazil

^e Pontifical Catholic University of Minas Gerais, Av. Dom José Gaspar 500, 30535-901, Belo Horizonte, Brazil

^f AB Sandvik Coromant R&D, Lerkrögsvägen 19, SE, 12680, Stockholm, Sweden



ARTICLE INFO

Article history:

Received 5 March 2020

Received in revised form

14 April 2020

Accepted 22 April 2020

Available online 28 April 2020

Keywords:

Titanium alloys

Aging

Phase transformation

Hardening

Synchrotron x-ray diffraction

ABSTRACT

The impact of starting microstructure on the isothermal behavior of β -metastable Ti–5Al–5Mo–5V–3Cr alloy during aging at 400 °C for 8 h was studied by means of in situ synchrotron X-ray diffraction. Results show that prior deformation does not accelerate phase precipitation during heating, but has an influence on secondary α precipitation during aging, and that the composition of the β matrix, which is affected by the amount of primary α formed depending on the preliminary processing route applied, plays a major role. At this aging temperature, α'' phase tends to form from the β matrix in high quantities without the presence of primary α phase or with a low fraction of this phase, and the conversion of α'' into α is sluggish, being faster in the β -heat-treated condition, whereas a continuous $\beta \rightarrow \alpha$ transformation occurs, with no reliable evidence of α'' precipitation, in the α - β -heat-treated condition. Isothermal precipitation was enough to promote a significant hardness increase in the alloy. Observation of the behavior of α'' based on its atomic y-coordinate and orthorhombicity helped to elucidate its transformation pathway.

© 2020 Elsevier B.V. All rights reserved.

1. Introduction

Metastable β -titanium alloys present extraordinary mechanical properties, namely high strength-to-weight ratios, toughness and fatigue resistance. For this reason, they have been increasingly employed in the aerospace industry. These alloys are highly hardenable, which makes them ideal for components with thick sections. In addition, their capacity of retaining the soft β phase upon fast cooling provides superior forming characteristics to these alloys, with subsequent strengthening by ageing [1]. Despite their advantages, β alloys have limitations that include higher costs, more complex processing and slightly higher densities when compared to α - β Ti alloys [2]. Ti–5Al–5Mo–5V–3Cr (Ti–5553, composition in wt %) is a β -metastable alloy which offers improvement in strength and

toughness over Ti–10V–2Fe–3Al (Ti–1023), another very prominent alloy of the same class [3,4]. While Ti–1023 can be heat-treated to achieve ultimate tensile strengths in the order of 1290 MPa, Ti–5553 can reach tensile strength levels as high as 1517 MPa, and its maximum section thickness for solution treatment and aging effectiveness is of 150 mm, against only 76 mm in Ti–1023. It is also expressively easier to be processed due to its shallower β approach curve, which allows a wider processing window for thermal and thermomechanical processing, thus becoming more competitive [4]. It is mainly employed in large section forgings for airframes [3].

The high strength of β -Ti alloys owes itself to the precipitation of fine laths of α phase within the β matrix. Due to the full retention of β phase upon quenching, these alloys lack nucleation sites for α during subsequent aging treatments. Nonetheless, they form the metastable ω phase when quenched from sufficiently high temperatures, referred to as athermal ω phase, and subsequent low temperature aging leads to the formation of a so-called isothermal ω phase. Although this phase is usually avoided in titanium alloys

* Corresponding author.

E-mail address: haroldo@sc.usp.br (H.C. Pinto).

because of its embrittling effect, it serves as a precursor to provide homogeneous nucleation sites for nanoscale α precipitation [5]. Thus, ω precipitation is extremely important for the microstructural engineering of β -metastable Ti alloys, which aims at microstructural refinement by the exclusive promotion of intragranular precipitation, resulting from α nucleation within the β matrix, with suppression of intergranular precipitation [6].

The outcomes of heat treatments in β -metastable Ti alloys, in terms of resulting microstructure and consequent mechanical properties, depend mainly on parameters such as heating rate and aging temperature. It has been shown that a maximum heating rate of 20 °C/min from a fully β -quenched condition is necessary to obtain a super-refined α phase morphology in Ti-5553 alloy [7]. The influence of solution treatment and aging on mechanical properties of Ti-5553 has been evaluated for solution treatments in the single β and in the dual $\alpha + \beta$ phase fields. Aging at a temperature of 450 °C for 8 h has resulted in maximum yield strength and minimum ductility in all conditions, and the increase of aging temperature has produced a decrease in yield strength and increase in elongation [2]. Pre-aging treatments at low temperatures are known to contribute to the refinement of the α phase precipitated during subsequent aging at higher temperatures, following the so-called duplex or two-step aging route, with consequent improvement of strength and fatigue properties [8]. Duplex aging relies on the formation of precursors such as isothermal ω or β' (as a result of spinodal decomposition) at lower temperatures to improve nucleation of the α phase at higher temperatures [3,9,10]. Ren et al. have shown that a duplex-aged Ti-5Al-5Mo-5V-3Cr-1Zr alloy exhibited a significant increase in ultimate tensile strength, but with drastic decrease in ductility in comparison with the single-aged alloy [11], while Zheng et al. affirm that the scale of the final α phase formed after aging at 350 °C/3h + 600 °C/2h is influenced by the isothermal ω phase that precipitated during slow heating to 350 °C [12].

The aging behavior of Ti-5553 alloy is widely studied. Nag et al. [13] have studied the elemental partitioning between α and β phases in a β -quenched Ti-5553 alloy during isothermal treatments and have concluded that, while aging at higher temperatures (700 °C) leads to pronounced partitioning of Al, Mo, V and Cr, such partitioning does not occur during aging at 400 °C. In this temperature, besides elemental partitioning, the growth of α precipitates is also restricted due to the low diffusivity at this temperature. Settefrati et al. have further confirmed that little partitioning occurs during low-temperature aging of the alloy [14]. Furthermore, it is known that, in addition to isothermal ω , metastable β alloys can also form the isothermal α'' phase [15–19]. This orthorhombic phase is believed to form isothermally in the presence of isothermal ω phase due to aluminum rejection from ω to the β matrix, resulting in Al-enriched regions near ω precipitates with Al contents higher than 6 wt% that evolve to form precipitates of the orthorhombic phase [20]. Settefrati et al. [21] have evaluated the possible phase transformation pathways in Ti-5553 alloy as influenced by the heating rate from a full β -metastable state to the aging temperature (620 °C) and have shown that a heating rate of 0.1 °C/s imposes the following transformation sequence: $\beta \rightarrow \beta + \omega_{iso} \rightarrow \beta + \alpha'' \rightarrow \beta + \alpha'' + \alpha \rightarrow \beta + \alpha$, whereas a heating rate of 1 °C/s was high enough to suppress the formation of ω_{iso} . The presence of primary α in the alloy has

retarded the precipitation of α'' . Aeby-Gautier et al. [15] have studied the isothermal precipitation of α'' in Ti-5553 and in a Ti-17 alloy after quenching from the β phase using in situ synchrotron highenergy X-ray diffraction and have shown that significantly high amounts of α'' form during aging at lower temperatures, with limited tendency to transform into α .

Most studies focus on the aging behavior of the alloy starting from a β -quenched microstructure. However, typical solution treatments applied prior to aging in the industry are carried out in the $\alpha + \beta$ field, usually 50–100 °F (28–56 °C) below the β -transus [22]. This means that the alloy is usually aged from a starting microstructure containing the β phase and a certain amount of primary α , which influences the chemical composition of the β matrix. Thus, it is important to analyze the behavior of the alloy with such microstructure. Also, there is no knowledge on the evaluation of the effects of prior deformation, which has been shown to be relevant due to the presence of deformation-induced defects such as dislocations and low-angle grain boundaries [23], on the subsequent precipitation kinetics in this alloy. In this scenario, the present work provides a study on the aging behavior of the Ti-5553 alloy with different starting microstructures, produced by the imposition of different heat treatment and thermomechanical processing routes, at a relatively low temperature after slow heating by means of in-situ synchrotron X-ray diffraction.

It is important to clarify that a recent study has presented the existence of a so far unknown isothermal orthorhombic phase denominated O* in a Ti-5553 alloy. This study defies the typically accepted idea of isothermal precipitation of the orthorhombic α'' martensite in metastable β titanium alloys and proposes that this phase might have been erroneously identified in these aged alloys, when in fact the present phase was the O*. Due to their orthorhombic lattices, O* and α'' share strong crystallographic similarities, ergo being easily mistaken. The use of high resolution transmission electron microscopy in depth is of vital importance for the correct identification of the precipitated phase [20]. In this work, the usual α'' denomination has been chosen.

2. Materials and methods

2.1. Material

The composition of the Ti-5553 alloy used in this work, determined as described elsewhere [24], is given in Table 1. Values of aluminum and molybdenum equivalents were calculated using the respective equations presented in the ASM handbook of titanium alloys [25]. A β -transus temperature of approximately 875 °C was determined for the alloy as described elsewhere [24].

2.2. Tailoring of initial microstructures

The alloy was thermally and thermomechanically treated at 950 °C (β field) and 800 °C ($\alpha + \beta$ field). Samples with dimensions of $\phi 10 \times 15$ mm were wire-cut from the as-received bar stock with their length parallel to the bar's length and underwent an initial homogenization treatment at 950 °C during 30 min followed by water quenching in an EDC® 10P-S furnace with vacuum and argon atmosphere protection. Deformation by uniaxial compression was

Table 1
Composition of Ti-5553 alloy used in this work [24].

Element	Ti	Al	Mo	V	Cr	Fe	O	C	N	H
wt%	Bal.	5.36	4.42	5.01	2.93	0.48	0.16	0.03	0.005	0.002
[Al]eq	6.9					[Mo]eq	12.6			

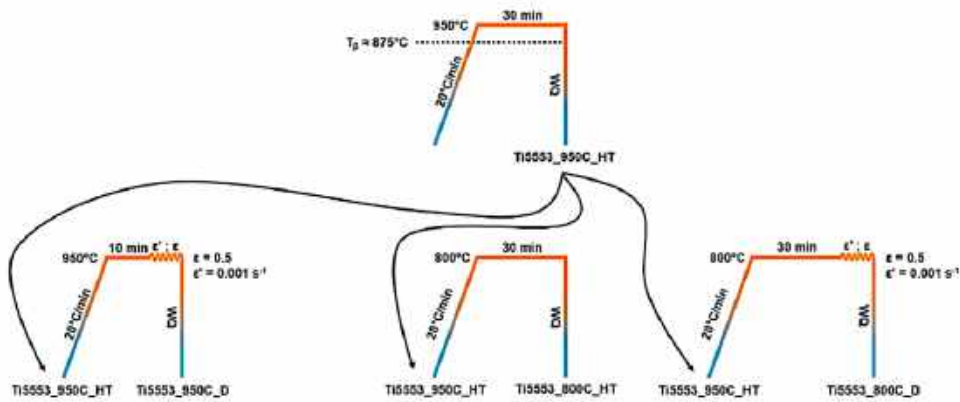


Fig. 1. Schematic framework of thermal and thermomechanical treatments imposed to Ti-5553 alloy.

imposed in a Gleeble® 3800 thermomechanical simulator with a strain rate of 10^{-3} s^{-1} to a compression ratio of 50% (true strain = 0.7). The alloy was also heat-treated at 800 °C without deformation. Fig. 1 shows a schematic representation of the framework of treatments imposed to the alloy and the names given to each condition based on treatment temperature ("950C" for 950 °C and "800C" for 800 °C) and type ("HT" for heat treatment and "D" for compression with strain rate of 0.001 s^{-1} , respectively).

2.3. Microstructural characterization

The alloy was metallographically prepared for light optical microscopy (LOM) and scanning electron microscopy (SEM) according to the procedure described elsewhere [24]. LOM analyses were done in a Zeiss® Axio Scope.A1 optical microscope and SEM analyses were carried out in a FEI® Inspect F50 microscope with field emission gun using backscattered electrons' (BSE) signal. In deformed conditions, images were recorded from the plane parallel to the compression axis.

2.4. Aging treatments using in situ synchrotron X-ray diffraction

Samples with $3 \times 4 \times 6 \text{ mm}^3$ were wire-cut from the heat-treated and compressed specimens for aging treatments using in situ X-ray diffraction. Regarding deformed specimens, samples were taken with their length parallel to the compression direction. Treatments were carried out at 400 °C during 8 h at the XTMS experimental station of the XRD1 beamline of the Brazilian Synchrotron Light Laboratory in an adapted Gleeble® 3550 thermomechanical simulator with a vacuum level of -10^{-3} torr. The temperature was defined in order to avoid hindering the precipitation of metastable phases such as isothermal ω and α' . A slow heating rate of 10 °C/min was employed for the same reason. The low treatment temperature should also contribute to minimize the oxidation of the material, given that diffraction experiments were carried out in reflection mode, restricting the probed volume to the surface of specimens. The energy of the beam was of 12 keV ($\lambda = 1.0332 \text{ \AA}$). Sections of Debye-Scherrer rings were acquired by a Rayonix® SX165 area detector with $39 \times 39 \mu\text{m}^2$ pixel size with an exposure time of 60 s and a spot size of $1 \times 2 \text{ mm}^2$. The detector was kept fixed at a diffraction angle of 30° , allowing the acquisition of an approximate 2θ range between 15° and 45° . The incidence angle (ω) was found to be close to 19° . The images of the rings' sections were processed using Dracon

software, a MATLAB® macro developed by the XTMS staff, to generate the corresponding diffractograms, which were quantitatively analyzed via Rietveld refinement on MAUD (Materials Analysis Using Diffraction) [26] software.

2.5. Transmission electron microscopy

TEM lamellae were prepared using the lift-out technique in a FEI® Helios NanoLab 600 DualBeam electron microscope. Analyses were carried out in a JEOL® JEM 2010 transmission electron microscope with a LaB₆ filament operated at 200 kV. Indexing of selected area diffraction patterns was done on PTCLab software [20].

2.6. Micro-hardness measurements

The micro-hardness of samples in their initial conditions, after heating to 400 °C and after aging at 400 °C for 8 h was measured in a Leica® VMHT-MOT tester with a load of 0.2 kgf. Measurements were done randomly on the surface of the samples, which were prepared according to the same procedure described in Section 2.3. Results hereby shown correspond to the average of ten measurements taken from the center of each specimen.

3. Results

3.1. Initial microstructures

Fig. 2 shows the initial microstructures produced by treatments described in Fig. 1. For specimens processed at 950 °C (Fig. 2a and b), only LOM images are shown because the microstructure is composed solely by the β phase, with no other phases detectable by SEM. Ti5553_950C_HT (Fig. 2a) and Ti5553_800C_HT (Fig. 2c) conditions present microstructures formed by equiaxed β grains, and a considerable amount of α phase is present both within grains and along grain boundaries in Ti5553_800C_HT. Deformed conditions present β grains elongated along the direction perpendicular to the compression axis. These microstructures have been analyzed in depth by electron backscatter diffraction (EBSD) elsewhere [24].

In Ti5553_800C_D condition (Fig. 2d), a much lower amount of α is present in comparison with Ti5553_800C_HT. The fractions of primary α in Ti5553_800C_HT and Ti5553_800C_D obtained by Rietveld refinement were $60.9 \pm 1.3 \text{ vol\%}$ and $22.7 \pm 1.2 \text{ vol\%}$, respectively. These results are slightly different from those obtained in a previous

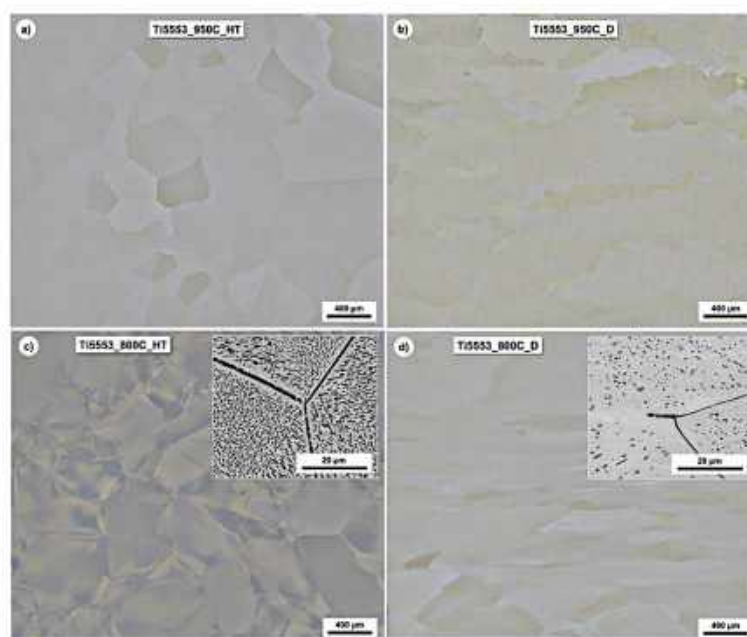


Fig. 2. Microstructures of a) Ti5553_950C_HT (LOM), b) Ti5553_950C_D (LOM), c) Ti5553_800C_HT (LOM with a BSE-SEM image in the inset) and d) Ti5553_800C_D (LOM with a BSE-SEM image in the inset). The compression axis is parallel to the height of images. In the SEM images, the darker phase is α and the brighter phase is β .

study of the produced microstructures [24]. This difference can be explained by the fact that, in the previous work, diffraction patterns were generated from the integration of full Debye-Scherrer rings ($\Delta\eta = 360^\circ$) acquired in transmission mode, which allows for better statistics with virtually no preferential orientation artifacts that could arise due to the coarse microstructure, whereas only a small section of rings ($\Delta\eta = 30^\circ$) was acquired in reflection mode in the present work.

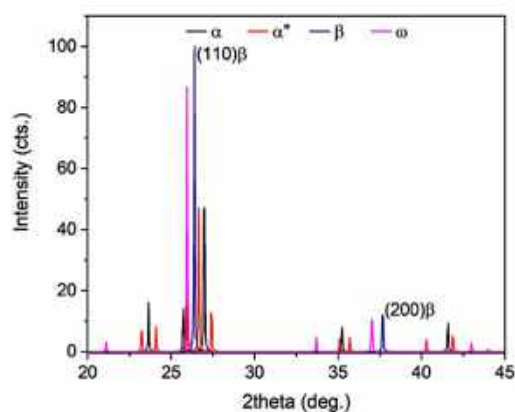


Fig. 3. Peak positions in a theoretical diffractogram of a sample containing equal amounts of α , α^* , β and ω phases with a beam energy of 12 keV.

3.2. Heating behavior

Fig. 3 shows a theoretical diffraction pattern with the same 2θ range as the one acquired during in situ XRD experiments for guidance. This pattern was calculated on PowderCell software [27] assuming equal amounts of α , α^* , β and ω (25 vol%), whose crystallographic information is shown in Table 2. Fig. 4 presents the evolution of these representative 2θ ranges of the integrated diffractograms for Ti5553_950C_HT, Ti5553_950C_D and Ti5553_800C_D during heating to 400 °C at 10 °C/min in the form of color-coded plots. The most noticeable change is the broadening of the β reflections, which can be attributed to the precipitation of isothermal ω . Such precipitation starts at ~ 225 °C, and ω peaks formed present themselves as “shoulders” of the main β reflections. This characteristic arises from the fact that the ω phase originates from embryos formed in uncorrelated linear defects along the $\langle 111 \rangle_\beta$ direction, each one diffracting independently, until the ω transformation temperature is reached and the correlation among these domains increases, originating discrete ω particles that diffract to produce the shoulder seen [28,29]. This nature has also been acknowledged as the origin of the diffuse scattering produced by the ω phase, which usually result in weak and broad XRD reflections [16,17,28]. It is interesting to notice that the $(200)_\beta$ reflection in deformed conditions is rather narrow in comparison with the heat-treated one, and in this condition the “shoulder” produced by the $(20\bar{2}1)_\omega$ peak can be seen already at room temperature, evidencing the presence of athermal ω phase precipitated during quenching. Another source of the broadening of $(110)_\beta$ reflection is the appearance of isothermal α^* reflections, which are clearly seen in Fig. 4a, starting at ~ 350 °C. Fig. 4b and c also show α^* reflections; however, these are quite faint. On the other hand, the

Table 2
Crystallographic data of the phases considered in this work.

Phase	Lattice system	Space group (group number)	Atomic positions
α	Hexagonal	$P6_3/mmc$ (194)	$(1/3, 2/3, 1/4)$ $(2/3, 1/3, 3/4)$
β	Cubic	$Im\bar{3}m$ (229)	$(0, 0, 0)$ $(1/2, 1/2, 1/2)$
ω	Hexagonal	$P6_5/mmm$ (191)	$(0, 0, 0)$ $(1/3, 2/3, 1/2)$ $(2/3, 1/3, 1/2)$
α''	Orthorhombic	$Cmcm$ (63)	$(0, y, 1/4)$ $(0, 1 - y, 3/4)$ $(1/2, 1/2 - y, 1/4)$ $(1/2, 1/2 - y, 3/4)$; $0.16 < y < 0.25$ [30]

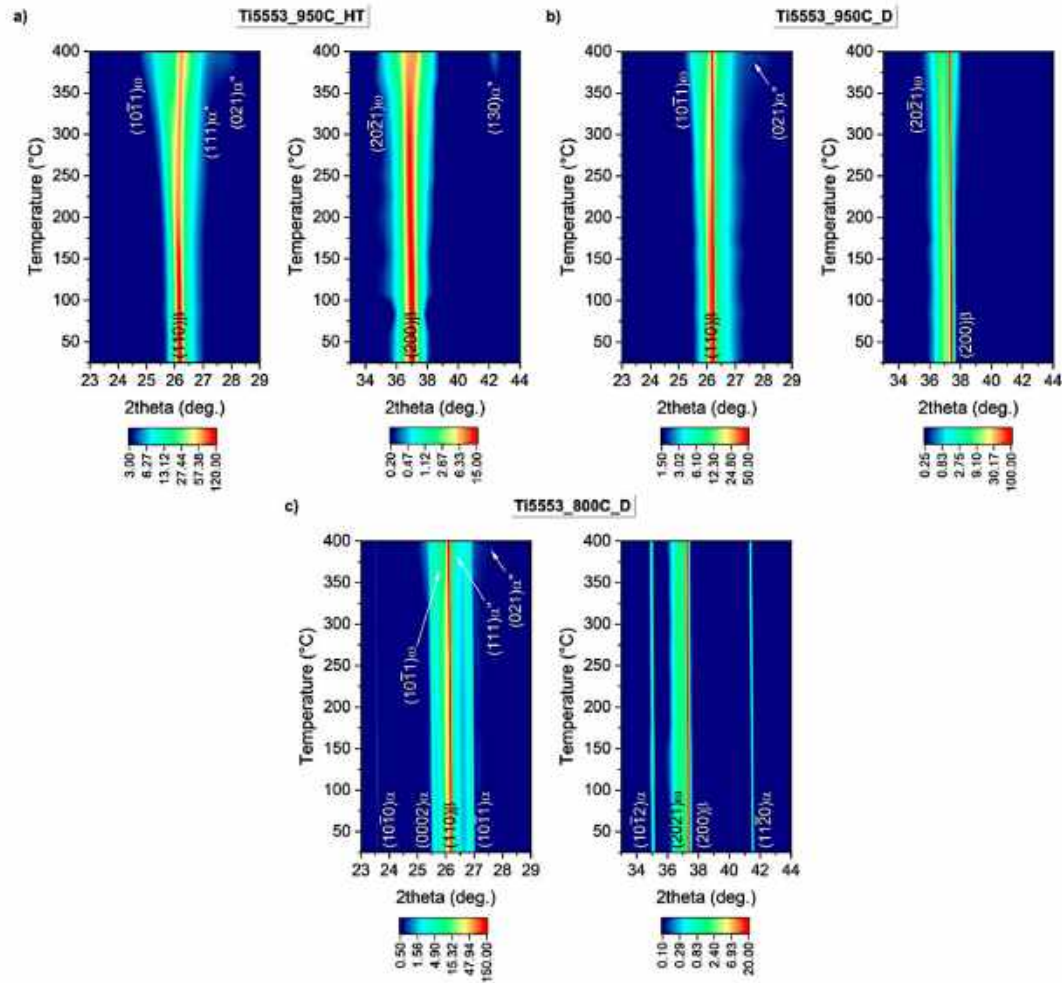


Fig. 4. Color-coded plots showing the evolution of reflections of a) Ti5553_950C_HT, b) Ti5553_950C_D and c) Ti5553_800C_D conditions during heating to 400 °C at 10 °C/min.

reflections of Ti5553_800C_HT condition did not show any significant changes during heating and have been therefore omitted. Fig. 5 shows electron diffraction patterns of Ti5553_950C_D condition before and after heating, where spots belonging to β , ω and α'' phases can be seen.

At the end of the heating stage, all conditions possessed the phase ratios shown in Table 3 (Rwp \leq 0.1291). Regarding Ti5553_800C_D condition, although the appearance of α'' reflections was observed during heating, their intensities were too low to enable distinction of

6

B. Callegari et al. / Journal of Alloys and Compounds 835 (2020) 155331

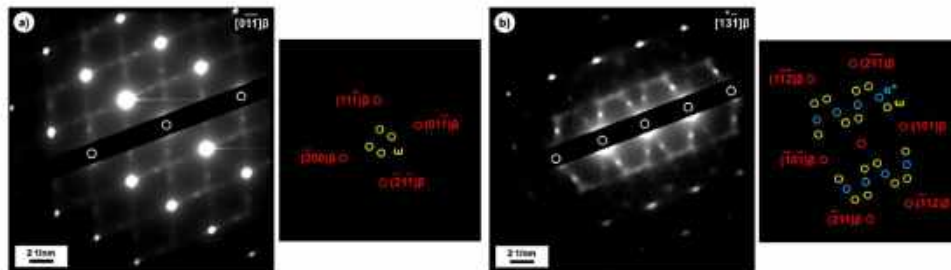


Fig. 5. Electron diffraction patterns of Ti5553_950C_D sample a) before and b) after heating to 400 °C at 10 °C/min.

Table 3

Phase fractions of all conditions of Ti-5553 alloy after heating to 400 °C at 10 °C/min.

Condition	α (vol%)	ω (vol%)	α' (vol%)	β (vol%)
Ti5553_800C_D	23.1 ± 1.4	5.9 ± 0.4	—	Bal.
Ti5553_800C_HT	66.5 ± 2.2	—	—	Bal.
Ti5553_950C_D	—	6.5 ± 1.4	2.1 ± 0.3	Bal.
Ti5553_950C_HT	—	9.4 ± 0.6	15.7 ± 1.0	Bal.

peaks for quantification. Therefore, in this condition, the amount of this phase is considered to be null at the end of heating and beginning of aging. Comparing all three conditions, it is possible to

observe that the precipitation kinetics of both isothermal ω and α' phases during heating decreases from Ti5553_950C_HT (Fig. 4a) to Ti5553_950C_D (Fig. 4b) and Ti5553_800C_D (Fig. 4c), which is interesting, given that deformation causes the formation of defects believed to act as additional nucleation sites and thus should accelerate precipitation in comparison with a purely heat-treated condition [19]. However, this does not appear to be the case. Particularly in Ti5553_800C_D condition, the composition of the β phase appears to play a bigger role, since the presence of primary α phase influences its composition, as will be discussed ahead.

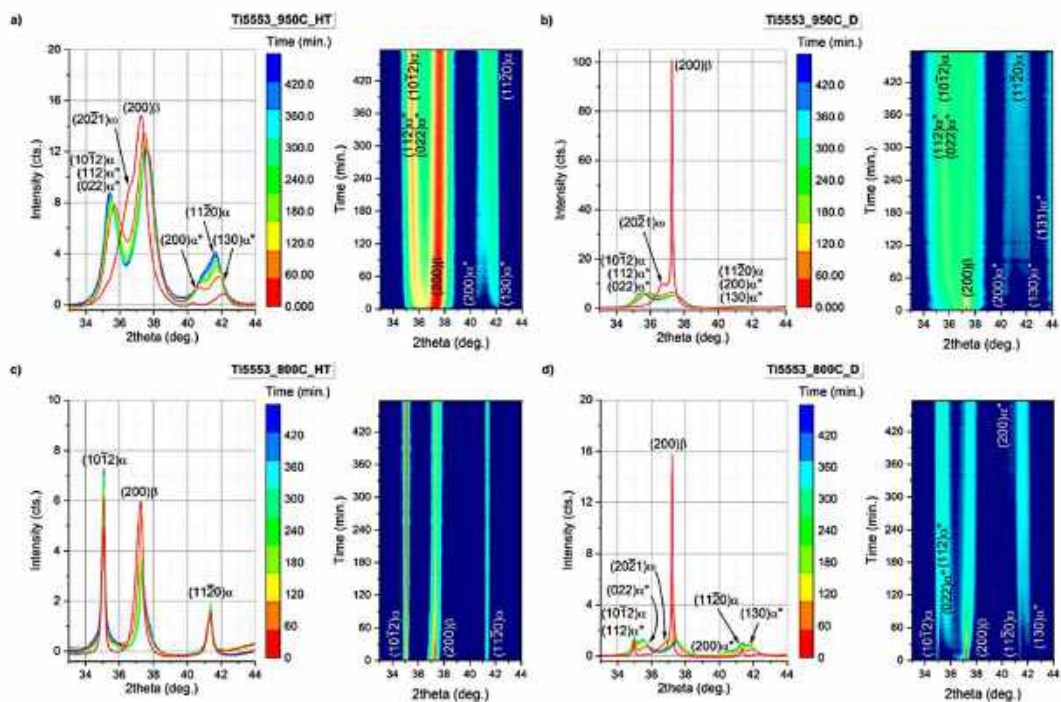


Fig. 6. 2D and color-coded plots showing the evolution of reflections of a) Ti5553_950C_HT, b) Ti5553_950C_D, c) Ti5553_800C_HT and d) Ti5553_800C_D conditions during aging at 400 °C for 8 h.

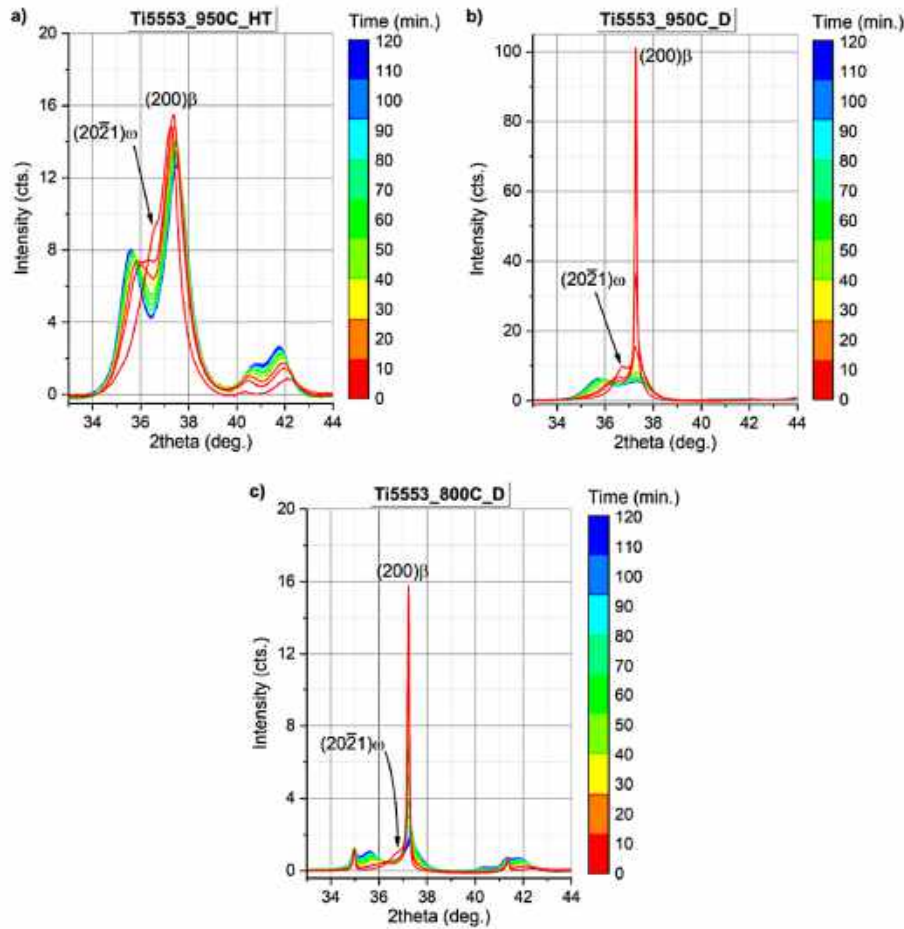


Fig. 7. 2D plots showing the evolution of reflections of a) Ti5553_950C_HT, b) Ti5553_950C_D and c) Ti5553_800C_D conditions during the first 2 h (120 min) of aging at 400 °C.

3.3. Aging behavior

Fig. 6 depicts the evolution of reflections during 8 h of aging at 400 °C for all conditions. To evidence such evolution, 2theta intervals comprising (200) β and neighboring reflections, as seen in Fig. 3, are shown. Peaks around this β reflection are less superimposed and narrower, which enables a better deconvolution and visualization of their behavior. The evolution is shown in the form of 2D and color-coded plots for complementary purposes. In all cases, the formation and/or increase of α'' reflections can be seen, at the expense of the reduction of β reflections and disappearance of ω reflections. Particularly in deformed conditions (Fig. 6b and d), a sharp intensity decrease of the β peak is observed within the first minutes of isothermal treatment, while the ω reflection also vanishes within the same interval. In fact, in all cases, such changes occur during the first 30 minutes of treatment, as shown in Fig. 7. The rapid intensity decrease of the β phase reflection suggests that, although deformed

conditions do not exhibit more rapid response during heating, their response is enhanced in the isothermal stage of the treatment. In Ti5553_950C_HT (Fig. 6a), one can also notice the evolution of the double (200) α'' and (130) α'' reflections into the single (11 $\bar{2}$ 0) α'' reflection, indicating the transformation of α'' into α . Such behavior is also present in Ti5553_950C_D (Fig. 6b); however, it is relatively sluggish in comparison with the first. In Ti5553_800C_D (Fig. 6d), the appearance of α'' reflections around α reflections is also visible, whereas in the Ti5553_800C_HT condition (Fig. 6c) no visible reflection of the α'' phase is seen, suggesting that β phase transforms directly into α .

4. Discussion

4.1. Phase evolution during aging

Fig. 8 depicts the phase evolution plots with the resulting

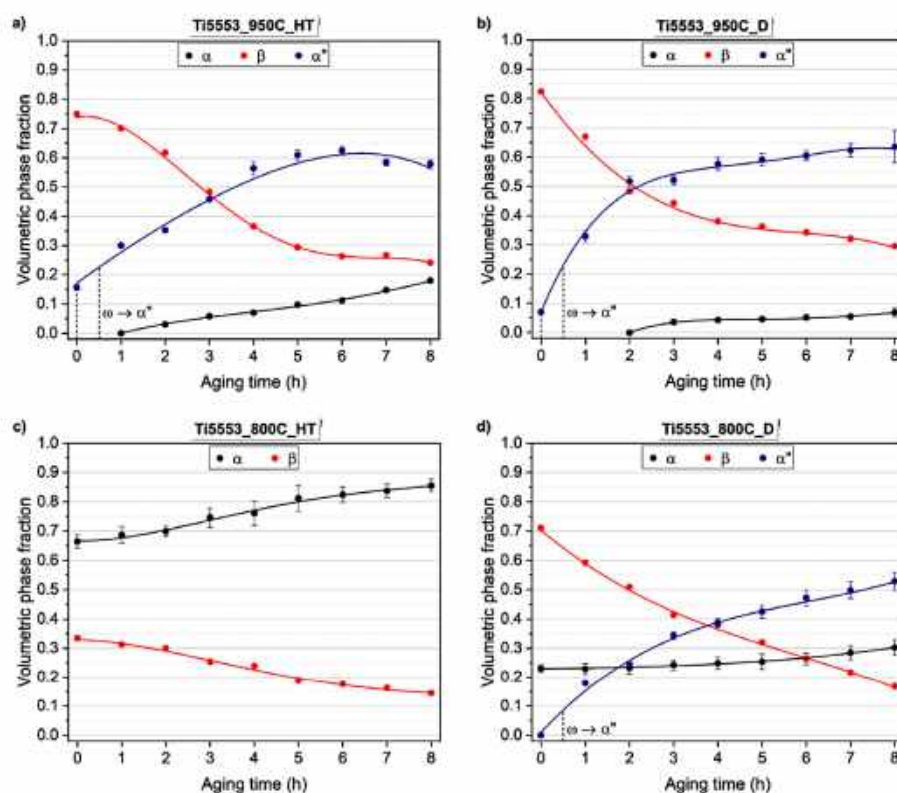


Fig. 8. Evolution of phase fractions as function of time for a) Ti5553_950C_HT, b) Ti5553_950C_D, c) Ti5553_800C_HT and d) Ti5553_800C_D conditions during aging at 400 °C for 8 h.

volumetric fractions obtained by Rietveld refinement. In all cases, except for Ti5553_800C_HT, where no evidence of the presence of ω phase was seen, its decomposition within the first 30 min of aging is indicated. Given the continuous decrease of the β fraction throughout aging, the most likely transformation pathway for ω decomposition is the $\omega \rightarrow \alpha''$ transformation. Again, in all conditions, apart from Ti5553_800C_HT, a high amount of α'' (>50 vol%) is formed, while relatively low amounts of α are precipitated. The condition with the highest final fraction of secondary α is Ti5553_950C_HT (~20 vol%), against ~7 vol% in Ti5553_950C_D. In Ti5553_800C_HT, around 20 vol% of the β matrix is decomposed into α . It is worth mentioning that α'' phase was not considered in the refinement of this condition due to the difficulty to fit this phase without any sufficiently resolved peaks in the diffraction patterns. Regarding Ti5553_800C_D condition (Fig. 8d), it is assumed that the increase in the volumetric fraction of α owes itself uniquely to the formation of secondary α , since the low temperature is insufficient to promote any coarsening of the primary α phase; thus, one can infer that ~7 vol% of secondary α precipitates in this condition. The continuous increase of the α fraction in this case from the beginning suggests that, as in Ti5553_800C_HT, this phase also tends to precipitate directly from the β phase, and not only from the decomposition of the α'' phase.

Aeby-Gautier et al. [15] have observed that, during low temperature aging, isothermal α'' tends to form in the alloy with a sluggish tendency to convert into α . In their work, a Ti-5553 alloy aged at 325 °C showed no signs of α precipitation from α'' , while in a Ti-17 alloy (Ti-5Al-4Mo-4Cr-2Sn-2Zr) aged at 424 °C a fraction of approximately 15 wt% of secondary α was formed. In the present work, an intermediate temperature for Ti-5553 was sufficient to promote the formation of α at some extent. Nonetheless, in deformed conditions (Fig. 8b and d), the precipitation of this phase is retarded. One hypothesis to explain the apparent relative stabilization of α'' would be the accommodation of the phase by dislocations. In the β -heat-treated condition (Fig. 8a), it is possible to observe the moment at which the rate of the $\beta \rightarrow \alpha''$ transformation overcomes the rate of the $\beta \rightarrow \alpha$ transformation, resulting in a decrease of the α'' fraction.

Nonetheless, aging treatments aim to obtain a microstructure composed by the stable α phase within a β matrix. Because at this temperature the microstructure does not appear to evolve towards this equilibrium condition within practical periods, but rather stabilizes with a considerably high amount of the metastable α'' phase or presents a sluggish $\alpha'' \rightarrow \alpha$ decomposition, this treatment temperature might not be regarded as ideal for a final aging treatment,

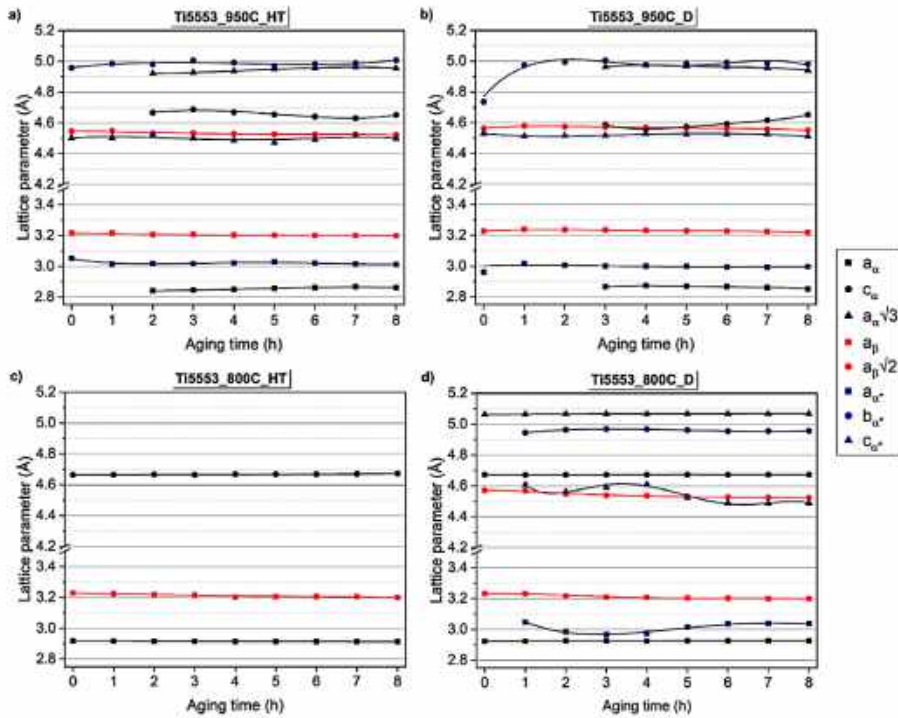


Fig. 9. Evolution of lattice parameters of α , β and α' phases of a) Ti5553_950C_HT, b) Ti5553_950C_D, c) Ti5553_800C_HT and d) Ti5553_800C_D conditions during aging at 400 °C for 8 h.

but as a first step in a duplex aging treatment route, in which the second treatment can be carried out at slightly higher temperatures to promote a faster precipitation of α .

Fig. 9 shows the evolution of lattice parameters of α , β and α' phases during aging of the Ti-5553 alloy. The values of $a_{\alpha}\sqrt{3}$ and $a_{\beta}\sqrt{2}$ are also shown to evaluate the tendency of the α' phase to transform into α based on its orthorhombicity [34]. This parameter is an indicative of the transformation direction of the α' phase because an HCP lattice (α phase) is obtained for $b_{\alpha'} = a_{\alpha}\sqrt{3}$ whereas $b_{\alpha'} = a_{\beta}\sqrt{2}$ results in a BCC lattice (β phase) [16,30]. In Ti5553_950C_HT (Fig. 9a) and Ti5553_950C_D (Fig. 9b), the proximity between $a_{\alpha}\sqrt{3}$ and $b_{\alpha'}$ depicts the likeliness of the $\alpha' \rightarrow \alpha$ transformation. In Fig. 9d, Ti5553_800C_D condition, these parameters do not show a close relationship, indicating that, in this case, α' does not tend to decompose into α , or at least not as much as in the previous cases. In all conditions, phase evolution is accompanied by the shrinkage of the β phase, whose cell length a_{β} decreases from -3.23 Å to 3.19 Å (with standard errors equal to or lower than 1.51×10^{-3} Å), as a result from solute depletion [18].

4.2. Aged microstructures

In Fig. 10 are shown the final microstructures of all conditions obtained at the end of the aging treatment. In Ti5553_950C_HT (Fig. 10a) and Ti5553_950C_D (Fig. 10b), it is possible to observe a

homogeneous dispersion of extremely refined acicular structures, less than 30 nm thick. Based on phase quantification results shown in the previous section, these precipitates consist in a mixture of α' and secondary α phases. In Ti5553_800C_HT (Fig. 10c), a considerably high amount of secondary α , which also presents itself relatively coarser, is seen along with bigger laths of primary α phase. With the use of higher magnification, an additional type of precipitates, also with an acicular morphology, but extremely refined, can be seen. Given the remarkable difference between the morphologies of these precipitates and of the secondary α laths, which are comparably coarser, these finer precipitates might correspond to the α' phase, indicating that, although no distinguishable peaks of this phase were seen in the diffraction patterns, a rather low amount of this phase might form in the alloy. Another hypothesis would be that these precipitates are actually from the α phase, but in an initial growth stage. The absence of resolvable α' reflections in Fig. 6c indicates that the second hypothesis is the most likely one to be true. In the Ti5553_800C_D condition, no apparent difference is seen between pre- (Fig. 2d) and post- (Fig. 10d) aging microstructures, with the presence of a coarse primary α phase within the β matrix. However, under higher magnification, the same refined precipitates are seen.

In Ti5553_800C_HT, the relative coarseness of secondary α precipitates suggests they form with lower nucleation rate and higher growth rate, which can be explained by the lack of potential nucleation sites such as defects and the ω phase, whose absence, in

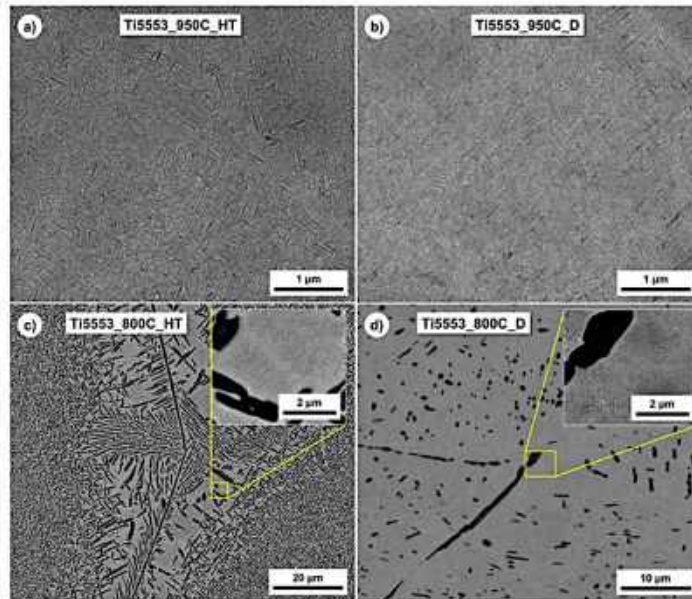


Fig. 10. BSE-SEM images of the microstructures of a) Ti5553_950C_HT, b) Ti5553_950C_D, c) Ti5553_800C_HT and d) Ti5553_800C_D conditions after aging at 400 °C for 8 h.

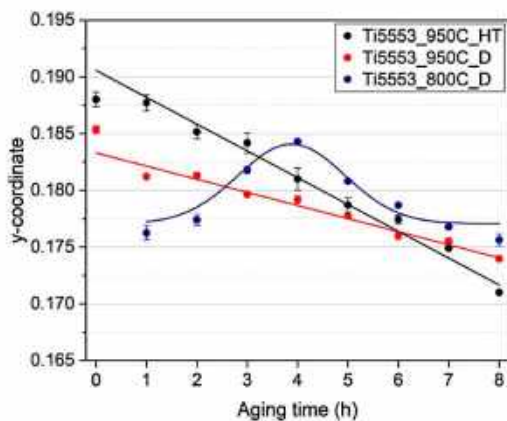


Fig. 11. Evolution of the atomic y-coordinate of the α'' phase in Ti5553_950C_HT, Ti5553_950C_D and Ti5553_800C_D during aging at 400 °C for 8 h.

its turn, can be explained by the composition of the β matrix within colonies of primary α grains, substantially enriched in β -stabilizing elements (Mo, V, Cr) and lean in α -stabilizing elements (Al) and Ti [31,32]; during aging, such partitioning induces the formation of secondary α , as discussed in the work of Barriobero-Vila et al. [33], and enables their accelerated growth. In Fig. 10c, the regions where the refined morphology is seen are exactly the ones where the β matrix is seen alone, whose composition clearly differs from that of

the β phase within primary α colonies, lying relatively closer to the same equilibrium composition of the phase in the β -quenched conditions, and where the precipitation of ω , if any, is more likely to take place and to promote microstructural refinement by nucleation enhancement.

4.3. Behavior of the α'' phase

Fig. 11 presents the behavior of the isothermal α'' phase during aging in terms of its atomic y-coordinate, which defines the position of atoms on the $(002)\alpha''$ plane along the $[010]\alpha''$ direction [30]. The value of this coordinate depends on the chemical composition of the α'' phase, i.e. an increase of solute content results in an increase of the phase's y-coordinate [16,34]. Like the orthorhombicity, it is also an indicative of the direction of the transformation of the α'' phase, given that a value of $y = 0.16$ results in an HCP lattice (α phase), while $y = 0.25$ results in a BCC lattice (β phase) [30]. It is possible to notice that the value of the y-coordinate in Ti5553_950C_HT and Ti5553_950C_D decreases approximately linearly ($R^2 \geq 0.953$) due to the transformation of the α'' phase into the stable α . The difference between the slopes of the fitted curves is in agreement with the difference between the $\alpha'' \rightarrow \alpha$ transformation rates in both conditions. In Ti5553_800C_D, the y-coordinate presents a peculiar behavior, with an increase during the first 4 h of aging followed by a decrease during the final hours of the isothermal treatment. This behavior can be explained by the altered initial composition of the β matrix, which, as mentioned above, is leaner in Ti and α -stabilizing elements and enriched in β stabilizers in the presence of the primary α phase. Therefore, in the first hours of aging, the initial increase of the y value might be a result of the enrichment of the α'' phase with alloying elements until a moment at which a critical chemical composition is reached. It is possible to observe in Fig. 8d that, during the first 4 h of isothermal treatment, the volumetric fraction

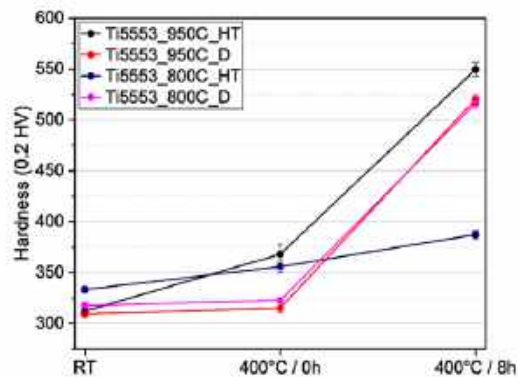


Fig. 12. Hardness evolution during slow heating to 400 °C and aging at 400 °C/8 h of all conditions of Ti-5553 alloy.

of α remains practically constant and, from the instant on, its increase, albeit slight, becomes noticeable, indicating a possible onset of the $\alpha'' \rightarrow \alpha$ transformation or simply an elemental partitioning between α'' and α with a consequent enrichment of the latter, due to the apparent lack of tendency of the $\alpha'' \rightarrow \alpha$ transformation seen in Fig. 9d. Furthermore, in Fig. 9d one can also observe the change in behavior of the lattice parameters of α'' between the first 4 h and the final 4 h of treatment. The behavior of α'' evidences the role of this phase as a regulator of the $\beta \rightarrow \alpha$ transformation, as defined by Guimarães et al. [18].

4.4. Hardness evolution

Fig. 12 presents the evolution of hardness during heating and aging of all conditions. In all cases, there has been an increase in hardness. Regarding initial conditions, the higher hardness of Ti5553_800C_HT is a consequence of the higher amount of primary α . On the other hand, the lower amount of primary α in Ti5553_800C_D appears to have a negligible effect on its hardness, whose value is only slightly higher than those of Ti5553_950C_HT and Ti5553_950C_D. In accordance with the previous discussion on phase evolution, the increase in hardness during heating has been more pronounced in Ti5553_950C_HT condition, where higher amounts of isothermal ω and α'' have precipitated. In Ti5553_950C_D and Ti5553_800C_D, where lower amounts of these phases formed during heating, the hardness increase has been inexpressive. In Ti5553_800C_HT, the increase owes itself to start of the direct α precipitation and possibly, as aforementioned, to the formation of isothermal ω and/or α'' in discrete amounts. The final hardness after aging comes as a result of the combination of α'' and secondary α precipitation. The lower hardness increase and final hardness of Ti5553_800C_HT can be attributed to the lower amount of the β matrix that has decomposed into α and to the rapid growth of the secondary α precipitates formed during aging, which resulted in relatively coarse laths. Ti5553_950C_HT presents the highest hardness value after aging due to the higher amount of refined secondary α . Furthermore, the fact that the final hardness values of Ti5553_800C_D and Ti5553_950C_D conditions are quite similar and high, but lower than that of Ti5553_950C_HT, further corroborates previous results showing that α precipitation in these conditions is retarded, with a consequent lower amount of this phase at the end of treatment.

The orthorhombic α'' phase is known as a "soft" martensite. In

Ti-Nb alloys, the hardness of α'' lies between 200 and 250 HV [35,36]. However, in more heavily alloyed systems, it presents higher hardness values, above 400 HV [37]. Hardness values in the order of 500 HV have been reported for Ti-5553 alloy after aging at 400 °C during 8 h [5]. Thus, α precipitation at an extremely refined scale, even with relatively low fractions, appears to have a significant impact on hardness. However, the hypothesis of underestimation of the α phase fraction in Ti5553_950C_HT and Ti5553_950C_D conditions must be taken into account, due to the superposition of its reflections with the broad reflections of the disordered and predominantly asymmetrical α'' phase [17]. The difficulty to correctly quantify α'' and α phases separately due to the overlapping of their reflections has already been reported [16–18].

5. Conclusions

The phase evolution of a β -metastable Ti-5Al-5Mo-5V-3Cr alloy during aging treatments at 400 °C for 8 h with different starting microstructures produced by heat treatment and thermo-mechanical processing at 950 °C (β field) and 800 °C ($\alpha+\beta$ field) has been evaluated by means of in situ synchrotron X-ray diffraction. From this study, the following conclusions can be drawn:

- With a slow heating rate (10 °C/min), transformations begin at the heating stage, with the precipitation of isothermal ω from -225 °C and of isothermal α'' from -350 °C in the alloy heat-treated in and quenched from the β phase field, whereas precipitation is hindered after deformation both in the β and in the $\alpha+\beta$ fields during heating. During isothermal treatment, on the other hand, deformation appears to enhance the aging response.
- Heat treatment in the $\alpha+\beta$ field produces a high amount of primary α phase and, in this condition, no considerable evidences of ω and α'' formation are seen, which shows that the composition of the β matrix plays a major role on phase transformations.
- During aging, the ω phase decomposes within the first 30 min of treatment in all conditions where it was present, and a high amount of α'' is formed throughout the entire treatment thereafter, except in the condition with a starting microstructure composed by a high amount of primary α , where an extremely high amount of secondary α precipitates and grows, indicating, in this case, a direct $\beta \rightarrow \alpha$ transformation.
- The conversion of α'' into α , with an extremely refined morphology, is again intensified in the β -heat-treated condition and sluggish in the β -deformed and $\alpha+\beta$ -deformed conditions, which is corroborated by the behavior of the lattice parameters of the α'' phase and of its atomic y-coordinate, which are indicative of the phase's solute content and transformation tendency into α .
- Hardness evolution shows that, albeit a high amount of the acknowledged "soft" α'' martensite is present, a refined α precipitation, even with low amounts, contributes to a significant increase in hardness during aging.

Funding

This work was supported by the National Council for Scientific and Technological Development – CNPq (grant number 161959/2015-6), by the Coordination for the Improvement of Higher Education Personnel – CAPES (grant number 88887.302880/2018-00 and PROBIAL project 88881.143948/2017-01) and by the German Academic Exchange Service – DAAD (project DAAD PPP-Brazil 2018 – ID 57390937). H. C. Pinto is CNPq fellow. The funding source had no involvement in the development of the research or in the preparation of the article.

Declaration of competing interest

The authors declare that they have no known competing financial interests or personal relationships that could have appeared to influence the work reported in this paper.

CRedit authorship contribution statement

B. Callegari: Conceptualization, Methodology, Formal analysis, Investigation, Writing - original draft. **K. Aristizabal:** Methodology, Investigation. **S. Suarez:** Methodology, Investigation. **L. Wu:** Methodology, Investigation, Resources. **R.S. Coelho:** Project administration, Funding acquisition. **P.P. Brito:** Project administration, Funding acquisition. **J.L. Garcia:** Resources. **F.A. Soldera:** Resources, Supervision, Project administration, Funding acquisition. **F. Mücklich:** Resources, Supervision, Project administration, Funding acquisition. **H.C. Pinto:** Conceptualization, Methodology, Writing - review & editing, Supervision, Project administration, Funding acquisition.

Acknowledgements

The Materials Department of the Federal University of São Carlos (DEMa – UFSCar, São Carlos, Brazil) and the Metals Characterization and Processing Laboratory of the Brazilian Center for Research in Energy and Materials (CNPEM, Campinas, Brazil) are acknowledged for granting access to their facilities for the conduction of thermal and thermomechanical treatments. The Brazilian Synchrotron Light Laboratory (LNLS, Campinas, Brazil) is acknowledged for the use of XTMS experimental station of the XRD1 beamline for the XRD experiments hereby presented. Authors also acknowledge the Institute of New Materials of the Saarland University (Saarbrücken, Germany) for the access to the transmission electron microscope. AB Sandvik Coromant R&D (Stockholm, Sweden) is greatly acknowledged for the provision of the studied material.

References

- [1] I. Polmear, D. Stjohn, J.-F. Nie, M. Qian, *Light Alloys: Metallurgy of the Light Metals*, fifth ed., Elsevier, 2017.
- [2] S. Shekhar, R. Sarkar, S.K. Kar, A. Bhattacharjee, Effect of solution treatment and aging on microstructure and tensile properties of high strength β titanium alloy, Ti-5Al-5V-5Mo-3Cr, Mater. Des. 66 (2015) 596–610, <https://doi.org/10.1016/j.matdes.2014.04.015>.
- [3] J.D. Cotton, R.D. Briggs, R.R. Boyer, S. Tamirisakandala, P. Russo, N. Shechtman, J.C. Fanning, State of the art in beta titanium alloys for airframe applications, JOM 67 (2015) 1281–1303, <https://doi.org/10.1007/s11837-015-1442-4>.
- [4] S.L. Nyakana, J.C. Fanning, R.R. Boyer, Quick reference guide for β titanium alloys in the 00s, J. Mater. Eng. Perform. 14 (2005) 799–811, <https://doi.org/10.1361/10594905X75646>.
- [5] J. Coakley, V.A. Vorontsov, N.G. Jones, A. Radecka, P.A.J. Bagot, K.C. Littrell, R.K. Heenan, F. Hu, A.P. Magyar, D.C. Bell, D. Dye, Precipitation processes in the Beta-Titanium alloy Ti-5Al-5Mo-5V-3Cr, J. Alloys Compd. 646 (2015) 946–953, <https://doi.org/10.1016/j.jallcom.2015.05.251>.
- [6] Y. Zheng, J.M. Sosa, H.L. Fraser, On the influence of athermal ω and α phase instabilities on the scale of precipitation of the α phase in metastable β -Ti alloys, JOM 68 (2016) 1343–1349, <https://doi.org/10.1007/s11837-016-1860-y>.
- [7] Y. Zheng, R.E.A. Williams, D. Wang, R. Shi, S. Nag, P. Kamal, J.M. Sosa, R. Banerjee, Y. Wang, H.L. Fraser, Role of ω phase in the formation of extremely refined intragranular α precipitates in metastable β -titanium alloys, Acta Mater. 103 (2016) 850–858, <https://doi.org/10.1016/j.actamat.2015.11.020>.
- [8] R.P. Koli, A. Devaraj, A review of metastable beta titanium alloys, Metals (Base) 8 (2018) 506–546, <https://doi.org/10.3390/met8070506>.
- [9] T. Gloriant, G. Tesier, F. Sun, I. Thibon, F. Prima, J.L. Souheyroux, Characterization of nanophase precipitation in a metastable β titanium-based alloy by electrical resistivity, dilatometry and neutron diffraction, Scripta Mater. 58 (2008) 271–274, <https://doi.org/10.1016/j.scriptamat.2007.10.007>.
- [10] B. Tang, Y. Chu, M. Zhang, C. Meng, J. Fan, H. Kou, J. Li, The ω phase transformation during the low temperature aging and low rate heating process of metastable β titanium alloys, Mater. Chem. Phys. 239 (2020) 122125, <https://doi.org/10.1016/j.matchemphys.2019.122125>.
- [11] L. Ren, W. Xiao, W. Han, C. Ma, L. Zhou, Influence of duplex aging on secondary α precipitates and mechanical properties of the near β -Ti alloy Ti-55531, Mater. Char. 144 (2018) 1–8, <https://doi.org/10.1016/j.matchar.2018.06.025>.
- [12] Y. Zheng, R.E.A. Williams, J.M. Sosa, T. Alam, Y. Wang, R. Banerjee, H.L. Fraser, The indirect influence of the ω phase on the degree of refinement of distributions of the α phase in metastable β -Titanium alloys, Acta Mater. 103 (2016) 165–173, <https://doi.org/10.1016/j.actamat.2015.09.053>.
- [13] S. Nag, R. Banerjee, J.Y. Hwang, M. Harper, H.L. Fraser, Elemental partitioning between α and β phases in the Ti-5Al-5Mo-5V-3Cr-0.5Fe (Ti-5553) alloy, Philos. Mag. 89 (2009) 535–552, <https://doi.org/10.1080/14786430802613158>.
- [14] A. Settefrati, E. Aeby-Gautier, B. Appolaire, M. Dehmas, G. Geandier, G. Khelifati, Low temperature transformation in the β -metastable Ti 5553 alloy, Mater. Sci. Forum (2013) 738–739, <http://doi.org/10.4028/www.scientific.net/MSF.738-739.97>.
- [15] E. Aeby-Gautier, A. Settefrati, F. Bruneseaux, B. Appolaire, B. Demand, M. Dehmas, G. Geandier, P. Boulet, Isothermal α' formation in β metastable titanium alloys, J. Alloys Compd. 577 (2013) 5439–5443, <https://doi.org/10.1016/j.jallcom.2012.02.046>.
- [16] P. Barriobero-Vila, G. Requena, S. Schwarz, F. Warchonicka, T. Buslaps, Influence of phase transformation kinetics on the formation of α in a β -quenched Ti-5Al-5Mo-5V-3Cr-1Zr alloy, Acta Mater. 95 (2015) 90–101, <https://doi.org/10.1016/j.actamat.2015.05.068>.
- [17] P. Barriobero-Vila, G. Requena, F. Warchonicka, A. Stark, N. Schell, T. Buslaps, Phase transformation kinetics during continuous heating of a β -quenched Ti-10V-2Fe-3Al alloy, J. Mater. Sci. 50 (2014) 1412–1426, <https://doi.org/10.1007/s10853-014-8701-6>.
- [18] R.P.M. Guimarães, B. Callegari, F. Warchonicka, K. Aristizabal, F. Soldera, F. Mücklich, H.C. Pinto, In-situ analysis of the phase transformation kinetics in the β -water quenched Ti-5Al-5Mo-5V-3Cr-1Zr alloy during ageing after fast heating, Quantum Beam Sci. 4 (2020) 1–16, <https://doi.org/10.3390/qbs4010012>.
- [19] O.M. Ivasishin, P.E. Markovskiy, S.L. Semiatin, C.H. Ward, Aging response of coarse- and fine-grained β titanium alloys, Mater. Sci. Eng. A. 405 (2005) 296–305, <https://doi.org/10.1016/j.msea.2005.06.027>.
- [20] Y. Zheng, R.E.A. Williams, H.L. Fraser, Characterization of a previously unidentified ordered orthorhombic metastable phase in Ti-5Al-5Mo-5V-3Cr, Scripta Mater. 113 (2016) 202–205, <https://doi.org/10.1016/j.scriptamat.2015.10.037>.
- [21] A. Settefrati, M. Dehmas, G. Geandier, B. Demand, E. Aeby-Gautier, B. Appolaire, G. Khelifati, J. Delfosse, Precipitation sequences in beta metastable phase of Ti-5553 alloy during ageing, Proc. 12th World Conf. Titan. (2012) 468–472.
- [22] J.C. Fanning, Properties of TIMETAL 555 (Ti-5Al-5Mo-5V-3Cr-0.6Fe), J. Mater. Eng. Perform. 14 (2005) 788–791, <https://doi.org/10.1361/10594905X75628>.
- [23] J.C. Teixeira, B. Appolaire, E. Aeby-Gautier, S. Denis, F. Bruneseaux, Modeling of the effect of the β phase deformation on the α phase precipitation in near- β titanium alloys, Acta Mater. 54 (2006) 4261–4271, <https://doi.org/10.1016/j.actamat.2006.05.019>.
- [24] B. Callegari, J.P. Oliveira, R.S. Coelho, P.P. Brito, N. Schell, F.A. Soldera, F. Mücklich, M.I. Sadik, J.L. Garcia, H.C. Pinto, New insights into the microstructural evolution of Ti-5Al-5Mo-5V-3Cr alloy during hot working, Mater. Char. 162 (2020) 110180, <https://doi.org/10.1016/j.matchar.2020.110180>.
- [25] R. Boyer, C. Eisch, E.W. Collins, Materials Property Handbook: Titanium Alloys, ASM International, 1994.
- [26] L. Lutterotti, S. Matthies, H.-R. Wenk, A.S. Schultz, J.W. Richardson, Combined texture and structure analysis of deformed limestone from time-of-flight neutron diffraction spectra, J. Appl. Phys. 81 (1997) 594, <https://doi.org/10.1063/1.364220>.
- [27] W. Kraus, G. Nolze, Powder cell - a program for the representation and manipulation of crystal structures and calculation of the resulting X-ray powder patterns, J. Appl. Crystallogr. 29 (1996) 301–303, <https://doi.org/10.1107/S0021889895014920>.
- [28] S. Banerjee, R. Tewari, G.K. Dey, Omega phase transformation - morphologies and mechanisms, Int. J. Mater. Res. 97 (2006) 963–977, <https://doi.org/10.3139/146.101327>.
- [29] N.G. Jones, R.J. Dashwood, M. Jackson, D. Dye, β Phase decomposition in Ti-5Al-5Mo-5V-3Cr, Acta Mater. 57 (2009) 3830–3839, <https://doi.org/10.1016/j.actamat.2009.04.031>.
- [30] M. Bönisch, M. Calin, L. Giebeler, A. Helth, A. Gebert, W. Skrotzki, J. Eckert, Composition-dependent magnitude of atomic shuffles in Ti-Nb martensites, J. Appl. Crystallogr. 47 (2014) 1374–1379, <https://doi.org/10.1107/S1600576714012576>.
- [31] A. Settefrati, E. Aeby-Gautier, M. Dehmas, G. Geandier, B. Appolaire, S. Audon, J. Delfosse, Precipitation in a near β titanium alloy on ageing: influence of heating rate and chemical composition of the beta-metastable phase, Solid State Phenom. 172–174 (2011) 760–765, <https://doi.org/10.4028/www.scientific.net/SSP.172-174.760>.
- [32] G. Geandier, E. Aeby-Gautier, A. Settefrati, M. Dehmas, B. Appolaire, Study of diffusible transformations by high energy X-ray diffraction, Compt. Rendus Phys. 13 (2012) 257–267, <https://doi.org/10.1016/j.crhy.2011.12.001>.
- [33] P. Barriobero-Vila, G. Requena, T. Buslaps, M. Alfeld, U. Boesenberg, Role of element partitioning on the α - β phase transformation kinetics of a bi-modal Ti-6Al-5V-2Sn alloy during continuous heating, J. Alloys Compd. 626 (2015) 330–339, <https://doi.org/10.1016/j.jallcom.2014.11.176>.
- [34] S. Banumathy, R.K. Mandal, A.K. Singh, Structure of orthorhombic martensitic phase in binary Ti-Nb alloys, J. Appl. Phys. 106 (2009), <https://doi.org/10.1063/1.3255966>.

- [35] Y. Mantani, M. Tajima, Phase transformation of quenched α' martensite by aging in Ti-Nb alloys, *Mater. Sci. Eng. A* (2006) 438–440, <https://doi.org/10.1016/j.msea.2006.02.180>, 315–319.
- [36] E.S.N. Lopes, A. Cremasco, C.R.M. Afonso, R. Caram, Effects of double aging heat treatment on the microstructure, Vickers hardness and elastic modulus of Ti-Nb alloys, *Mater. Char.* 62 (2011) 673–680, <https://doi.org/10.1016/j.matchar.2011.04.015>.
- [37] F.M. Bai, X. Ye, H.Y. Zhang, H.W. Zhou, M. Song, Y.X. Sun, Y.Z. He, A significant increase in the hardness of nanotwinned titanium alloys prepared via the martensitic phase transformation, *Mater. Lett.* 255 (2019) 126507, <https://doi.org/10.1016/j.matlet.2019.126507>.